Photochemical Study of Vitamin K and Vitamin B Derivatives and Their Applications as Photo-induced Antimicrobial Agents

By

ZHENG ZHANG

DISSERTATION

Submitted in partial satisfaction of the requirements for the degree of

DOCTOR OF PHILOSOPHY

in

Agricultural and Environmental Chemistry

in the

OFFICE OF GRADUATE STUDIES

of the

UNIVERSITY OF CALIFORNIA

DAVIS

Approved:

Gang Sun, Chair

Cort Anastasio

Luxin Wang

Committee in Charge

2021

ACKNOWLEDGMENT

I would like to grant oceans of thanks to my advisor, Professor Gang Sun, for his guidance and help in my research. Dr. Sun has been my advisor since my senior year as an undergraduate. With his help, I obtained my Master's degree. Dr. Sun is always enthusiastic about research, which largely influences me during my road to the Ph.D. degree. Every time I share my ideas with Dr. Sun, he encourages me and offers constructive suggestions at the same time. He is always there and ready to discuss with me when I have trouble in my research and get confused. He encourages his students in divergent thinking and tries his best to provide the platform on which we can be ourselves to the best and the fullest. Dr. Sun is no doubt the best advisor and instructor in my research and in my life. I couldn't believe I can finish my Ph.D. degree without his instruction and help.

My deep and sincere thanks go to my qualification exam committee: Prof. Cort Anastasio (chair), Prof. Luxin Wang, Prof. Peter Green, Prof. Roger Boulton, and Prof. Charlie Li, for their rigorous scholarship, numerous insightful comments, and valuable suggestions. Also, I appreciate Prof. Anastasio and Porf. Wang for serving as my dissertation committee members.

My thanks also go to all my lab mates in Dr. Gang Sun's group for their valuable suggestions and critiques which are of help and importance in making this dissertation. Dr. Yang Si led me to the world of scientific research when I was an undergraduate student in this group. He helps me discover my great interest in the scientific world. Cunyi Zhao, Peixin Tang, Yue Ma, and Jiahan Zou provide me with substantial suggestions and helps in my research. I also appreciate Xinyue Wang and Yixuan Pan who greatly helped me conduct the experiments and collect the experimental data as undergraduate research assistants.

I also want to express my sincere attitude to all my collaborators. In particular, I would like to gratefully acknowledge Prof. Luxin Wang, Prof. Nitin Nitin, Prof. Brian G Murphy, Prof. Tina Jeoh, Dr. Ahmed Y El-Moghazy, Dr. Lina Sheng, Nicharee Wisuthiphaet, and Diego Castillo for their cooperation and thoughtful discussions. The involvement of all my collaborators largely enriches the research content and increases the research depth.

I want to thank my friends, Haoqian Miao, Bofeng Pan, Huitao Ling, and Yichen Li, who made my life in Davis memorable. My life in Davis would not be colorful and wonderful without them.

Moreover, I want to specifically thank my girlfriend, Miss Wanrong Wu. Thank you for your support, encouragement, love, and your patience.

Lastly, and most importantly, I want to thank my family, my father, Guorong Zhang, and my mother, Jie Zheng. They are always there and encourage me to challenge myself and pursue my dreams. Their unconditional and endless love will always keep me running forward.

Photochemical Study of Vitamin K and Vitamin B Derivatives and Their Applications as Photo-induced Antimicrobial Agents

Abstract

The photoactivity of a series of vitamin K and vitamin B derivatives was investigated systematically by combining theoretical and computational modeling methods with empirical evidences and experiments. The photochemical properties of lipophilic vitamin K derivatives, including vitamin K_1, K_2, K_3, and K_4, water-soluble vitamin K_3, as well as water-soluble vitamin B_2 derivatives including riboflavin and flavin mononucleotide, are the examples discussed in this work. Some of the vitamins are proven to efficiently generate oxidative triplet excited state (T_1) and reactive oxygen species (ROS), such as hydroxyl radicals ($HO\cdot$), hydrogen peroxide (H_2O_2), and singlet oxygen ($^1O_2$), via the intersystem crossing (ISC) process followed by the type I or type II photoreaction under proper photoirradiation conditions. The generated active species are non-selectively and efficiently bio-lethal to diverse microorganisms including Gram-positive and Gram-positive bacteria, as well as viruses. Meanwhile, some vitamins exhibit excellent photoinduced antimicrobial durability while maintaining their robust antimicrobial function under long-term photo exposure, representing the good photosensitizer nature of these vitamins.

In this dissertation, chapter 1 introduces the basic photochemistry principles and photoreaction mechanisms of the aromatic ketone, the parent structure of vitamin K derivatives. Representative inorganic and organic photosensitizers are then identified and discussed. Meanwhile, some natural photosensitizers that can be extracted from natural products are screened. The photoactivity and photochemical properties of some common vitamins are presented as well.

In Chapter 2, the photochemistry of the lipophilic vitamin $K_{1\text{-}4}$ is discussed in detail by employing the Gaussian computational modeling package. Vitamin K_3 was proven the robust

photosensitizer in generating either HO· or $^1O_2$ via type I or type II photoreaction among four vitamin K derivatives. In the following experiments, vitamin K_3 demonstrated its highly efficient photoinduced antibacterial function and excellent durability against both Gram-negative and Gram-positive bacteria under daylight irradiation. The successful combination of the theoretical modeling and experiments provides a solid platform to study the photochemistry of photosensitizers at the molecular level.

In Chapter 3, vitamin K_1, vitamin K_3, or vitamin K_4 were blended with hydrophobic polyacrylonitrile (PAN) or hydrophobic poly (vinyl alcohol-co-ethylene) (PVA-co-PE) and electrospun to nanofibrous membranes with fibrous diameters of 200-290 nm. The VK_3/PVA-co-PE nanofibrous membrane was proven to be the most efficient photoactive nano-membrane in generating ROS under daylight irradiation. The VK_3/PVA-co-PE nanofibrous membrane exhibits robust and non-selective microbicidal performance against Gram-negative *Escherichia coli* bacteria, Gram-positive *Listeria innocua* bacteria, T7 bacteriophage virus, and Feline Infectious Peritonitis coronavirus under daylight irradiation. Excellent photoinduced antimicrobial durability of the VK_3/PVA-co-PE nanofibrous membrane was proven, which confirms the conclusion in chapter 2 and indicates that the application potential of VK_3 as a daylight-induced antimicrobial agent was promising.

In chapter 4, the photoactivity of a water-soluble vitamin K_3, menadione sodium bisulfite (MSB), is discovered and discussed in detail for the first time. It was proven that the triplet MSB could efficiently inactivate bacteria even in the absence of hydrogen donors under UVA (365 nm) irradiation. The determinant factor that affects the photoinduced antibacterial function of MSB is the distance between the photoactive site and the target microorganisms. Excellent photoinduced

antibacterial durability of MSB was observed, indicating the photochemical reaction cycles of vitamin Ks with the aromatic ketone structure.

In chapter 5, the photochemistry of two water-soluble vitamin B_2 derivatives, riboflavin (RF) and flavin mononucleotide (FMN) was studied and discussed. Both RF and FMN were found to produce H_2O_2 and $^1O_2$ via type I or II photoreaction due to the formation of the oxidative T_1. However, RF and FMN show limited photoinduced antibacterial function against bacteria under cool white (370-750 nm) or UVA irradiation. The RF/PVA-co-PE and FMN/PVA-co-PE nanofibrous membranes exhibit good photoinduced antibacterial function against bacteria under UVA irradiation, which is probably due to the intimate contact of the photoactive nanofibrous membranes with target bacteria. Therefore, a close bacterial contact should be provided to RF or FMN to achieve better photoinduced antibacterial performance.

The final chapter concludes the photochemistry and photoactivity of vitamin derivatives and their photoinduced antimicrobial function, which may be applied in the fabrication of safe-to-use, highly efficient, extremely durable, and environmentally friendly photoinduced antimicrobial materials that can be applied in bioprotection and food safety related areas.

List of Figures

Figure 2.4. UV-vis spectra of various VKs along with the spectrum of the D65 standard daylight source.

Figure 2.5. Computed frontier molecular orbitals and UV-vis spectrum of various chemically modified VK_1 derivatives (a) hydrogenation (b) ring opening after epoxidation by using CH_3OH as nucleophiles (c) oxidation of the double bond.

Figure 2.6 Photo-reactivity of the type I reaction for the vitamin K derivatives. (a) ESP-mapped electron density of the ground and triplet states of VKs. The δ represents ESP charges on carbonyl oxygens of VKs. (b and c) Detailed mechanisms of type I reaction and computed △G for each step of the reactions. The (i), (ii), (iii), and (ix) represent VK_1, VK_2, VK_3, and VK_4, respectively. (d to f) Quantification of HO· generated by various VKs under different irradiation resources (d for D65, e for UVA, and f for UVB) versus time (irradiation in white and dark in gray). (g) Summary of the HO· generation efficiencies of various VKs under different light irradiations.

Figure 2.7. Photo-reactivity of type II reaction of vitamin K derivatives. (a and b) Detailed mechanisms of the type II reaction and computed △G values of the reactions. (c to f) Singlet oxygen production of the four VKs under UVA and UVB irradiation versus time. (g) Summary of singlet oxygen production of the four VKs under UVA and UVB irradiation. (h to j) HO· production of four VKs under light irradiation in insufficient hydrogen donor environment (h for UVA and i for UVB).

Figure 2.8. Hydrogen donor effect on the photo-reactivity of vitamin K_3. (a to e) UV-vis spectra of VK_3 in various solvent systems (from a to e, acetonitrile, isopropanol, ethyl alcohol, cyclohexane, and tetrahydrofuran, respectively) with their theoretically computed frontier molecular orbitals. (f) ESP-mapped electron density of the ground state and triplet state of vitamin

K_3 in various solvent systems. (g to j) Quantification of HO· generated by VK_3 in various solvent systems under different irradiation resources.

Figure 2.9. Comparison between calculated UV-vis spectra (a) and experimental UV-vis spectra (b) of VK_3 in various solvents.

Figure 2.10. Daylight-induced antibacterial performance of vitamin K_3 (a and e) Time-dependent bactericidal activity of VK_3 against *E.coli* (a) and *L.innocua* (e) under daylight irradiation. (b and f) Seven-cycle bactericidal activity of VK_3 against *E.coli* (b) and *L.inncoua* (f) under daylight irradiation. (c and g) SEM images of *E.coli* (c) and *L.innocua* (g) in PBS without any treatment. (d and h) SEM images of *E.coli* (d) and *L.innocua* (h) in VK_3 suspension after 90-min daylight irradiation.

Figure 3.1. Fabrication and Biocidal Functions of VNFMs. (a) Schematic illustration of photoactivated biocidal function of VNFMs. (b) Mechanism of the photoactive ROS generation cycle of VNFMs. (c) Micro-structure of various VNFMs.

Figure 3.2. Microstructure of electrospun (a) PVA-co-PE and (b) PAN nanofibrous membranes.

Figure 3.3. Fiber diameter distribution of electrospun nanofibrous membranes (n=50) (a) PVA-co-PE (b) PVA-co-PE/VK_1 (c) PVA-co-PE/VK_3 (d) PVA-co-PE/VK_4 (e) PAN (f) PAN/VK_1 (g) PAN/VK_3 (h) PAN/VK_4.

Figure 3.4. ^{1}H NMR spectrum of (a) PAN (b) PVA-co-PE (c) PAN/VK_1 (d) PVA-co-PE/VK_1 (e) PAN/VK_3 (f) PVA-co-PE/VK_3 (g) PAN/VK_4 (h) PVA-co-PE/VK_4.

Figure 3.5. Diffuse reflection UV-vis spectra and excitation analysis of VNFMs. (a) VK_1NFMs, (b) VK_3NFMs, and (c) VK_4NFMs.

Figure 3.6. UV-DRS spectra of various VNFMs along with the emission spectrum of the D65 standard daylight source.

Figure 3.7. Production of reactive oxygen species by VNFMs under various photo-irradiation resources. Hydroxyl radical production of VNFMs under (a) D65, (b) UVA, and (c) UVB. Hydrogen peroxide production of VNFMs under (d) D65, (e) UVA, and (f) UVB. Singlet oxygen production of VNFMs under (g) D65, (h) UVA, and (i) UVB. Summary of (j) hydroxyl radical production, (k) hydrogen peroxide production, and (l) singlet oxygen production of VNFMs.

Figure 3.8. Gibbs free energy and frontier orbital analysis of the Type I photoreaction, and relative singlet oxygen production from the Type II photoreaction. Computed Type I photoreaction $\triangle G$ for (a) VK_1, (b)VK_3, and (c)VK_4 with PAN and PVA-co-PE. The color represents the ESP-mapped electron density of the VKs and polymers. The δ is the ESP charge on the carbonyl oxygen in VKs. (d) Summarized $\triangle G$ for each step in the Type I photoreaction. (e) Orbital energy analysis on VKs and hydrogen donors. (f) Singlet oxygen production of VK_1, VK_3, VK_4, and Rose Bengal under D65, UVA, and UVB irradiation.

Figure 3.9. Photo-induced antibacterial function of VNFMs. Time-dependent bactericidal activity of (a) PVA-co-PE/VK_3 and (b) PAN/VK_3 VNFMs against *E. coli* under D65 and UVA (c and d) irradiation. Time-dependent bactericidal activity of PVA-co-PE/VK_3 VNFM against *L. innocua* under (e) D65 and (f) UVA irradiation. For (a-f), VNFM without light (Dark w/VK_3) and pristine nanofibrous membrane with light (UVA or D65 w/out VK_3) are used as controls. Five-time cycle bactericidal activity of PVA-co-PE/VK_3 VNFM against (g) *E. coli* and (h) *L. innocua* under D65 irradiation. SEM morphology of (i) *E. coli* and (k) *L. innocua* without any treatment. SEM morphology of (j) *E. coli* and (l) *L. innocua* on PVA-co-PE/VK_3 VNFM after 60-min and 90-min D65 irradiation, respectively.

Figure 3.10. Daylight-induced antiviral function of PVA-co-PE/VK_3 VNFMs. (a) Time-dependent antiviral activity of PVA-co-PE/VK_3 VNFM against T7 bacteriophage under D65 irradiation (PVA-co-PE/VK_3 VNFM without daylight and pristine PVA-co-PE nanofibrous membrane with daylight as controls). (b) Five-time cycle antiviral activity of PVA-co-PE/VK_3 VNFM against T7 bacteriophage under D65 irradiation. (c) Antiviral results against FIPV of PVA-co-PE/VK_3 VNFM and pristine PVA-co-PE nanofibrous membranes under daylight D65 irradiation. (d) RT-PCR results of the FIPV on the materials.

Figure 4.1. Photo reactivity of MSB. (a) Schematic Jablonski diagram describing the photoexcitation process of MSB and following photoreactions. (b) UV-vis absorption spectrum of 20 μM MSB in H_2O (Inset: UV-vis spectrum of 1mM MSB in H_2O) and computational frontier molecular orbitals of MSB. HOMO: highest occupied molecular orbital; LUMO: lowest unoccupied molecular orbital; SOMO: semi occupied molecular orbital. (c) Proposed photoreaction mechanism of MSB in aerobic environment. (d) ESP-mapped electron density of ground-state and triplet-state MSB. The δ is the ESP charge on the carbonyl oxygen of MSB in each state.

Figure 4.2. Computational and experimental UV-vis spectra of MSB in H_2O (The calculated spectrum was fixed to have the same absorbance peak height as the experimental spectrum).

Figure 4.3. Photo-reactivity of type I and type II reactions of MSB. (a) Computed Gibbs energy changes (△G) for the type I and type II photoreactions. (b) UV-vis spectra of 20 μM MSB in H_2O under UVA (365 nm) irradiation after various time durations. Productions of (c) hydroxyl radical and (d) hydrogen peroxide from 20 μM MSB in 10% EtOH/H_2O solution, and I singlet oxygen production from 20 μM MSB in 0.01M PBS solution under UVB (312 nm), UVA (365 nm) and

cool white (CW, 370-750 nm) photoirradiation or dark conditions (irradiation in white and dark periods in gray).

Figure 4.4. UV-vis absorption spectra of 0.2 mM MSB in 10% EtOH/H2O under UVA (365 nm) irradiation.

Figure 4.5. (a) p-NDA Photostability under CW, UVA, and UVB irradiation. (b) p-NDA decomposition in MSB solution under UVB irradiation.

Figure 4.6. ROS production from MSB and VK_3. (a) Chemical structures of MSB and VK_3. (b) UV-vis spectra of 20 μM MSB or VK_3 in 10% EtOH/H_2O solution. Production of (c) hydroxyl radical and (d) hydrogen peroxide from 20 μM MSB or VK_3 in H_2O, PBS, and 10% EtOH/H_2O solutions under the same photoirradiation conditions after 20-min exposure. I Singlet oxygen production from 20 μM MSB or VK_3 in 10% EtOH/PBS under the photoirradiation conditions after 20-min exposure.

Figure 4.7. UVB (312 nm) induced antibacterial performance of 2 mM MSB in 4% EtOH/PBS against *E. coli*.

Figure 4.8. Photo-induced antibacterial function of MSB in 4% EtOH/PBS solution. UVA (365 nm) induced antibacterial activity of 2 mM MSB in 4% EtOH/PBS against (a) *E. coli* and (b) *L. innocua*. Five-time cycle bactericidal activity of 2 mM MSB against (c) *E. coli* and (d) *L. innocua* in 4% EtOH/PBS under UVA (365 nm) irradiation for 90 min. Cool white light (CW) induced antibacterial activity of 2 mM MSB in 4% EtOH/PBS against (e) *E. coli* and (f) *L. innocua*.

Figure 4.9. Photo-induced antibacterial function of MSB in PBS solution. UVA (365 nm) induced antibacterial activity of 2 mM MSB in PBS against (a) *E. coli* and (b) *L. innocua*. Five-time cycle bactericidal activity of 2 mM MSB against (c) *E. coli* and (d) *L. innocua* in PBS under UVA (365

nm) irradiation for 60 min. Cool white light (CW) induced antibacterial activity of 2 mM MSB in PBS against (e) *E. coli* and (f) *L. innocua***.**

Figure 4.10. Fluorescent live/dead bacterial viability assay of *E. coli* (a, b, e, and f) and *L. innocua* (c, d, g, and h) cells in PBS without MSB under dark conditions (a to d) or in PBS with 2 mM MSB (e to h) under UVA (365 nm) irradiation for 60 min.

Figure 4.11. Solvent effect on the photo-induced antibacterial function of MSB. (a) UVA (365 nm) induced antibacterial activity of 2 mM MSB in various solvent systems. (b) UVA (365 nm) induced degradation of 20 μM Reactive Black 5 by 0.2 mM MSB in various solvent systems. (c) Hydroxyl radical production from 50 μM MSB in various solvent systems under UVB (312 nm) irradiation. (d) Hydrogen peroxide production from 50 μM MSB in various solvent systems after 20-min UVB (312 nm) irradiation.

Figure 4.12. Chemical structure of Reactive Black 5.

Figure 4.13. Amphiphilicity of MSB and solubility of VK_3 in ethanol and ethyl acetate. (a) Surface tension test with various MSB concentrations in deionized (DI) water. (b) Light transmittance of 2 mM VK_3 in 8% EtOH/PBS and 8% EtOAc/PBS solution systems at 660 nm after 10 min, 20 min, and 30 min of placement at room temperature. (c) UVA (365 nm) induced antibacterial activities of 2 mM VK_3 and 2 mM MSB in 4% EtOAc/PBS and 4% EtOH/PBS solution systems against *E. coli.* (d) Clarity of 2 mM VK_3 in 8% EtOH/PBS and 8% EtOAc/PBS solution systems at 0 min and 30 min of replacement at room temperature, respectively.

Figure 4.14. The acceleration effect of $CHCl_3$ on MSB antibacterial function. (a) *E. coli* affinity to PBS, $CHCl_3$, and EtOAc. (b) UVA (365 nm) induced antibacterial activity of 0.25 mM VK_3 in 0.4% $CHCl_3$/PBS and 0.4% EtOAc/PBS solution systems. (c) UVA (365 nm) induced antibacterial

activity of 0.25 mM MSB in 0.4% $CHCl_3$/PBS and 0.4% EtOAc/PBS solution systems. (d) Hydrogen peroxide production from 0.25 mM MSB in various solvent systems after 20-min UVA (365 nm) irradiation.

Figure 4.15. Dark toxicity of 2 mM MSB or VK_3 toward E. coli in 4% EtOH/PBS and 4% EtOAc/PBS solution systems after 30-min incubation.

Figure 5.1. Photoreactivity of RF and FMN. (a) Schematic Jablonski diagram illustrating the photoexcitation process of VB_2 derivatives and following photoreactions. (b) Type I and type II photoreactions of VB_2 derivatives after the formation of the lowest triplet excited state. (c) UV-vis absorption spectrum of 20 μM FMN in H_2O and computational frontier molecular orbitals of FMN. HOMO: highest occupied molecular orbital; LUMO: lowest unoccupied molecular orbital. (d) UV-vis absorption spectrum of 20 μM RF in H_2O and computational frontier molecular orbitals of RF. ESP-mapped electron density of ground-state and triplet-state (e) FMN and (f) RF. The δ is the ESP charge on the carbonyl oxygen of RF or FMN in each state.

Figure 5.2. Computational UV-vis spectra of (a) FMN and (b) RF in H_2O.

Figure 5.3. Photoreactivity of the type I and type II photoreactions of FMN and RF. (a) Hydrogen peroxide production from 20 μM RF or FMN in H_2O and (b) singlet oxygen production from 2 μM RF or FMN in 0.01M PBS solution under CW and UVA (365 nm) photoirradiation or dark conditions (irradiation in white and dark periods in gray). Hydrogen donor effect on the hydrogen abstraction reaction on the 20 μM RF or FMN in various solution systems under (c) CW and (d) UVA (365 nm) photoirradiation. Photostability of 20 μM (e and g) RF or (f and h) FMN under (e and f) CW and (g and h) UVA (365 nm) photoirradiation. (i) Orbital energy analysis on RF, FMN, and hydrogen donor (take EtOH as an example). Photoinduced hydrogen abstraction reaction on

(j) carbonyl and (k) imine groups in the triplet VB_2 derivatives. (l) Gibbs free energy change of the intramolecular hydrogen abstraction reactions in the triplet VB_2 derivatives. (m) Gibbs free energy change of the singlet oxygen photosensitization reaction. (n) SOMO of the VB_2-NH·. (o) Intramolecular hydrogen abstraction in the triplet VB_2 derivatives and the Gibbs free energy change of the formed dihydroflavin (VB_2H_2).

Figure 5.4. Computational UV-vis spectra of (a) lumichrome and (b) lumiflavin in H_2O.

Figure 5.5. (a) Hydrogen peroxide and (b) singlet oxygen production of 20 μM FMN or MSB in 10% EtOH/H_2O solution under CW, UVA (365 nm), and UVB (312 nm) photoirradiation or dark conditions (irradiation in white and dark periods in gray).

Figure 5.6. Photoinduced antibacterial function of RF and FMN in PBS solution. (a) 2 mM RF or FMN in the PBS solution against *E. coli* under UVA (365 nm) irradiation. Different concentrated (b) FMN and (c) RF in PBS solution against *E. coli* under UVA (365 nm) irradiation for 30 min. 2 mM FMN in the PBS solution against (d) *E. coli* or (e) *L. innocua* under UVA (365 nm) irradiation for 30, 60, and 90 min. 2 mM FMN in the 4%EtOH/PBS solution against (f) *L. innocua* under UVA (365 nm) irradiation for 30, 60, and 90 min.

Figure 5.7. Photoinduced antibacterial activity of MB in PBS solution. 2 mM MB in PBS solution against (a) *E. coli* and (b) *L.inncoua* under CW and UVA (365 nm) irradiation for 60 min. (c) Photoinduced singlet oxygen production of 2 mM FMN or MB in PBS under CW and UVA irradiation. (d) Photoinduced antibacterial activity of 2 mM FMN, 2 mM MB, and 2 mM FMN+2 mM MB in PBS solution against *E. coli* under UVA irradiation for 30 min.

Figure 5.8. Photoinduced antibacterial activity of RF/PVA-co-PE and FMN/PVA-co-PE nanofibrous membranes. SEM images and nanofiber diameters of (a) PVA-co-PE, (b) RF/PVA-

co-PE, and (c) FMN/PVA-co-PE nanofibrous membranes (n=30). (d) Time-dependent photoinduced antibacterial activity of RF/PVA-co-PE and FMN/PVA-co-PE nanofibrous membranes against *E. coli* under UVA irradiation. (e) Photoinduced antibacterial activity of RF/PVA-co-PE and FMN/PVA-co-PE nanofibrous membranes against *E. coli* under CW irradiation for 20 min. Photoinduced antibacterial activity of RF/PVA-co-PE and FMN/PVA-co-PE nanofibrous membranes against *L.innocua* under (f) UVA and (g) CW irradiation for 20 min. Five-time cycle photoinduced bactericidal activity of (h) FMN/PVA-co-PE and (i) RF/PVA-co-PE nanofibrous membranes against *E. coli* under UVA irradiation (20 min/cycle). (j) SEM images of *E. coli* and *L. inncoua* in PBS solution. SEM images of (k) *E. coli* and (l) *L. innocua* on the FMN/PVA-co-PE and RF/PVA-co-PE nanofibrous membranes under UVA irradiation for 30 min.

List of Tables

Table of Contents

Chapter 1. Introduction and Literature Review

Abstract

In recent years, because of the frequent outbreaks of emerging infectious diseases (EID) and public hygiene concerns, antimicrobial materials have drawn more attention in several fields, particularly in medical textiles and healthcare-related aspects. Among all existing functional materials, photo-induced antimicrobial materials gain tremendous interest from both academia and industry due to their clean energy consumption, high microbial inactivation efficacy, and environmentally friendly nature of the photoreaction process. Photoactive chemicals can effectively generate reactive oxygen species (ROS) under proper light exposure, which are considered efficient in inactivating microorganisms as a result of the generated oxidative ROS that can non-selectively destroy cellular components in bacteria and functional proteins or nucleic acids in viruses.

This chapter describes the basic photochemistry information such as the photoexcitation and photoreaction of photoactive chemicals including inorganic metal oxides and organic photosensitizers, as well as some natural products that are photoactive and capable of generating biocidal ROS. The application of photoactive chemicals in the preparation of photoinduced antimicrobial materials is also discussed to better reveal the potential of the photoactive chemicals in the microorganism inactivation-related fields.

1.1 Background

Over the past few centuries, global outbreaks of infectious diseases, such as the Black Death in the 14th century and the influenza pandemics in the 20th century, have caused at least 50 million deaths and changed the course of human history, and left indelible memories of miseries[1]. With the improvement of science, technology, and health care condition, the outbreak of infectious

diseases has been mostly efficiently controlled yet still brings suffering to humankind[2]. For instance, the Ebola virus disease in 2014 in West Africa caused significant losses to human life and property, as well as social development[3]. The Coronavirus Disease 2019 (COVID-19, caused by SARS CoV-2) pandemic that is still ravaging the world has caused tremendous losses of human life and depression of the economy in the world[4]. In this case, antimicrobial functional materials by introducing biocidal agents that can inactivate microbes are drawing researchers' attention. A series of biocidal agents, such as chitosan, peptides, and silver nanoparticles, are widely applied in the preparation of bioprotective personal protective equipment (PPE)[5-7]. Nevertheless, the bioprotective functions of these materials are always questioned, especially on the durability and stability during uses, due to their irreversible consumption of the biocides. Rechargeable bioprotective halamine materials have been widely investigated and applied in recent years[8-9]. However, potential release of an irritant chlorine from the halamine materials is a concern, which puts limitations in their applications in certain products.

Photo-induced antimicrobial materials prepared by introducing photoactive chemicals are considered to have high biocidal efficiency, green energy consumption, high durability, and low toxicity, which reveal their great potentials in applications of hygienic and human health protective products. Both inorganic or organic photoactive chemicals have found applications in the antimicrobial-related fields so far and can generate biocidal ROS including singlet oxygen ($^1O_2$), hydroxyl radicals ($HO\cdot$), and hydrogen peroxide (H_2O_2) under proper light exposure on surfaces of materials. In general, the most commonly used inorganic photoactive agents with antimicrobial and detoxifying functions are titanium dioxide, zinc oxide, and some other semiconductors[10]. Organic photosensitizers mainly include benzophenone derivatives[11], anthraquinone derivatives[12], naphthoquinone derivatives[13], phenols[14], and some conjugated heterocycle compounds like

porphyrins[15], benzoylpyridine derivatives[16], as well as some synthetic dyes, such as Rose Bengal[17]. Some natural product extracts[18] and vitamins[19] are also reported to be photoactive and applied in photoinduced antimicrobial-related applications.

This chapter intends to introduce the photoexcitation and photoreaction mechanisms in semiconductors and various common photoreactions in organic photosensitizers that can generate ROS, particularly type I photoreaction in aromatic ketones and type II photosensitization reactions. Some other possible photoreactions in aromatic ketones are also discussed, such as photoreduction[20], photo redox[21], photohydration[22], and decarboxylation[23-24] reactions that may compete with type I photoreaction, resulting in a reduction of ROS production. Meanwhile, this chapter introduces several basic and common inorganic and organic photoactive chemicals that can be employed as photoinduced antimicrobial agents. Especially, some natural or natural derivatized photoactive agents and vitamins are discussed to explore green, sustainable, and safer photoactive chemicals that could be used in medical or food storage-related aspects.

1.2 Mechanism of Photoexcitation and Photoreactions

Although both inorganic metal oxides (such as TiO_2) and organic photosensitizers are photoactive and capable of generating ROS under proper photoirradiation, their excitation process and photoreaction mechanisms are different. Under proper photoirradiation, electrons in TiO_2 can be excited from the valence band to the conduction band[25-26]. The formed conduction band electrons (e^-) and valence band holes (h^+) are both reactive and can be oxidized and reduced to generate ROS that are lethal to microorganisms. Differently, the excitation of organic photosensitizers (such as benzophenone) is generally electron excitation from the highest occupied molecular orbital (HOMO) to the lowest unoccupied molecular orbital (LUMO)[27]. After the formation of excited states, type I or type II photoreactions can happen to generate ROS.

Meanwhile, some other competitive photoreactions such as photoreduction and photodecarboxylation could happen, which may reduce the production of ROS via the suppressed type I or type II photoreactions.

1.2.1 Photoexcitation process and photoreactions in metal oxides

In general, the most commonly used inorganic photoinduced metal oxides with antimicrobial and detoxifying functions are titanium dioxide, silicon dioxide, zinc oxide, nickel oxide, and some other semiconductors[10]. Among them, TiO_2 nanoparticles are the most widely utilized one due to their highly efficient photoreaction under ultraviolet (UV) and visible light exposure. TiO_2 nanoparticles can decompose toxic organic materials into small molecules under UVA irradiation[28]. The photoreactivity of TiO_2 nanoparticles depends on various structural properties, such as morphology, crystallinity, surface area, and doped metals, etc. Under proper photoirradiation, TiO_2 nanoparticles have been proven to inactivate both Gram-positive and Gram-negative bacteria under photoirradiation[29-30], due to the production of biocidal ROS. The photoinduced ROS generation mechanism of TiO_2 is depicted in Figure 1.1.

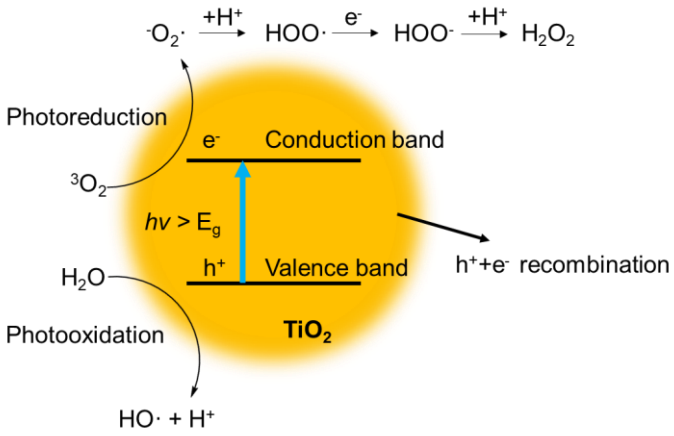

Figure 1.1. Schematic diagram of the photoexcitation and photoreaction process of TiO_2 in aerobic environment.

The widely accepted mechanism is that the semiconductor, TiO_2, can produce conduction band e^- and valence band h^+ when irradiated by UVA that provides the necessary photo energy to overcome the bandgap energy of TiO_2 (E_g=3.2 eV)[28, 31]. The reactions occur on surfaces of the TiO_2 particles, and as a result, nanoparticles possessing ultrahigh specific areas are the most effective form of TiO_2. The majority of the formed electron (e^-) and hole (h^+) would recombine within a short time with the emission of heat[32]. Also, the e^- and h^+ could reduce oxygen or oxidize water to produce ROS, respectively. The e^- could react with triplet oxygen ($^3O_2$) absorbed on the surface of the material and then generate superoxide radical anion ($\cdot O_2^-$), which could subsequently generate hydroperoxyl radical (HOO·) and H_2O_2 by reacting with protons. At the same time, the h^+ can oxidize the organics or react with OH^- or H_2O and oxidize them into HO·. The h^+, H_2O_2, and HO· are reactive and have a high tendency to oxidize various sorts of organic compounds and microbes. In addition, TiO_2 has the potential to be excited by sunlight or daylight by doping metals that can improve the visible light absorbance band of TiO_2[33], which can broaden TiO_2 based photoinduced materials' application fields. Besides, the excited TiO_2 would eventually go back to its original ground state without consumption, which also reveals its good durability as photoinduced antimicrobial agents. However, although TiO_2 related photoactive materials have above mentioned strong points, they do have their inherent shortcomings. For instance, TiO_2 particles used for preparing photo-induced antimicrobial materials are nanoparticles[34], which could penetrate human skins and are toxic to human[35]. Meanwhile, the photoactivity of TiO_2 nanoparticles can not only kill bacterial and chemical compounds around the material but also affect the material matrix, impairing the physical and chemical properties of the materials[10]. Besides, TiO_2 and other inorganic photocatalysts inherently do not have interactions with material matrixes, which also limits the applications of the inorganic photoinduced antimicrobial materials.

1.2.2 Photoexcitation, Type I, and Type II photoreactions

Some organic photoactive chemicals were also proven to be microbiocidal under certain photoirradiation due to the photoinduced generation of ROS. The ROS generation processes can be divided into the type I reaction with the accompanied formation of HO· and H_2O_2, and the type II photosensitization reaction with the generation of $^1O_2$[27]. Nevertheless, both type I and type II photoreactions start from the lowest triplet excited state (T_1) that is relatively stable with a longer lifetime than that of the singlet state[36]. The excitation process and formation of the T_1 can be explained by referring to the Jablonski diagram in Figure 1.2.

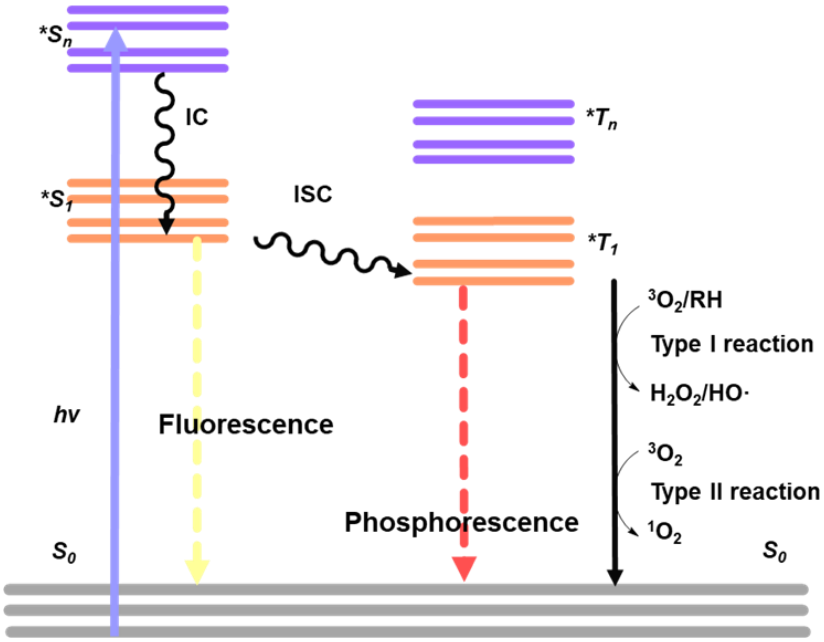

Figure 1.2. Jablonski diagram of the excitation process.

Under photoirradiation, electrons in the ground state (S_0) could be excited to higher singlet excited states (S_n) by absorbing a photon whose energy is equal or higher than the energy gap between S_n and S_0. The formed S_n is unstable with a very short lifetime which can subsequently rapidly relax back to the lowest singlet excited state (S_1) via an internal conversion (IC) process[37].

The S_1 is relatively more stable than S_n but is still less stable than S_0. Then S_1 could relax back to S_0 by IC with nonradiative emission of heat or by radiative emission of fluorescence, or further transfer to T_1 via an intersystem crossing (ISC) process. The quantum yield of ISC is highly dependent on the structures of the molecules. Aromatic ketones, such as benzophenones and naphthoquinones, have very high ISC efficiency, yet aliphatic ketones have very low ISC efficiency[38]. The formed T_1 has slightly lower energy than S_1 and a relatively long lifetime because the relaxation from T_1 to S_0 is spin-forbidden according to El-Sayed's rules[39]. Thus, T_1 should be the most stable excited state from which many photoreactions can start. T_1 could react with electron-rich substrates to form $HO\cdot$ and H_2O_2 or sensitize ground-state triplet oxygen ($^3O_2$) to much more oxidative $^1O_2$. The detailed photoreaction mechanisms will be discussed later. Besides, T_1 could go back to S_0 by radiative emission of phosphorescence, although the process is relatively time-consuming because of the forbidden relaxation[39].

Some aromatic ketones, such as benzophenones, anthraquinones, and naphthoquinones (the parent ring of vitamin K derivatives), are known to be photoactive due to their high ISC efficiency because of the aryl ketone structure[40-45]. The aryl ketone structure has proven to influence the energy of S_1, T_2, and T_1 states, which can largely impact the ISC efficiency via indirect ISC process[36]. The excitation and Jablonski diagram of benzophenone (BP) is depicted in Figure 1.3a as a representative to depict the indirect ISC process of aromatic ketones.

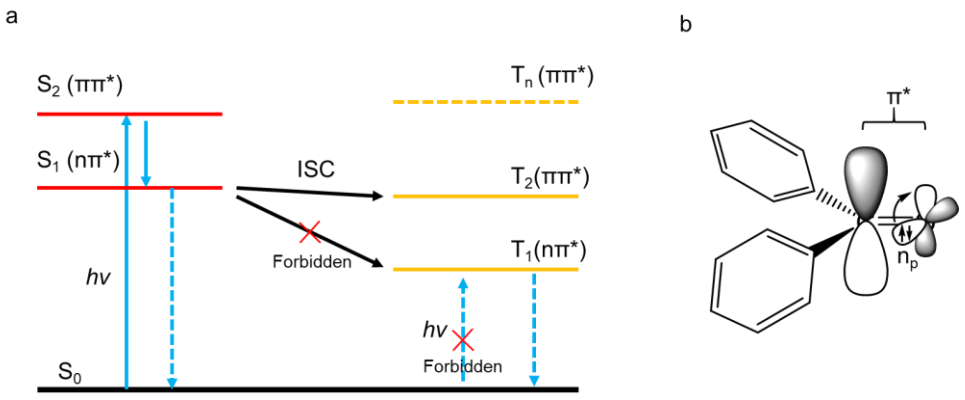

Figure 1.3. (a) Jablonski diagram of benzophenone excitation and ISC process. (b) nπ* transition of the carbonyl group in aromatic ketones under photoirradiation.

Under photoirradiation, electrons in benzophenone can be efficiently excited. Several electron transition types could happen during the excitation process. Electron excited from π bonding orbitals into the carbonyl carbon p* orbital (π* antibonding orbital) forms a ππ* excitation, or electron excited from carbonyl oxygen n_p orbital (nonbonding orbital) into the carbonyl carbon p* orbital forms an nπ* transition (depicted in Figure 1.3b). The nπ* excited states have lower energy than the ππ* excited states[38] (Figure 1.3a). As we have discussed above, most photoreactions start from T_1. However, T_1 (nπ*) of benzophenone cannot be directly formed via S_0-T_1 transition due to the spin forbidden by El-Sayed's rules. T_1 can be formed by the indirect ISC from S_1, which was proven in gaseous benzophenone[37] whose Jablonski diagram is depicted in Figure 1.3a. Under photoirradiation, the electron in benzophenone is effectively excited from the π bonding orbital to the π* antibonding orbital forming an S_2 with ππ* transition. The S_2 can rapidly relax back to S_1 via the IC process. Meanwhile, the aryl ketone structure enables an efficient ISC of the nπ* excited S_1 to an isoenergetic T_2 with ππ* transition. This process is spin allowed by El-Sayed's rules ($S_{\pi\pi^*}$-$T_{n\pi^*}$ and $S_{n\pi^*}$-$T_{\pi\pi^*}$ are allowed, whereas $S_{\pi\pi^*}$-$T_{\pi\pi^*}$ and $S_{n\pi^*}$-$T_{n\pi^*}$ are forbidden). The T_2 can then subsequently go back to lower-energy T_1 efficiently. However, the indirect ISC pathway is not

available for aliphatic ketones[38]. The ISC rate from nπ* excited S_1 to T_1 of aliphatic ketones is much lower than aromatic ketones, which maybe because of the non-isoenergetic S_1 and T_2 due to the absence of the aromatic ring. It is worth noting that either direct ISC (S_1-T_1) or direct excitation from S_0 to T_1 are spin-forbidden in benzophenone. The T_2 is a long-live intermediate during the ISC process from S_1 to T_1.

The nπ* excited T_1 is a biradical with very high oxidative property[38]. The electron in the lone pair of the carbonyl oxygen is excited to carbonyl carbon π* antibonding orbital, leaving the electronegative oxygen more electron-deficient and more oxidative. Thus, the T_1 is considered the most reactive excited state in benzophenone[38]. Although the ππ* excited states are also produced during the excitation, they are known with charge transfer (CT) feature and regarded as the most unreactive states in benzophenone[38]. The formation and reactivity of the T_1 are also largely impacted by substituents and solvent media[38]. The substituents can shift the nπ* T_1 to ππ* T_1 through inductive effects. Electron-donating functional groups can decrease the energy of n_p orbital while increasing the energy of π* orbital. The increased energy gap, therefore, influences the formation of T_1. Additionally, the nπ* excited T_1 is oxidative and electrophilic, and the introduction of an electro-donating functional group could increase the electron density in the carbonyl group and decrease the oxidative property, which makes the T_1 less reactive in the hydrogen abstraction reaction. On the contrary, the addition of electro-withdrawing functional groups was proven to benefit the reactivity of T_1. Moreover, the introduction of a functional group on the ortho position of the aromatic ring should be avoided due to possible intramolecular interactions or reactions, such as the hydrogen-bonding effect[46]. Increasing solvent polarity could also shift nπ* excited T_1 to ππ* excited T_1[46].

Starting from T_1, various photoreactions could happen due to the oxidative property of the excited states. Two photoreactions that could generate ROS are known as type I and type II reactions. The detailed type I and type II photoreaction mechanisms of benzophenone are depicted in Figure 1.4.

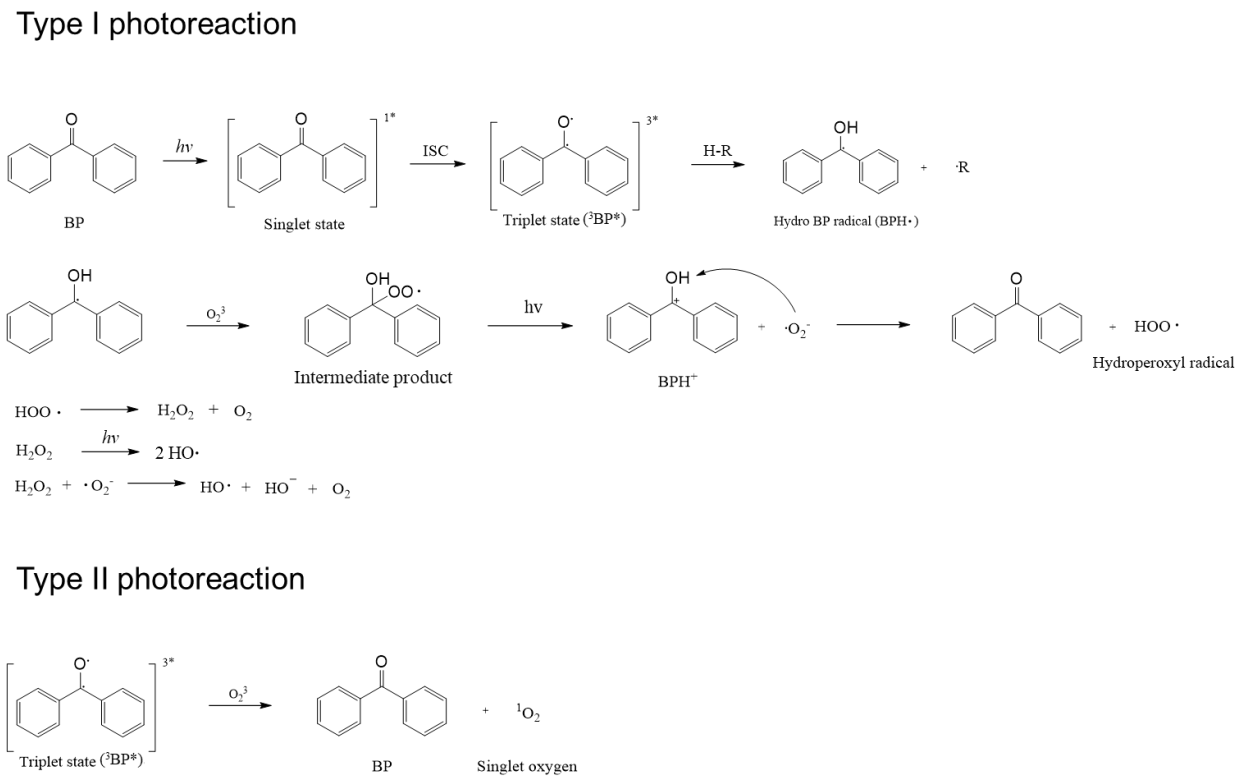

Figure 1.4. Type I and type II photoreaction mechanisms of benzophenone under photoirradiation in an aerobic environment.

After the formation of T_1 (BP^{3*}), type I photoreaction could happen, which is also the predominant photoreaction of the biradical triplet state. According to the literature, hydrogen abstraction and addition to C-C double bonds are favored by T_1[38]. Whereas, the T_1 is relatively stable in the cleavage of the C-C bonds. Because of the excited electron from the n_p orbital of the carbonyl oxygen to π^* antibonding orbital of the carbonyl carbon, the formed $n\pi^*$ excited T_1 is extremely

electron-deficient in the carbonyl oxygen and has an oxygen radical center, which enables the T_1 to abstract a hydrogen atom from nearby hydrogen donors (RH), resulting in the formation of a hydro benzophenone radical (BPH·). This photoreduction process can be also detected in an environment without appropriate hydrogen donors but with good electron donors[38]. For example, the benzophenone T_1 could directly abstract an electron from amines to form a radical anion via electron transfer, followed by a proton transfer to achieve the hydrogen atom transfer to form the BPH·[47]. The benzophenone T_1 could also firstly couple with the electron-rich amines to form a transition state via charge transfer, after which a hydrogen transfer could happen from the amines to the formed BPH·[38]. The electron donors could reduce both ππ* and nπ* T_1 through the energy transfer process[38]. The H abstraction reaction is highly dependent on the hydrogen donors. Appropriate hydrogen donors could be aliphatic C-H bonds, such as the H in the methylene group, and the α-H adjacent to hydroxyl groups[38]. After the formation of the BPH·, the radical could be trapped by oxygen to form an intermediate product (See type I photoreaction in Figure 1.4). The intermediate is unstable and could be disassociated to $\cdot O_2^-$ and BPH^+ under photoirradiation or via thermal decay. The $\cdot O_2^-$ could further react with BPH^+ and abstract a proton to form HOO·. The formed HOO· could transform to HO· and H_2O_2 via a series of radical reactions[11, 48].

Singlet molecular oxygen ($^1O_2$) could be formed via type II photoreaction[49]. Compared with the type I photoreaction, type II photoreaction is a photosensitization process that has no requirement on the electron transition (ππ* or nπ*) of the triplet excited state. In the type II photoreaction, $^1O_2$ is generated through an energy transfer process from T_1 of the photosensitizer (BP^{3*}) to the ground-state triplet oxygen ($^3O_2$) by a collision. Although there is no requirement on the electron transition of the T_1, several other requests should be satisfied[50]: (1) The photosensitizers should have a high absorption coefficient under the excitation light irradiation.

The high absorption coefficient could provide the photosensitizers with tremendous amounts of singlet excited states that could potentially transfer to triplet excited states via ISC. (2) The energy of the triplet state of the photosensitizers should be equal to or larger than 95 kJ mol^{-1} ($E_T \geqslant 95$ kJ mol^{-1}), which is the required energy to sensitize triplet oxygen to singlet oxygen via the energy transfer process. (3) The photosensitizers should have a high quantum yield of triplet states ($\Phi > 0.4$) and long triplet lifetime ($\tau > 1$ μs). Besides, the photosensitizers should have (4) high photostability since singlet oxygen is oxidative and could therefore damage and decompose the structure of some photosensitizers, leading to the loss of the photoactive function.

It is worth noting that both type I and type II photoreactions consume no photosensitizers, and the re-formation of the ground-state photoactive chemicals could be achieved. Therefore, the photoactivity of the photosensitizers should be ideally constant with no reduction. However, certain reduction of photoreactivity could be observed during the experiments, which may be caused by other competitive side photoreactions that could consume the T_1 or change the structure of the photosensitizers.

1.2.3 Some other photochemical reactions

Except for the type I and type II photoreactions, several side reactions could happen from the T_1 benzophenone due to its highly oxidative property. These side photoreactions could compete with the type I and type II photoreactions and therefore lower the ROS production and the photoinduced antimicrobial efficacy. This section intends to analyze some probable photoreactions that may influence the hydrogen abstraction and oxygen photosensitization process.

Figure 1.5 depicts the addition reaction of an alkene with triplet benzophenone, namely Paterno−Büchi oxetane formation reaction[51]. The $n\pi^*$ excited benzophenone T_1 is electron-

deficient and a very strong electrophile. In this case, the T_1 could react with the electron-rich alkenes, and an addition reaction could be achieved. The addition reaction is also known as a predominant photoreaction in the triplet benzophenone, which largely competes with the H abstraction reaction. In this case, a low ROS production in an alkene existed benzophenone system should be observed due to the triplet quenching effect via the addition reaction.

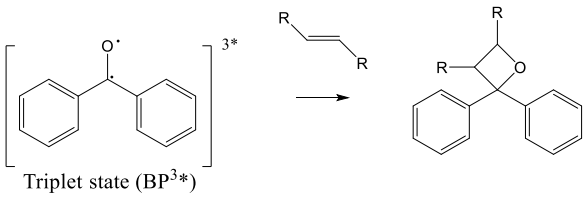

Figure 1.5. Paterno−Büchi oxetane formation reaction between triplet benzophenone and alkenes.

The triplet excited benzophenone could transfer its energy to other substances via the Dexter energy transfer (ET) process[52]. As shown in Figure 1.6, the benzophenone moiety in the benzophenone grafted norbornadiene (G_n-NBD) could be excited to its triplet excited states via the ISC process. The energy in the benzophenone T_1 could transfer to the norbornadiene moiety via an energy transfer process. The absorbed energy in the norbornadiene could trigger the Diels-alder reaction and generate the quadricyclane compound (G_n-QC). In this reaction, the benzophenone T_1 is efficiently quenched by the substrates and new substances are produced. Thus, if the system contains any substrates that could absorb the energy of benzophenone T_1, the ROS production could be decreased due to this competitive photoreaction.

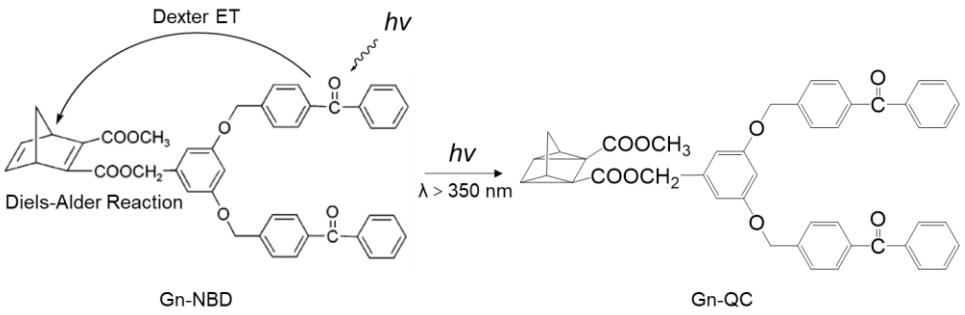

Figure 1.6. The energy transfer process between the triplet benzophenone and norbornadiene and subsequent Diels-Alder reaction.

Other than the competitive photoreactions starting from benzophenone T_1, some competitive reactions could happen on BPH·, which could produce alcohol structures that could not go back to original benzophenone ketone structures, resulting in a consumption of the photoactive agents[11, 53]. Figure 1.7 depicts some possible reactions starting from BPH· after the H abstraction reaction.

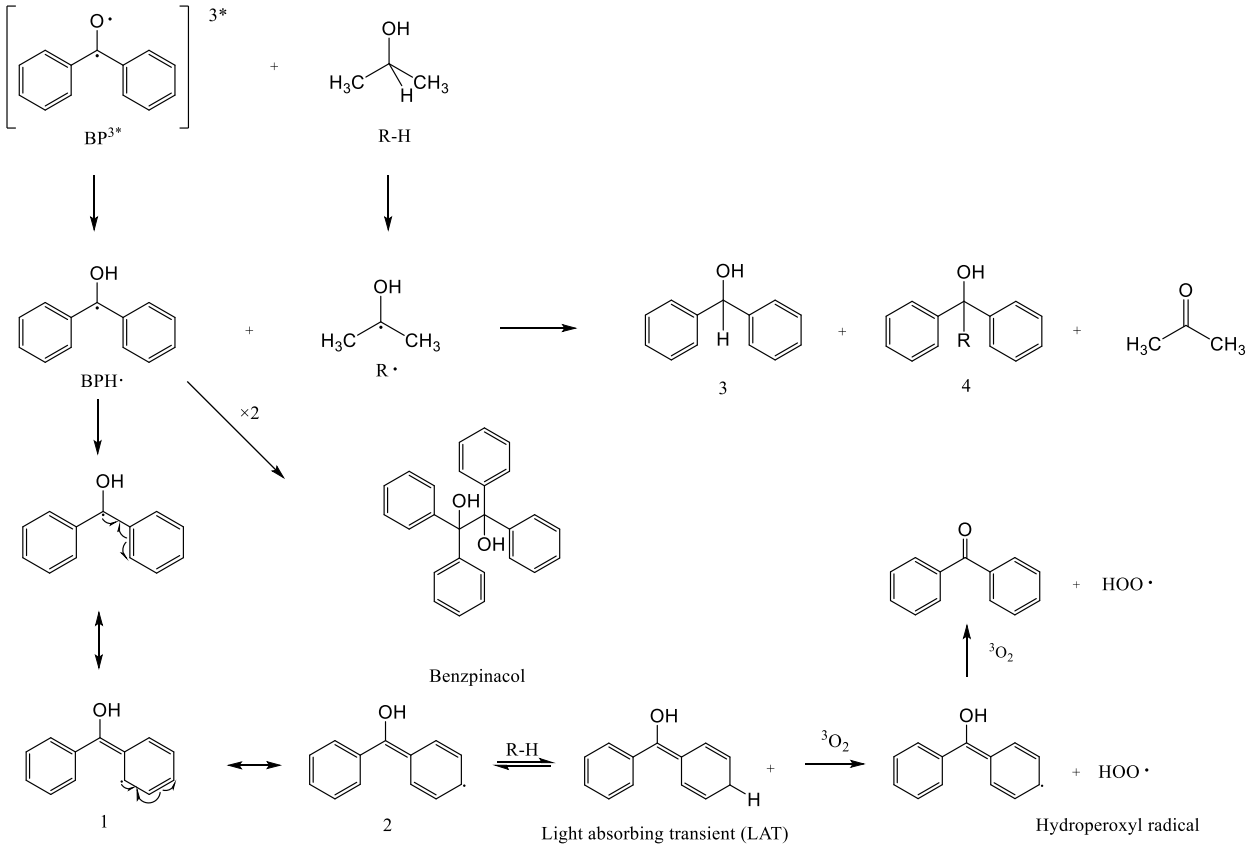

Figure 1.7. Some side-photoreactions during the type I photoreaction process.

After the formation of BPH· via the abstraction reaction between triplet benzophenone (BP^{3*}) and hydrogen donor (RH, take isopropanol as an example), there are several reaction paths to choose for BPH· besides reaction with oxygen to generate ROS. As shown in Figure 1.7, a structural resonance could happen on BPH· to form intermediate 1. The radical center in intermediate 1 is on the ortho-position of the aromatic ring. The intermediate 1 could transform to intermediate 2 via resonance to form a para-radical center. The intermediate 2 could further abstract hydrogen from hydrogen donors to form a light-absorbing transient structure (LAT)[11, 53]. The LAT structure could be quenched by reducing agents to the original benzophenone, or it could be oxidized by oxygen to original benzophenone with the accompanied formation of hydroperoxyl radicals[11]. The LAT

structure was proven to be antimicrobial under dark conditions due to its rapid reaction with oxygen and the resulted hydroperoxyl radicals that could further transform to hydroxyl radicals and hydrogen peroxide. Meanwhile, the formation of LAT does not consume any benzophenone due to the regeneration process. The BPH· could also further react with the hydrogen donor radical (R·) after the hydrogen abstraction reaction. As shown in Figure 1.7, the BPH· could further abstract hydrogen from the isopropyl radical to form an alcohol product 3 with the accompanied formation of acetone, or it could couple with the isopropyl radical to form a product 4[53]. The latter reaction is also considered as the mechanism of the photoinduced crosslinking reaction. It is worthy to know that neither product 3 nor 4 could go back to the original benzophenone structure. Therefore, the formation of these alcohol products is generally an irreversible photoreaction that competes with the type I photoreaction, resulting in the reduction of the photoreactivity and a discount in the ROS production after long time exposure to light. Another reaction that may lead to the irreversible consumption of photoactive agents is the pinacol coupling reaction of two molecular BPH·, after which the formation of benzpinacol product is observed[53]. This reaction could also result in the reduction of photoreactivity.

Some other photoreactions related to the triplet excited states could occur, such as photo redox, photohydration, and photodecarboxylation reactions[20-24]. Structure changes on the aromatic ketones could happen after these photoreactions, which may influence the photoexcitation process and the electron transition process.

Hydroxyl aromatic ketones could be oxidized to form corresponding oxidation products in an acidic system under photoirradiation, according to the literature[21]. The primary hydroxyl benzophenone in acidic solutions under UV irradiation can be oxidized to form aldehyde

benzophenone (Figure 1.8). Similar photoreactions could happen on the secondary hydroxyl anthraquinone compounds[54] (Figure 1.9). The anthraquinone could be firstly excited to its triplet state, which can be subsequently protonated and oxidized to its ketone products.

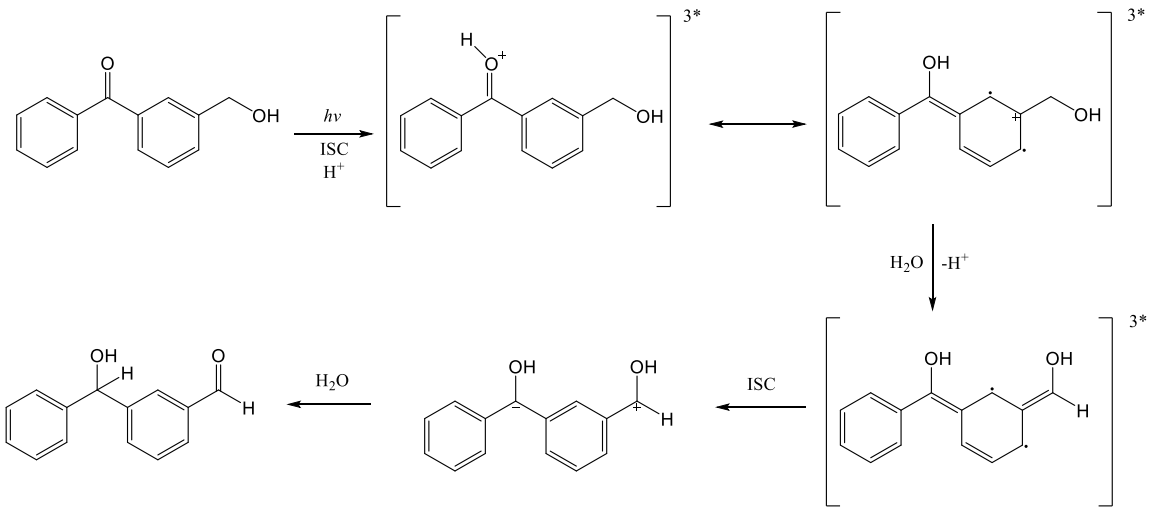

Figure 1.8. Photoredox reaction of primary hydroxyl benzophenone in an acidic environment under photoirradiation.

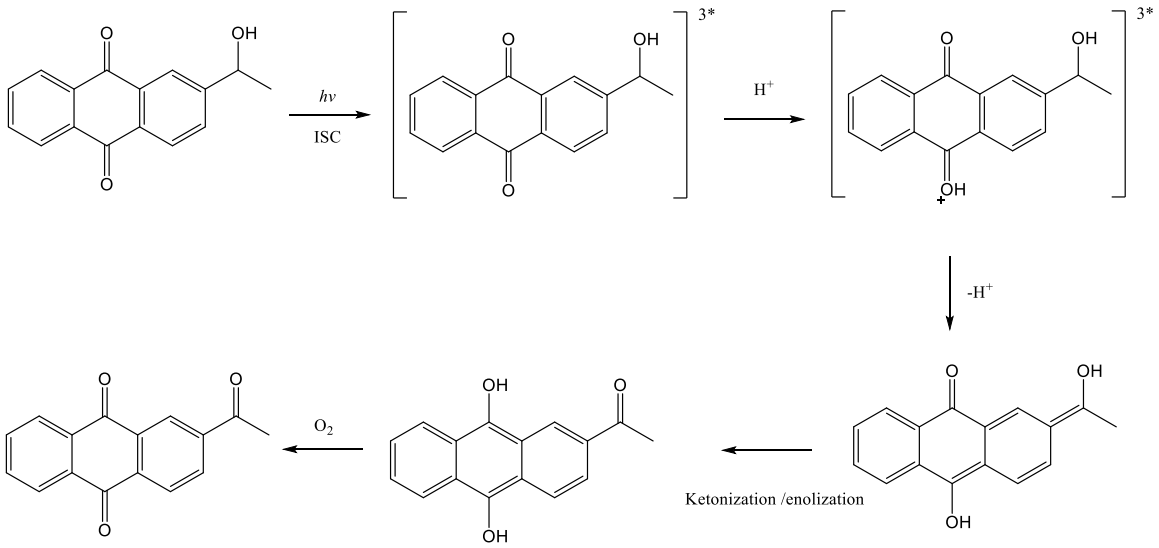

Figure 1.9. Photoredox reaction of secondary hydroxyl anthraquinone in an acidic environment under photoirradiation.

Some researchers also investigated the photohydration reaction of the benzophenone in acid solution under UV irradiation[22]. The mechanism of the photohydration reaction is depicted in Figure 1.10. The ground-state benzophenone is irradiated to S_1 and then to T_1 through the ISC process. The T_1 is then protonated by the H^+ in the solution and forms the T_1^+ intermediate with the positive charge locating on the ortho or meta position on the benzene ring. The positively charged intermediate is easy to be attacked by the H_2O to form ortho- and meta-intermediates. These two intermediates are not stable and tend to reform benzophenone via dehydration reaction.

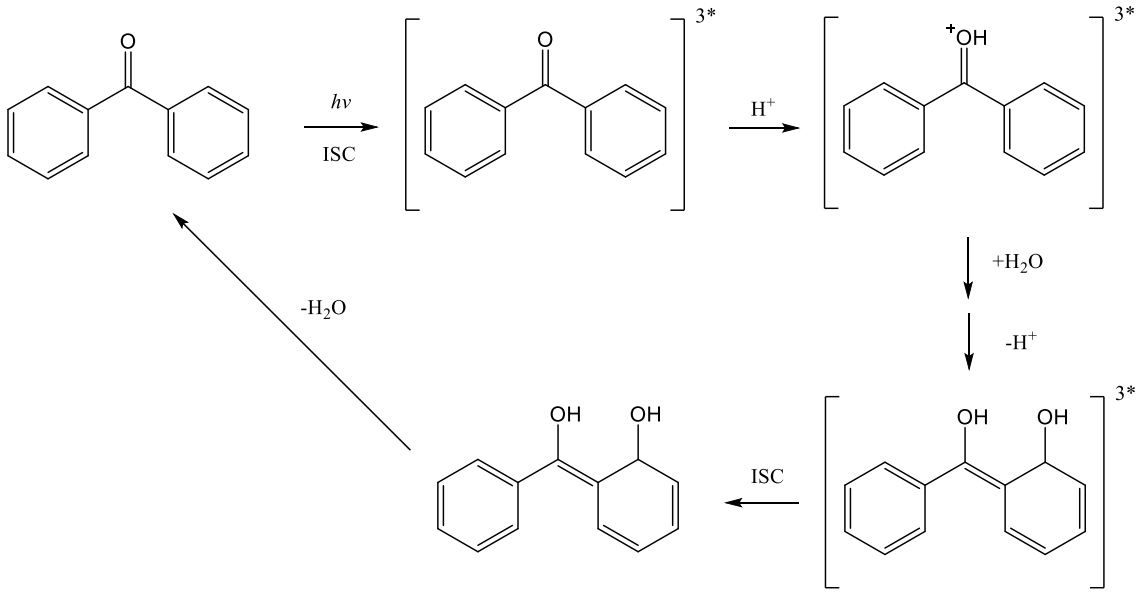

Figure 1.10. Photohydration reaction of benzophenone in an acidic environment under photoirradiation.

Photodecarboxylation reaction is another probable photoreaction in carboxylic aromatic ketones in an acidic solution system[24]. The mechanism of the photodecarboxylation reaction in ketoprofen is depicted in Figure 1.11. Ketoprofen is excited by UV light and then forms S_1 and T_1. The T_1 is subsequently protonated by the H^+ in the solution and form T_1^+, which can proceed

decarboxylation reaction and subsequently form carbon dioxide and a biradical by intramolecular charge transfer.

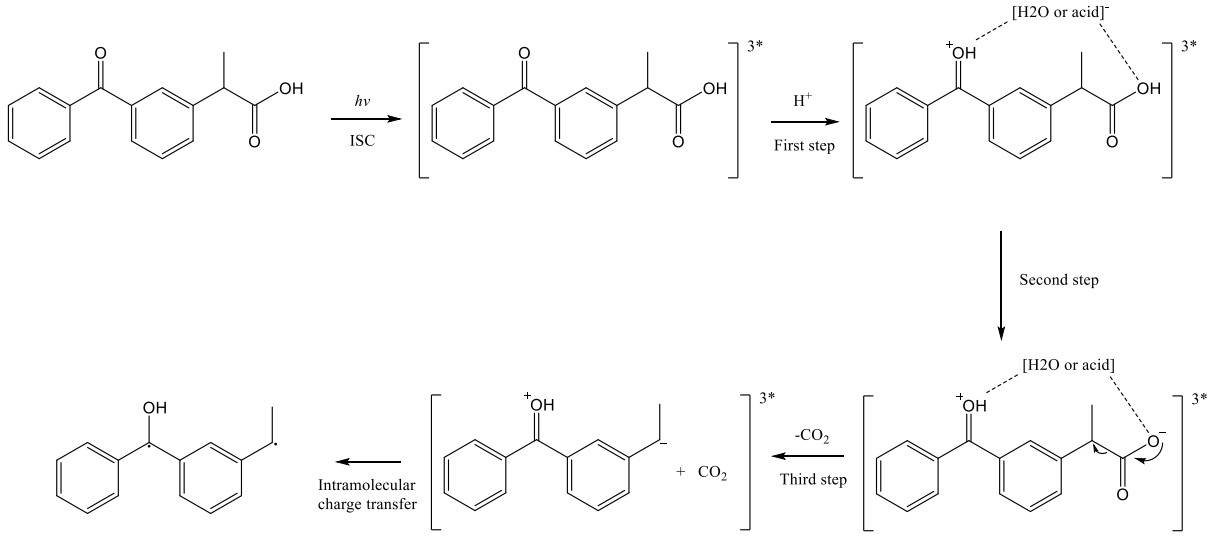

Figure 1.11. Photodecarboxylation reaction of ketoprofen in an acidic environment under photoirradiation.

Overall, the photoreactions of aromatic ketones are highly dependent on the hydrogen donor, electron donor, solvent media, pH value, as well as their chemical structures. Additional photoinduced reactions in other photosensitizers will be discussed in the latter sections.

1.3 General Photoactive Antimicrobial Agents

Inorganic photoactive chemicals, such as semiconductors and carbon nanomaterials are known to generate ROS under photoirradiation. Some organic photosensitizers including quinones, naphthols, tetrapyrroles, synthetic dyes, and some transition metal complexes are also capable of generating ROS under photoirradiation via type I or type II photoreactions. This section intends to conclude some general inorganic and organic photoactive chemicals that could potentially be utilized as photoinduced antimicrobial agents. Also, their photoreaction mechanisms are discussed.

1.3.1 Inorganic photoactive antimicrobial agents

Carbon nanomaterials are a series of carbonaceous materials, such as fullerenes, carbon dots (CDs), carbon nanotubes (CNT), carbon nanohorns, graphene (GR), and graphene oxide (GO)[55-56]. The basic skeleton structure consists of tremendous sp^2-hybridized carbon atoms[57], which gives the carbon nanomaterials unique physical and chemical properties. Carbon nanomaterials are widely used in biosensing, bioimaging, and biomedicine applications[58]. Many carbon nanomaterials are capable of generating ROS under photoirradiation, whereas the photoreaction mechanisms varied from different carbon nanomaterials[58]. Researchers found that graphemic carbon materials could react with dissolved oxygen under photoirradiation. The photoreaction usually takes place at the graphene edge or defect sites, resulting in the generation of $\cdot O_2^-$ and H_2O_2[59]. Carbon quantum dots (CQD) were also reported to generate $^1O_2$ with a high yield under photoirradiation. Besides the conventional photosensitization with the energy coming from T_1 to S_0, the ISC from S_1 to T_1 is also considered as a contributor that promotes the oxygen photosensitization process of CQD[60]. Some carbon dots were also reported to generate $\cdot O_2^-$ via photoinduced electron transfer process[61]. Carbon nanotubes (CNT) were also reported to generate $^1O_2$, $\cdot O_2^-$, and $HO\cdot$ under photoirradiation via photosensitization and electron transfer to oxygen[62]. However, CNT has also proven to be a ROS quencher, yet the quenching effect is still not fully understood[62-63]. One possible reason could be the photoinduced disassociation of the excited CNT (CNT*) to CNT^+ with the formation of hydrated electron (e^-_{aq}) that is reductive and could be trapped by oxidative ROS.

Semiconductor nanomaterials are another category of photoactive chemicals that have been diversely used due to their excellent physical and chemical properties. The ROS generated from semiconductor materials are attributed to the photoinduced-formation of the conduction band

electrons (e^-) and valence band holes (h^+), which has been discussed in the previous section. The formed e^- and h^+ could react with oxygen and water to produce ROS. The semiconductor nanomaterials, therefore, reveal great potential as photosensitizers in photodynamic therapy (PDT) and antimicrobial applications. However, researchers are still trying to improve the photoreactivity of the semiconductor nanomaterials by all means. Some researchers tried to introduce doping materials[64] and surface defects[65] to expanding the light absorption of the semiconductors from UV to visible or even near-infrared region (NIR). Furthermore, the quantum efficiency and electron-hole recombination suppression were considered by researchers to improve the photoreactivity of the semiconductors[28].

Some defective inorganic nanomaterials, such as defective RuO_2 nanoparticles[66] and Gd-doped zinc oxide nanobullet[67], were also proven photoactive to produce $^1O_2$ and $\cdot O_2^-$ during the photoirradiation process. The particle size, morphology, and crystal defects of these materials are considered to greatly impact the generation of ROS[68].

1.3.2 Organic photoactive antimicrobial agents

Quinones and benzophenones are large groups of photoactive chemicals that are well known for their high photoreactivity in the generation of ROS via type I and type II photoreactions. The basic skeleton of these photoactive chemicals is the aryl ketone which has a high ISC efficiency due to the indirect ISC process. The photoexcitation and photoreaction mechanisms have been discussed in the previous chapter. Under photoirradiation, quinones and benzophenones could be excited to its triplet state, which can then abstract hydrogen or electron and react with oxygen to form ROS. Benzophenone (BP), anthraquinone (AQ), and naphthoquinone (NQ) are derivatives of the photoactive chemicals and have proven highly photoactive in generating ROS. The chemical structures of these photoactive chemicals are shown in Figure 1.12. Because of the

aryl ketone structure, the ISC quantum yield for BP and AQ are close to unity, and for 1,4-NQ is 0.74[40-45, 69], which provides the reaction with tremendous T_1. It is worthy to know that the substituents on the chemicals have a great influence on photoreactivity. The introduction of electron-withdrawing groups such as carboxylic acid and dianhydride, or very mild electron-donating groups such as methyl and ethyl groups would not affect the electron transition and hydrogen abstraction reaction[38]. However, the introduction of strong electron-donating groups such as amino and hydroxyl groups would reduce the oxidative property of triplet, resulting in a reduction of HO· and H_2O_2 production. As shown in Figure 1.12, 3,3′,4,4′-benzophenonetetracarboxylic dianhydride reveals robust photoactivity under the daylight and UVA irradiation and could generate large amounts of ROS against the microorganisms[11, 70]. The introduction of the electron-withdrawing anhydride group does not change the electron transition and T_1 oxidative property. On the contrary, the introduction of the amino group to anthraquinone or hydroxyl group to naphthoquinone causes the reduction in ROS production[69]. Besides, the photoreactivity of these chemicals is also affected by solvent media and pH values.

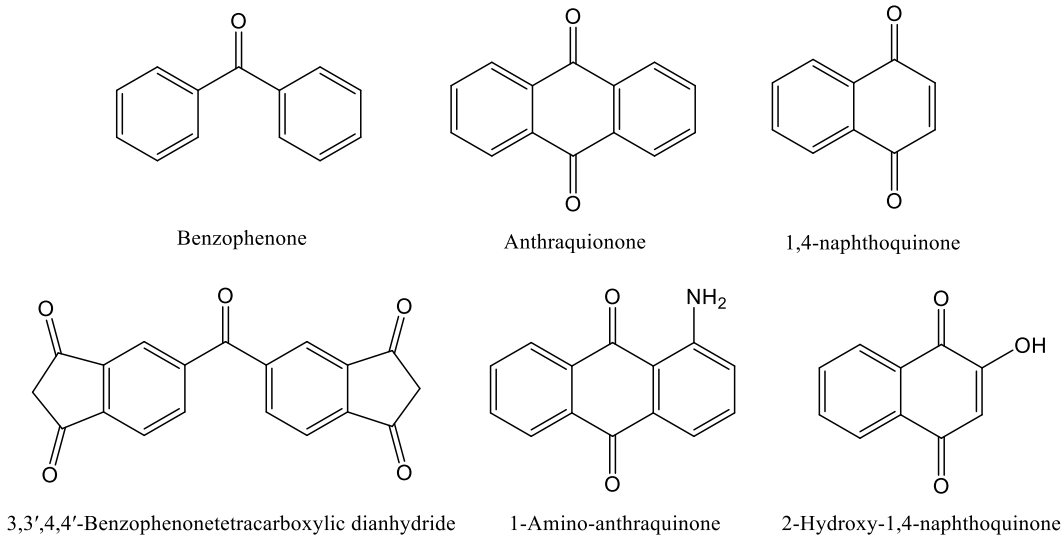

Figure 1.12. Chemical structures of representative benzophenones and quinones.

Some benzophenone heterologous chemicals are also reported to produce ROS under photoirradiation, which share a similar photoreaction mechanism to aromatic ketones[16]. These chemicals are reported to have nπ* lowest triplet excited states that allow hydrogen abstraction for various degrees. Chemical structures of some photoactive benzophenone heterologous are shown in Figure 1.13.

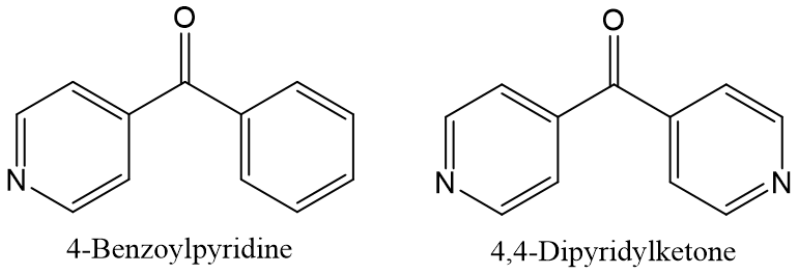

Figure 1.13. Chemical structures of some photoactive benzoylpyridine derivatives.

Naphthol compounds, such as 1-naphthol and 5-hydroxy-1-naphthol, are another group of photoactive chemicals that are capable of generating ROS including $^1O_2$, $\cdot O_2^-$, and H_2O_2[71]. However, the photoreaction mechanism of these types of chemicals is different from quinones due to their low ISC quantum yields, which is depicted in Figure 1.14. Under photoirradiation, ground-state naphthol is excited to its S_1. According to literature, the ISC quantum yield of naphthol is low so that the ISC efficiency is questionable[71]. Therefore, the photoreaction starts from S_1, and a photoionization process could occur with the formation of a proton (H^+), solvated electron (e^-_{aq}), and a naphoxyl radical (·ONaph). The e^-_{aq} could be trapped by the dissolved oxygen efficiently to produce $\cdot O_2^-$. On the other hand, the ionization product ·ONaph could not react with dissolved oxygen but react with $\cdot O_2^-$ and proton to form a hydration intermediate, which could then form NQ. Meanwhile, the formed $\cdot O_2^-$ could combine with protons to produce H_2O_2. Thus, naphthol compounds have the potential to be used as photoinduced antimicrobial agents as well.

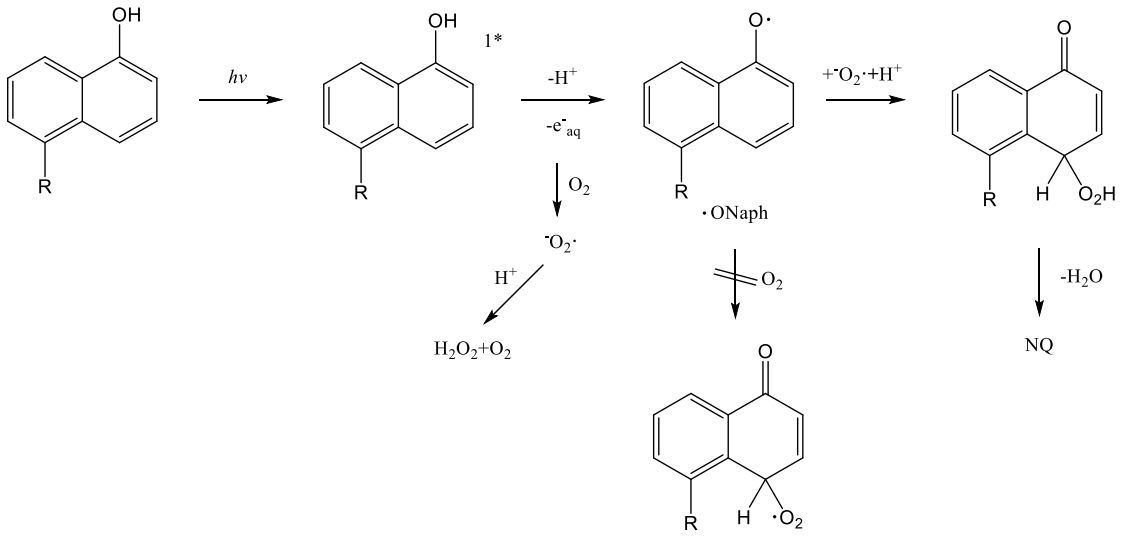

Figure 1.14. Photoreaction of naphthol compounds under photoirradiation in an aerobic environment.

Compounds with tetrapyrrole structures had been studied since 1900 when they were proven to be photoactive for the first time[72]. These types of chemicals were used in PDT in 1970 initially in the United States because of their robust capability in generating $^1O_2$ via energy transfer from photosensitizer T_1 to molecular oxygen[72]. Also, their excellent physical and chemical properties such as strong absorbance in visible or NIR region, substantial triplet quantum yield, low dark toxicity, and rapid clearance from normal tissues offer great potential to be used as PDT agents[73]. Porphyrins, chlorins, bacteriochlorins, and phthalocyanines are typical photoactive tetrapyrroles and are widely used in photoinduced antimicrobial and anticancer-related applications[73]. Skeletal chemical structures of photoactive tetrapyrroles are shown in Figure 1.15.

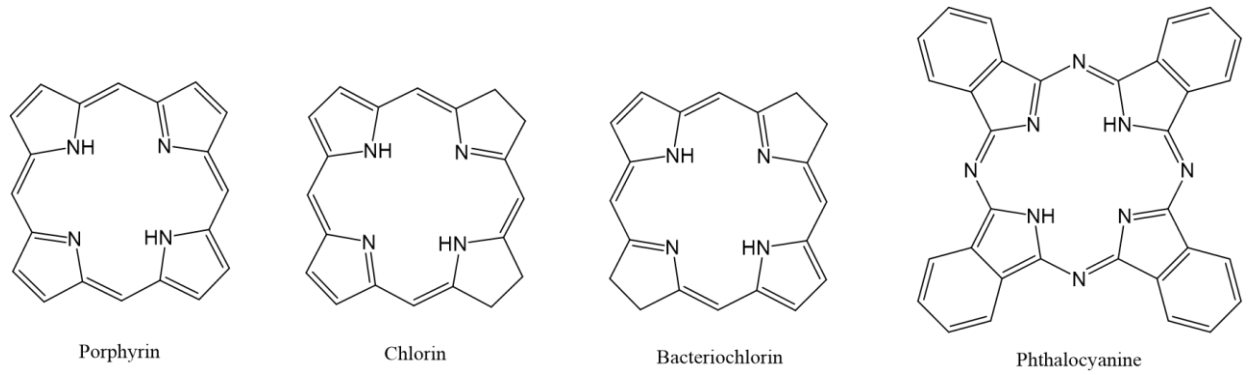

Figure 1.15. Basal chemical structures of photoactive tetrapyrrole derivatives.

Some synthetic dyes were also proven photoactive to produce ROS, especially $^1O_2$ via type II photoreaction, under photoirradiation. Basic photoactive synthetic dyes generally include phenothiazinium salts (e.g., Methylene Blue), xanthene compounds (e.g., Rose Bengal), squaraines, and boron-dipyrromethene (BODIPY) dyes[73]. Most of these photoactive dyes could be excited in the range of 500~700 nm, which are widely applied in antimicrobial and anticancer PDT. Chemical structures of some representative photoactive synthetic dyes are summarized in Figure 1.16.

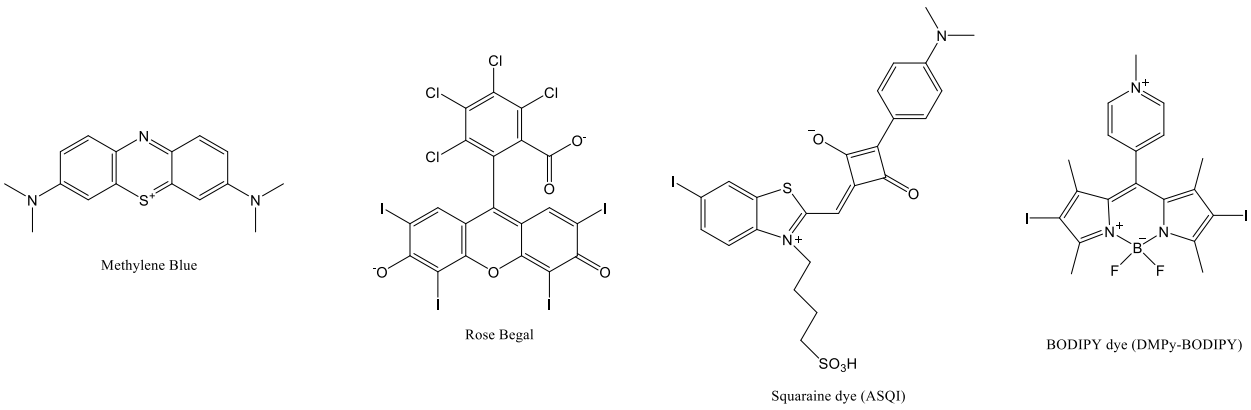

Figure 1.16. Chemical structures of some photoactive synthetic dyes.

Phenalenone compounds are also used as effective photoactive generators of $^1O_2$ under photoirradiation[74]. A cationic phenalenone compound (SAPYR) was successfully synthesized, and

its $^1O_2$ quantum yield was proven to be as high as 0.99[75]. The chemical structure of the phenalenone compound is shown in Figure 1.17. The chemical was proven to be excited at around 380 nm and reveals efficient antibacterial activity.

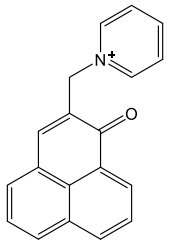

SAPYR

Figure 1.17. Chemical structure of a photoactive phenalenone compound (SAPYR).

Transition metal coordinated complexes are another new group of photosensitizers that could generate ROS, such as Ru and Ir complexes[73, 76]. Chemical structures of some transition metal coordinated compounds are shown in Figure 1.18. These compounds were proven to be excited at 450~600 nm and used to inactivate microorganisms and tumor cells.

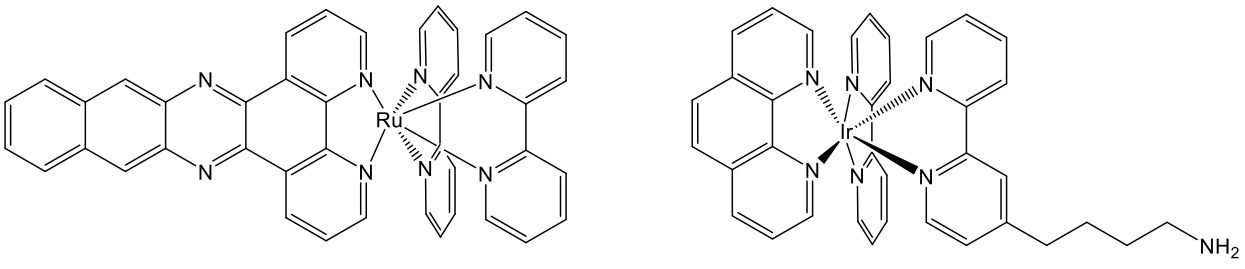

Ruthenium Iridium

Figure 1.18. Chemical structures of photoactive transition metal complexes.

1.4 Natural Photoactive Antimicrobial Agents

Some photoactive chemicals could be extracted from natural products and used as photoinduced antimicrobial agents because of the formation of ROS. This section intends to

introduce some representative natural photosensitizers isolated from nature, such as plants and microorganisms. Also, some vitamin derivatives that could be extracted from natural products or used as food additives are discussed.

1.4.1 Natural products isolated photoactive antimicrobial agents

A diverse range of natural photosensitizers extracted from plants or microorganisms were introduced, according to the literature[18]. These natural photosensitizers include furanocoumarins, polyacetylenes, thiophenes, polyphenols, xanthonoids, alkaloids, curcumins, phenalenones, anthraquinones, porphyrins, and perylenequinones. Under proper photoirradiation, these chemicals could be excited and undergo photoreactions via different mechanisms. Chemical structures of some representative natural photosensitizers are summarized in Figure 1.19.

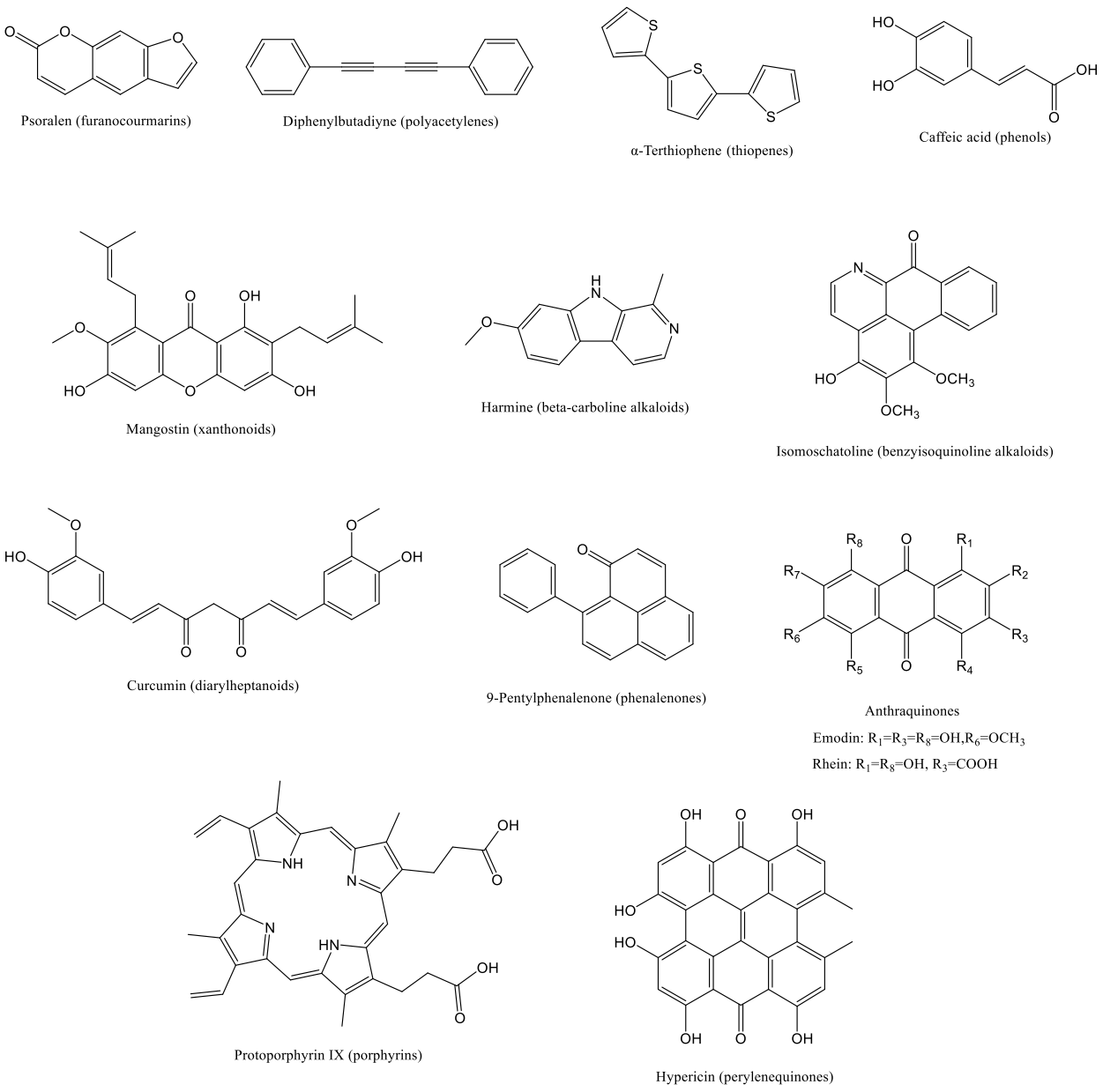

Figure 1.19. Chemical structures of some natural photosensitizers.

Furanocoumarins are a series of chemicals with flat tricyclic planes that could be extracted from plants, such as celery[77-78]. The flat plane structure enables the furanocoumarin to insert into the DNA. Clinical usage of furanocoumarins is under UVA light (usually> 320 nm). Under the photoirradiation, a photoinduced crosslinking reaction could happen between one nucleobase and the double bond in the furanocoumarin[77]. Also, furanocoumarin could react with RNA, cell

membranes, and proteins. However, the $^1O_2$ quantum yield of some furanocoumarins is relatively low, thus the type II photoreaction is not the predominant photoreaction during the photoirradiation[79].

Polyacetylenes compounds feature for their carbon-carbon triple bonds or alkynyl groups. These compounds are widely found in Asteraceae species[80]. Thiophenes could be generated by polyacetylenes via a sulfur addition to polyacetylenes[81]. The irradiation light wavelengths of these compounds are generally from 314 nm to 350 nm[18]. Thiophenes were also reported to be capable of extracted from plants[18]. Most aliphatic polyacetylene could generate limited $^1O_2$ under photoirradiation, whereas aromatic polyacetylene could generate both oxygen radicals and $^1O_2$ via type I and type II photoreactions[80, 82]. Unlike the aromatic polyacetylene which is a mixer of type I and II photoreactions, thiophene is a pure type II reaction photosensitizer with a high $^1O_2$ quantum yield[18]. In general, the photoactivity efficiency ranks as thiophene >aromatic polyacetylene > aliphatic polyacetylene, under photoirradiation[83].

Polyphenols are widely found in natural products such as grapes and green tea[84-85]. Some polyphenols including caffeic acid, gallic acid, proanthocyanidin, and (−)-epigallocatechin have proven photoactive under blue light (400 nm) irradiation[14]. HO· and H_2O_2 are detected during the photoirradiation process of polyphenols. The polyphenols are demonstrated to effectively inactivate both Gram-positive and Gram-negative bacteria under blue light irradiation.

Xanthonoids are a group of natural phenolic compounds formed from the xanthone backbone and widely distributed in Clusiaceae plants. Some xanthonoids could be extracted from microorganisms, such as bacteria and *Ascomycetes*[86]. However, the photochemical properties of xanthonoids are recorded controversially in literature. A representative xanthonoid, mangostin,

was proven to produce $^1O_2$ under 400-800 nm photoirradiation[87]. The formed $^1O_2$ could lead to cell apoptosis, lipid peroxidation, and DNA damage. On the other hand, another group of researchers proves that xanthonoids mainly produce HO·, H_2O_2, and $\cdot O_2^-$ via type I photoreaction under UVA photoirradiation, resulting in DNA damage[88]. On the contrary, the function of $^1O_2$ was proven to be negligibly small. A more detailed photochemistry study should be performed to know better about xanthonoids derivatives.

Alkaloids are large groups of natural products, so the photoactive alkaloids compounds are abundant. Alkaloids could be divided into several subclasses, such as beta-carbolines and benzylisoquinoline. Various tricyclic beta-carbolines have been isolated[89]. Some alkaloids could be found in the human body, for example, in a very little amount in eyes or skins[90]. All beta-carbolines compounds are recorded to have high triplet excited state quantum yield, which makes the compounds produce H_2O_2 and $^1O_2$[91]. The formed reactive oxygen species could further damage DNA, enzymes, and lipid membranes. Harmine, one beta-carboline alkaloid compound, could damage DNA and suppress tumor cells under UVA irradiation[92-93]. Benzylisoquinoline-like alkaloids could be extracted from Annonaceae plants[94]. Isomoschatoline, a benzylisoquinoline, was proven to be excited under a light in the range of 600-700 nm to produce $^1O_2$[94]. This compound shows an inactivation function toward both Gram-negative and Gram-positive bacteria.

Curcumins are commonly found in Curcuma plants and now widely used as natural photoactive agents. This type of natural photosensitizers consists of linear diarylheptanoids. It has been proven that curcumin could show certain antibacterial functions in a dark environment[95]. Under blue light (462±3 nm) irradiation, the antibacterial activity of curcumin further increased due to the formation of $^1O_2$ against both Gram-positive and Gram-negative bacteria[96]. Meanwhile, curcumin under light irradiation reveals tumor cell inactivation function[97]. According to literature,

the cell membrane is the main target of curcumin, and severe cell membrane damage could be observed with the leakage of cellular content[98]. The major drawback of curcumin in practical application might be its poor water solubility, which may attribute to its intramolecular bonding and inherent hydrophobic molecular structure[99].

Natural phenalenones can be found in various fungus and plants, such as Kingdom Fungi and Kingdom Plantae[18]. The skeleton and photoactive backbone of this type of natural product is the tricyclic phenalenone, which was proven to have a very high $^1O_2$ quantum yield (close to 1) under the excitation light whose wavelengths ranges from 337 nm to 436 nm[100]. Hydroxyl or aryl substitutions could be found in some natural phenalenones, and some of them were proven to effectively suppress tumor cells under proper photoirradiation.

Anthraquinones have proven photoactive and are widely used in the preparation of photoinduced antibacterial materials[101-103]. Some anthraquinones dyes are chemically synthesized, such as 2-ethyl anthraquinone and Vat Yellow GCN[12]. Natural anthraquinones by introducing hydroxyl or amino substitutions onto aromatic rings widely exist in plants[104] and funguses[105]. The photochemical property of anthraquinone was discussed earlier and could be affected by substitutions, hydrogen bonding effect, and solvent polarity. Similarly, the substitutions in natural anthraquinones could affect their photoactivity by alternating the energy of excited states and changing the electron transition[46]. In this case, the $^1O_2$ quantum yield of natural anthraquinones varies distinctly. For example, the hydroxyl substituents in position 1 make the T_1 energy higher than S_1, resulting in a non-spontaneous ISC process and, therefore, a lower triplet population and less $^1O_2$ production. Interestingly, substitution on position 2 does not alternate the energy of T_1 and S_1, and an improved $^1O_2$ production via type II photoreaction can be observed. Additionally, hydroxyl substitution on position 1 makes the absorption spectrum redshift, due to the electron-

donating effect (p-π conjugation) and the consequent charge transfer (CT) effect. However, the hydroxyl substitution on position 2 has a slighter spectrum redshift effect, comparing to position 1-substituted anthraquinones. Besides, position 1-substituted anthraquinones are highly affected by the intramolecular hydrogen bond between the -OH and carbonyl oxygen. Overall, most natural anthraquinones can be excited by light with a broad wavelength range (400~450 nm), whereas the $^1O_2$ production varies significantly[18].

Protoporphyrin IX (Pp IX) is one of the natural photoactive porphyrin compounds. Pp IX is the intermediate precursor of haem in the biosynthetic process[106]. Each nucleated cell must have the capability of synthesizing Pp IX, even to a minimum extend. Under the excitation light at 500 nm and 630 nm, Pp IX shows a high $^1O_2$ quantum yield of 0.77 via type II photoreaction after the formation of triplet excited states[15, 107]. Thus, the Pp IX shows great potential to be used in PDT-related applications.

Natural perylenequinones are chemicals with a phenanthroperylene quinone backbone substituted with hydroxyl and alkyl groups that could be extracted from plants and microorganisms[108]. A representative natural perylenequinone, hypericin, is isolated from St. Johns wort and has proven photoactive in generating $^1O_2$ with a quantum yield reaching approximately 0.4 via type II photoreaction under excitation at 532 nm[108-109]. Also, the hypericin could generate $\cdot O_2^-$ by electron transfer via type I photoreaction[110], which enables hypericin to be employed in photoinduced antiviral applications[111].

1.4.2 Vitamin-based photoactive antimicrobial agents

Vitamins are a large class of organic compounds that are necessary for maintaining human health[112-113]. Vitamins are neither raw materials of body tissues nor energy source, but a regulating

substance, which plays an important role in metabolisms. Different aqueous and lipophilic vitamins are needed by humans due to their indispensable roles as cofactors or coenzymes during the metabolism process. Vitamins cannot be synthesized in the human body, or the amount of synthesis is insufficient. Although the vitamin demand is small, they must be frequently supplied by foods. Many vitamins have proven to be photoactive in generating oxidative ROS vita type I or type II photoreactions[114-116]. However, some of them are photosensitive and unstable under photoirradiation. Furthermore, some vitamins are demonstrated as excellent hydroxyl radical and singlet oxygen quenchers[117-119]. Photoreactions and photostability of some of the vitamins including vitamin A, B, C, D, E, and K are discussed in this section. The chemical structures of some vitamins are shown in Figure 1.20. Especially, vitamins with photoactivity in generating ROS are highlighted with yellow color.

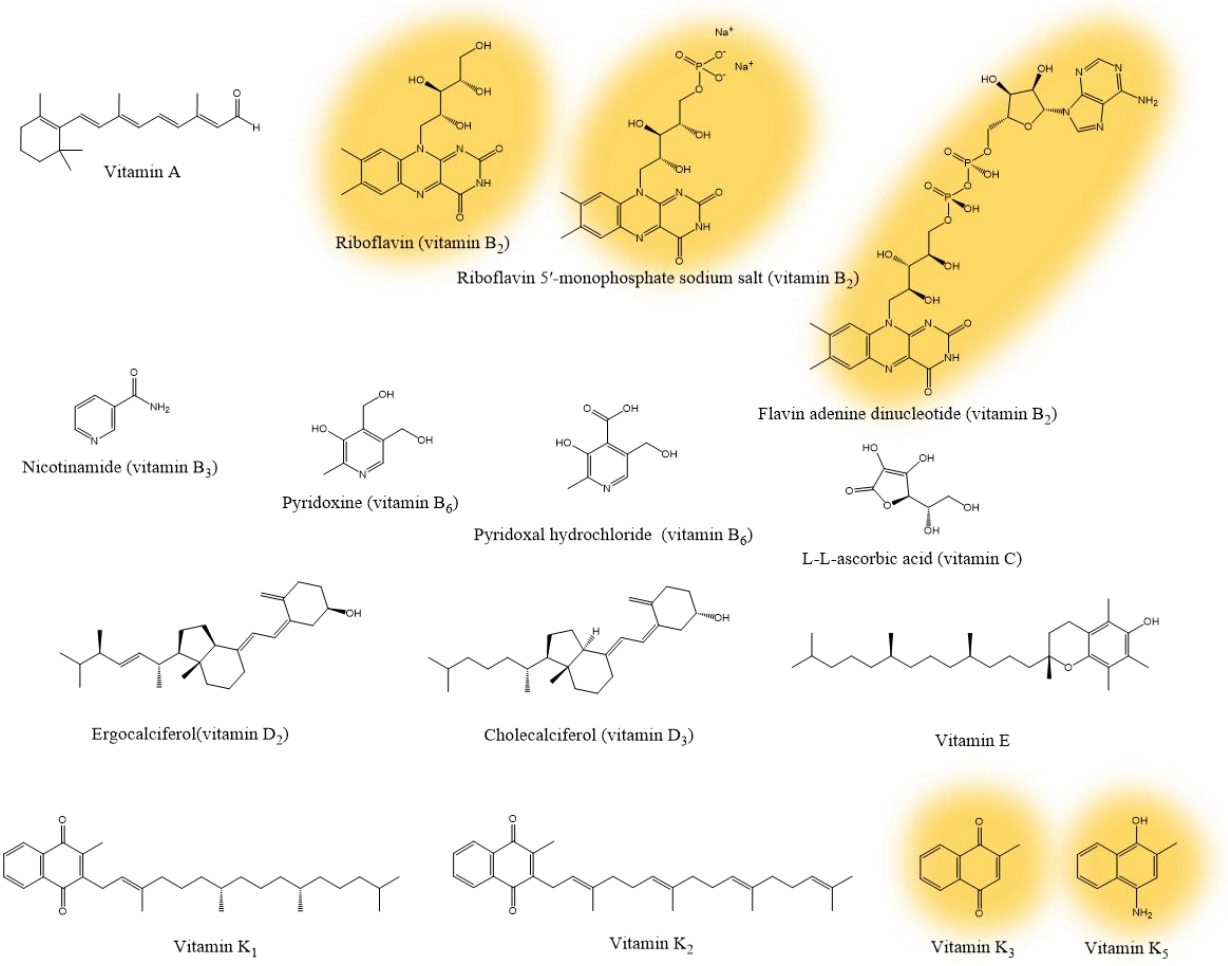

Figure 1.20. Chemical structures of some vitamins.

Vitamin As are retinols or carotenoids that function importantly in visual perception[120]. It has been reported that vitamin A could produce $^1O_2$ with a low quantum yield of 0.06 under UVB (308 nm) irradiation[116]. Under UVA irradiation (330-370 nm), no detectable $^1O_2$ was recorded. Vitamin A is unstable under photo exposure, especially under UVB irradiation, and a spectral change was clearly observed. Some researchers found that vitamin A could self-crosslink under photoirradiation via Diels-Alder reaction, owing to its olefins structure[121]. Especially, with the presence of photosensitizers, vitamin A is vulnerable to be attacked by oxidative $^1O_2$ to form peroxides[119].

Vitamin Bs are a very large group of vitamins, such as vitamin B_2, vitamin B_3, and vitamin B_6. Among them, vitamin B_2 includes riboflavin (RF), riboflavin 5′monophosphate sodium salt hydrate (FMN), and flavin adenin dinucleotide (FAD). The $^1O_2$ quantum yields of vitamin B_3 and vitamin B_6 are reported to be 0.64 and 0.16 under UVB (308 nm) irradiation, respectively, whereas almost no $^1O_2$ production was found under UVA irradiation[116]. Vitamin B_2 derivatives all show apparent $^1O_2$ production under both UVA (0.61 for RF, 0.58 for FMN, and 0.13 for FAD) and UVB (0.64 for RF, 0.64 for FMN, and 0.12 for FAD) irradiation[116]. It is worth noting that the UVA seems to trigger more $^1O_2$ generation from these vitamin B_2 compounds compared to UVB irradiation. Some literature also reveals that vitamin B_2 is able to produce $\cdot O_2^-$ and H_2O_2 by electron transfer process via type I photoreaction[122-123]. However, both vitamin B_3 and vitamin B_6 are considered as good ROS scavengers[124-125]. Vitamin B_3 could quench the $^1O_2$, $\cdot O_2^-$, and $HO\cdot$ as antioxidants to protect the cellular membranes in rat brains[124]. Vitamin B_6 is reported to effectively scavenge $^1O_2$ and protect cells from oxidative stress induced by ROS[125]. Besides, vitamin B_2 derivatives are described to be significantly degradable under blue LED light irradiation, partially due to the formed ROS, according to literature[123].

Vitamin C (L-ascorbic acid) may be one of the most common vitamins in our daily life as an oral nutrient supplement. It is also a very important antioxidant in the human body[126]. According to the literature, vitamin C is photo-inactivate in the ultraviolet region due to its minimum absorption above 300 nm[127]. It can be degraded under aerobic conditions, even in a dark environment[128]. The degradation of vitamin C under such circumstances is attributed to the regular oxidation by air. Also, this process is highly influenced by solution pH, dissolved oxygen concentration, and any transition metal existed[128]. However, the UV or light irradiation generally accelerates the decomposition of vitamin C, especially in the presence of photosensitizers, such as

phenone, quinone, and naphthoquinone[129]. ROS produced by the photosensitizers under photoirradiation could attack the enol moiety of vitamin C, leading to a photooxidation and the formation of ketone structures[130]. Thus, vitamin C is regarded as an effective ROS scavenger and could protect cells from oxidative stress.

Vitamin Ds are essential for normal mineralization and bone growth[131]. Both cholecalciferol (vitamin D_3) and ergocalciferol (vitamin D_2) can be found in various food sources, such as milk[118]. Vitamin Ds are proven as limited $^1O_2$ photosensitizers with a quantum yield of 0.02 and 0.007 for vitamin D_2 and vitamin D_3 under UVB (308 nm) irradiation, respectively[116]. Vitamin D in milk is electron-rich and could therefore be oxidized by $^1O_2$ generated by other photosensitizers existed, such as riboflavin[118]. Thus, vitamin D is generally considered $^1O_2$ suspectable because of the singlet oxygen addition on the double bond, leading to an epoxide formation.

Vitamin E (α-tocopherol) presents in mammalian skin and could provide antioxidant functions to defense skin[132]. Interestingly, Vitamin E is known to generate $^1O_2$ with a quantum yield of 0.15 under UVB (308 nm) irradiation via type II photoreaction[116]. Meanwhile, vitamin E is a good quencher of $^1O_2$ with the accompanied formation of quinone compounds[133-134]. This photoactive vitamin has almost no UVA absorbance and therefore no $^1O_2$ production. However, under UVB irradiation, the chemical structure of vitamin E is changed, and the UV absorbance shifts to the UVA region with a lower $^1O_2$ quantum yield (from 0.15 under UVB to 0.05 under UVA)[116]. In this case, vitamin E is also considered photo-unstable under UVB irradiation.

Vitamin Ks (phylloquinone) function as cofactors in bone metabolisms and blood coagulation[135-136]. Natural vitamin Ks including vitamin K_1 and vitamin K_2 diversely exist in green leafy vegetables and fermented foods[137-138]. Vitamin K_1 shows high UVA absorption in the UVA

region yet with a very limited $^1O_2$ quantum yield (0.02)[116]. This may be attributed to the double bond in the side chain that could transfer electrons to carbonyl oxygen during the photoirradiation[115]. The intramolecular electron transfer process could compete with the ISC process, leading to a reduced population of T_1. Besides, vitamin K_1 is reported to be photo-unstable under photoirradiation[116, 139]. The olefin side chain could be crosslinked with the carbonyl oxygen after photoirradiation, leading to a UV absorption spectral change. Synthetic vitamin Ks, such as lipophilic vitamin K_3 and water-soluble vitamin K_5 have proven photoactive in generating $^1O_2$, $\cdot O_2^-$, and HO· under UVA irradiation and biocidal against a wide range of Gram-negative and Gram-positive bacteria[140-141]. Especially, the ISC quantum yield of vitamin K_3 is as high as 0.86 due to the aromatic ketone structure without any electron-rich side-chain moiety[69]. Vitamin K_5 has been proposed as a food preservative due to its low toxicity and proven to have some antitumor effects[141]. Therefore, the application of these vitamins in the photoinduced antimicrobial-related aspects is promising.

1.5 Application of Photoactive Chemicals in the Preparation of Photoinduced Antimicrobial Materials.

Aromatic ketone compounds including anthraquinone, benzophenone, and naphthoquinone have proven highly photoactive in generating ROS due to their high ISC efficiency. Therefore, anthraquinone and benzophenone derivatives are widely employed in the preparation of photo-induced antimicrobial cotton and nanofibrous materials. Some other photoreactive photosensitizers, such as naphthoquinones, Rose Bengal, thiophene, porphyrin, and vitamin B_2 are also made into photoactive materials to inactivate microorganisms due to their active role in the generation of ROS.

Two photoactive anthraquinones, 2-ethyl anthraquinone (2-EtAQ) and Vat Yellow GCN, were employed to dye cotton fabrics via a vat dyeing process[12]. The prepared anthraquinone-containing cotton fabrics demonstrated excellent photoinduced antimicrobial function by generating biocidal ROS under UVA irradiation (365 nm). Both 2-EtAQ and Vat Yellow GCN dyed cotton fabrics show non-selective bactericidal performance against Gram-positive *S. aureus* and Gram-negative *E. coli.* 2-EtAQ Shows a better microbial reduction rate (98.46% against *E. coli* and 93.4% against *S. aureus* after 30-min UVA irradiation) than Vat Yellow GCN (68.66% against *E. coli* and 72.3% against *S. aureus* after 30-min UVA irradiation). The photoinduced microbial inactivation function durability after a long-time UVA exposure and repeated laundering process was also discussed. Both the two dyed cotton fabrics maintain the microbicidal function against *E. coli*, but a little decreased efficacy against *S. aureus* after 5-time washes. 3,3′,4,4′-Benzophenone tetracarboxylic acid (BPTCA) was also employed as the ROS generators in the preparation of photoinduced antimicrobial cotton fabrics via an esterification reaction[70]. Similar to anthraquinones, BPTCA incorporated on cellulose chains was proven to produce HO· and H_2O_2 via type I photoreaction under UVA irradiation (365 nm). Additionally, the BPTCA modified cotton shows non-selective bacterial inactivation performance against both Gram-positive *S. aureus* and Gram-negative *E. coli*, giving a 99.99% bacterial reduction after 60-min UVA irradiation.

Anthraquinones and benzophenones were also applied on nanomaterials to obtain photoactive nanomaterials with increase ROS production. Anthraquinone-2-carboxylic acid was covalently modified on the cellulose nanocrystals (CNC) by using N, N'-carbonyldiimidazole (CDI) as a linkage[142]. HO· and H_2O_2 were reported efficiently produced after UVA (365 nm) irradiation. Interestingly, a LAT structure was found in the nanomaterials and demonstrated to

produce HO· under dark conditions, which was not reported in the anthraquinone-modified cotton fabrics[12]. 3,3′,4,4′-Benzophenone tetracarboxylic dianhydride (BPTCD) was chemically bonded to poly (vinyl alcohol-co-ethylene) nanofibrous membrane via an esterification reaction[11]. The prepared BPTCD modified nanofibrous membrane reveals robust ROS generation efficiency under daylight irradiation (300-800 nm), with one to two orders of magnitude higher $HO\cdot/H_2O_2$ production reported comparing to other daylight-driven photoactive materials. Six log (99.9999%) bacterial reduction could be achieved on the prepared BPTCD-modified nanofibrous membrane against both Gram-negative *E. coli* and Gram-positive *L. innocua* after 60-min daylight irradiation. The antibacterial performance of this nanomaterial does not decay after 5 times of repeated exposures to concentrated bacteria suspension and daylight irradiation, which again proves the durability of aromatic ketones as photoinduced antimicrobial agents. More interestingly, researchers found that the LAT was formed in the nanomaterial to a very large extent after daylight irradiation. The LAT was proven oxygen-sensitive and could be quenched by forming HO· and H_2O_2 under dark conditions via the reaction shown in Figure 1.7. The contact bactericidal test of the prepared functional nanomaterial was performed and proven to be highly efficient. Six log (99.9999%) bacterial reduction against both *E. coli* and *L. innocua* could be achieved after 120-min contact under dark conditions, even after 5-time cycles. Meanwhile, the material demonstrated a high inactivation rate against T-7 bacteriophage virus (99.999% reduction) after 5-min daylight exposure or 30-min LAT contact under dark conditions. Nanostructure could probably amplify the photoinduced ROS generation, antibacterial, and antiviral function of the photoactive materials due to its ultra-high specific surface area.

Some naphthoquinone derivatives, such as 5-hydroxy-1,4-naphthoquinone (juglone), are natural photosensitizers that could be derived from natural products. Type I photoreaction was reported in juglone, leading to the generation of radicals[143]. A 2-hydroxy-1,4 naphthoquinone (lawsone) rich alcoholic extraction from Lawsonia inermis dried leaf was employed to prepare herbal topic gel for the management of skin and hair[144]. The lawsone-rich extraction was applied on various types of bacteria under red light irradiation (λ_{max} at 500 nm) to evaluate the photodynamic antibacterial activity of the lawsone. According to the UV absorption spectra, naphthoquinones can be excited from ground states to triplet states during the light irradiation, which is responsible for the photoinduced antibacterial activity of naphthoquinones in the extraction[144]. Under the red-light irradiation, the antibacterial activity of the lawsone extract can be increased by 20%, compared with that under dark conditions, which demonstrates the potential photo-induced antibacterial performance of lawsone.

Rose Bengal was employed in the preparation of a face mask against COVID-19[17]. Cotton fabrics were firstly modified with 2-diethylaminoehtyl chloride to form a cationic surface with positive charges. The anionic rose Bengal can be effectively absorbed on the modified cotton via electrostatic interaction. The prepared cotton fabric with rose Bengal functionalized could efficiently produce $^1O_2$ under daylight irradiation via type II photoreaction, which was proven to be responsible for its high biocidal efficiency (99.9999%) against bacteria (*E. coli* and *L. innocua*) and bacteriophage (T7) after 60-min daylight exposure. Moreover, the antimicrobial efficiency decays negligibly (>99.9%) after 15 times repeated washings or 7 days of light exposure, demonstrating the durability of the photoactive antimicrobial agents.

Water-soluble anionic polythiophene and cationic porphyrin were synthesized to prepare a complex through electrostatic interaction[145]. The complex can be effectively excited under white

light (400-800 nm), and an efficient energy transfer from thiophene to porphyrin via Dexter energy transfer could happen. An enhanced $^1O_2$ production was observed. The $^1O_2$ production of the complex is much higher than the sum of the isolated thiophene and porphyrin, which leads to a 70% bacterial viability reduction against Gram-negative *E. coli* and Gram-positive *Bacillus subtilis* only after 5-min white light irradiation. The positively charged complex shows much better antibacterial activity, partially due to its better affinity to the negatively charged bacterial cells and consequent shorter $^1O_2$ diffusion radius to the target bacteria cells.

Riboflavin (RF) was evenly dispersed in chitosan (CS) to prepare photoinduced antimicrobial material for ensuring food safety and extending product shelf-life with the assistance of the produced $^1O_2$ via type II photoreaction[146]. Through solvent casting, chitosan films with different riboflavin concentrations were successfully fabricated, and their antimicrobial activity was evaluated under blue light irradiation (455 nm) for 4h. It was demonstrated that the pure chitosan film with no blue light irradiation nor riboflavin shows no microbial inactivating function against any bacteria. Pure chitosan film under photoirradiation or 5% riboflavin-containing chitosan films (CS-RF) under dark conditions exhibit no antibacterial activity neither. In contrast, 5% CS-RF film shows apparent antibacterial activity against *Listeria monocytogenes*, *Vibrio parahaemolyticus*, and *Shewanella baltica* after 4-h blue light irradiation. Bacteria loaded on fresh salmon without CS-RF wrapped was found readily increased in 8 h, whereas fresh salmon wrapped with 3% CS-RF film under light irradiation exhibited a 3-log bacterial reduction against *Listeria monocytogenes* and *Shewanella baltica*, and no *Vibrio parahaemolyticus* bacterial cell was detected. The CS-RF film indicates the great potential of riboflavin in food storage and food shelf-life extension as safe, green, and environmentally friendly food packaging materials. A transition metal-based nanoparticles containing RF ware prepared and demonstrated as novel up-conversion

photoactive materials that could be excited at a less energetic but more biological tissue-permeable NIR light (980 nm) and applied in PDT application[19]. Under NIR light irradiation, the transition metals could be excited and transfer the excitation energy to RF via energy transfer, resulting in the populated formation of triplet RF. The triplet RF could react with oxygen to produce $\cdot O_2^-$ and HO· via type I photoreaction, or $^1O_2$ via type II photoreaction. The formed ROS led to a distinctive cell viability reduction on the human breast cancer cells after 10-min NIR light irradiation.

Overall, photoactive chemicals that could produce biocidal ROS via type I or type II photoreaction could be widely applied in the preparation of photoinduced functional materials with bright application prospects. These materials exhibit great potential in photoinduced antimicrobial application, personal protective equipment preparation, food safety, food storage, and photodynamic therapy.

1.6 Research Objectives

Based on the literature review of the photoactive chemicals and their application in the photoinduced antimicrobial applications, the photo-induced generation of biocidal active species exhibits promising potential as a new approach to prepare functional photo-driven antimicrobial materials. However, currently used photoactive agents show prominent defects when employed as photoinduced ROS generators. Inorganic photoactive agents, such as TiO_2 and ZnO particles, are restricted in nanoscale when employed in the applications due to the size effect on the excitation bandgap energy[147]. For instance, TiO_2 is widely added to sunscreen in the form of nanoparticles. The nanoparticles in the sunscreen can effectively deflect and absorb UVA and UVB rays in the sunlight. However, the TiO_2 nanoparticles could penetrate the healthy protective layers of the human skin and enter blood circulation via different pathways, even within a short period of

sunscreen utilization time[148]. Also, the ZnO was found in human blood and urine after the use of sunscreen. The nanoparticles could reach distant tissues and organs, which may put consumers at risk. The organic photoactive chemicals have demonstrated high photoreactivity in generating ROS and robust photoinduced antimicrobial function when employed in the preparation of photoactive bio-protective materials. However, some synthetic benzophenone and anthraquinone derivatives are proven carcinogenic and could induce cancers in rats and mice[149-151]. Therefore, vitamin-based photoactive ROS generators should be theoretically explored and practically demonstrated in the fabrication of safe, green, sustainable, and environmentally friendly photoinduced antimicrobial materials that could be applied in bio protection and food safety related aspects.

The specific objectives are listed including:

(1). Photochemistry and photoreaction mechanism demonstration of some lipophilic vitamin K derivatives with aromatic ketone structure and their photoinduced antimicrobial performance in the solvent system.

(2) Application of the lipophilic vitamin Ks in the preparation of personal protective equipment against bacteria and viruses.

(3) Photochemistry demonstration of the water-soluble vitamin K and its photoinduced antimicrobial activity in solvent systems.

(4) Photochemistry demonstration of the water-soluble vitamin B derivatives and their photoinduced antimicrobial function in both solvent systems and nanofibrous polymeric membranes.

Objective 1 was achieved by analyzing 2 types of natural lipophilic vitamin Ks including vitamin K_1 and vitamin K_2, and 2 types of synthetic lipophilic vitamin Ks including vitamin K_3 and vitamin K_4 (Chapter 2). The photochemical property of the 4 vitamin Ks was firstly predicted using the Gaussian modeling package as a theoretical direction. Both type I and type II photoreaction tendencies of the four vitamin Ks are computed and were proven highly consistent with their corresponding $HO\cdot$ and $^1O_2$ production. The theoretical model provides a solid basis on which photoreactivity can be fully discussed and demonstrated. Moreover, the photoinduced antibacterial activity of vitamin K_3 was proven robust against both Gram-negative and Gram-positive bacteria with excellent durability under daylight irradiation. After that, the vitamin Ks were blended with poly (vinyl alcohol-co-ethylene) (PVA-co-PE) or polyacrylonitrile (PAN) to fabricate photoinduced antibacterial and antiviral nanomaterials by electrospinning technique (Chapter 3). The prepared vitamin K containing nanofibrous membranes exhibit robust antimicrobial function against bacteria, T7 bacteria phage, and coronavirus. Meanwhile, the photoactive functional materials could maintain their high photoinduced biocidal performance after 5 times repeated exposure to microorganisms and daylight irradiation, which proves the durable photoinduced antimicrobial activity.

A unique water-soluble vitamin K_3 was discussed in Chapter 4. The photochemistry and photoreaction mechanisms of this vitamin were also demonstrated by combining the theoretical model and well-designed experiments. The water-soluble vitamin K_3 exhibits great antibacterial activity and excellent durability in solvent systems under UVA irradiation. The solvent effect which could affect the antimicrobial efficacy by tuning the distance between the photoactive core and the microbes target was also discussed.

Chapter 5 presents the photochemical property of two water-soluble vitamin B derivatives. The two vitamin Bs were proven to efficiently generate ROS under UVA irradiation via type I and type II photoreactions. Their photoinduced antimicrobial function in both solvent systems and nanofibrous polymeric membranes was evaluated. The prepared vitamin B containing nanofibrous membranes exhibit robust and non-selective antibacterial activity against bacteria. Like their photoreactivity in solvents, the photoinduced antibacterial performance of the vitamin B containing membranes decays dramatically under UVA irradiation, resulting from the photoinduced decomposition of vitamin Bs.

Overall, the systematic study and experimental results on vitamin derivatives in this dissertation report the possibility to employ photoactive vitamins as novel, safe, green, and environmentally friendly photoreactors in bioprotection and food safety related applications.

1.7 References

(1) Morens, D. M.; Folkers, G. K.; Fauci, A. S. The Challenge of Emerging and Re-Emerging Infectious Diseases. *Nature* **2004,** *430* (6996), 242-249.

(2) Weatherall, D.; Greenwood, B.; Chee, H. L.; Wasi, P. Science and Technology for Disease Control: Past, Present, and Future. *Disease Control Priorities in Developing Countries* **2006,** *2*, 119-38.

(3) Holmes, E. C.; Dudas, G.; Rambaut, A.; Andersen, K. G. The Evolution of Ebola Virus: Insights from the 2013–2016 Epidemic. *Nature* **2016,** *538* (7624), 193-200.

(4) Sohrabi, C.; Alsafi, Z.; O'Neill, N.; Khan, M.; Kerwan, A.; Al-Jabir, A.; Iosifidis, C.; Agha, R. World Health Organization Declares Global Emergency: A Review of the 2019 Novel Coronavirus (COVID-19). *International Journal of Surgery* **2020,** *76*, 71-76.

(5) Gao, Y.; Cranston, R. Recent Advances in Antimicrobial Treatments of Textiles. *Textile Research Journal* **2008,** *78* (1), 60-72.

(6) Simoncic, B.; Tomsic, B. Structures of Novel Antimicrobial Agents for Textiles-a Review. *Textile Research Journal* **2010,** *80* (16), 1721-1737.

(7) Zhou, C.; Wang, M.; Zou, K.; Chen, J.; Zhu, Y.; Du, J. Antibacterial Polypeptide-Grafted Chitosan-Based Nanocapsules as an "Armed" Carrier of Anticancer and Antiepileptic Drugs. *ACS Macro Letters* **2013,** *2* (11), 1021-1025.

(8) Si, Y.; Li, J.; Zhao, C.; Deng, Y.; Ma, Y.; Wang, D.; Sun, G. Biocidal and Rechargeable N-Halamine Nanofibrous Membranes for Highly Efficient Water Disinfection. *ACS Biomaterials Science & Engineering* **2017,** *3* (5), 854-862.

(9) Si, Y.; Cossu, A.; Nitin, N.; Ma, Y.; Zhao, C.; Chiou, B. s.; Cao, T.; Wang, D.; Sun, G. Mechanically Robust and Transparent N-Halamine Grafted Pva-Co-Pe Films with Renewable Antimicrobial Activity. *Macromolecular Bioscience* **2017,** *17* (3), 1600304.

(10) Sun, G.; Hong, K. H. Photo-Induced Antimicrobial and Decontaminating Agents: Recent Progresses in Polymer and Textile Applications. *Textile Research Journal* **2013,** *83* (5), 532-542.

(11) Si, Y.; Zhang, Z.; Wu, W.; Fu, Q.; Huang, K.; Nitin, N.; Ding, B.; Sun, G. Daylight-Driven Rechargeable Antibacterial and Antiviral Nanofibrous Membranes for Bioprotective Applications. *Science Advances* **2018,** *4* (3), eaar5931.

(12) Zhuo, J.; Sun, G. Antimicrobial Functions on Cellulose Materials Introduced by Anthraquinone Vat Dyes. *ACS Applied Materials & Interfaces* **2013,** *5* (21), 10830-10835.

(13) Sheng, L.; Zhang, Z.; Sun, G.; Wang, L. Light-Driven Antimicrobial Activities of Vitamin K_3 against *Listeria Monocytogenes*, *Escherichia coli* O157: H7 and *Salmonella Enteritidis*. *Food Control* **2020,** *114*, 107235.

(14) Nakamura, K.; Ishiyama, K.; Sheng, H.; Ikai, H.; Kanno, T.; Niwano, Y. Bactericidal Activity and Mechanism of Photoirradiated Polyphenols against Gram-Positive and-Negative Bacteria. *Journal of Agricultural and Food Chemistry* **2015,** *63* (35), 7707-7713.

(15) Nishimura, T.; Hara, K.; Honda, N.; Okazaki, S.; Hazama, H.; Awazu, K. Determination and Analysis of Singlet Oxygen Quantum Yields of Talaporfin Sodium, Protoporphyrin IX, and Lipidated Protoporphyrin Ix Using near-Infrared Luminescence Spectroscopy. *Lasers in Medical Science* **2020**, *35*, 1289-1297.

(16) Görner, H. Photoinduced Oxygen Uptake for Benzoylpyridines and Dipyridylketones in Aqueous Solution. *Journal of Photochemistry and Photobiology A: Chemistry* **2009,** *208* (2-3), 141-146.

(17) Tang, P.; Zhang, Z.; El-Moghazy, A. Y.; Wisuthiphaet, N.; Nitin, N.; Sun, G. Daylight-Induced Antibacterial and Antiviral Cotton Cloth for Offensive Personal Protection. *ACS Applied Materials & Interfaces* **2020,** *12* (44), 49442-49451.

(18) Siewert, B.; Stuppner, H. The Photoactivity of Natural Products–an Overlooked Potential of Phytomedicines? *Phytomedicine* **2019,** *60*, 152985.

(19) Xu, F.; Li, J.; Zhu, T.-T.; Yu, S.-S.; Zuo, C.; Yao, R.-S.; Qian, H.-S. A New Trick (Hydroxyl Radical Generation) of an Old Vitamin (B_2) for near-Infrared-Triggered Photodynamic Therapy. *RSC Advances* **2016,** *6* (104), 102647-102656.

(20) Filipescu, N.; Minn, F. L. Photoreduction of Benzophenone in Isopropyl Alcohol. *Journal of the American Chemical Society* **1968,** *90* (6), 1544-1547.

(21) Ma, J.; Li, M.-D.; Phillips, D. L.; Wan, P. Reaction Mechanisms and Structural Characterization of the Reactive Intermediates Observed after the Photolysis of 3-(Hydroxymethyl) Benzophenone in Acetonitrile, 2-Propanol, and Neutral and Acidic Aqueous Solutions. *The Journal of Organic Chemistry* **2011,** *76* (10), 3710-3719.

(22) Ramseier, M.; Senn, P.; Wirz, J. Photohydration of Benzophenone in Aqueous Acid. *The Journal of Physical Chemistry A* **2003,** *107* (18), 3305-3315.

(23) Li, M.-D.; Ma, J.; Su, T.; Liu, M.; Yu, L.; Phillips, D. L. Direct Observation of Triplet State Mediated Decarboxylation of the Neutral and Anion Forms of Ketoprofen in Water-Rich, Acidic, and PBS Solutions. *The Journal of Physical Chemistry B* **2012,** *116* (20), 5882-5887.

(24) Li, M.-D.; Huang, J.; Liu, M.; Li, S.; Ma, J.; Phillips, D. L. Investigation of the Role of Protonation of Benzophenone and Its Derivatives in Acidic Aqueous Solutions Using Time-Resolved Resonance Raman Spectroscopy: How Are Ketyl Radicals Formed in Aqueous Solutions? *The Journal of Physical Chemistry B* **2015,** *119* (6), 2241-2252.

(25) Sunada, K.; Kikuchi, Y.; Hashimoto, K.; Fujishima, A. Bactericidal and Detoxification Effects of TiO_2 Thin Film Photocatalysts. *Environmental Science & Technology* **1998,** *32* (5), 726-728.

(26) Chatterjee, D.; Dasgupta, S. Visible Light Induced Photocatalytic Degradation of Organic Pollutants. *Journal of Photochemistry and Photobiology C: Photochemistry Reviews* **2005,** *6* (2-3), 186-205.

(27) Baptista, M. S.; Cadet, J.; Di Mascio, P.; Ghogare, A. A.; Greer, A.; Hamblin, M. R.; Lorente, C.; Nunez, S. C.; Ribeiro, M. S.; Thomas, A. H. Type I and Type Ii Photosensitized Oxidation Reactions: Guidelines and Mechanistic Pathways. *Photochemistry and Photobiology* **2017,** *93* (4), 912-919.

(28) Mills, A.; Le Hunte, S. An Overview of Semiconductor Photocatalysis. *Journal of Photochemistry and Photobiology A: Chemistry* **1997,** *108* (1), 1-35.

(29) Wei, C.; Lin, W. Y.; Zainal, Z.; Williams, N. E.; Zhu, K.; Kruzic, A. P.; Smith, R. L.; Rajeshwar, K. Bactericidal Activity of TiO_2 Photocatalyst in Aqueous Media: Toward a Solar-Assisted Water Disinfection System. *Environmental Science & Technology* **1994,** *28* (5), 934-938.

(30) Li, Q.; Mahendra, S.; Lyon, D. Y.; Brunet, L.; Liga, M. V.; Li, D.; Alvarez, P. J. Antimicrobial Nanomaterials for Water Disinfection and Microbial Control: Potential Applications and Implications. *Water Research* **2008,** *42* (18), 4591-4602.

(31) Serpone, N. Is the Band Gap of Pristine TiO_2 Narrowed by Anion-and Cation-Doping of Titanium Dioxide in Second-Generation Photocatalysts? *The Journal of Physical Chemistry B* **2006,** *110* (48), 24287-24293.

(32) Radetić, M. Functionalization of Textile Materials with TiO_2 Nanoparticles. *Journal of Photochemistry and Photobiology C: Photochemistry Reviews* **2013,** *16*, 62-76.

(33) Anpo, M.; Kishiguchi, S.; Ichihashi, Y.; Takeuchi, M.; Yamashita, H.; Ikeue, K.; Morin, B.; Davidson, A.; Che, M. The Design and Development of Second-Generation Titanium Oxide Photocatalysts Able to Operate under Visible Light Irradiation by Applying a Metal Ion-Implantation Method. *Research on Chemical Intermediates* **2001,** *27,* (4-5), 459-467.

(34) Gerischer, H. Photocatalysis in Aqueous Solution with Small TiO_2 Particles and the Dependence of the Quantum Yield on Particle Size and Light Intensity. *Electrochimica Acta* **1995,** *40* (10), 1277-1281.

(35) Wu, J.; Liu, W.; Xue, C.; Zhou, S.; Lan, F.; Bi, L.; Xu, H.; Yang, X.; Zeng, F.-D. Toxicity and Penetration of TiO_2 Nanoparticles in Hairless Mice and Porcine Skin after Subchronic Dermal Exposure. *Toxicology Letters* **2009,** *191* (1), 1-8.

(36) Fang, W. H.; Phillips, D. L. The Crucial Role of the $S_1/T_2/T_1$ Intersection in the Relaxation Dynamics of Aromatic Carbonyl Compounds Upon n→ π* Excitation. *ChemPhysChem* **2002,** *3* (10), 889-892.

(37) Spighi, G.; Gaveau, M.-A.; Mestdagh, J.-M.; Poisson, L.; Soep, B. Gas Phase Dynamics of Triplet Formation in Benzophenone. *Physical Chemistry Chemical Physics* **2014,** *16* (20), 9610-9618.

(38) Dorman, G.; Nakamura, H.; Pulsipher, A.; Prestwich, G. D. The Life of Pi Star: Exploring the Exciting and Forbidden Worlds of the Benzophenone Photophore. *Chemical Reviews* **2016,** *116* (24), 15284-15398.

(39) El-Sayed, M. A. Triplet State. Its Radiative and Nonradiative Properties. *Accounts of Chemical Research* **1968,** *1* (1), 8-16.

(40) Ohara, K.; Mitsumori, R.; Takebe, M.; Kuzuhara, D.; Yamada, H.; Nagaoka, S.-i. Vitamin K Analogue as a New Fluorescence Probe for Quantitative Antioxidant Assay. *Journal of Photochemistry and Photobiology A: Chemistry* **2010,** *215* (1), 52-58.

(41) Favero, L.; Granucci, G.; Persico, M. Surface Hopping Investigation of Benzophenone Excited State Dynamics. *Physical Chemistry Chemical Physics* **2016,** *18* (15), 10499-10506.

(42) Zhang, Z.; Hao, S.; Zhu, H.; Wang, W. Photoreactions of 1, 4-Naphthoquinone with Lysozyme Studied by Laser Flash Photolysis and Steady-State Analysis. *Journal of Photochemistry and Photobiology B: Biology* **2008,** *92* (2), 77-82.

(43) Damschen, D. E.; Merritt, C. D.; Perry, D. L.; Scott, G. W.; Talley, L. D. Intersystem Crossing Kinetics of Aromatic Ketones in the Condensed Phase. *The Journal of Physical Chemistry* **1978,** *82* (21), 2268-2272.

(44) Borisevich, N.; Bubekov, Y. I.; Tolstorozhev, G.; Vishchakas, Y.; Kabelka, V.; Milyauskas, A. Picosecond Study of the Intersystem Crossing in Aromatic Ketone Vapors. *Chemical Physics Letters* **1983,** *103* (2), 115-117.

(45) Wagner, P. J. Type Ii Photoelimination and Photocyclization of Ketones. *Accounts Of Chemical Research* **1971,** *4* (5), 168-177.

(46) Diaz, A. N. Absorption and Emission Spectroscopy and Photochemistry of 1, 10-Anthraquinone Derivatives: A Review. *Journal of Photochemistry and Photobiology A: Chemistry* **1990,** *53* (2), 141-167.

(47) Grimm, M. L.; Allen, W. J.; Finn, M.; Castagnoli Jr, N.; Tanko, J. M. Reaction of Benzophenone Triplet with Aliphatic Amines. What a Potent Neurotoxin Can Tell us About the Reaction Mechanism. *Bioorganic & Medicinal Chemistry* **2011,** *19* (4), 1458-1463.

(48) Liu, N.; Sun, G. Production of Reactive Oxygen Species by Photoactive Anthraquinone Compounds and Their Applications in Wastewater Treatment. *Industrial & Engineering Chemistry Research* **2011,** *50* (9), 5326-5333.

(49) Görner, H. Photoreduction of 9, 10-Anthraquinone Derivatives: Transient Spectroscopy and Effects of Alcohols and Amines on Reactivity in Solution. *Photochemistry and Photobiology* **2003,** *77* (2), 171-179.

(50) DeRosa, M. C.; Crutchley, R. J. Photosensitized Singlet Oxygen and Its Applications. *Coordination Chemistry Reviews* **2002,** *233*, 351-371.

(51) Belmadoui, N.; Encinas, S.; Climent, M. J.; Gil, S.; Miranda, M. A. Intramolecular Interactions in the Triplet Excited States of Benzophenone–Thymine Dyads. *Chemistry–A European Journal* **2006,** *12* (2), 553-561.

(52) Chen, J.; Li, S.; Zhang, L.; Liu, B.; Han, Y.; Yang, G.; Li, Y. Light-Harvesting and Photoisomerization in Benzophenone and Norbornadiene-Labeled Poly (Aryl Ether) Dendrimers Via Intramolecular Triplet Energy Transfer. *Journal of the American Chemical Society* **2005,** *127* (7), 2165-2171.

(53) Scully, A. D.; Horsham, M. A.; Aguas, P.; Murphy, J. K. Transient Products in the Photoreduction of Benzophenone Derivatives in Poly (Ethylene-Vinyl Alcohol) Film. *Journal of Photochemistry and Photobiology A: Chemistry* **2008,** *197* (2-3), 132-140.

(54) Ma, J.; Su, T.; Li, M.-D.; Du, W.; Huang, J.; Guan, X.; Phillips, D. L. How and When Does an Unusual and Efficient Photoredox Reaction of 2-(1-Hydroxyethyl) 9, 10-Anthraquinone Occur? A Combined Time-Resolved Spectroscopic and Dft Study. *Journal of the American Chemical Society* **2012,** *134* (36), 14858-14868.

(55) Panwar, N.; Soehartono, A. M.; Chan, K. K.; Zeng, S.; Xu, G.; Qu, J.; Coquet, P.; Yong, K.-T.; Chen, X. Nanocarbons for Biology and Medicine: Sensing, Imaging, and Drug Delivery. *Chemical Reviews* **2019,** *119* (16), 9559-9656.

(56) Zhang, L.; Zhu, C.; Huang, R.; Ding, Y.; Ruan, C.; Shen, X.-C. Mechanisms of Reactive Oxygen Species Generated by Inorganic Nanomaterials for Cancer Therapeutics. *Frontiers in Chemistry* **2021,** *9*, 630969.

(57) Karousis, N.; Suarez-Martinez, I.; Ewels, C. P.; Tagmatarchis, N. Structure, Properties, Functionalization, and Applications of Carbon Nanohorns. *Chemical Reviews* **2016,** *116* (8), 4850-4883.

(58) Cui, X.; Xu, S.; Wang, X.; Chen, C. The Nano-Bio Interaction and Biomedical Applications of Carbon Nanomaterials. *Carbon* **2018,** *138*, 436-450.

(59) Liu, X.; Sen, S.; Liu, J.; Kulaots, I.; Geohegan, D.; Kane, A.; Puretzky, A. A.; Rouleau, C. M.; More, K. L.; Palmore, G. T. R. Antioxidant Deactivation on Graphenic Nanocarbon Surfaces. *Small* **2011,** *7* (19), 2775-2785.

(60) Ge, J.; Lan, M.; Zhou, B.; Liu, W.; Guo, L.; Wang, H.; Jia, Q.; Niu, G.; Huang, X.; Zhou, H. A Graphene Quantum Dot Photodynamic Therapy Agent with High Singlet Oxygen Generation. *Nature Communications* **2014,** *5* (1), 1-8.

(61) Zhang, L.; Lin, Z.; Yu, Y.-X.; Jiang, B.-P.; Shen, X.-C. Multifunctional Hyaluronic Acid-Derived Carbon Dots for Self-Targeted Imaging-Guided Photodynamic Therapy. *Journal of Materials Chemistry B* **2018,** *6* (41), 6534-6543.

(62) Wu, B.; Zhu, D.; Zhang, S.; Lin, W.; Wu, G.; Pan, B. The Photochemistry of Carbon Nanotubes and Its Impact on the Photo-Degradation of Dye Pollutants in Aqueous Solutions. *Journal of Colloid and Interface Science* **2015,** *439*, 98-104.

(63) Fenoglio, I.; Tomatis, M.; Lison, D.; Muller, J.; Fonseca, A.; Nagy, J. B.; Fubini, B. Reactivity of Carbon Nanotubes: Free Radical Generation or Scavenging Activity? *Free Radical Biology and Medicine* **2006,** *40* (7), 1227-1233.

(64) Qin, Y.; Ding, Z.; Guo, W.; Guo, X.; Hou, C.; Jiang, B.-P.; Liu, C.-G.; Shen, X.-C. A Full Solar Light Spectrum Responsive B@ ZrO_2–Ov Photocatalyst: A Synergistic Strategy for Visible-to-Nir Photon Harvesting. *ACS Sustainable Chemistry & Engineering* **2020,** *8* (34), 13039-13047.

(65) Mou, J.; Lin, T.; Huang, F.; Shi, J.; Chen, H. A New Green Titania with Enhanced NIR Absorption for Mitochondria-Targeted Cancer Therapy. *Theranostics* **2017,** *7* (6), 1531-1542.

(66) Huang, R.; Ding, Z.; Jiang, B. P.; Luo, Z.; Chen, T.; Guo, Z.; Ji, S. C.; Liang, H.; Shen, X. C. Artificial Metalloprotein Nanoanalogues: In Situ Catalytic Production of Oxygen to Enhance Photoimmunotherapeutic Inhibition of Primary and Abscopal Tumor Growth. *Small* **2020,** *16* (46), 2004345.

(67) Liu, Y.; Wang, Y.; Zhen, W.; Wang, Y.; Zhang, S.; Zhao, Y.; Song, S.; Wu, Z.; Zhang, H. Defect Modified Zinc Oxide with Augmenting Sonodynamic Reactive Oxygen Species Generation. *Biomaterials* **2020,** *251*, 120075.

(68) Wang, G.; Chen, X.; Liu, S.; Wong, C.; Chu, S. Mechanical Chameleon through Dynamic Real-Time Plasmonic Tuning. *ACS Nano* **2016,** *10* (2), 1788-1794.

(69) Elgawish, M. S.; Shimomai, C.; Kishikawa, N.; Ohyama, K.; Nakashima, K.; Kuroda, N. Microplate Analytical Method for Quinones by Pulse Photo-Irradiation and Chemiluminescence Detection. *Analyst* **2012,** *137* (20), 4802-4808.

(70) Hou, A.; Feng, G.; Zhuo, J.; Sun, G. UV Light-Induced Generation of Reactive Oxygen Species and Antimicrobial Properties of Cellulose Fabric Modified by 3, 3′, 4, 4′-Benzophenone Tetracarboxylic Acid. *ACS Applied Materials & Interfaces* **2015,** *7* (50), 27918-27924.

(71) Oelgemöller, M.; Mattay, J.; Görner, H. Direct Photooxidation and Xanthene-Sensitized Oxidation of Naphthols: Quantum Yields and Mechanism. *The Journal of Physical Chemistry A* **2011,** *115* (3), 280-285.

(72) Moan, J.; Peng, Q. An Outline of the Hundred-Year History of Pdt. *Anticancer Research* **2003,** *23* (5A), 3591-3600.

(73) Abrahamse, H.; Hamblin, M. R. New Photosensitizers for Photodynamic Therapy. *Biochemical Journal* **2016,** *473* (4), 347-364.

(74) Segado, M.; Reguero, M. Mechanism of the Photochemical Process of Singlet Oxygen Production by Phenalenone. *Physical Chemistry Chemical Physics* **2011,** *13* (9), 4138-4148.

(75) Cieplik, F.; Späth, A.; Regensburger, J.; Gollmer, A.; Tabenski, L.; Hiller, K.-A.; Bäumler, W.; Maisch, T.; Schmalz, G. Photodynamic Biofilm Inactivation by SAPYR—an Exclusive Singlet Oxygen Photosensitizer. *Free Radical Biology and Medicine* **2013,** *65*, 477-487.

(76) Gill, M. R.; Thomas, J. A. Ruthenium (II) Polypyridyl Complexes and DNA—from Structural Probes to Cellular Imaging and Therapeutics. *Chemical Society Reviews* **2012,** *41* (8), 3179-3192.

(77) Kitamura, N.; Kohtani, S.; Nakagaki, R. Molecular Aspects of Furocoumarin Reactions: Photophysics, Photochemistry, Photobiology, and Structural Analysis. *Journal of Photochemistry and Photobiology C: Photochemistry Reviews* **2005,** *6* (2-3), 168-185.

(78) Scott, B. R.; Pathak, M. A.; Mohn, G. R. Molecular and Genetic Basis of Furocoumarin Reactions. *Mutation Research/Reviews in Genetic Toxicology* **1976,** *39* (1), 29-74.

(79) Redmond, R. W.; Gamlin, J. N. A Compilation of Singlet Oxygen Yields from Biologically Relevant Molecules. *Photochemistry and Photobiology* **1999,** *70* (4), 391-475.

(80) Arnason, T.; Wat, C.-K.; Downum, K.; Yamamoto, E.; Graham, E.; Towers, G. N. Photosensitization of *Escherichia coli* and *Saccharomyces Cerevisiae* by Phenylheptatriyne from *Bidens Pilosa*. *Canadian Journal of Microbiology* **1980,** *26* (6), 698-705.

(81) Croes, A. F.; Jacobs, J. J.; Arroo, R. R.; Wullems, G. J. Thiophene Biosynthesis in Tagetes Roots: Molecular Versus Metabolic Regulation. *Plant Cell. Tissue and Organ Culture* 1994, *38*, 159-165.

(82) Kagan, J. Phenylheptatriyne: Occurrence, Synthesis, Biological Properties, and Environmental Concerns. *Chemosphere* **1987,** *16* (10-12), 2405-2416.

(83) Marchant, Y. Y.; Cooper, G. K. Structure and Function Relationships in Polyacetylene Photoactivity. *ACS Symposium Series* **1987,** *339*, 241-254.

(84) Liu, Z.-Q.; Ma, L.-P.; Zhou, B.; Yang, L.; Liu, Z.-L. Antioxidative Effects of Green Tea Polyphenols on Free Radical Initiated and Photosensitized Peroxidation of Human Low Density Lipoprotein. *Chemistry and Physics of Lipids* **2000,** *106* (1), 53-63.

(85) Yilmaz, Y.; Toledo, R. T. Major Flavonoids in Grape Seeds and Skins: Antioxidant Capacity of Catechin, Epicatechin, and Gallic Acid. *Journal of Agricultural and Food Chemistry* **2004,** *52* (2), 255-260.

(86) Hänsel, R.; Sticher, O. *Pharmakognosie-Phytopharmazie* 2006.

(87) Sun, D.; Zhang, S.; Wei, Y.; Yin, L. Antioxidant Activity of Mangostin in Cell-Free System and Its Effect on K562 Leukemia Cell Line in Photodynamic Therapy. *Acta Biochim Biophys Sin* **2009,** *41* (12), 1033-1043.

(88) Hirakawa, K.; Yoshida, M.; Oikawa, S.; Kawanishi, S. Base Oxidation at 5′ Site of Gg Sequence in Double-Stranded DNA Induced by UVA in the Presence of Xanthone Analogues:

Relationship between the DNA-Damaging Abilities of Photosensitizers and Their Homo Energies. *Photochemistry and Photobiology* **2003,** *77* (4), 349-355.

(89) Dai, J.; Dan, W.; Schneider, U.; Wang, J. B-Carboline Alkaloid Monomers and Dimers: Occurrence, Structural Diversity, and Biological Activities. *European Journal of Medicinal Chemistry* **2018,** *157*, 622-656.

(90) Gonzalez, M. M.; Rasse-Suriani, F. A.; Franca, C. A.; Diez, R. P.; Gholipour, Y.; Nonami, H.; Erra-Balsells, R.; Cabrerizo, F. M. Photosensitized Electron Transfer within a Self-Assembled nor Harmane–2′-Deoxyadenosine 5′-Monophosphate (DAMP) Complex. *Organic & Biomolecular Chemistry* **2012,** *10* (47), 9359-9372.

(91) Varela, A. P.; Burrows, H. D.; Douglas, P.; da Graça Miguel, M. Triplet State Studies of β-Carbolines. *Journal of Photochemistry and Photobiology A: Chemistry* **2001,** *146* (1-2), 29-36.

(92) Vignoni, M.; Erra-Balsells, R.; Epe, B.; Cabrerizo, F. M. Intra-and Extra-Cellular DNA Damage by Harmine and 9-Methyl-Harmine. *Journal of Photochemistry and Photobiology B: Biology* **2014,** *132*, 66-71.

(93) Yañuk, J. G.; Denofrio, M. P.; Rasse-Suriani, F. A.; Villarruel, F. D.; Fassetta, F.; Einschlag, F. S. G.; Erra-Balsells, R.; Epe, B.; Cabrerizo, F. M. DNA Damage Photo-Induced by Chloroharmine Isomers: Hydrolysis Versus Oxidation of Nucleobases. *Organic & Biomolecular Chemistry* **2018,** *16* (12), 2170-2184.

(94) Andreazza, N. L.; de Lourenço, C. C.; Hernandez-Tasco, Á. J.; Pinheiro, M. L. B.; Stefanello, M. É. A.; Costa, E. V.; Salvador, M. J. Antimicrobial Photodynamic Effect of Extracts and Oxoaporphine Alkaloid Isomoschatoline from *Guatteria Blepharophylla*. *Journal of Photochemistry and Photobiology B: Biology* **2016,** *160*, 154-162.

(95) Lee, H.-J.; Kang, S.-M.; Jeong, S.-H.; Chung, K.-H.; Kim, B.-I. Antibacterial Photodynamic Therapy with Curcumin and Curcuma Xanthorrhiza Extract against *Streptococcus Mutans*. *Photodiagnosis and Photodynamic Therapy* **2017,** *20*, 116-119.

(96) Bhavya, M.; Hebbar, H. U. Efficacy of Blue LED in Microbial Inactivation: Effect of Photosensitization and Process Parameters. *International Journal of Food Microbiology* **2019,** *290*, 296-304.

(97) Lin, H.-Y.; Lin, J.-N.; Ma, J.-W.; Yang, N.-S.; Ho, C.-T.; Kuo, S.-C.; Way, T.-D. Demethoxycurcumin Induces Autophagic and Apoptotic Responses on Breast Cancer Cells in Photodynamic Therapy. *Journal of Functional Foods* **2015,** *12*, 439-449.

(98) Tyagi, P.; Singh, M.; Kumari, H.; Kumari, A.; Mukhopadhyay, K. Bactericidal Activity of Curcumin I Is Associated with Damaging of Bacterial Membrane. *PloS one* **2015,** *10* (3), e0121313.

(99) Jagannathan, R.; Abraham, P. M.; Poddar, P. Temperature-Dependent Spectroscopic Evidences of Curcumin in Aqueous Medium: A Mechanistic Study of Its Solubility and Stability. *The Journal of Physical Chemistry B* **2012,** *116* (50), 14533-14540.

(100) Schmidt, R.; Tanielian, C.; Dunsbach, R.; Wolff, C. Phenalenone, a Universal Reference Compound for the Determination of Quantum Yields of Singlet Oxygen O_2 ($^1\triangle_g$) Sensitization. *Journal of Photochemistry and Photobiology A: Chemistry* **1994,** *79* (1-2), 11-17.

(101) Gao, A.; Zhang, H.; Sun, G.; Xie, K.; Hou, A. Light-Induced Antibacterial and UV-Protective Properties of Polyamide 56 Biomaterial Modified with Anthraquinone and Benzophenone Derivatives. *Materials & Design* **2017,** *130*, 215-222.

(102) Liu, N.; Sun, G.; Zhu, J. Photo-Induced Self-Cleaning Functions on 2-Anthraquinone Carboxylic Acid Treated Cotton Fabrics. *Journal of Materials Chemistry* **2011,** *21* (39), 15383-15390.

(103) Liu, N.; Sun, G. Grat Polymerization and Antibacterial Activity on Textiles Introduced by Photosensitive Anthraquinones. *AATCC Review* **2011,** *11* (5), 56-61.

(104) Machatova, Z.; Barbierikova, Z.; Poliak, P.; Jančovičová, V.; Lukeš, V.; Brezova, V. Study of Natural Anthraquinone Colorants by EPR and UV/Vis Spectroscopy. *Dyes and Pigments* **2016,** *132*, 79-93.

(105) Gessler, N.; Egorova, A.; Belozerskaya, T. Fungal Anthraquinones. *Applied Biochemistry and Microbiology* **2013,** *49* (2), 85-99.

(106) Kennedy, J.; Pottier, R.; Pross, D. Photodynamic Therapy with Endogenous Protoporphyrin: Ix: Basic Principles and Present Clinical Experience. *Journal of Photochemistry and Photobiology B: Biology* **1990,** *6* (1-2), 143-148.

(107) Sinclair, R. S.; Tait, D.; Truscott, T. G. Triplet States of Protoporphyrin IX and Protoporphyrin IX Dimethyl Ester. *Journal of the Chemical Society, Faraday Transactions 1: Physical Chemistry in Condensed Phases* **1980,** *76*, 417-425.

(108) Falk, H. From the Photosensitizer Hypericin to the Photoreceptor Stentorin—the Chemistry of Phenanthroperylene Quinones. *Angewandte Chemie International Edition* **1999,** *38* (21), 3116-3136.

(109) Ehrenberg, B.; Anderson, J. L.; Foote, C. S. Kinetics and Yield of Singlet Oxygen Photosensitized by Hypericin in Organic and Biological Media. *Photochemistry and Photobiology* **1998,** *68* (2), 135-140.

(110) Weiner, L.; Mazur, Y. Epr Studies of Hypericin. Photogeneration of Free Radicals and Superoxide. *Journal of the Chemical Society, Perkin Transactions 2* **1992,** (9), 1439-1442.

(111) Tang, J.; Colacino, J. M.; Larsen, S. H.; Spitzer, W. Virucidal Activity of Hypericin against Enveloped and Non-Enveloped DNA and RNA Viruses. *Antiviral Research* **1990,** *13* (6), 313-325.

(112) Eggersdorfer, M.; Laudert, D.; Letinois, U.; McClymont, T.; Medlock, J.; Netscher, T.; Bonrath, W. One Hundred Years of Vitamins—a Success Story of the Natural Sciences. *Angewandte Chemie International Edition* **2012,** *51* (52), 12960-12990.

(113) Fitzpatrick, T. B.; Basset, G. J.; Borel, P.; Carrari, F.; DellaPenna, D.; Fraser, P. D.; Hellmann, H.; Osorio, S.; Rothan, C.; Valpuesta, V. Vitamin Deficiencies in Humans: Can Plant Science Help? *The Plant Cell* **2012,** *24* (2), 395-414.

(114) Massad, W. A.; Bertolotti, S.; Garcia, N. A. Kinetics and Mechanism of the Vitamin B_2-Sensitized Photooxidation of Isoproterenol. *Photochemistry and photobiology* **2004,** *79* (5), 428-433.

(115) Görner, H. Photoprocesses of P-Naphthoquinones and Vitamin K_1: Effects of Alcohols and Amines on the Reactivity in Solution. *Photochemical & Photobiological Sciences* **2004,** *3* (1), 71-78.

(116) Knak, A.; Regensburger, J.; Maisch, T.; Bäumler, W. Exposure of Vitamins to UVB and UVA Radiation Generates Singlet Oxygen. *Photochemical & Photobiological Sciences* **2014,** *13* (5), 820-829.

(117) Yang, T.; Liu, L.; Deng, Y.; Guo, Z.; Zhang, G.; Ge, Z.; Ke, H.; Chen, H. Ultrastable Near-Infrared Conjugated-Polymer Nanoparticles for Dually Photoactive Tumor Inhibition. *Advanced Materials* **2017,** *29* (31), 1700487.

(118) King, J. M.; Min, D. B. Riboflavin-Photosensitized Singlet Oxygen Oxidation Product of Vitamin D_2. *Journal of the American Oil Chemists' Society* **2002,** *79* (10), 983-987.

(119) Crank, G.; Pardijanto, M. S. Photo-Oxidations and Photosensitized Oxidations of Vitamin A and Its Palmitate Ester. *Journal of Photochemistry and Photobiology A: Chemistry* **1995,** *85* (1-2), 93-100.

(120) Perusek, L.; Maeda, T. Vitamin A Derivatives as Treatment Options for Retinal Degenerative Diseases. *Nutrients* **2013,** *5* (7), 2646-2666.

(121) Mousseron-Canet, M. Photochemical Transformation of Vitamin A. *Methods in Enzymology* **1971**, *18*, 591-615.

(122) Schnellbaecher, A.; Binder, D.; Bellmaine, S.; Zimmer, A. Vitamins in Cell Culture Media: Stability and Stabilization Strategies. *Biotechnology and Bioengineering* **2019,** *116* (6), 1537-1555.

(123) Liang, J.-Y.; Yuann, J.-M. P.; Hsie, Z.-J.; Huang, S.-T.; Chen, C.-C. Blue Light Induced Free Radicals from Riboflavin in Degradation of Crystal Violet by Microbial Viability Evaluation. *Journal of Photochemistry and Photobiology B: Biology* **2017,** *174*, 355-363.

(124) Kamat, J.; Devasagayam, T. Nicotinamide (Vitamin B_3) as an Effective Antioxidant against Oxidative Damage in Rat Brain Mitochondria. *Redox Report* **1999,** *4* (4), 179-184.

(125) Bilski, P.; Li, M.; Ehrenshaft, M.; Daub, M.; Chignell, C. Vitamin B_6 (Pyridoxine) and Its Derivatives Are Efficient Singlet Oxygen Quenchers and Potential Fungal Antioxidants. *Photochemistry and Photobiology* **2000,** *71* (2), 129-134.

(126) Bendich, A.; Machlin, L.; Scandurra, O.; Burton, G.; Wayner, D. The Antioxidant Role of Vitamin C. *Advances in Free Radical Biology & Medicine* **1986,** *2* (2), 419-444.

(127) Koutchma, T. Advances in Ultraviolet Light Technology for Non-Thermal Processing of Liquid Foods. *Food and Bioprocess Technology* **2009,** *2* (2), 138-155.

(128) Aguilar, K.; Garvín, A.; Lara-Sagahón, A. V.; Ibarz, A. Ascorbic Acid Degradation in Aqueous Solution During UV-Vis Irradiation. *Food Chemistry* **2019,** *297*, 124864.

(129) Görner, H. Photoreactions of p-Benzo-, p-Naphtho-and p-Anthraquinones with Ascorbic Acid. *Photochemical & Photobiological Sciences* **2004,** *3* (10), 933-938.

(130) Shen, J.; Griffiths, P. T.; Campbell, S. J.; Utinger, B.; Kalberer, M.; Paulson, S. E. Ascorbate Oxidation by Iron, Copper and Reactive Oxygen Species: Review, Model Development, and Derivation of Key Rate Constants. *Scientific Reports* **2021,** *11* (1), 1-14.

(131) Morris, H. A.; Turner, A. G.; Anderson, P. H. Vitamin-D Regulation of Bone Mineralization and Remodelling During Growth. *Frontiers in Bioscience* **2012**, E4, 677-689

(132) Dad, S.; Bisby, R. H.; Clark, I. P.; Parker, A. W. Formation of Singlet Oxygen from Solutions of Vitamin E. *Free Radical Research* **2006,** *40* (3), 333-338.

(133) Kramer, K. A.; Liebler, D. C. UVB Induced Photooxidation of Vitamin E. *Chemical Research in Toxicology* **1997,** *10* (2), 219-224.

(134) Kaiser, S.; Di Mascio, P.; Murphy, M. E.; Sies, H. Physical and Chemical Scavenging of Singlet Molecular Oxygen by Tocopherols. *Archives of Biochemistry and Biophysics* **1990,** *277* (1), 101-108.

(135) Hamidi, M. S.; Gajic-Veljanoski, O.; Cheung, A. M. Vitamin K and Bone Health. *Journal of Clinical Densitometry* **2013,** *16* (4), 409-413.

(136) Cranenburg, E. C.; Schurgers, L. J.; Vermeer, C. Vitamin K: The Coagulation Vitamin that Became Omnipotent. *Thrombosis and Haemostasis* **2007,** *98* (07), 120-125.

(137) Damon, M.; Zhang, N. Z.; Haytowitz, D. B.; Booth, S. L. Phylloquinone (Vitamin K_1) Content of Vegetables. *Journal of Food Composition and Analysis* **2005,** *18* (8), 751-758.

(138) Tarvainen, M.; Fabritius, M.; Yang, B. Determination of Vitamin K Composition of Fermented Food. *Food Chemistry* **2019,** *275*, 515-522.

(139) Wilson, R. M.; Walsh, T. F.; Whittle, R. Photooxidation of Vitamin K Chromenol Derivatives. *Journal of the American Chemical Society* **1982,** *104* (15), 4162-4166.

(140) Xu, F.; Vostal, J. G. Inactivation of Bacteria via Photosensitization of Vitamin K_3 by UV-A Light. *FEMS Microbiology Letters* **2014,** *358* (1), 98-105.

(141) Xu, F.; Li, Y.; Ahmad, J.; Wang, Y.; Scott, D. E.; Vostal, J. G. Vitamin K_5 Is an Efficient Photosensitizer for Ultraviolet A Light Inactivation of Bacteria. *FEMS Microbiology Letters* **2018,** *365* (4), fny005.

(142) Zhu, Y.; Sulkanen, A.; Liu, G.-Y.; Sun, G. Daylight-Active Cellulose Nanocrystals Containing Anthraquinone Structures. *Materials* **2020,** *13* (16), 3547.

(143) Abdul-Monem, M. M. Naturally Derived Photoinitiators for Dental and Biomaterials Applications. *European Dental Research and Biomaterials Journal* **2020**, *1*, 72–78.

(144) Kulkarni, S.; Kale, V.; Velankar, K. To Study the Photodynamic Antimicrobial Activity of Henna Extract and Preparation of Topical Gel Formulation. *The Journal of Phytopharmacology* **2018**, *7* (3), 242-252.

(145) Xing, C.; Xu, Q.; Tang, H.; Liu, L.; Wang, S. Conjugated Polymer/Porphyrin Complexes for Efficient Energy Transfer and Improving Light-Activated Antibacterial Activity. *Journal of the American Chemical Society* **2009,** *131* (36), 13117-13124.

(146) Su, L.; Huang, J.; Li, H.; Pan, Y.; Zhu, B.; Zhao, Y.; Liu, H. Chitosan-Riboflavin Composite Film Based on Photodynamic Inactivation Technology for Antibacterial Food Packaging. *International Journal of Biological Macromolecules* **2021,** *172*, 231-240.

(147) Zhang, Z.; Wang, C.-C.; Zakaria, R.; Ying, J. Y. Role of Particle Size in Nanocrystalline TiO_2-Based Photocatalysts. *The Journal of Physical Chemistry B* **1998,** *102* (52), 10871-10878.

(148) Sanches, P. L.; Geaquinto, L. R. d. O.; Cruz, R.; Schuck, D. C.; Lorencini, M.; Granjeiro, J. M.; Ribeiro, A. R. L. Toxicity Evaluation of TiO_2 Nanoparticles on the 3d Skin Model: A Systematic Review. *Frontiers in Bioengineering and Biotechnology* **2020,** *8*, 575.

(149) Rhodes, M.; Bucher, J.; Peckham, J.; Kissling, G.; Hejtmancik, M.; Chhabra, R. Carcinogenesis Studies of Benzophenone in Rats and Mice. *Food and Chemical Toxicology* **2007,** *45* (5), 843-851.

(150) Kerdivel, G.; Le Guevel, R.; Habauzit, D.; Brion, F.; Ait-Aissa, S.; Pakdel, F. Estrogenic Potency of Benzophenone UV Filters in Breast Cancer Cells: Proliferative and Transcriptional Activity Substantiated by Docking Analysis. *PLoS One* **2013,** *8* (4), e60567.

(151) Doi, A. M.; Irwin, R. D.; Bucher, J. R. Influence of Functional Group Substitutions on the Carcinogenicity of Anthraquinone in Rats and Mice: Analysis of Long-Term Bioassays by the National Cancer Institute and the National Toxicology Program. *Journal of Toxicology and Environmental Health, Part B* **2005,** *8* (2), 109-126.

Chapter 2. Photoactivities of Vitamin K Derivatives and Potential Applications as Daylight-Activated Antimicrobial Agents

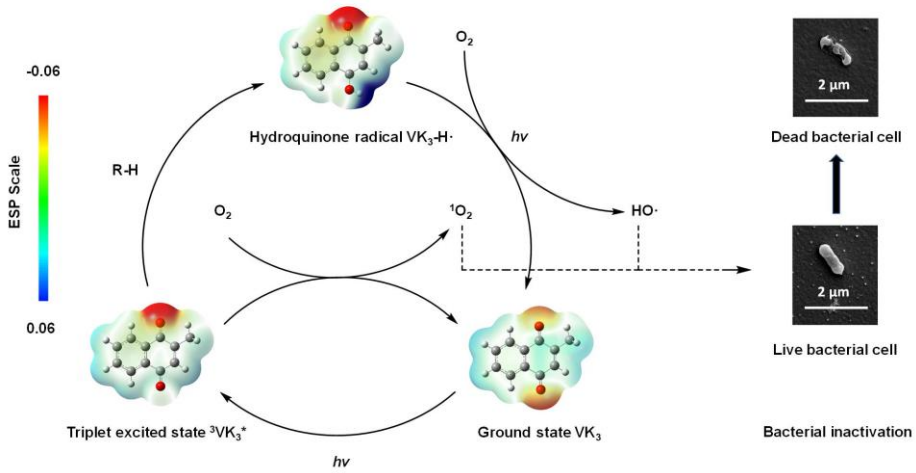

Abstract

Photoactivities of four natural or natural-derivatized vitamin K (VK) species were investigated by using a combination of theoretical computational modeling, prediction, and specially designed experimental tests. The results revealed that these VK compounds are photo-active in generation of reactive oxygen species of hydroxyl radicals and singlet oxygen under daylight, UVA, and UVB irradiations. Two possible photo-reaction paths exist in an environment of good or poor hydrogen donors. Vitamin K_3 (VK_3), as an aromatic naphthoquinone compound, was predicted and demonstrated as the most effective photo-active agent under a broad range of UV-vis wavelengths and in production of both hydroxyl radicals and singlet oxygen. VK_1 and VK_2 are less active than VK_3 due to existence of double bond in their side chains of naphthoquinone. VK_4 is different in photo-activities due to the loss of aromatic ketone structure. As an example, VK_3 was tested against Gram-negative *Escherichia coli* and Gram-positive *Listeria innocua* under daylight irradiation and exhibited complete kill of *Escherichia coli* (six log

reduction in 60 min of daylight exposure) and *Listeria innocua* (five log reduction in 90 min of daylight exposure). In addition, VK_3 retained its high bactericidal efficacy toward both *Escherichia coli* and *Listeria innocua* after seven times of repeated daylight exposures, indicating excellent reusability as a green biocide. This work provides insight into the development of green and sustainable photo-induced antimicrobial materials for bio-medical and food safety applications.

2.1 Introduction

Photoactive chemicals can produce reactive oxygen species (ROS), including hydroxyl radicals (HO·), hydrogen peroxide (H_2O_2), and singlet oxygen ($^1O_2$), under irradiation of light [1], which are good green biocides and can be applied in biomedical and food safety areas [2-3]. Chemicals including colorants and TiO_2 and ZnO nanoparticles can produce different ROS under ultraviolet exposure [4-5], which may have applications under appropriate conditions, such as continuous light exposure and restricted UV wavelengths. However, the photo-active nanoparticles are in nano size and bring in an additional concern of nano-toxicity [6-8], limiting their applications in consumer products [9]. Many organic photosensitizers such as porphyrin and Rose Bengal can produce very lethal but short-lived $^1O_2$ under UVA (315-400 nm) exposure [10-12], while benzophenone and anthraquinone derivatives can predominately produce HO· and H_2O_2 under daylight or UVA irradiation efficiently [3, 13-16]. All of them have found applications in different fields but also are restricted due to potential human and environmental safety concerns on the chemicals [17-18]. The photo-induced antimicrobial functions are advantageous since the ROS produced are the most powerful biocides capable of killing various pathogens rapidly without producing toxic byproducts, and the process is most sustainable with only light and oxygen required. Therefore, the development of environmentally friendly, especially natural or natural-

derived, photoactive chemicals has become a desire in biomedical and food safety related applications.

Vitamin K_{1-5} (VK_{1-5}) are compounds with structures similar to anthraquinone derivatives containing aromatic rings and ketone structure, except Vitamin K_4 (VK_4) and Vitamin K_5 (VK_5) which are the reduced ketone derivatives of Vitamin K_3 (VK_3) [19-22]. Vitamin K_1 (VK_1) is a natural vitamin in green leafy vegetables with low toxicity [23] and has been used as an oral nutrient supplementary or injection to prevent bleeding caused by vitamin K deficiency [24]. Vitamin K_2 (VK_2) is also a natural product in fermented food or animal food and functions similarly as VK_1 in the human body [25]. VK_3 is an intermediate in conversion from VK_1 to VK_2 with the help of bacteria and other microorganisms and has been reported with demonstrated photo-active functions [26]. VK_4 and VK_5 as derivatives of VK_3 do not contain aromatic ketone structure but have been reported with photo-activity to generate ROS [20]. There are also a few more VK_2 derivatives containing longer aliphatic conjugated double bond systems, but structurally similar to VK_2 [27]. As a result, many compounds in the VK family have demonstrated photo-active functions but without detailed reaction mechanism proposed. While the naturally based VK compounds may play an essential role in understanding and development of photo-active biocidal materials, we have conducted a detailed investigation of the photo-reactivity of these compounds with the desire for the development of naturally based chemicals as photo-active biocides for biomedical and food safety applications.

Here, we present a systematic study of photo activities of VK compounds by using Gaussian computational modeling to propose and then experimental tests to demonstrate possible reaction mechanisms involved in these compounds under varied irradiation light wavelengths. The research uncovered and illustrated the mechanisms of the generation of different ROS species and

proved corresponding mechanisms of the photochemical processes of individual VK compounds. VK_5 is unstable and presents structure alternations under UV irradiation [20, 28]. Four VK compounds, VK_1, VK_2, VK_3, and VK_4, were selected as representatives and utilized in all computational modeling, measurements of UV-vis spectra, and detection of ROS generation. Moreover, as an example, time-dependent daylight-induced antibacterial tests of VK_3 were also performed to fully prove its robust bactericidal function and excellent durability to be used as a daylight-induced green, efficient, and sustainable biocidal agent.

2.2 Experimental Methods

2.2.1 Materials

Phylloquinone (VK_1) and menadione (VK_3) were purchased from Chem-Impex International Inc. Menadiol diacetate (VK_4) and p-nitroso-N, N-dimethylaniline (p-NDA) was purchased from TCI Co. LTD. Menatetrenone (VK_2, MK-4), acetonitrile (ACN), isopropanol (IPA), ethyl alcohol (EtOH), cyclohexane (CYC), tetrahydrofuran (THF), L-histidine, and 2 wt% osmium tetroxide (OsO_4) aqueous solution were purchased from Sigma-Aldrich. Luria-Bertani (LB) broth, LB agar, Tryptic soy broth, and Tryptic soy agar (TSA) were purchased from Thermo Fisher Scientific. Phosphate-buffered saline (PBS) was obtained from USB Co. Ltd. All of the chemicals or supplies were used as received without any further purification.

2.2.2 Computational details

All calculations were performed by using computational software package Gaussian 09 ver. 08. The ground state geometries were optimized at unrestricted DFT-B3LYP/6-31G(d,p) level of theory in the conductor-like polarizable continuum model (CPCM) using H_2O as the solvent. The singlet and triplet excited energy calculations were further performed at TDDFT-B3LYP/6-31G

(d,p) level of theory in the CPCM-H_2O solvent model based on the optimized ground-state structure. The ground state geometries of vitamin K_3 in various solvents were optimized at the same ground-state geometry optimization level and model using CAN, EtOH, IPA, CYC, and THF as solvents, respectively. The singlet and triplet excited energy calculations were also performed at TDDFT-B3LYP/6-31G (d,p) level of theory in the CPCM model in the corresponding solvent. The ESP (electrostatic potential) calculation was performed by single-point energy calculations with CHELPG5 ESP population analysis at unrestricted DFT-B3LYP/6-31G(d,p) level of theory in CPCM model in the corresponding solvents. The total electron density was first plotted and subsequently mapped with ESP-derived charges to show an out-shell distribution of charges on the molecular structure. The Gibbs free energies were obtained by frequency calculations at unrestricted DFT-B3LYP/6-31G(d,p) level of theory in the CPCM- H_2O model based on the optimized ground state or triplet excited state geometries.

2.2.3 Measurements of hydroxyl radicals

The production of HO· was quantitatively measured by p-NDA, which is a selective radical scavenger specifically toward HO·[29-30]. Daylight irradiation device (Spectrolinker XL-1500, Spectronics Corporation) equipped with D65 standard daylight tubes (GE F15T8-D) with an irradiance power of 6.5 mW cm^{-2} was employed in this experiment. The irradiance distance was controlled at 16 cm between lamps and test samples. UVA or UVB irradiation device (Spectrolinker XL-1000, Spectronics Corporation) equipped with UVA (Spectroline BLE-8T365) or UVB tubes (Spectroline BLE-8T312) with irradiance power of 3.0 mW cm^{-2} was also used in this experiment to provide UV irradiance. The irradiance distance between UV lamps and samples was controlled at 12 cm. In the HO· quantification of VKs in solvents, VK (20 μM) and p-NDA (40 μM) were dissolved in the specific solvent to obtain a homogeneous solution, which was then

placed under photoirradiation or in dark condition for different time durations, alternatively. The concentration of the residual p-NDA in the solution was quantitatively measured by a UV-vis spectroscopy (Evolution 600 UV-visible spectrophotometer, Thermo Scientific). The production of HO· can be obtained by referring to the stoichiometry between HO· and p-NDA in the specific quenching reaction quantitatively[29-30].

2.2.4 Measurements of singlet oxygen

The production of $^1O_2$ was measured by a widely used method as previously described [15]. A mixture of ethanol and 0.01 M phosphate buffer solution (pH=7.35) (volume ratio 10%: 90%) was employed as a solvent to dissolve VK and p-NDA to obtain a VK (20 μM) and p-NDA (40 μM) solution. L-histidine (0.01 M) was then added into the solution to react with $^1O_2$ and form a transannular intermediate that could subsequently oxidize p-NDA. The sample solution was then placed under photoirradiation and the production of $^1O_2$ was measured photometrically by referring to the additional consumption of p-NDA in the solution.

2.2.5 Bacterial culture

Antibacterial experiments were performed on two typical etiological bacteria, Gram-negative *Escherichia coli* O157:H7 [American Type Culture Collection (ATCC) 700728] and Gram-positive *Listeria innocua* (ATCC 33090). Ten milliliters of LB broth was incubated with a *E. coli* colony at 37 ℃ for 18 hours. After that, a bacterial culture of around 1×10^8 CFU mL^{-1} (assessed by plate count) was obtained for further experiments. Ten milliliters of Tryptic soy broth was incubated with a *L.innocua* colony at 37 ℃ for 24 hours, and a bacterial culture of around 4×10^7 CFU mL^{-1} (assessed by plate count) was obtained for following experiments.

2.2.6 Antibacterial assays

VK_3 stock solution (50 mM) was freshly prepared in ethanol for each antibacterial experiment. 40 μL of VK_3 stock solution, 10 μL bacterial culture solution, and 950 μL of 0.01M PBS buffer were homogeneously mixed to get a VK_3/bacteria suspension and added into 24 well cell cuture plate (Corning Incorporated, USA), and then the samples were exposed to daylight for a certain time to perform the time-dependent antibacterial test. For each time point, the bacteria suspensions were extracted out from well cell plate and were serially diluted ($\times10^0$, $\times10^1$, $\times10^3$, and $\times10^5$) to be plated on LB agar (*E.coli*) or TSA agar (*L.innocua*) for the bacterial enumeration. For the antibacterial reuse test, 7 groups (cycle 1-7 times) of VK_3/bacteria suspension samples were exposed under daylight for 60 min (*E.coli*) or 90 min (*L.innocua*). After the first round of irradiation, the cycle-1 samples were extracted out from the cell well plate and plated on agar plate. 10 μL bacterial culture suspension was added into the remaining 6 groups of VK_3 suspension samples to perform the second-round irradiation. The same operation was carried on until 7 times of reuse tests were finished. After applying the sample suspensions onto the agar plate, LB agars were incubated at 37 ℃ for 18 hours and TSA were incubated at 37 ℃ at least for 24 hours to ensure the quantification of the CFU number to determine the survived bacteria.

2.2.7 SEM images

The bacteria in VK_3 suspension after light irradiation or in PBS were harvested by centrifuging at a speed of 8000 rpm for 10 min. The precipitate was washed by 4% EtOH/PBS for two more times to remove residual VK_3. The bacteria were then treated with 1 wt% OsO_4 aqueous solution for 30 min, after which the bacteria were rinsed with DI water for two times to remove the OsO_4. The bacteria samples were subsequently dehydrated by pure ethanol. Finally, the bacterial samples in ethanol were placed on copper tape and coated with gold for SEM analysis.

2.2.8 Characterization

UV-vis absorption spectra were collected with a Thermo Scientific Evolution 600 spectrometer. SEM images of bacteria in PBS or VK_3 suspension were obtained from a Thermo Scientific Quattro S.

2.3 Results and Discussion

2.3.1 Photo-reactivity of four vitamin K derivatives

Benzophenone and anthraquinone derivatives are aromatic ketones and widely used as photo-initiators in chemical reactions [31-33]. These chemicals mostly generate HO· and H_2O_2 as main ROS under UV irradiation [30, 34] by undergoing a similar photo-reaction process. The excited molecules can go intersystem crossing (ISC) with high efficiency to their triplet excited states (T_1), which then react with dissolved ground-state triplet oxygen ($^3O_2$) to produce ROS [35-37]. Aromatic carbonyl and similar structures such as VK_{1-3} compounds enable excellent UV absorption and indirect ISC, satisfying El-Sayed's rules [38-40]. These VK compounds (Figure 2.1a) under photo-irradiation, can be excited from the ground state (S_0) to their multiple singlet excited states (S_n) that are very active and short-lived. Within an extremely short time, the S_n status molecules will rapidly relax back to the lowest singlet excited states (S_1) thermodynamically via internal conversion (IC) process. The short-lived S_1 could either go back to their S_0 with the emission of fluorescence or transfer to the triplet states (T_1) through the ISC. The process can be illustrated in the Jablonski diagram (Figure 2.1b). Due to the unique aromatic carbonyl structure and its high corresponding ISC efficiency, the naphthoquinone-containing VK_{1-3} (VK) should have a rare possibility to go through the step of the relaxation of S_1 with the emission of fluorescence [41]. Instead, they should predominately undergo the ISC path and change to the triplet (T_1) status with a relatively longer lifetime [41-43]. After the formation of the triplet excited VK (^{3}VK*), photoreactions of the excited molecules with oxygen will begin from and end with the formation

of ground-state VK and different ROS [44]. Figure 2.1c and Figure 2.2 depict two types of photoreaction paths possible to the ^{3}VK* under aerobic conditions [15, 43]. The type I photoreaction preferably happens in the presence of sufficient hydrogen donors, leading to the formation of the potent biocides, H_2O_2 and HO· [15, 45]. The type I reaction route requires an nπ* excitation configuration of the carbonyl group in triplet excited state to ensure a smooth operation of hydrogen abstraction reaction [46-47]. The generated hydro naphthoquinone radical (VK-H·) could undergo the reaction with oxygen in the air finally producing hydroperoxide radical (HOO·) that could then convert to H_2O_2 and HO·, but not $^1O_2$. Type II reaction is a photoreaction that occurs via an energy exchange through the collision between ^{3}VK* and $^3O_2$ with primarily very active $^1O_2$ and ground-state VK formed. The excitation of VK_4 is slightly different from other three VK compounds as analyzed in computational modeling but the excited molecule will undergo through the two photo-reaction paths. Thus, with the assistance of photo-irradiation and oxygen, a sustainable generation of biocidal ROS can be theoretically achieved without the consumption of the VK derivatives.

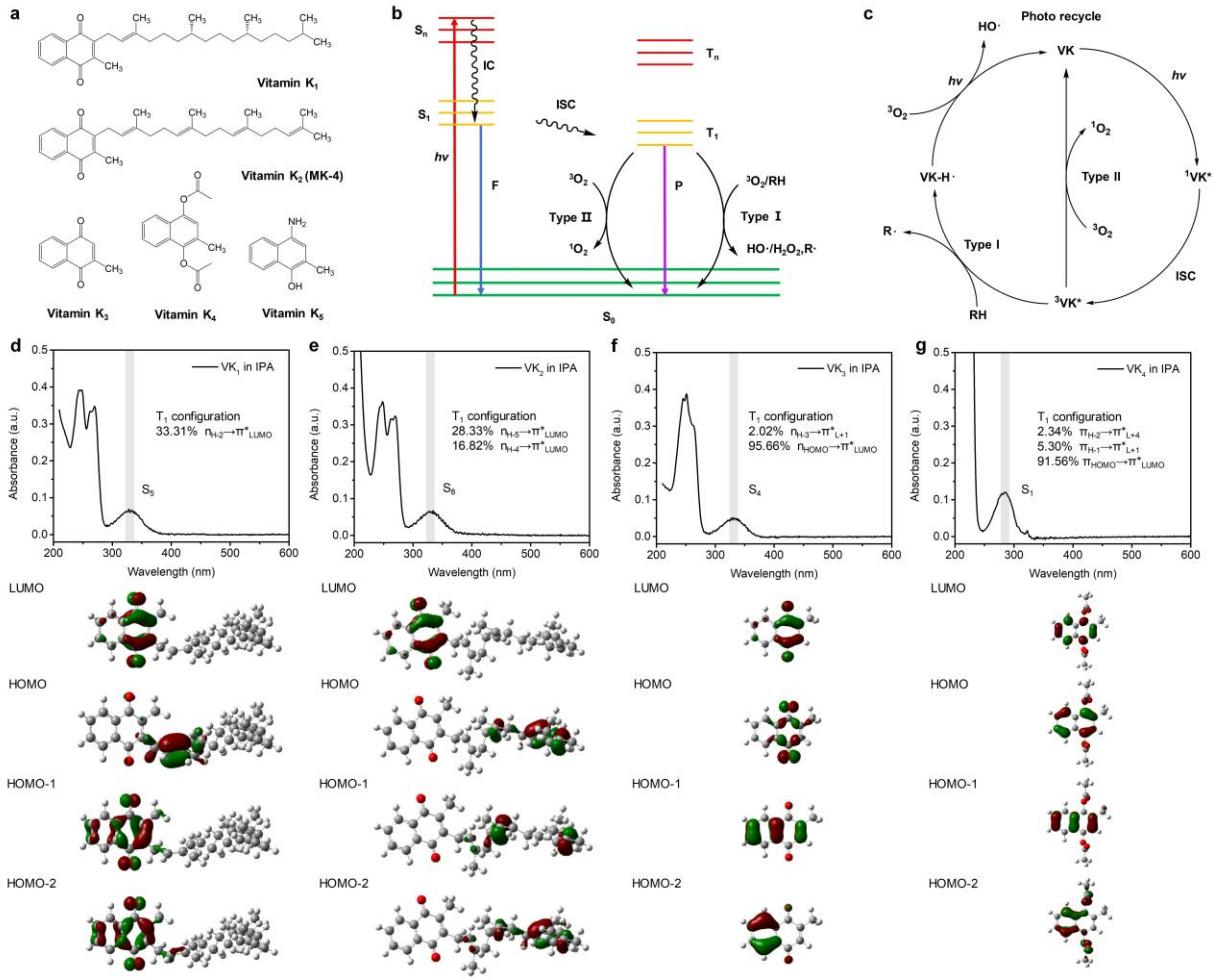

Figure 2.1. Photo-reactivity and excitation of four Vitamin K (VK) derivatives. (a) Chemical structures of VK_1, VK_2, VK_3, VK_4, and VK_5. **(b)** Schematic Jablonski diagram of the photoexcitation process and potential chemical reactions of VKs. **(c)** Mechanism of the photo-induced ROS generation cycle. **(d to g)** Measured UV-vis absorption (pathlength=1cm) of 20 μM VK_1, VK_2, VK_3, and VK_4 in isopropanol and their theoretically computed frontier molecular orbitals; the HOMO and LUMO represent for the highest occupied molecular orbital and lowest unoccupied molecular orbitals, respectively.

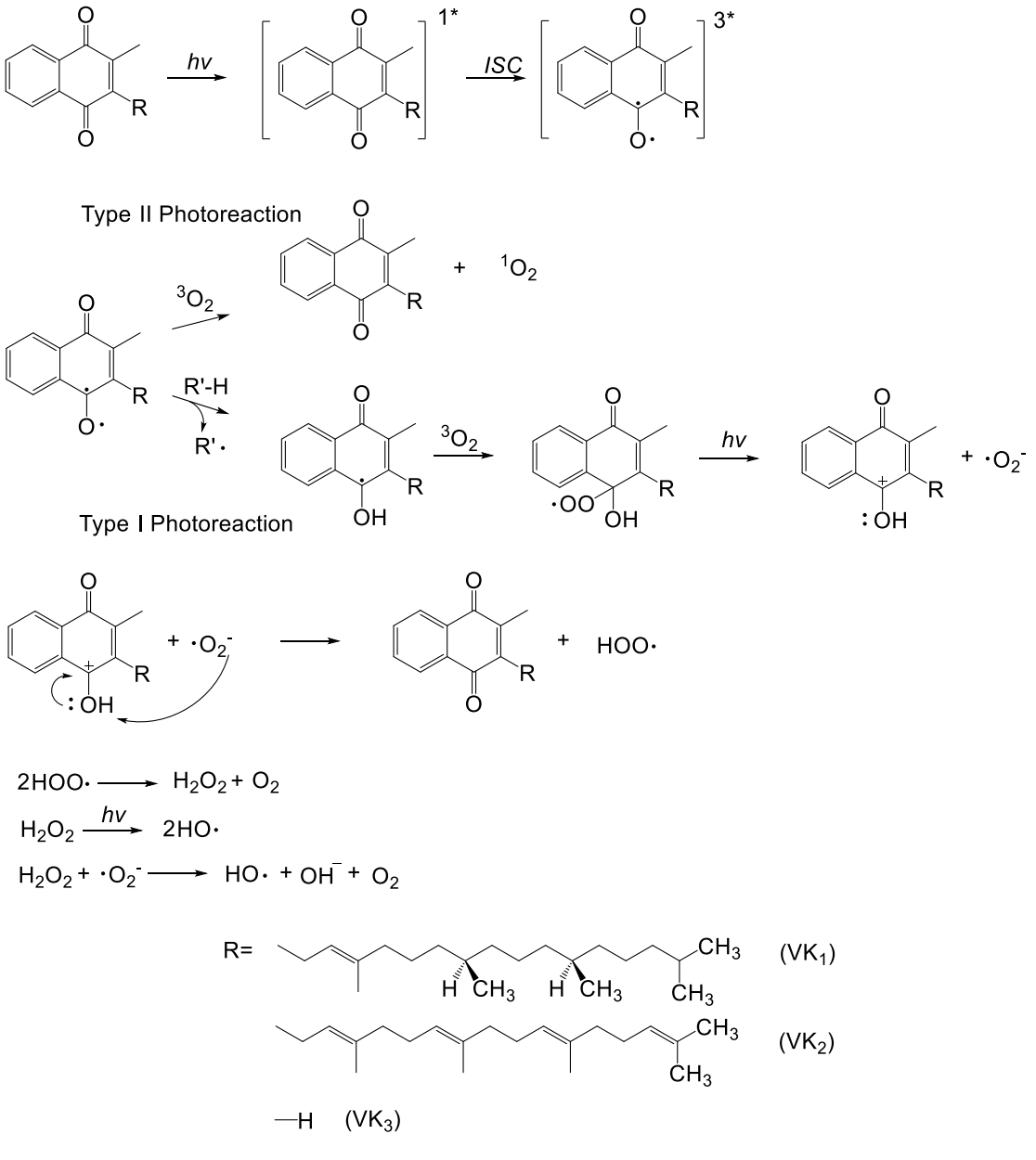

Figure 2.2. Mechanisms of type I and II photoreactions of VK1-3.

With the above analysis of the potential photochemistry of the VK compounds, excitation features of VK_1, VK_2, VK_3, and VK_4 were obtained by using computational modeling following time-dependent density functional theory (TD-DFT), and experimental UV-visible spectra of the compounds were measured. The TD-DFT calculations (Table 2.1) of four VKs reveal that the S_0 to S_1 excitations of VK_1, VK_2, and VK_3 are very weak with small or even zero oscillator strengths,

but their excitations from S_0 to S_n are prominent. VK_4, however, is different from the S_0 to S_1 excitation as the main excitation. The computed UV-vis absorption peaks of VKs (Figure 2.3) matched well with those measured in Figure 2.1d-g, and the calculated maximum absorption wavelengths (λ_{max}) of the VKs are only a few nanometers away from those obtained experimentally, proving the accuracy of the calculation method. The experimental λ_{max} of VK_1, VK_2, VK_3, and VK_4 are 333 nm, 334nm, 333nm, and 285 nm, respectively (grey area in Figures 2.1d, 2.1e, 2.1f, and 2.1g). Accordingly, the main absorbance and excitation of VK_1, VK_2, and VK_3 are in the UVA region (315-400 nm) whereas that of VK_4 is primarily in a higher-energy UVB region (280-315 nm) or even close to UVC region (<280 nm). Due to the fact that daylight may also irradiate some UVA wavelength, VK_1, VK_2, and VK_3 may exhibit certain photo-activity under standard daylight (D65, 300-800 nm) irradiation whereas VK_4 may not have detectable photo-activity (Figure 2.4). Under UVB irradiation, the photo-activity of the four VKs should be comparable based on a physical stimulation process because of their similar oscillator strengths of the singlet state excitations (Table 2.1). Figures 2.1d-g depict configurations of frontier molecular orbitals that could qualitatively reveal the T_1 configurations of the VKs. The lowest unoccupied molecular orbital (LUMO) for VK_1 is a typical π^* orbital whose electron density resides more on the carbonyl carbon. The highest occupied molecular orbital (HOMO) of VK_1 is a π characterized orbital which has a significant π character on the unsaturated side chain moiety (C=C bond). Similarly, the LUMO of VK_2 is also a π^* orbital, and a HOMO orbital of π character is found in the side aliphatic double bonds of VK_2 molecule. VK_3 is clearly different from both VK_1 and VK_2 in frontier molecular orbital configurations. Typical π^* characteristic LUMO on carbonyl carbon is found in VK_3, whereas the HOMO is a typical n-configured orbital localized on the lone electron pair of the carbonyl oxygen, indicating its high photo-reactivity in the hydrogen abstraction in the type I

photoreaction. HOMO and LUMO of VK_4 are distinctly different from VK_1, VK_2, and VK_3. Although the LUMO of VK_4 is in π^* configuration, its π electrons distribute over the whole conjugated aromatic rings instead of on the carbonyl carbon, which indicates that the ester carbonyl group is not involved in the excitation and transition process. The HOMO of VK_4 is also a π orbital whose electron density concentrates on the same aromatic conjugation system, resulting in a localized π_{HOMO}-π^*_{LUMO} excitation, different from aromatic carbonyl groups.

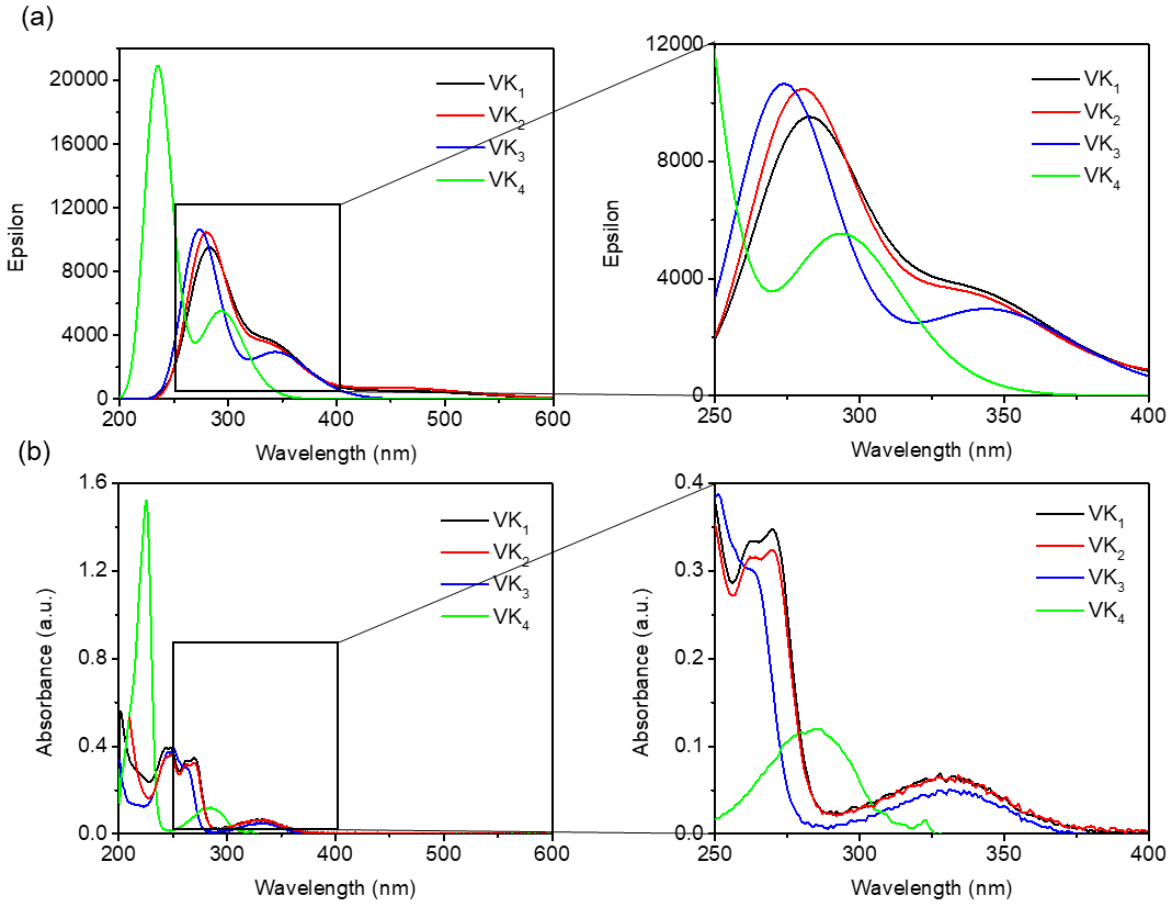

Figure 2.3. Comparison between calculated UV-vis spectra (a) and experimental UV-vis spectra (b) of the four VKs.

Vitamin	Singlet state	^{a}f	$^{b}\lambda_{max}$ (nm)
K_1	S_1	0.0000	487.28
	S_2	0.0070	423.96
	S_3	0.0001	395.48
	S_4	0.0009	373.72
	S_5	0.0808	340.49
	S_6	0.0635	289.01
	S_7	0.1588	281.35
K_2	S_1	0.0114	482.08
	S_2	0.0015	435.11
	S_3	0.0079	421.87
	S_4	0.0003	417.04
	S_5	0.0000	405.60
	S_6	0.0004	396.60
	S_7	0.0000	369.58
	S_8	0.0792	338.72
	S_9	0.2419	280.72
	S_{10}	0.0207	266.52
K_3	S_1	0.0000	449.31
	S_2	0.0000	405.03
	S_3	0.0018	365.88
	S_4	0.0707	344.93
	S_5	0.2630	273.70
K_4	S_1	0.1319	294.27
	S_2	0.0054	280.64
	S_3	0.0141	240.00
	S_4	0.0112	239.97
	S_5	0.0441	237.13
	S_6	0.4509	234.68

[a]Ocsillator strength and [b]Theoretical absorbance in nm.

Table 2.1. TD-DFT Calculated singlet excitation states of the four VKs in water.

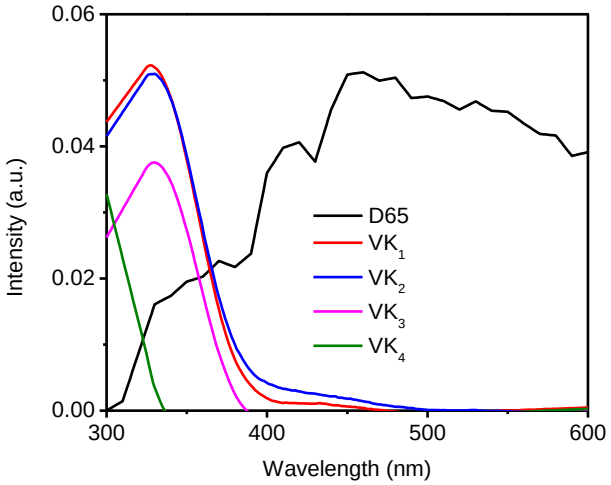

Figure 2.4. UV-vis spectra of various VKs along with the spectrum of the D65 standard daylight source.

Vitamin	[a]*f*	[b]λ_{max} (nm)	[c]E_T (eV)	% of Molecular Orbital Contribution
K_1	0.0000	553.75	1.9318	HOMO-6→LUMO (2.08%, ππ*) HOMO-5→LUMO (9.38%, ππ*) HOMO-2→LUMO (33.31%, nπ*) HOMO→LUMO (50.42%, ππ*)
K_2	0.0000	548.29	1.9157	HOMO-8→LUMO (3.93%, ππ*) HOMO-5→LUMO (28.33%, nπ*) HOMO-4→LUMO (16.82%, nπ*) HOMO-3→LUMO (36.25%, ππ*) HOMO-2→LUMO (5.03%, ππ*) HOMO-1→LUMO (5.07%, ππ*)
K_3	0.0000	535.60	2.1396	HOMO-3→LUMO+1 (2.02%, nπ*) HOMO→LUMO (95.66%, nπ*)
K_4	0.0000	469.62	2.4546	HOMO-2→LUMO+4 (2.34%, ππ*) HOMO-1→LUMO+1 (5.30%, ππ*) HOMO→LUMO (91.56%, ππ*) HOMO←LUMO (2.22%, ππ*)

[a]Ocsillator strength, [b]Theoretical absorbance in nm, and [c]Energy of the triplet excited state in eV.

Table 2.2. TD-DFT Calculated lowest triplet excited states of the four VKs in water.

The detailed orbital contributions and configurations of the T_1 orbitals of four VKs are summarized in Table 2.2. Based on the calculation results, both VK_1 and VK_2 reveal a mixture of n_{HOMO}-π^*_{LUMO} /π_{HOMO}-π^*_{LUMO} character in their T_1 states. The n_{HOMO}-π^*_{LUMO} characterized T_1 are usually formed by excitation from a lower HOMO with n characterization to a π^* LUMO. VK_3 presents an almost exclusive n_{HOMO}-π^*_{LUMO} characterized T_1, representing the transition is typically from n characterized HOMO to π^* characterized LUMO. VK_4 also shows a direct transition of a local π electron from HOMO to LUMO in its T_1 status resulting in the π_{HOMO}-π^*_{LUMO} characterization. In summary, the configurations of T_1 status of excited molecules of VK_1, VK_2, and VK_3, are 33.31%, 45.15%, and 97.68% in n_{HOMO}-π^*_{LUMO}, but 99.20% in π_{HOMO}-π^*_{LUMO} for VK_4, respectively. Besides, the energies of the T_1 (E_T) of the four VKs are also summarized in Table 2.2, all of which are higher than 0.9846 eV (95 kJ/mol), a specific energy requirement of the E_T for the type II photoreaction in generating $^1O_2$ [43]. Therefore, both of the type I and type II photoreactions are theoretically possible for all four VKs under photoirradiation.

Thus, in a hydrogen donor sufficient environment, VK_3 should abstract hydrogen atoms and generate HO· and H_2O_2 under photo-irradiation via the type I reaction primarily, due to the "bi-radical-like" character of its n_{HOMO}-π^*_{LUMO} configured T_1, which is extremely active in the hydrogen abstraction reaction [47]. A competition between the type I and II reactions should exist in both VK_1 and VK_2 because of their relatively low n_{HOMO}-π^*_{LUMO} percentages. However, VK_4 should be the least active one to generate HO· through the type I reaction owing to the inactive π_{HOMO}-π^*_{LUMO} character of T_1 in abstracting hydrogen [48].

From the above analyses, frontier orbitals of VK_1, VK_2, and VK_3 revealed a significant difference in potential photo activities. According to the structural features of these compounds,

the double bonds in the aliphatic chains of the aromatic ketone always increase the energies of the π characteristic HOMO (π_{HOMO}) of both VK_1 and VK_2. Therefore, we speculate that removal of the aliphatic double bonds in both compounds would result in increased type I photo activities of their products. Thus, a theoretical calculation on potential derivatives of VK_1 with the double bond broken by different reactions was conducted, and the results are (Figure 2.5 and Table 2.3) fully supportive and precisely matching the speculations. By referring to the computed UV-vis spectra of the chemically modified VK_1 derivatives, no apparent absorption shift was observed, which indicates the chemical modification does not affect the optical properties of the modified VK_1 a lot. Besides, from the computed frontier molecular orbitals and the orbital contributions to their triplet excited states, the chemical modification of VK_1 increases nπ* characterization percentage, which implies the stronger hydrogen abstraction ability and higher HO· production, compared with the original VK_1, shedding light on future developments of new VK based photo-active chemicals. Thus, the analyses of photoexcitation of the selected four VK compounds have provided interesting information in predicting and understanding their potential photo-induced reactions.

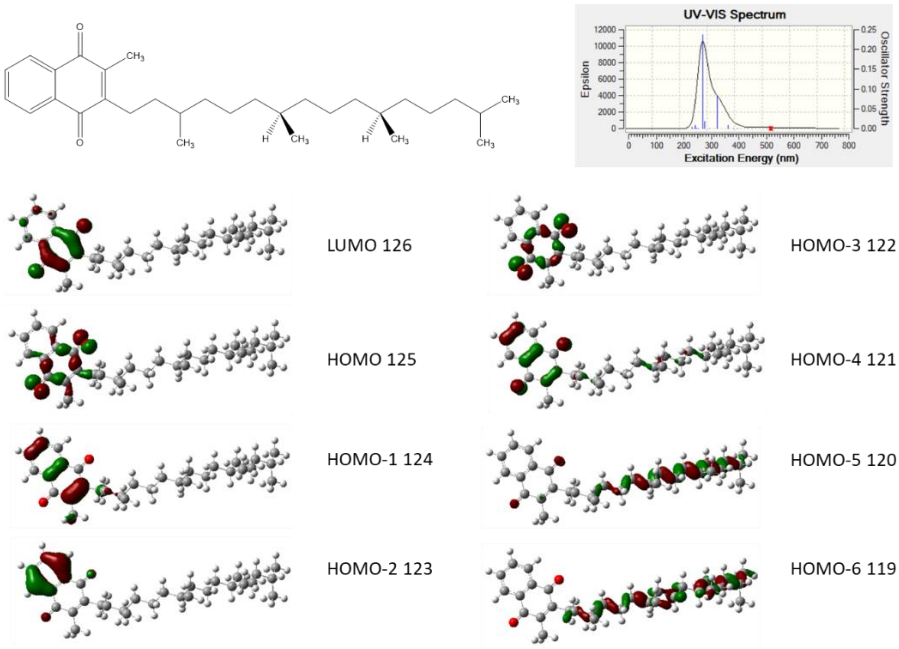

(a)

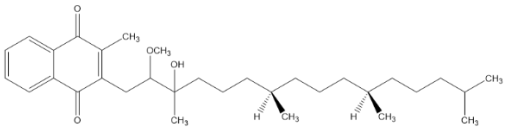

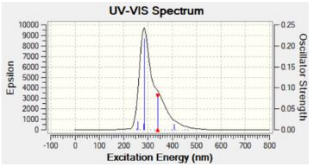

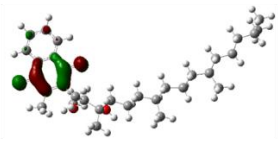

LUMO 138

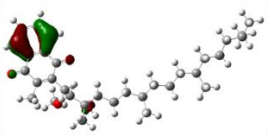

HOMO-3 134

HOMO 137

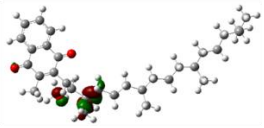

HOMO-4 133

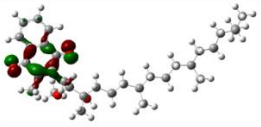

HOMO-1 136

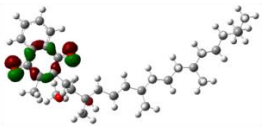

HOMO-5 132

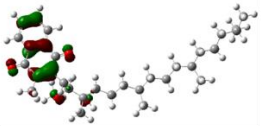

HOMO-2 135

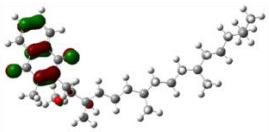

HOMO-6 131

(b)

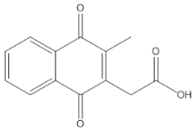

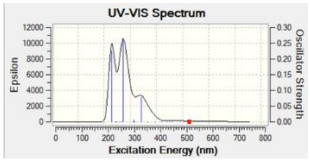

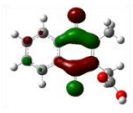

LUMO 61

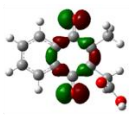

HOMO-3 57

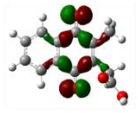

HOMO 60

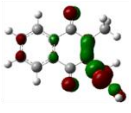

HOMO-4 56

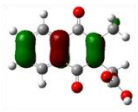

HOMO-1 59

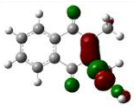

HOMO-5 55

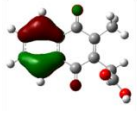

HOMO-2 58

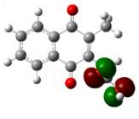

HOMO-6 54

(c)

Figure 2.5. Computed frontier molecular orbitals and UV-vis spectrum of various chemically modified VK_1 derivatives: (a) hydrogenation, (b) ring opening after epoxidation by using CH_3OH as nucleophiles, and (c) oxidation of the double bond.

Vitamin Derivatizatives	% of Molecular Orbital Contribution
(a)	HOMO-4→LUMO (3.55%, ππ*) HOMO-1→LUMO (8.40%, ππ*) HOMO→LUMO (83.19%, nπ*)
(b)	HOMO-6→LUMO (13.30%,ππ*) HOMO-1→LUMO (78.96%, nπ*)
(c)	HOMO-3→LUMO+1 (2.30%, nπ*) HOMO→LUMO (94.79%, nπ*)

Table 2.3. TD-DFT Calculated lowest triplet excited states of the VK_1 derivatives in water.

2.3.2 Photo-reactivity of the type I reaction of the vitamin K derivatives

To further investigate the photo activities of the four compounds, electrostatic potential (ESP) mapped electron density of the corresponding S_0 and T_1 structures were also computed. As shown in Figure 2.6a, the ESP charge (δ) of the carbonyl oxygens in T_1 of both VK_1 and VK_2 become more negative, meaning an increment of electron density compared to their S_0, caused by their high ratios of π_{HOMO}-π^*_{LUMO} excitation configurations in their T_1 [30]. The electron sufficiency in triplet carbonyl oxygen makes the T_1 inactive in abstracting hydrogen to proceed with the type I reaction. Compared with S_0, the δ of carbonyl oxygen in T_1 of VK_3 becomes more positive, which implies an electron deficiency of the excited carbonyl oxygen. Hydrogen abstraction from electron-rich hydrogen donor to the electron-deficient carbonyl oxygen in $^3VK_3^*$ is, therefore, more preferable. For VK_4, almost no change in electron charge is observed in both of its S_0 and T_1

statuses in the carbonyl oxygen because the carbonyl oxygen is not involved in the excitation and formation of T_1. Based on the earlier analysis, the π_{HOMO}-π^*_{LUMO} configuration of T_1 of VK_4 is mainly achieved by local excitation of π electrons of the aromatic conjugation system. Overall, based on the ESP analysis, the results are consistent with the molecular orbital analysis in the previous section.

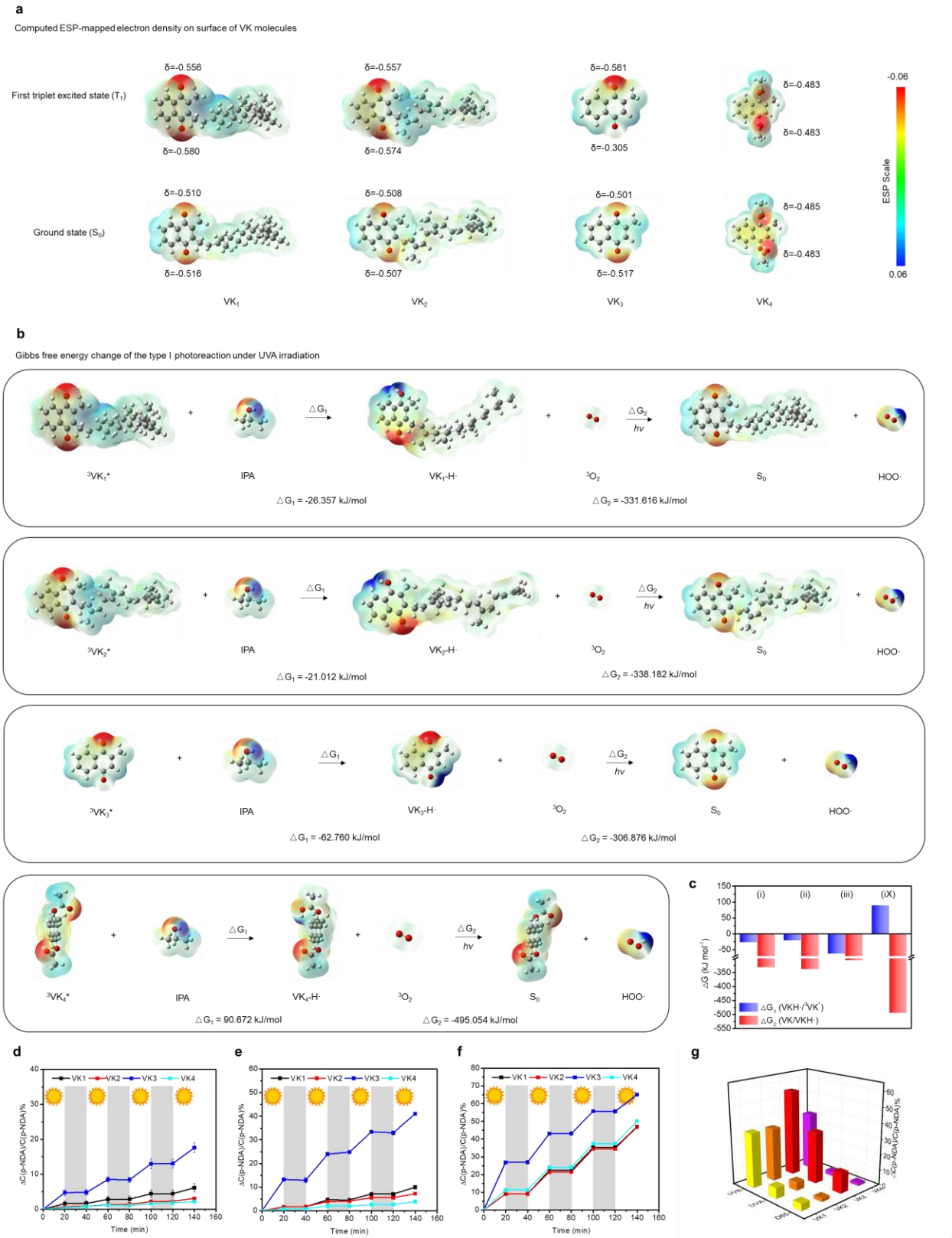
a
Computed ESP-mapped electron density on surface of VK molecules
First triplet excited state (T1)
Ground state (S0)
δ=-0.556
δ=-0.580
δ=-0.557
δ=-0.574
δ=-0.561
δ=-0.305
δ=-0.483
δ=-0.483
δ=-0.510
δ=-0.516
δ=-0.508
δ=-0.507
δ=-0.501
δ=-0.517
δ=-0.485
δ=-0.483
VK1
VK2
VK3
VK4
-0.06
ESP Scale
0.06
b
Gibbs free energy change of the type I photoreaction under UVA irradiation
3VK1*
IPA
VK1-H·
3O2
S0
HOO·
△G1 = -26.357 kJ/mol
△G2 = -331.616 kJ/mol
3VK2*
IPA
VK2-H·
3O2
S0
HOO·
△G1 = -21.012 kJ/mol
△G2 = -338.182 kJ/mol
3VK3*
IPA
VK3-H·
3O2
S0
HOO·
△G1 = -62.760 kJ/mol
△G2 = -306.876 kJ/mol
3VK4*
IPA
VK4-H·
3O2
S0
HOO·
△G1 = 90.672 kJ/mol
△G2 = -495.054 kJ/mol
c
(i)
(ii)
(iii)
(iX)
△G (kJ mol-1)
△G1 (VKH·/3VK*)
△G2 (VK/VKH·)
d
e
f
g
VK1
VK2
VK3
VK4
Time (min)
△C(p-NDA)/C(p-NDA)/%

Figure 2.6 Photo-reactivity of the type I reaction for the vitamin K derivatives. (a) ESP-mapped electron density of the ground and triplet states of VKs. The δ represents ESP charges on carbonyl oxygens of VKs. **(b and c)** Detailed mechanisms of type I reaction and computed △G for each step of the reactions. The (i), (ii), (iii), and (ix) represent VK_1, VK_2, VK_3, and VK_4, respectively. **(d to f)** Quantification of HO· generated by various VKs under different irradiation resources (d for D65, e for UVA, and f for UVB) versus time (irradiation in white and dark in gray). **(g)** Summary of the HO· generation efficiencies of various VKs under different light irradiations.

To quantitatively analyze the type I reactions of the four VKs, reaction feasibilities of VKs with isopropanol (IPA) as a hydrogen donor were analyzed by referring to computed Gibbs free energy changes (△G). Two essential steps of the reactions ($\triangle G_1$ and $\triangle G_2$ in Figure 2.6b) constitute the type I reaction after the formation of corresponding T_1. The detailed calculation results of relevant states of the VKs are presented in Table 2.4. Based on the results, the total △G and $\triangle G_2$ values of the four reactions are negative (Figure 2.6b), implying the possibility of the type I reaction for all VKs. However, the differences in $\triangle G_1$ values reveal that the hydrogen abstraction reaction is crucial in the photo-reduction process [49]. The $\triangle G_1$ value of the reaction between VK_3 and IPA is the most negative, indicating the highest reaction tendency of this step reaction. Meanwhile, the $\triangle G_1$ values of both VK_1 and VK_2 are relatively smaller but still negative, revealing their relatively lower possibility of the hydrogen abstraction reaction than VK_3. The $\triangle G_1$ for VK_4, however, shows as a positive value, meaning a non-spontaneous hydrogen abstraction reaction. Thus, although the total △G values for the four VK reactions are negative, the hydrogen abstraction reaction is the rate-determining step in the type I reaction. Hence, the reactions of four VKs are in the order of VK_3 the fastest, followed by VK_1 and VK_2, and then the VK_4 as the lowest.

The calculated Gibbs free energy changes of the reactions again support the analysis we made previously. Combining all the above conducted theoretical analyses on the type I reactions of the four VK compounds, VK_3 should be the most reactive one, and VK_1 and VK_2 in the second place, whereas VK_4 the most inert one under the same reaction conditions.

	Gibbs Free Energy (Hartree)			
States	**VK_1**	**VK_2**	**VK_3**	**VK_4**
VK	-1358.928618	-1355.309164	-574.355098	-880.786524
^{3}VK*	-1358.856955	-1355.237000	-574.253613	-880.697186
VK-H·	-1359.508971	-1355.886980	-574.944875	-881.304628

Table 2.4. TD-DFT Calculated Gibbs free energy of the relevant states of VKs. Other molecules including $^3O_2$, $^1O_2$, HOO·, RH (take isopropanol as hydrogen donor template), and R· were calculated using same method at same calculational level.

The type I reactivities of the four VKs were evaluated experimentally, and p-nitroso-N,N-dimethylaniline (p-NDA) was employed as a radical scavenger that could quantitatively react with HO· [15, 29]. Superoxide radical ($\cdot O_2^-$), H_2O_2, and $^1O_2$ produced during the photoreaction could not directly react with p-NDA [29, 50]. The triplet sensitizer produced during the photoirradiation could not react chemically with p-NDA[51]. Isopropanol was used as a solvent since it can dissolve all four liposoluble VKs and p-NDA, while its α-tertiary C-H is a good hydrogen donor for the type I reaction [15]. According to the UV-vis absorbance of the compounds, D65, UVA, and UVB were employed as light sources. The four VKs were subjected to repeated test cycles of 20-min light exposure plus 20 min retained under dark.

As shown in Figure 2.6d, e, and f, the HO· were mainly generated during photo-irradiation, the amounts of the radicals were basically unchanged during retention under dark condition,

proving the photo-induced type I photoreaction of the VKs. No obvious decay of the photo-activity was observed in all three tests even after four cycles, implying the excellent durability of the VKs in the type I reaction. Besides, VK_3 shows the highest amount of HO· generated and reveals its best photo-reactivity in the type I reaction. The generation of HO· by four VKs under three light sources are summarized in Figure 2.6g. Under the exposure to D65 or UVA lights, the HO· generation efficiencies of VK_1 and VK_2 were much weaker than that of VK_3 but are still higher than that of VK_4. Under UVB irradiation, VK_3 still demonstrated as the strongest one in generating HO·, however, the efficiencies in generating HO· by VK_1, VK_2, and VK_4 become comparable. Under D65 or UVA irradiations, VK_4 molecules cannot be excited, and the majority of them stay in S_0 due to its limited absorbance in these ranges of wavelengths. Its HO· generation efficiency is, therefore, the lowest due to no photoexcitation and consequently no photoreaction. The UVB exposure, in contrast, could sufficiently excite VK_4 molecules to their T_1 that can proceed with the following photoreaction (Figure 2.6b). Although the $\triangle G_1$ of the VK_4 reaction is positive, the negative total $\triangle G$ indicates the possibility in the type I reaction even though in relatively lower efficiency. Besides, because of the existence of ample hydrogen donors and HO· scavengers in solution, the reaction is believed to be dragged to the thermodynamically spontaneous direction. Hence, the HO· generation efficiency of VK_4 became comparable to that of VK_1 and VK_2 under the most powerful UVB irradiation.

The quantification results of the HO· generation of the four VKs in the type I reaction are fully consistent with the computational data, proving the proposed mechanisms of the photoreactions. Accordingly, VK_3 is the best candidate for the type I photoreaction in generating HO· in a broad UV-vis range, and VK derivatives possessing similar structures could be the potential candidates. As we have demonstrated computationally, four VK_1 derivatives with double

bonds removed (Figure 2.5) could be new candidates as well, which will be investigated in future studies.

2.3.3 Photo-reactivity of the type II reaction for the vitamin K derivatives

Similarly, the reactivities of the four VKs for undergoing the type II reaction from their triplet excited states (^{3}VK*) with $^3O_2$ were analyzed by calculating their corresponding $\triangle$G values of the reactions, and the results are shown in Figure 2.7a. The ESP difference of the ground-state $^3O_2$ and the generated $^1O_2$ indicates that the latter one is more blue (more positive in ESP scale) and much more oxidative due to its electron deficiency, which is consistent with the common sense that $^1O_2$ is more oxidative than ground-state $^3O_2$. Different from the results obtained in the previous section, all $\triangle$G values for the reactions of four excited statuses (^{3}VK*) with oxygen were all negative indicating that the type II photoreaction is spontaneous for all VKs (Figure 2.7b). Among the four VKs, VK_3 still has the highest negative $\triangle$G, implying its highest photo-activity in the type II reaction in generating $^1O_2$ (Figure 2.7b). However, the $\triangle$G values of VK_4 becomes the second highest and is only a little bit smaller than that of VK_3, indicating increased type II reactivity and ability to generate $^1O_2$ by VK_4. The $\triangle$G values of VK_1 and VK_2 are still very close due to the similarity of their structures. However, these lower values of the $\triangle$G represent their lower feasibility of the type II reaction as well. Therefore, we predict that the VK_3 should be the strongest photosensitizer in the type II reaction, followed by the VK_4, whereas VK_1 and VK_2 are the weakest in generating $^1O_2$, under the photo-irradiation. Here again, the photoexcitation of the n_{HOMO}-π^*_{LUMO} characteristics for triplet excited state is the critical structural requirements for chemicals going through the type I photoreaction, while the π_{HOMO}-π^*_{LUMO} transition may mainly lead to the type II photoreaction.

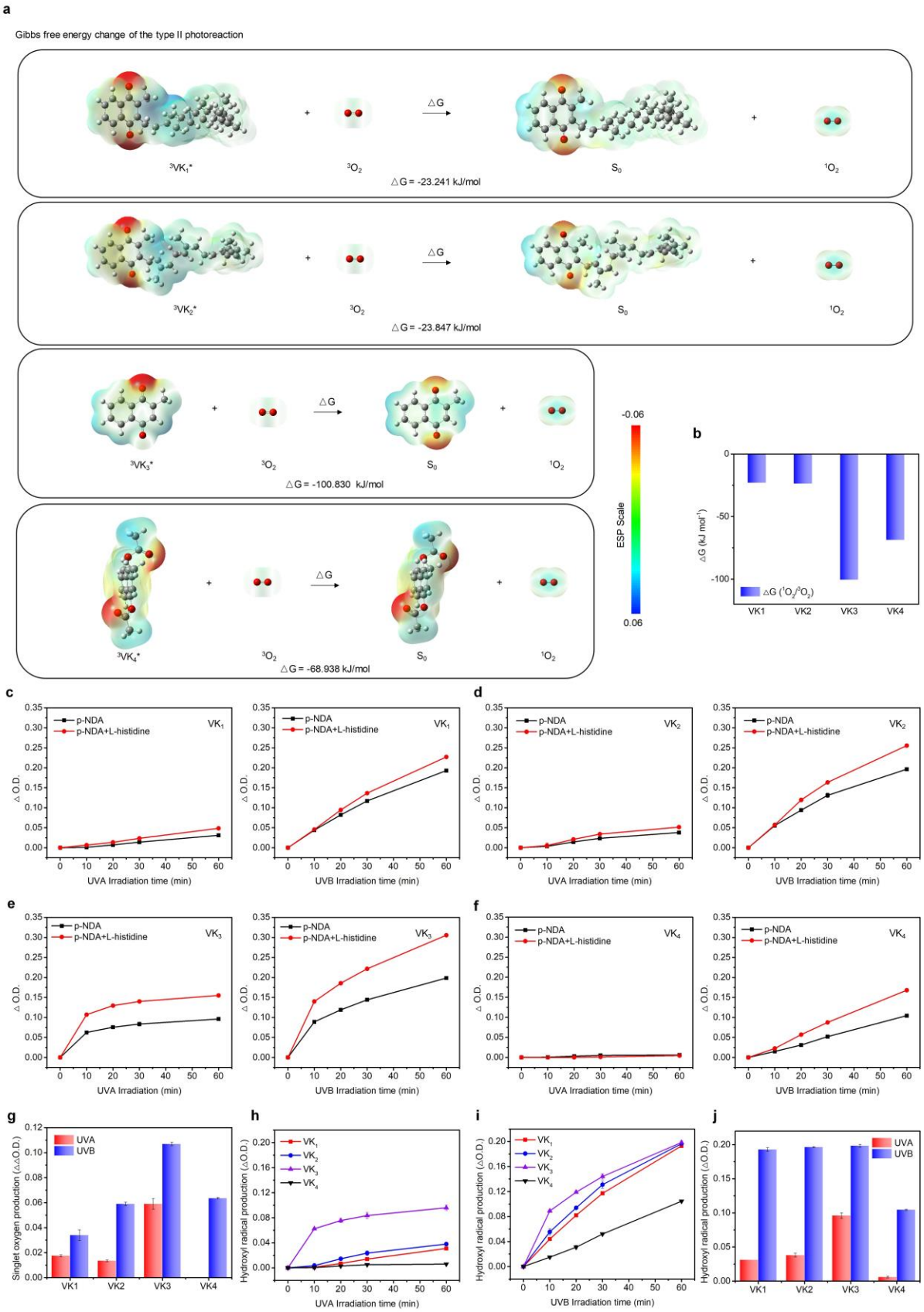
a
Gibbs free energy change of the type II photoreaction
△G = -23.241 kJ/mol
△G = -23.847 kJ/mol
△G = -100.830 kJ/mol
△G = -68.938 kJ/mol
ESP Scale
b
△G (kJ mol⁻¹)
△G (¹O₂/³O₂)
VK1
VK2
VK3
VK4
c
d
e
f
p-NDA
p-NDA+L-histidine
△ O.D.
UVA Irradiation time (min)
UVB Irradiation time (min)
g
Singlet oxygen production (△△O.D.)
UVA
UVB
h
Hydroxyl radical production (△O.D.)
i
j

Figure 2.7. Photo-reactivity of type II reaction of vitamin K derivatives. (a and b) Detailed mechanisms of the type II reaction and computed △G values of the reactions. **(c to f)** Singlet oxygen production of the four VKs under UVA and UVB irradiation versus time. **(g)** Summary of singlet oxygen production of the four VKs under UVA and UVB irradiation. **(h to j)** HO· production of four VKs under light irradiation in relatively insufficient hydrogen donor environment (10% EtOH/PBS system, h for UVA and i for UVB).

The type II reaction of the four VKs was experimentally evaluated in order to validate the prediction on their feasibility of reacting with oxygen in the air without good hydrogen donors. The product of the type II reaction is $^1O_2$, and a widely used $^1O_2$ detection method was employed by using a system of p-NDA with L-histidine [15, 50]. p-NDA itself could not be directly oxidized by $^1O_2$, however, with the presence of L-histidine, $^1O_2$ will firstly be quenched by the amino acid and subsequently become a transannular intermediate that can oxidize p-NDA, leading to a visible color fading. Compared with the system without L-histidine, more p-NDA should be consumed since HO· that are formed via the type I photoreaction will result in the direct oxidation of p-NDA; meanwhile, the $^1O_2$ produced in the type II photoreaction could also react with it under the assistance of L-histidine. As shown in Figures 2.7c, 3d, 3e, and 3f increased p-NDA consumptions were observed in all four VKs under both UVA and UVB photo-irradiations, proving both type I and II photoreactions of these VKs. The amounts of $^1O_2$ produced by the four VKs under UVA or UVB irradiation are summarized in Figure 2.7g, proving their feasibility of undergoing the type II reaction and consistence with the Gibbs free energy change results (Figure 2.7b). Under UVA irradiation, VK_3 should be the most active to go the type II reaction generating more $^1O_2$. VK_1 and VK_2 produce a comparable amount of $^1O_2$ under the UVA irradiation, but the amounts of $^1O_2$ produced were still much lower than that of VK_3. However, the $^1O_2$ production of VK_4 under the

UVA irradiation was negligible, which implies its low photo-reactivity, consistent with the low HO· production in the previous section due to no excitation of VK_4 under the UVA region. Under UVB irradiation, VK_4 shows a strong capacity of generating $^1O_2$ thanks to the sufficient excitation and the improved △G. The type II reactivity of VK_4 is still lower than that of VK_3 but now becomes higher than those of VK_1 and VK_2, proving that the computational results are correct. It is worth mentioning that the solvent used in the $^1O_2$ tests is a mixture of ethyl alcohol and DI water (volume ratio 10%: 90%) due to the low solubility of these VKs in water. The solvent mixture is, therefore, a relatively deficient hydrogen donor system comparing to the pure isopropanol system. Thus, the HO· generation efficiency of the four VKs in this hydrogen donor deficient system was also studied. Figures 2.7h and 2.7i describe the amounts of HO· generated by the four VKs in the solvent system under UVA and UVB irradiation versus time. The HO· productions are summarized in Figure 2.7j. Under UVA irradiation, the HO· production of VK_3 is still the highest even in the hydrogen donor deficient system. VK_1 and VK_2 show weaker HO· generation ability when compared with VK_3, which is consistent with the △G calculation results of the type I reaction. VK_4 exhibits the lowest HO· production due to its photo-inactivity under UVA exposure. Different from the HO· quantification results in isopropanol, the sequence of HO· production of the four VKs in the hydrogen donor deficient systems under UVB irradiation satisfies the △G calculation of the type I reaction perfectly, that is, $VK_3 > VK_1 \approx VK_2 > VK_4$, especially in the first 20 minutes test when the hydrogen donors in the solution are still relatively sufficient to support the type I photoreaction (Figure 2.7i). In figure 2.7j, VK_3 only shows a little bit higher HO· production comparing to VK_1 and VK_2, which may be because of the insufficient hydrogen donors that restrict the HO· production of VK_3 under the most potent UVB irradiation. Thus, the abnormal high

HO· production of VK_4 in isopropanol can be ascribed to the abundance of hydrogen donor in isopropanol solution.

Overall, based on the outcomes of both HO· and the $^1O_2$ tests, the computationally modeled type I and type II photoreaction mechanisms of the four compounds were supported by experimental results. VK_3 is the best in the VK family, followed by both VK_1 and VK_2, to go through both types of reaction mechanisms and producing both HO· and $^1O_2$ in hydrogen donor-rich or deficient conditions under D65, UVA or UVB irradiation. However, due to the dominating n_{HOMO}-π^*_{LUMO} feature of VK_3, it shows the strongest capacity in generating HO· and $^1O_2$, implying its highest photo-reactivity for the two types of photoreactions. VK_4 shows the worst photo-reactivity due to its inefficient light absorption under D65 or UVA irradiation. However, under UVB irradiation, VK_4 is the second best one below VK_3 in generation of $^1O_2$, much better than VK_1 and VK_2, though still least effective in generating HO·. So VK_4 is photoactive under very restricted conditions and producing mostly $^1O_2$, while VK_3 is almost unrestricted under broad photo-irradiation resources and in varied solvent systems. Thus, more VK_3 similar structures are proposed (Figure 2.5) as future alternatives. Moreover, the robust photo-reactivity in generating ROS by VK_3 makes it representative photoactive vitamin K in the following study.

2.3.4 Hydrogen donor effect on the photo-reactivity of vitamin K_3

Based on the above assessments, VK_3 was proven to be the most effective VK compound in generating both HO· and $^1O_2$. However, the type I photoreaction has special functions of producing HO· and H_2O_2, which are more oxidative and stable biocidal ROS than $^1O_2$, respectively. Thus, hydrogen donors could affect the hydrogen abstraction step in the type I photoreaction, and computational analysis and experimental tests of different hydrogen donors were performed.

Solvent	Main Excited State in UVA Range			
	λ_{max} (nm)	*f*	Excited State	Configuration
ACN	344.84	0.0711	S_4	ππ*
	365.54	0.0019	S_3	ππ*
IPA	344.77	0.0722	S_4	ππ*
	365.05	0.0019	S_3	ππ*
EtOH	344.80	0.0716	S_4	ππ*
	365.29	0.0019	S_3	ππ*
CYC	341.42	0.0715	S_4	ππ*
	357.48	0.0022	S_3	ππ*
THF	344.15	0.0727	S_4	ππ*
	363.34	0.0020	S_3	ππ*

Solvent	Lowest Triplet Excited State (T1)				ΔE_{ST}
	λ_{max} (nm)	*f*	E_T (eV)	% of MO Contribution	**(eV)**
ACN	536.07	0.0000	2.3129	HOMO-3→LUMO+1(2.02%, nπ*) HOMO→LUMO (95.66%, nπ*)	0.4461
IPA	536.78	0.0000	2.3098	HOMO-3→LUMO+1(2.01%, nπ*) HOMO→LUMO (95.65%, nπ*)	0.4466
EtOH	536.44	0.0000	2.3113	HOMO-3→LUMO+1(2.02%, nπ*) HOMO→LUMO (95.65%, nπ*)	0.4463
CYC	546.96	0.0000	2.2668	HOMO→LUMO (95.58%, nπ*)	0.4545
THF	539.09	0.0000	2.2999	HOMO→LUMO (95.64%, nπ*)	0.4483

Table 2.5. TD-DFT Calculated singlet and triplet excited states of VK_3 in various solvents.

UV-vis absorption spectra of VK_3 in solvents of acetonitrile (ACN), isopropanol (IPA), ethyl alcohol (EtOH), cyclohexane (CYC), and tetrahydrofuran (THF), respectively, were measured (Figures 2.8a to 2.8e). The solvents with varied C-H bond structural features could serve as hydrogen donors in the type I photoreaction but with varied reaction potentials. The experimentally measured maximum absorbance wavelengths (λ_{max}) of VK_3 in various solvent systems were almost the same, which are 332 nm, 332 nm, 332 nm, and 331 nm for VK_3 in ACN, IPA, EtOH, and THF, respectively, and the computed UV-vis spectra matched with those

measured perfectly (Figure 2.9), validating the computational modeling method. A slight shift of the λ_{max} for VK_3 in CYC was observed at about 325 nm, which may be due to the nonpolar nature of the solvent alternating the frontier molecular orbital excitations of VK_3. The similar shift of the λ_{max} absorbance of VK_3 in CYC was observed in the computation results (Figure 2.9). However, the oscillator strength values of VK_3 in these solvents are similar (Table 2.5), implying similar photo absorbance capacities of VK_3 in these systems with different polarities. Based on the frontier molecular orbital computation, the configurations of T_1 of VK_3 in the above solvents are all in n_{HOMO}-π^*_{LUMO} characterization with very high ratios (Table 2.5), indicating the high possibility for the type I photoreaction of VK_3 in these solvents. The configurations of T_1 of VK_3 in the above solvents were further confirmed by employing the computed ESP method, as shown in Figure 2.8f. In all five solvents, the electron density on the carbonyl oxygen in T_1 becomes more positive compared with that in S_0. The electron deficiency on the T_1 carbonyl oxygen reveals the feasibility of the hydrogen abstraction reaction in the type I reaction. Thus, the above analysis suggested that VK_3 retains the same photoexcitation properties in the five solutions. As a result, any difference in the HO· production should be a result caused by different solvents with their respective hydrogen donating ability. Here, the quantifications of HO· were tested in these five solvents by using p-NDA as a scavenger under D65, UVA, and UVB photo-irradiation to find out the most efficient hydrogen donor in the photoreaction under different irradiation resources.

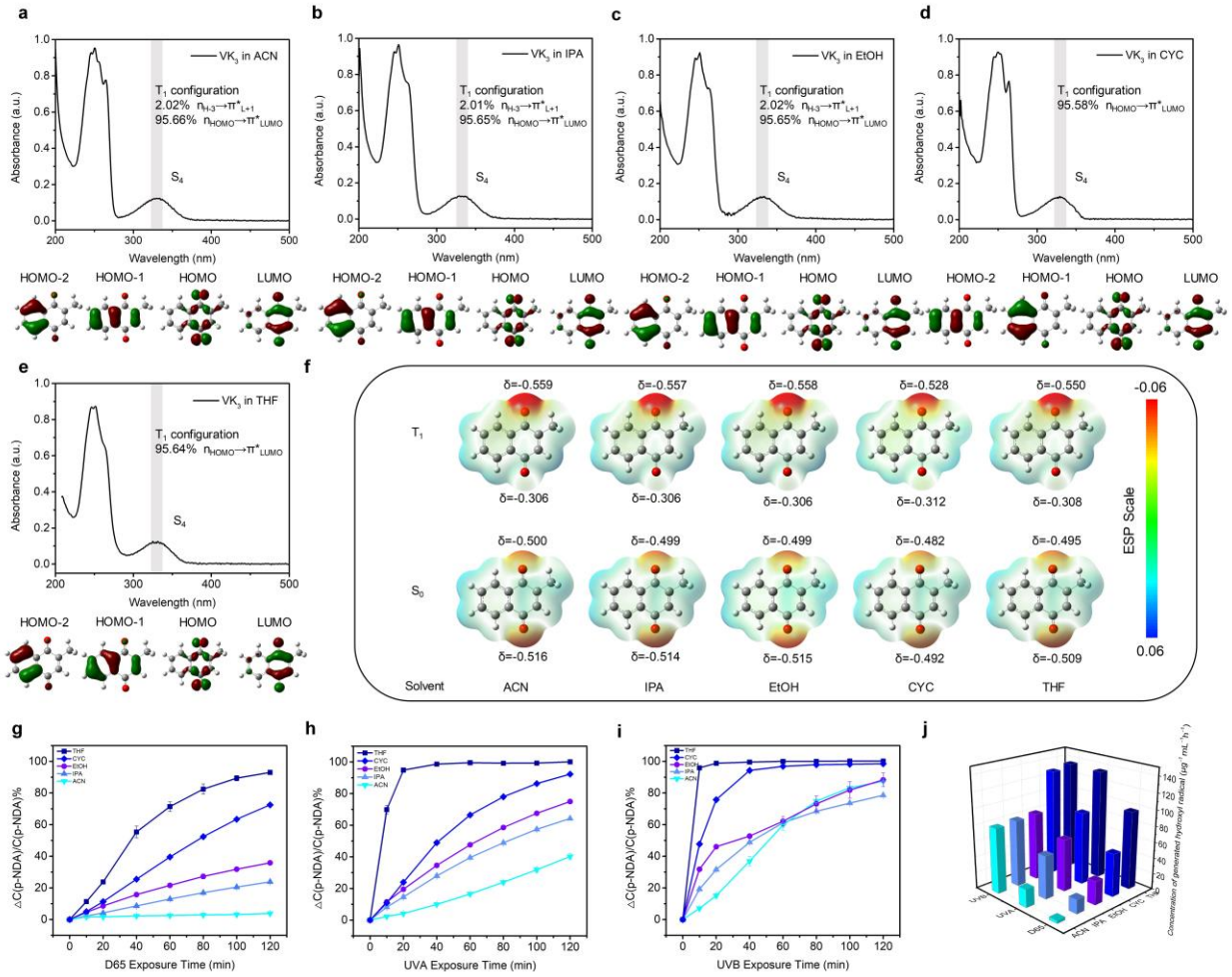

Figure 2.8. Hydrogen donor effect on the photo-reactivity of vitamin K_3. (a to e) UV-vis spectra of VK_3 in various solvent systems (from a to e, acetonitrile, isopropanol, ethyl alcohol, cyclohexane, and tetrahydrofuran, respectively) with their theoretically computed frontier molecular orbitals. **(f)** ESP-mapped electron density of the ground state and triplet state of vitamin K_3 in various solvent systems. **(g to j)** Quantification of HO· generated by VK_3 in various solvent systems under different irradiation resources.

As shown in Figure 2.8g, under D65 irradiation, VK_3 in THF shows the most robust capacity in generating HO·, followed by CYC, EtOH, IPA, and ACN, consequently. The same tendency was also observed under UVA and UVB irradiation. The distinct hydrogen donor effects

of the five solvents could be explained by their different bond disassociation enthalpies (BDE) which represents the homolytic cleavage energy of the solvent molecules. According to the literature, the BDE of the α C-H bond in THF, CYC, EtOH, IPA, and ACN are 384.56 kJ/mol [52], 399.19 kJ/mol [53-54], 384.56 kJ/mol [52], 372.02 kJ/mol [52], and 401.28 kJ/mol [52] at 298K, respectively. The high BDE of ACN makes it the least active hydrogen donor among the five solvents [55-56], whereas although CYC has a relatively higher BDE, it could still serve as a good hydrogen donor in the photochemistry study on benzophenone [56]. The BDE values of THF (384.56 kJ/mol) and CYC (399.19 kJ/mol) also satisfy the HO· production efficiency sequence, which implies that THF is a better hydrogen donor than CYC. However, abnormal HO· production efficiencies occur in both EtOH and IPA solvent systems. Although their BDE values are lower than or similar to those of CYC and THF, the HO· production efficiency of VK_3 in these two solvents was not high. This may be due to the fact that both ethanol and isopropanol are very good HO· scavengers leading to the HO· consumption competence between alcohols and p-NDA in the solvent, resulting in reduced color fading of p-NDA and HO· production [57-58].

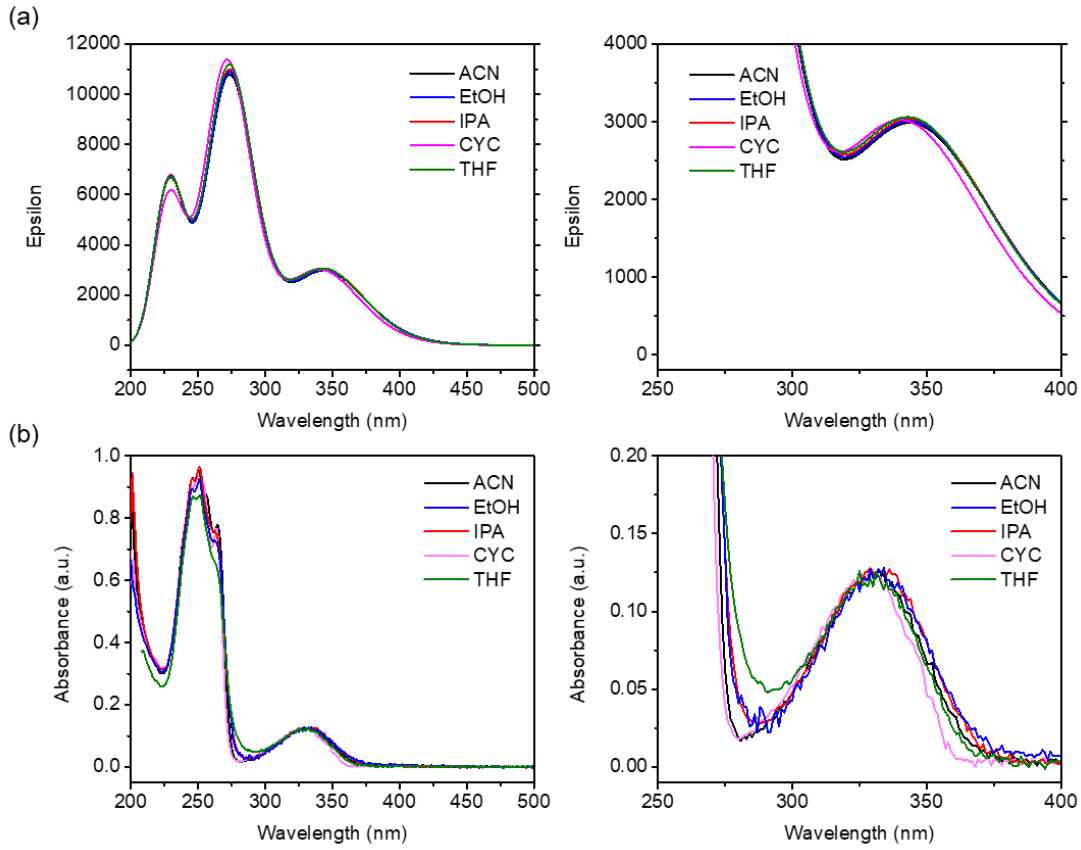

Figure 2.9. Comparison between calculated UV-vis spectra (a) and experimental UV-vis spectra (b) of VK_3 in various solvents.

Thus, the hydrogen-donating capacity of the five molecules provided some insights into finding new matrix materials that may work as hydrogen donors in the photoreactions. Meanwhile, controllable ROS productions of either HO· and H_2O_2 in hydrogen donor-rich system via the type I photoreaction or $^1O_2$ in hydrogen donor-deficient system via the type II photoreaction could be achieved by alternating matrix materials. This could lead to further development of light-induced antimicrobial materials for different applications.

2.3.5 Daylight-induced antibacterial performance of vitamin K_3

Two typical etiological bacteria, Gram-negative *Escherichia coli* O157:H7 (*E.coli*) and Gram-positive *Listeria innocua* (*L.innocua*) were added into 4% EtOH/PBS containing 20 mM VK_3 and exposed to daylight irradiation to evaluate the antibacterial activity of VK_3. For the time-dependent daylight-induced antibacterial assay, two control groups (EtOH/PBS without VK_3 under daylight irradiation, and VK_3/EtOH/PBS under dark condition) were performed to eliminate any bactericidal effect caused by VK_3 itself or daylight irradiation. 10 μL of 1×10^8 colony-forming units (CFU) mL^{-1} *E.coli* suspension or 4×10^7 CFU mL^{-1} of *L.innocua* suspension was added into 990 μL of VK_3/EtOH/PBS or EtOH/PBS to form initial bacterial suspension (1×10^6 CFU mL^{-1} for *E.coli* and 4×10^5 CFU mL^{-1} for *L.innocua*) for further antibacterial tests. Then the bacterial samples were exposed to daylight irradiation or dark for different time durations, after each time point the bacterial proliferation was assessed by agar plate counting. Figure 2.10a and 2.10e depict the time-dependent antibacterial performance of VK_3 under daylight irradiation. It is obvious to notice that both *E.coli* and *L.innocua* were completely inactivated by VK_3 after certain period of daylight irradiation. VK_3 showed effective antibacterial performance achieving 6 log reduction (99.9999%) of *E.coli* and 5 log reduction (99.999%) of *L.innocua* after 60-min and 90-min daylight irradiation, respectively. In contrast, for the control groups that bacteria in EtOH/PBS under daylight irradiation or in VK_3/EtOH/PBS under dark condition, significant bacterial growth was found in both groups after 60-min (for *E.coli*) or 90-min (for *L.innocua*) durations, indicating that EtOH, daylight irradiation, and VK_3 itself have negligible impact on the inactivation of bacteria at corresponding conditions. The inactivation of bacteria was exclusively caused by the ROS resulted from daylight irradiation of VK_3. Compared to previously reported natural photo-induced antibacterial chemicals, VK_3 reveals stronger bactericidal ability with lower concentration [59-60]. Interestingly, *L.innocua* showed stronger resistance comparing to *E.coli*, to ROS, which could

be because of the distinct cell wall structures of these two bacteria. According to the literature, the bactericidal mechanism of ROS are all non-selective oxidation of the substances on the surface of cell wall membranes leading to a cell wall destruction followed by the oxidation of intracellular DNA or RNA [30]. Gram-negative bacteria have a thinner cell wall membrane whose thickness is within 2 nm. In contrast, the thickness of the cell wall membrane of Gram-positive bacteria reached 20~80 nm, which makes the Gram-positive bacteria harder to be inactivated [61].

To evaluate durability and reusability of the daylight-induced antibacterial functions of VK_3, 7-times cyclic daylight-induced antibacterial tests were performed on both *E.coli* and *L.innocua*. As shown in Figure 2.10b and 2.10f, the seven cyclic daylight-induced antibacterial tests indicated that the bactericidal efficacy of VK_3 kept nearly constant with 6 log reduction of *E.coli* and 5 log reduction of *L.innocua*, revealing that VK_3 could still produce enough ROS to inactivate bacteria even after 7 times of repeated uses, which demonstrates that VK_3 is a durable and reusable green and sustainable biocide.

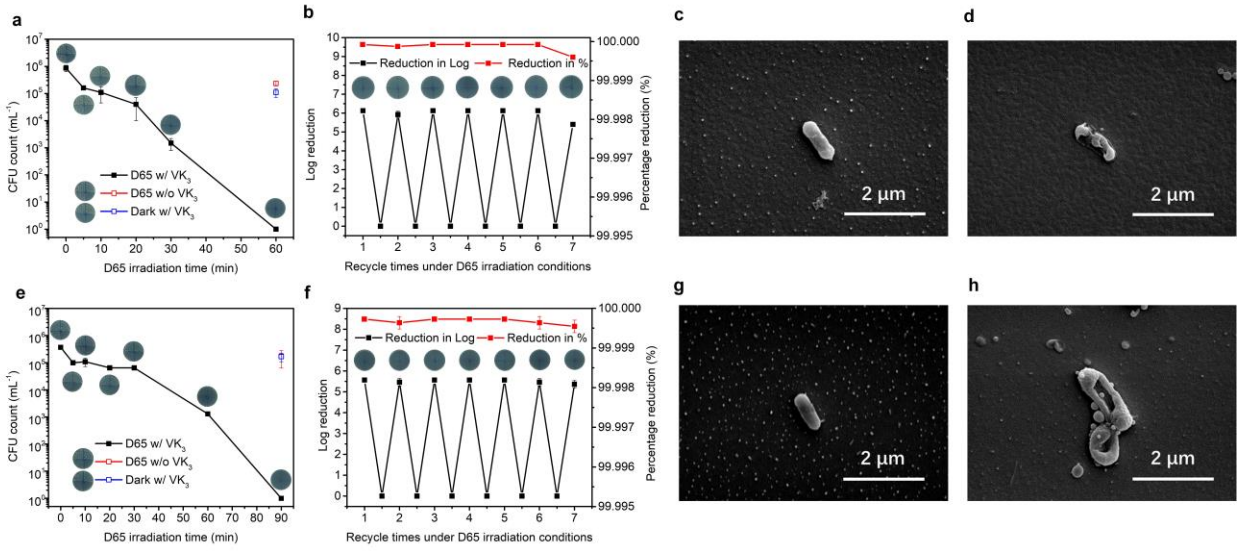

Figure 2.10. Daylight-induced antibacterial performance of vitamin K_3 (a and e) Time-dependent bactericidal activity of VK_3 against *E.coli* (a) and *L.innocua* (e) under daylight

irradiation. **(b and f)** Seven-cycle bactericidal activity of VK_3 against *E.coli* (b) and *L.inncoua* (f) under daylight irradiation. **(c and g)** SEM images of *E.coli* (c) and *L.innocua* (g) in PBS without any treatment. **(d and h)** SEM images of *E.coli* (d) and *L.innocua* (h) in VK_3 suspension after 90-min daylight irradiation.

The morphological changes of bacteria in VK_3 suspension after daylight exposure were also obtained by employing scanning electron microscope (SEM). As shown in Figure 2.10c and 2.10g, both *E. coli* and *L. innucua* in PBS without any treatment remain their intact and smooth membranes. In contrast, cell wall membrane damage and structure deformation of both *E. coli* and *L. innucua* were observed in the test groups containing VK_3 and irradiated under daylight for 90 min. The sharp morphological changes of the bacteria cells with or without VK_3 reveal the rapid ROS generation efficiency and cell destruction function of VK_3 under daylight irradiation.

2.4 Conclusion

We successfully analyzed and examined the photo-reactivities of four vitamin K derivatives by using the computational modeling process and designed experimental methods. Among these four VKs, VK_3 reveals its highest reactivity to undergo both type I and type II photoreactions and can generate $HO\cdot$ and $^1O_2$ under photoirradiation of D65, UVA, and UVB irradiations. Structural features of aromatic ketones and n_{HOMO}-π^*_{LUMO} configuration of its T_1 state make this compound special among others. VK_1 and VK_2 are less effective in photo-reactivity than VK_3 due to existence of unsaturated bonds in side chains, though possessing aromatic ketone structure. Similarly, the structural feature of VK_4 makes it have λ_{max} in UVB region and preference in going through type II reaction because of its π_{HOMO}-π^*_{LUMO} T_1 orbital configuration. The hydrogen-donating effect of different solvents was also studied for the photoreactions. Moreover, VK_3 showed robust and instant inactivate function toward both Gram-postive and Gram-negative

bacteria under daylight irradiation, and the functions are durable and reusable. The results provided some new insights into designing and preparing naturally based photoactive antimicrobial materials for different applications.

2.5 Reference

(1) Zhuo, J. Photoactive Chemicals for Antimicrobial Textiles. *Antimicrobial Textiles* **2016**, 197-223.

(2) Pyrgiotakis, G.; Vedantam, P.; Cirenza, C.; McDevitt, J.; Eleftheriadou, M.; Leonard, S. S.; Demokritou, P. Optimization of a Nanotechnology Based Antimicrobial Platform for Food Safety Applications Using Engineered Water Nanostructures (EWNS). *Scientific Reports* **2016,** *6*, 21073.

(3) Gao, A.; Zhang, H.; Sun, G.; Xie, K.; Hou, A. Light-Induced Antibacterial and UV-Protective Properties of Polyamide 56 Biomaterial Modified with Anthraquinone and Benzophenone Derivatives. *Materials & Design* **2017,** *130*, 215-222.

(4) Jalvo, B.; Faraldos, M.; Bahamonde, A.; Rosal, R. Antimicrobial and Antibiofilm Efficacy of Self-Cleaning Surfaces Functionalized by TiO_2 Photocatalytic Nanoparticles against *Staphylococcus Aureus* and *Pseudomonas Putida*. *Journal of Hhazardous Materials* **2017,** *340*, 160-170.

(5) Kumar, R.; Umar, A.; Kumar, G.; Nalwa, H. S. Antimicrobial Properties of ZnO Nanomaterials: A Review. *Ceramics International* **2017,** *43* (5), 3940-3961.

(6) Gerischer, H. Photocatalysis in Aqueous Solution with Small TiO_2 Particles and the Dependence of the Quantum Yield on Particle Size and Light Intensity. *Electrochimica Acta* **1995,** *40* (10), 1277-1281.

(7) Zhang, Z.; Wang, C.-C.; Zakaria, R.; Ying, J. Y. Role of Particle Size in Nanocrystalline TiO_2-Based Photocatalysts. *The Journal of Physical Chemistry B* **1998,** *102* (52), 10871-10878.

(8) Kočí, K.; Obalová, L.; Matějová, L.; Plachá, D.; Lacný, Z.; Jirkovský, J.; Šolcová, O. Effect of TiO_2 Particle Size on the Photocatalytic Reduction of CO_2. *Applied Catalysis B: Environmental* **2009,** *89* (3-4), 494-502.

(9) Wu, J.; Liu, W.; Xue, C.; Zhou, S.; Lan, F.; Bi, L.; Xu, H.; Yang, X.; Zeng, F.-D. Toxicity and Penetration of TiO_2 Nanoparticles in Hairless Mice and Porcine Skin after Subchronic Dermal Exposure. *Toxicology Letters* **2009,** *191* (1), 1-8.

(10) Tim, M. Strategies to Optimize Photosensitizers for Photodynamic Inactivation of Bacteria. *Journal of Photochemistry and Photobiology B: Biology* **2015,** *150*, 2-10.

(11) Li, C.; Lin, F.; Sun, W.; Wu, F.-G.; Yang, H.; Lv, R.; Zhu, Y.-X.; Jia, H.-R.; Wang, C.; Gao, G. Self-Assembled Rose Bengal-Exopolysaccharide Nanoparticles for Improved Photodynamic Inactivation of Bacteria by Enhancing Singlet Oxygen Generation Directly in the Solution. *ACS Applied Materials & Interfaces* **2018,** *10* (19), 16715-16722.

(12) Hynek, J.; Rathouský, J.; Demel, J.; Lang, K. Design of Porphyrin-Based Conjugated Microporous Polymers with Enhanced Singlet Oxygen Productivity. *RSC Advances* **2016,** *6* (50), 44279-44287.

(13) Zhuo, J.; Sun, G. Antimicrobial Functions on Cellulose Materials Introduced by Anthraquinone Vat Dyes. *ACS Applied Materials & Interfaces* **2013,** *5* (21), 10830-10835.

(14) Liu, N.; Sun, G.; Zhu, J. Photo-Induced Self-Cleaning Functions on 2-Anthraquinone Carboxylic Acid Treated Cotton Fabrics. *Journal of Materials Chemistry* **2011,** *21* (39), 15383-15390.

(15) Liu, N.; Sun, G. Production of Reactive Oxygen Species by Photoactive Anthraquinone Compounds and Their Applications in Wastewater Treatment. *Industrial & Engineering Chemistry Research* **2011,** *50* (9), 5326-5333.

(16) Hou, A.; Sun, G. Multifunctional Finishing of Cotton Fabrics with 3, 3′, 4, 4′-Benzophenone Tetracarboxylic Dianhydride: Reaction Mechanism. *Carbohydrate Polymers* **2013,** *95* (2), 768-772.

(17) Rhodes, M.; Bucher, J.; Peckham, J.; Kissling, G.; Hejtmancik, M.; Chhabra, R. Carcinogenesis Studies of Benzophenone in Rats and Mice. *Food and Chemical Toxicology* **2007,** *45* (5), 843-851.

(18) Hadibarata, T.; Yusoff, A. R. M.; Aris, A.; Hidayat, T.; Kristanti, R. A. Decolorization of Azo, Triphenylmethane and Anthraquinone Dyes by Laccase of a Newly Isolated Armillaria Sp. F022. *Water, Air, & Soil Pollution* **2012,** *223* (3), 1045-1054.

(19) Dobrinescu, C.; Iorgulescu, E. E.; Mihailciuc, C.; Macovei, D.; Wuttke, S.; Kemnitz, E.; Parvulescu, V. I.; Coman, S. M. One-Pot Hydroacetylation of Menadione (Vitamin K_3) to Menadiol Diacetate (Vitamin K_4) by Heterogeneous Catalysis. *Advanced Synthesis & Catalysis* **2012,** *354* (7), 1301-1306.

(20) Xu, F.; Li, Y.; Ahmad, J.; Wang, Y.; Scott, D. E.; Vostal, J. G. Vitamin K_5 Is an Efficient Photosensitizer for Ultraviolet A Light Inactivation of Bacteria. *FEMS Microbiology Letters* **2018,** *365* (4), fny005.

(21) Cornelius, J.; Yang, H. The Determination of Vitamin K_5 by Gas Chromatography. *Journal of Chromatographic Science* **1967,** *5* (6), 327-328.

(22) Merrifield, L. S.; Yang, H. Factors Affecting the Antimicrobial Activity of Vitamin K_5. *Appl. Environ. Microbiol.* **1965,** *13* (5), 766-770.

(23) Booth, S. L. Vitamin K: Food Composition and Dietary Intakes. *Food & Nutrition Research* **2012,** *56* (1), 5505.

(24) Holmes, M. V.; Hunt, B. J.; Shearer, M. J. The Role of Dietary Vitamin K in the Management of Oral Vitamin K Antagonists. *Blood Reviews* **2012,** *26* (1), 1-14.

(25) van Hylckama Vlieg, J. E.; Veiga, P.; Zhang, C.; Derrien, M.; Zhao, L. Impact of Microbial Transformation of Food on Health—from Fermented Foods to Fermentation in the Gastro-Intestinal Tract. *Current Opinion in Biotechnology* **2011,** *22* (2), 211-219.

(26) Xu, F.; Vostal, J. G. Inactivation of Bacteria Via Photosensitization of Vitamin K_3 by UV-A Light. *FEMS Microbiology Letters* **2014,** *358* (1), 98-105.

(27) Kimura, K.; Hirota, Y.; Kuwahara, S.; Takeuchi, A.; Tode, C.; Wada, A.; Osakabe, N.; Suhara, Y. Synthesis of Novel Synthetic Vitamin K Analogues Prepared by Introduction of a Heteroatom and a Phenyl Group That Induce Highly Selective Neuronal Differentiation of Neuronal Progenitor Cells. *Journal of Medicinal Chemistry* **2017,** *60* (6), 2591-2596.

(28) Oelgemöller, M.; Mattay, J.; Görner, H. Direct Photooxidation and Xanthene-Sensitized Oxidation of Naphthols: Quantum Yields and Mechanism. *The Journal of Physical Chemistry A* **2010,** *115* (3), 280-285.

(29) Bors, W.; Michel, C.; Saran, M. On the Nature of Biochemically Generated Hydroxyl Radicals Studies Using the Bleaching of p-Nitrosodimethylaniline as a Direct Assay Method. *EuropeanJournal of Biochemistry* **1979,** *95* (3), 621-627.

(30) Si, Y.; Zhang, Z.; Wu, W.; Fu, Q.; Huang, K.; Nitin, N.; Ding, B.; Sun, G. Daylight-Driven Rechargeable Antibacterial and Antiviral Nanofibrous Membranes for Bioprotective Applications. *Science Advances* **2018,** *4* (3), eaar5931.

(31) Wang, G.; Hill, N. S.; Zhu, D.; Xiao, P.; Coote, M. L.; Stenzel, M. H. Efficient Photoinitiating System Based on Diaminoanthraquinone for 3d Printing of Polymer/Carbon Nanotube Nanocomposites under Visible Light. *ACS Applied Polymer Materials* **2019,** *1* (5), 1129-1135.

(32) Lee, J.; Moon, B. Synthesis of Telechelic Anthraquinone-Functionalized Polybutadiene Via Romp and Study of Its Photo-Oxidation and UV Crosslinking Behaviors. *Journal of Polymer Science Part A: Polymer Chemistry* **2018,** *56* (12), 1249-1258.

(33) Zhuo, J.; Sun, G. Light-Induced Surface Graft Polymerizations Initiated by an Anthraquinone Dye on Cotton Fibers. *Carbohydrate Polymers* **2014,** *112*, 158-164.

(34) Wang, G.; Hill, N. S.; Zhu, D.; Xiao, P.; Coote, M. L.; Stenzel, M. H. An Efficient Photoinitiating System Based on Diaminoanthraquinone for 3d Printing of Polymer/Carbon Nanotube Nanocomposites under Visible Light. *ACS Applied Polymer Materials* **2019,** *1* (5), 1129-1135.

(35) Lamola, A. A.; Hammond, G. S. Mechanisms of Photochemical Reactions in Solution. XXXIII. Intersystem Crossing Efficiencies. *The Journal of Chemical Physics* **1965,** *43* (6), 2129-2135.

(36) Anslyn, E. V.; Dougherty, D. A. *Modern Physical Organic Chemistry* **2006**.

(37) Allen, N. S.; Hamzah, H.; Edge, M.; Liauw, C. M.; Catalina, F.; Edge, R.; Navaratnam, S. Photochemistry and Photopolymerisation of Substituted 2-Methylanthraquinones and Novel 2-Acryloxymethylanthraquinone in Radiation Curing. *Journal of Photochemistry and Photobiology A: Chemistry* **2018,** *356*, 530-544.

(38) Huix-Rotllant, M.; Siri, D.; Ferré, N. Theoretical Study of the Photochemical Generation of Triplet Acetophenone. *Physical Chemistry Chemical Physics* **2013,** *15* (44), 19293-19300.

(39) Marazzi, M.; Mai, S.; Roca-Sanjuán, D.; Delcey, M. l. G.; Lindh, R.; González, L.; Monari, A. Benzophenone Ultrafast Triplet Population: Revisiting the Kinetic Model by Surface-Hopping Dynamics. *The Journal of Physical Chemistry Letters* **2016,** *7* (4), 622-626.

(40) Dormán, G. r.; Nakamura, H.; Pulsipher, A.; Prestwich, G. D. The Life of Pi Star: Exploring the Exciting and Forbidden Worlds of the Benzophenone Photophore. *Chemical Reviews* **2016,** *116* (24), 15284-15398.

(41) Ohara, K.; Mitsumori, R.; Takebe, M.; Kuzuhara, D.; Yamada, H.; Nagaoka, S.-I. Vitamin K Analogue as a New Fluorescence Probe for Quantitative Antioxidant Assay. *Journal of Photochemistry and Photobiology A: Chemistry* **2010,** *215* (1), 52-58.

(42) Oelgemöller, M.; Hoffmann, N. Studies in Organic and Physical Photochemistry–an Interdisciplinary Approach. *Organic & Biomolecular Chemistry* **2016,** *14* (31), 7392-7442.

(43) DeRosa, M. C.; Crutchley, R. J. Photosensitized Singlet Oxygen and Its Applications. *Coordination Chemistry Reviews* **2002,** *233*, 351-371.

(44) Ma, J.; Zhang, X.; Phillips, D. L. Time-Resolved Spectroscopic Observation and Characterization of Water-Assisted Photoredox Reactions of Selected Aromatic Carbonyl Compounds. *Accounts of Chemical Research* **2019**.

(45) Görner, H. Photoreduction of 9, 10-Anthraquinone Derivatives: Transient Spectroscopy and Effects of Alcohols and Amines on Reactivity in Solution. *Photochemistry and Photobiology* **2003,** *77* (2), 171-179.

(46) Ramamurthy, V.; Schanze, K. S. *Organic Photochemistry and Photophysics* **2005.**

(47) Scaiano, J. C. Intermolecular Photoreductions of Ketones. *Journal of Photochemistry* **1973,** *2* (2), 81-118.

(48) Demeter, A.; Horváth, K.; Böőr, K.; Molnár, L.; Soós, T.; Lendvay, G. R. Substituent Effect on the Photoreduction Kinetics of Benzophenone. *The Journal of Physical Chemistry A* **2013,** *117* (40), 10196-10210.

(49) Michelin, C.; Hoffmann, N. Photosensitization and Photocatalysis—Perspectives in Organic Synthesis. *ACS Catalysis* **2018,** *8* (12), 12046-12055.

(50) Kraljić, I.; Mohsni, S. E. A New Method for the Detection of Singlet Oxygen in Aqueous Solutions. *Photochemistry and Photobiology* **1978,** *28* (4-5), 577-581.

(51) Kraljic, I.; Mohsni, S. E.; Arvis, M. A General Method for the Identification of Primary Reactions in Sensitized Photooxidations. *Photochemistry and Photobiology* **1978**, *27* (5), 531-537.

(52) Laarhoven, L. J.; Mulder, P.; Wayner, D. D. Determination of Bond Dissociation Enthalpies in Solution by Photoacoustic Calorimetry. *Accounts of Chemical Research* **1999,** *32* (4), 342-349.

(53) Lide, D. R. *CRC Handbook of Chemistry and Physic* **2004**.

(54) McMillen, D. F.; Golden, D. M. Hydrocarbon Bond Dissociation Energies. *Annual Review of Physical Chemistry* **1982,** *33* (1), 493-532.

(55) Allonas, X.; Grotzinger, C.; Lalevee, J.; Fouassier, J.; Visconti, M. Structure/Properties Relationships in Photoinitiators of Polymerization: 12. A Novel Bifunctional Compound. *European Polymer Journal* **2001,** *37* (5), 897-906.

(56) Chilton, J.; Giering, L.; Steel, C. The Effect of Transient Photoproducts in Benzophenone-Hydrogen Donor Systems. *Journal of the American Chemical Society* **1976,** *98* (7), 1865-1870.

(57) Asmus, K.; Möckel, H.; Henglein, A. Pulse Radiolytic Study of the Site of Hydroxyl Radical Attack on Aliphatic Alcohols in Aqueous Solution. *The Journal of Physical Chemistry* **1973,** *77* (10), 1218-1221.

(58) Zhao, J.; Zhang, Y.; Quan, X.; Chen, S. Enhanced Oxidation of 4-Chlorophenol Using Sulfate Radicals Generated from Zero-Valent Iron and Peroxydisulfate at Ambient Temperature. *Separation and Purification Technology* **2010,** *71* (3), 302-307.

(59) Nakamura, K.; Ishiyama, K.; Sheng, H.; Ikai, H.; Kanno, T.; Niwano, Y. Bactericidal Activity and Mechanism of Photoirradiated Polyphenols against Gram-Positive and-Negative Bacteria. *Journal of Agricultural and Food Chemistry* **2015,** *63* (35), 7707-7713.

(60) Nakamura, K.; Yamada, Y.; Ikai, H.; Kanno, T.; Sasaki, K.; Niwano, Y. Bactericidal Action of Photoirradiated Gallic Acid via Reactive Oxygen Species Formation. *Journal of Agricultural and Food Chemistry* **2012,** *60* (40), 10048-10054.

(61) Mai-Prochnow, A.; Clauson, M.; Hong, J.; Murphy, A. B. Gram Positive and Gram Negative Bacteria Differ in Their Sensitivity to Cold Plasma. *Scientific Reports* **2016,** *6*, 38610.

Chapter 3. Daylight-Induced Antibacterial and Antiviral Nanofibrous Membranes Containing Vitamin K Derivatives for Personal Protective Equipment

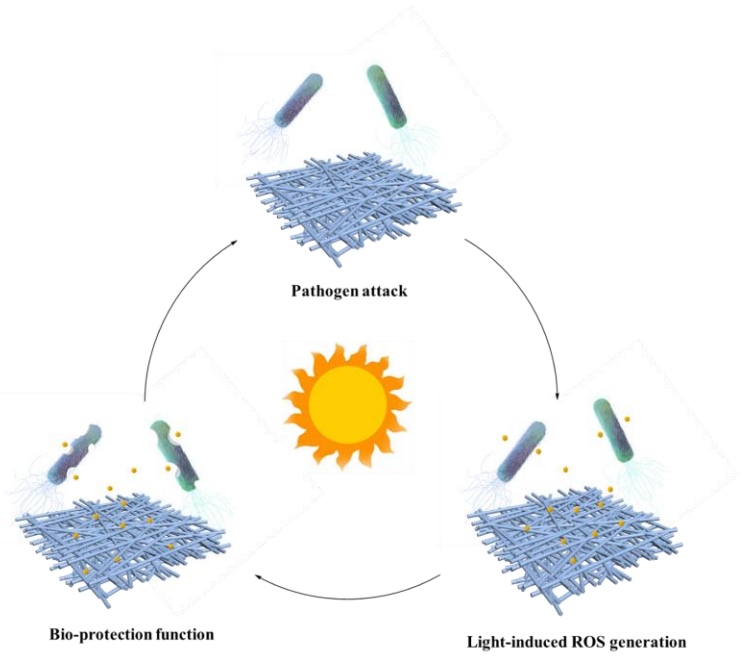

Abstract

During the development of antibacterial and antiviral materials for personal protective equipment (PPE), daylight active functional polymeric materials containing Vitamin K compounds (VKs) and impacts of polymer structures to the functions were investigated. As examples, hydrophobic polyacrylonitrile (PAN) and hydrophilic poly (vinyl alcohol-co-ethylene) (PVA-co-PE) polymers were directly blended with three VK compounds and electro-spun into VK-containing nanofibrous membranes (VNFMs). The prepared VNFMs exhibited robust photoactivity in generating reactive oxygen species (ROS) under both daylight (D65, 300-800 nm) and ultraviolet A (UVA, 365 nm) irradiation, resulting in high antimicrobial and antiviral efficiency (>99.9%) within a short exposure time (<90 min). Interestingly, PVA-co-PE/VK_3 VNFM showed a higher ROS production rates and better biocidal functions than that of the

PAN/VK_3 VNFM under the same photo-irradiation conditions, indicating that PVA-co-PE is a better matrix polymer material for these functions. Moreover, the prepared PVA-co-PE/VK_3 VNFM maintains its powerful microbicidal function even after five times of repeated exposures to bacteria and viruses, showing the stability and reusability of the antimicrobial materials. The fabrication of photo-induced antimicrobial VNFMs may provide new insights into the development of non-toxic and reusable photo-induced antimicrobial materials that could be applied in personal protective equipment with improved biological protection.

3.1 Introduction

Public health issues have drawn increased attention in recent years due to the frequent occurrence of emerging infectious diseases (EID) caused by pathogens[1-2]. Over the past few centuries, global outbreaks of infectious diseases, such as the Black Death (*Yersinia pestis*) in the 14th century and the influenza pandemics in the 20th century, have caused at least 50 million deaths and changed the course of human history and left indelible memories of miseries[3]. With the improvement of science, technology, and health care condition, the outbreak of infectious diseases has been efficiently controlled yet still brings suffering to humankind[4]. For instance, the Ebola virus disease in 2014 in West Africa and the Zika virus in 2015 in Brazil and elsewhere caused significant losses to human life and property, as well as social development[5-6]. The Coronavirus Disease 2019 (COVID-19, caused by SARS CoV-2) pandemic that is ravaging the world has caused tremendous losses of human life and a depression of the economy in the world[7]. During a pandemic of respiratory diseases, people or health care workers are strongly required to appropriately use personal protective equipment (PPE) including facial masks and full-body suits [8-9]. The current PPE can prevent direct exposures of the wearers to the microbial pathogens [10-12] but cannot inactivate them, leaving the pathogens potentially alive and infectious on the surface of

the PPE, which increases risks of infections caused by cross-contamination or post-infection during the PPE removal process[13-14]. Besides, in a sudden epidemic, there is a severe PPE shortage due to its disposable characteristics[15-16]. Therefore, reusable self-cleaning PPE materials with antimicrobial properties have been considered as a solution to overcome the shortage and improve protective functions of the PPE[17-18].

Many antimicrobial agents, including chitosan, peptides, silver nanoparticles, and quaternary ammonium salts, have been applied in the preparation of antibacterial materials[17-19]. Yet most of the materials could only provide slow inactivation against microorganisms, and many are not effective in killing viruses. In addition, the functions are not refreshable. For instance, quaternary ammonium salts usually take few hours to exhibit maximum functions[20]. Therefore, rapid inactivation of a broad spectrum of microorganisms by contact is a requirement for biological protective clothing for health care workers. Rechargeable halamine materials, which can generate oxidative chlorine and inactivate microorganism rapidly, have been proven as effective biocidal materials in recent years[21-22]. Some hydantoin derivative modified textiles can be functional even after 50 times of repeated launderings and bleach recharging[23]. However, the release of free chlorine prevents their applications in certain PPE products such as face masks and respirators. By comparison, photoactive chemicals that can produce oxidative biocidal reactive oxygen species (ROS) are considered as effective, durable, and low toxicity candidates to be employed in preparing antimicrobial materials in the preparation of reusable face masks or respirators[24-25]. Photoactive nanoparticles such as TiO_2 and ZnO are reported to generate ROS including singlet oxygen ($^1O_2$), hydroxyl radical ($HO\cdot$), and hydrogen peroxide (H_2O_2) under ultraviolet (UV) exposure[26-27]. However, their excitation bandgap energy restricts the size of these photo-catalysts in the nanoscale range [28-30], which raises health concerns because of the potential skin penetration

and inhalation by human [31]. Organic photosensitizers such as porphyrin and Rose Bengal were also reported to produce cell-lethal $^1O_2$ under UVA exposure, but the diffusion of $^1O_2$ to pathogen targets may be limited due to its short lifetime[32-33]. Another group of photo-active chemicals are anthraquinone and benzophenone derivatives, which have been proven to generate the most potent oxidant[34], HO·, the most stable oxidant, H_2O_2, and $^1O_2$ efficiently under daylight or UVA irradiation[35-38]. These photosensitizers, however, are all synthesized instead of natural or naturally derived, and some of them are potentially carcinogenic[39]. Thus, there is an urgent need to find bio-based photoactive chemicals that are capable of generating ROS efficiently under daylight exposure as environmentally friendly, non-toxic, and reusable antimicrobial agents that could be applied in fabricating durable PPE.

Vitamin Ks (VKs) are photoactive chemicals derived from natural products[40-41] and essential in blood clotting and bone health[42-43]. They have shown high photoactivity under light irradiation, resulting in a production of ROS in various solvent systems[44-45]. Especially, under daylight irradiation, VK_3 has demonstrated robust and durable antibacterial function in the PBS buffer system [44]. To further investigate the potential of using VKs as photoactive agents in the preparation of reusable antimicrobial PPE materials, we prepared VK containing photo-induced antimicrobial nanofibrous membranes (VNFM) that can work under both daylight and UVA irradiation. Specific aims were accomplished in this study include, which proves that both hydrophobic polyacrylonitrile (PAN) and hydrophilic poly (vinyl alcohol-co-ethylene) (PVA-co-PE) present daylight active functions by directly mixing with VKs. Electrospun nanofibrous membranes (VNFM) from the polymeric systems demonstrate robust generation of biocidal ROS and rapid and reusable microbial inactivation functions against bacteria and viruses under daylight

irradiation. This work proves the feasibility of applying the materials in preparing reusable daylight-induced biocidal PPEs such as surgical face masks or respirators.

3.2. Experimental Methods

3.2.1 Materials

Phylloquinone (VK_1) and menadione (VK_3) were purchased from Chem-Impex Int'l Inc. (Wood Dale, USA) Menadiol diacetate (VK_4) was purchased from TCI Chemicals, USA. Rose Bengal was purchased from Acros Organics. Poly(vinyl alcohol-co-ethylene) (PVA-co-PE, ethylene content of 27 mol%), polyacrylonitrile (PAN), isopropanol, ethyl alcohol, 2 wt% osmium tetroxide (OsO_4), potassium iodide, sodium hydroxide, ammonium molybdate, dimethylformamide, potassium hydrogen phthalate, deuterated dimethyl sulfoxide (DMSO-d_6), L-histidine, chloroform, sodium phosphate dibasic, potassium phosphate monobasic, sodium chloride, potassium chloride, maximum recovery diluent, and crystal violet were purchased from Sigma-Aldrich. p-Nitroso dimethylaniline (p-NDA), Luria-Bertani (LB) broth, LB agar, Tryptic soy broth (TSB), Tryptic soy agar (TSA), and Dulbecco Modified Eagle's Medium (DMEM) were purchased from Thermo Fisher Scientific. Fetal bovine serum was purchased from Gemini Biotec. PowerUp SYBR Green Master Mix was purchased from Applied Biosystems. All the chemicals were used as received without any further purification.

3.2.2 Computational details

All calculations were performed by using computational software package Gaussian 09 ver. 08. The optimization of the ground state geometries of VKs and matrix polymer (n=3) were carried on DFT-B3LYP/6-311G (d,p) level of theory in the polarizable continuum model using the integral equation formalism variant (IEFPCM) in H_2O solvent. The excitations of the VKs were further

performed at TDDFT-B3LYP/6-311G (d,p) level of theory in the IEFPCM-H_2O solvent model based on the optimized VKs structures above. The Gibbs free energies were obtained by frequency calculations at DFT-B3LYP/6-311G (d,p) level of theory in the IEFPCM-H_2O solvent based on the optimized geometries.

3.2.3 Fabrication of PAN/VK and PVA-co-PE/VK VNFMs

The electrospinning technique was employed to obtain nanofibrous membranes. PAN polymer particles were dissolved in dimethylformamide at 85°C with stirring for 6 hours to obtain a homogeneous PAN solution at a concentration of 7 wt %. PVA-co-PE polymer particles were dissolved in a mixture of water and isopropanol (weight ratio of 30%: 70%) at 85°C with stirring for 6 hours to obtain a PVA-co-PE solution in a concentration of 7 wt %. Then VK (5 wt % of polymer) was added into this solution and mixed sufficiently. The solution was subsequently filled in four 20-mL syringes equipped with metallic needles. The solution pumping rate was controlled by a syringe pump (Kent Scientific) at a speed of 2 mL h^{-1}. A high voltage electrostatic source of 28 kV (EQ30, Matsusada Inc.) was applied to the metallic needles. The formed electro-spun VNFM membrane was collected on a metallic roller covered by a wax paper. The membranes were directly used in other tests.

3.2.4 Measurement of hydroxyl radicals

The production of hydroxyl radicals was quantitively measured by instantly quenching the formed radicals with p-NDA, a radical scavenger [37, 46]. A Spectro-linker XL-1500 (Spectronics Corporation) equipped with six 15-Watt D65 standard daylight tubes (GE F15T8-D) was employed in this experiment. The irradiance distance between lamps and test samples was regulated at 16 cm. A Spectrolinker XL-1000 (Spectronics Corporation) equipped with five 8-Watt

UVA (Spectroline BLE-8T365) or UVB tubes (Spectroline BLE-8T312) was used to provide UV irradiance. The irradiance distance between UV lamps and samples was regulated at 12 cm. 10 mg of the VNFM was immersed in 10 mL of 50 μM p-NDA solution and then placed under photoirradiation for varied durations. The decomposition of p-NDA was measured photometrically by referring to the absorption intensities at 440 nm. The production of HO· by the VNFM can be quantitatively calculated according to the specific stoichiometry between HO· and p-NDA[46].

3.2.5 Measurement of singlet oxygen

For the singlet oxygen production test on VNFMs, p-NDA (50 μM) and L-histidine (0.01 M) were dissolved in 0.01 M phosphate buffer solution (pH=7.35). 10 mg of the VNFM was immersed in 10 mL of the prepared solution and then placed under photoirradiation for certain periods. The production of singlet oxygen by the VNFM was obtained by the p-NDA consumption difference between L-histidine added and L-histidine free systems[37, 47]. For the relative singlet oxygen quantum yield tests, a mixture of ethanol and 0.01 M phosphate buffer solution (pH=7.35) (volume ratio 1: 9) was employed as the solvent of a VK (or Rose Bengal) (20 μM) and p-NDA (40 μM) solution. L-histidine (0.01M) was added into the solution to capture the generated singlet oxygen. The mixture solution was then placed under photoirradiation, and the relative singlet oxygen quantum yield can be measured using Rose Bengal as a standard.

3.2.6 Measurement of hydrogen peroxide

The production of hydrogen peroxide was detected by an indirect quantification method according to the literature[25]. Potassium iodide (66 g L^{-1}), sodium hydroxide (2 g L^{-1}), and ammonium molybdate tetrahydrate (0.2 g L^{-1}) were dissolved in water to obtain reagent A. Potassium hydrogen phthalate (20 g L^{-1}) was dissolved in water to obtain reagent B. 10 mg of the

prepared VNFM was immersed in 10 mL of water which was then placed under photoirradiation for different time of periods. At each time point, 1 mL of the sample solution was extracted and mixed with 1 mL reagent A and 1 mL reagent B, and the mixture was vigorously vortexed for 10 seconds to mix homogeneously. The mixture was subsequently placed in a dark environment for 5 min to react sufficiently. The concentration of the formed hydrogen peroxide in the sample solution can be determined quantitatively according to the absorbance at 351 nm by using a UV-vis spectroscopy.

3.2.7 Incubation of bacteria and bacteriophages

Antibacterial experiments were performed on the prepared PVA-co-PE/VK_3 and PAN/VK_3 VNFMs against two typical etiological bacteria, Gram-negative *E. coli* O157: H7 [American Type Culture Collection (ATCC) 700728)] and Gram-positive *L. innocua* (ATCC 33090). 10 mL of LB broth was inoculated with a colony of *E. coli* at 37 ℃ for 18 h. After that, a bacterial culture of around 1×10^9 CFU mL^{-1} (assessed by plate counting assay) was obtained for further antimicrobial test. Meanwhile, a colony of *L. innocua* was inoculated in 10 mL of TSA broth at 37 ℃ for 24 h, after which a bacterial culture of around 3×10^8 CFU mL^{-1} (assessed by plate counting assay) was obtained.

An antiviral test was performed on PVA-co-PE/VK_3 VNFM against T7 bacteriophages. 1×10^5 PFU mL^{-1} of T7 Bacteriophage (ATCCBAA-1025-B2) were inoculated in previously cultured *E. coli* BL21 (ATCC BAA-1025) in tryptic soy broth (TSB) at 37℃ for 4 hours. The *E. coli*-T7 phage mixture was incubated at 37℃ for 15 minutes for initial infection before centrifuged at 13,000 rpm for 1 minute to harvest the infected *E. coli* cells. The broth was then discarded, and the bacterial cells were resuspended in 15 mL of fresh TSB and incubated at 37℃ with constant shaking until there was no visible turbidity. The remaining bacterial cells were lysed by adding 3

mL of chloroform into the mixture, vortexed, and cooled on ice for 15 minutes. The solution was then centrifuged at 6,000 rpm for 10 minutes to precipitate the cell debris. The supernatant containing phage particles was collected and centrifuged at 13,000 rpm for 10 minutes to harvest the T7 bacteriophage particles. After washing the phage pellet twice with PBS, T7 phages were resuspended in PBS and stored at 4℃. The titer of the T7 phage solution was enumerated to obtain a titer of 1×10^7 PFU mL^{-1} by plaque counting assay.

3.2.8 Photo-induced antibacterial tests

For the time-dependent photo-induced antibacterial test, 10 μL of the 1×10^9 CFU mL^{-1} *E. coli* or 3×10^8 CFU mL^{-1} *L.innocua* suspension was uniformly loaded on the surface of the VNFM or control samples in a size of 2 × 2 cm^2. The samples were then placed under dark conditions or photoirradiation for different time of periods. At each specific time point, the samples were vortexed vigorously for 1 min with 1 mL of water to collect the bacteria on the nanofibrous membranes. The harvested bacteria suspension was then serially diluted for 10^0, 10^1, 10^3, and 10^5 times and subsequently plated on LB agar (for *E. coli*) or TSA agar (for *L. innocua*) for bacterial culture. The agar plates with bacteria were further cultured at 37 ℃ for 18 h (for *E. coli*) or 24 h (for *L. innocua*). The reduction of the bacteria caused by the VNFMs under photoirradiation was evaluated by counting the remaining bacteria on the agar plates through plate counting assay. For the cyclic daylight-induced antibacterial test, 10 μL of the 1×10^9 CFU mL^{-1} *E. coli* or 3×10^8 CFU mL^{-1} *L.innocua* suspension was uniformly dropped onto the surface of five-group PVA-co-PE/VK_3 VNFMs in a size of 2 × 2 cm^2. After the first-cycle daylight irradiation, the bacteria on the round-1 VNFMs were collected and inoculated on agar plate for further plate counting assay. Another fresh 10 μL bacteria suspension was loaded onto the remaining four groups to carry on the second-cycle daylight irradiation. The same process was performed five times to achieve the antibacterial

durability test. After that, the agar plates were further cultured at 37 ℃ for 18 h (for *E. coli*) or 24 h (for *L. innocua*). The bacterial inactivation durability of the PVA-co-PE/VK_3 VNFM was accessed by plate counting assay.

3.2.9 SEM imaging of bacteria

The bacteria in the control or treated groups were firstly harvested in 1 mL water by vigorous shaking for 3 min. The collected bacteria suspension was centrifuged for 10 min at a speed of 8000 rpm to separate and concentrate bacteria from water. The precipitated bacteria were treated with 1 wt% OsO_4 aqueous solution for 30 min in a dark environment. The bacteria sample was then dehydrated by ethanol. After that, 10 μL of the bacteria-ethanol suspension was dropped on a copper tape and coated with gold before SEM analysis.

3.2.10 Daylight-induced T7 bacteriophage inactivation tests

For the time-dependent daylight-induced antiviral test, 10 μL of 1×10^7 PFU mL^{-1} T7 bacteriophage suspension was uniformly loaded on the surface of the PVA-co-PE/VK_3 VNFM or control samples in a size of 2 × 2 cm^2. The samples were then placed under dark conditions or daylight irradiation for different durations. At each specific time point, the samples were vortexed vigorously with 3 mL of maximum recovery diluent to collect the T7 phages from the nanofibrous membranes. After 100-fold serial dilutions, 100 μL of the phage dilution was mixed with 200 μL of *E. coli* BL21 (1×10^9 CFU mL^{-1}) suspension and incubated for 10 minutes at 37℃. 3 mL of Molten LB agar at 45℃ was then mixed with the T7 phage-*E. coli* mixture, followed by immediately pouring onto a prewarmed LB agar plate. After agar solidification, the plates were incubated overnight at room temperature, after which the phage plaques were counted and standardized to the initial concentration. For the cyclic daylight-induced antiviral test, 10 μL of

1×10^7 PFU mL^{-1} T7 phage suspension was uniformly dropped onto the surface of the five-group PVA-co-PE/VK_3 VNFMs in a size of 2 × 2 cm^2. After the first-cycle daylight irradiation of 60 minutes, the T7 phages on the first-cycle VNFMs were recovered and cultured as above-mentioned for further plate counting assay. Another fresh 10 μL T7 phage suspension was loaded onto the remaining four groups to proceed the second-cycle daylight irradiation. The same process was performed five times to accomplish the antiviral durability test. The T7 phage- *E. coli* LB agar plates were incubated overnight at room temperature, followed by plate counting assay.

3.2.11 Daylight-induced feline infectious peritonitis virus (FIPV) inactivation test

FIPV was employed in this work as a surrogate for SARS-CoV-2. 80 μL of FIPV (WSU-79-1146, GenBank DQ010921) infectious supernatant equivalent to 4×10^4 TCID50 of FIPV was pipetted onto the surface of 2 cm^2 pieces of the PVA-co-PE/VK_3 VNFM and PVA-co-PE NFM samples. The FIPV-treated membranes were then placed in 47mm polystyrene Petri Dishes (*Fisher Scientific)* under D65 irradiation. Samples as control for no light exposure were also placed inside the instrument protected from light. After 30 minutes of D65 irradiation, the membrane was placed into a 5.0 mL MaxyClear amber polypropylene microtube (Axygen Scientific) containing 500 μL of Dulbecco Modified Eagle's Medium (DMEM) and vortexed for 30 seconds to recover the virus from the membrane. The infectivity of the recovered inoculum was determined using a viral plaquing assay. FIPV susceptible Crandell-Reese feline kidney cells (CRFK, ATCC) were grown to 90% confluency in a 96-well tissue culture plate (Genesee Scientific) using DMEM with 4.5g/L glucose (Corning) and 10% fetal bovine serum. Five serial 10-fold dilutions of the recovered FIPV inoculum extending from 10^{-1} to 10^{-5} (final concentration in DMEM) were made and 200 μL of each dilution were added to each well in 6-well replicates and incubated at 37 ^oC and 5% CO_2. At 72 hours post-infection the CRFK cells were fixed with methanol and stained with crystal violet.

Individual wells were evaluated visually for evidence of virus-induced cytopathic effect (CPE), scored as CPE positive or negative, and the TCID50 was determined based upon the equation $\log_{10}$TCID50 = [total # wells CPE positive/# replicates] + 0.5 to reflect infectious virions per milliliter of supernatant[48]. FIPV copy number post-treatment was determined in parallel via quantitative real-time reverse transcription polymerase chain reaction (qRT-PCR). Viral RNA was isolated from 140 μL of the recovered inoculum using QIAamp Viral RNA Mini Kit (Qiagen) and subsequently reverse transcribed using High-Capacity RNA-to-cDNA Kit (Applied Biosystems) following the manufacturers' protocols. qRT-PCR performed on Applied Biosystems' QuantStudio 3 Real-Time PCR System with PowerUp SYBR Green Master Mix per 10 μL protocol. cDNA templates were amplified using the FIPV forward primer, 5'-GGAAGTTTAGATTTGATTTGGCAATGCTAG, and the FIP reverse primer, 5'-AACAATCACTAGATCCAGACGTTAGCT targeting the terminal portion of FIPV 7b gene. Cycling conditions as follows: 50°C for 2 min, 95°C for 2 min, followed by 40 cycles of 95°C for 15 s, 58°C for 30 s, 72°C for 1 min. Each reaction was performed in triplicates with water template as a negative control and plasmid DNA containing the cloned amplicon of interest as a positive control. FIPV copy number was calculated based on standard curves generated from viral transcripts cloned into plasmid vector pCR2.1 (Invitrogen)[49] and normalized to the culture medium volume.

3.2.12 Characterization

SEM images of the prepared VNFMs, as well as the SEM images of bacteria in control or sample groups, were obtained from a Thermo Scientific Quattro S environmental scanning electron microscope. The diffusion reflection UV-vis spectra of the above nanofibrous membranes were collected with a UV-vis spectrophotometer (Evolution 600, Thermo Fisher Scientific) equipped

with DRA-EV-600 diffuse reflectance accessory (Labsphere). ^{1}H NMR spectra were collected by using a 400 MHz Bruker Advance HD spectrometer, and DMSO-d_6 was used as solvents.

3.3 Results and Discussion

3.3.1 Fabrication and biocidal functions of VNFMs

Polyacrylonitrile (PAN) is a polar and hydrophobic vinyl polymer, and poly (vinyl alcohol-co-ethylene (PVA-co-PE, ethylene 27 Mol %) is a hydrophilic vinyl polymer. Both are popular polymers widely used in various textile fibers and plastic films and were directly blended with VK compounds, respectively. The mixtures were electrospun into nanofibrous membranes as textile personal protective materials to block the penetration of pathogens with good air permeability [50]. The electrospinning process of the nanofibrous membranes followed a method reported in literature[25] . The two polymers were chosen since the chemical structures of the media could affect the generation of ROS from different VK derivatives under photoirradiation [44]. In this case, we assume that the electrospun matrix polymer should provide photoreaction conditions similar to the literature[44], including surface morphology and membrane thickness, for the generation of biocidal ROS. Figure 3.1a illustrates the photoactivated biocidal function of the prepared VNFMs. Due to the porous structure and super high specific surface area of the prepared VNFMs, the pathogens can be intercepted by the nanofibers efficiently. Once the pathogens are in contact with the surface of the VNFMs, VKs, the photoactive chemicals, in the VNFMs could generate various ROS (HO·, H_2O_2, and $^{1}O_2$) under light irradiation. The ROS could damage cellular components of pathogens, such as lipid bilayer membranes of encapsulated viruses and bacteria as well as genetic materials and proteins of the viral and bacterial pathogens, leading to efficient pathogen inactivation [51-52]. Figure 3.1b describes the photoactivated ROS production mechanism and cycles of the reactions on the VNFMs. Under photoirradiation, VK is excited to the triplet excited state (T_1) which

proceeds with two potential pathways, namely, Type I and Type II photoreactions. In the Type I photoreaction, polymer matrix plays a significant role in the production of HO· and H_2O_2 by serving as a hydrogen donor during the reaction process. After the hydrogen abstraction occurs, the VK-H radical can return to the ground state VK accompanied by the formation of HO· or H_2O_2 after reaction with oxygen in air[44]. However, in Type II photoreaction, there is no specific requirement on the hydrogen-donating capability of the matrix polymer itself[53]. An energy exchange happened between the excited triplet VK and the ground-state triplet molecular oxygen ($^3O_2$), after which more oxidative singlet oxygen ($^1O_2$) and ground-state VK are formed. In this case, changing the matrix polymer species should only affect the generation of HO· and H_2O_2, but not $^1O_2$. Based on this mechanism, both Type I and Type II photoreactions consume no photoactive VK species, indicating that the prepared VNFMs should be able to be reused several times, maintaining robust ROS generation efficiency.

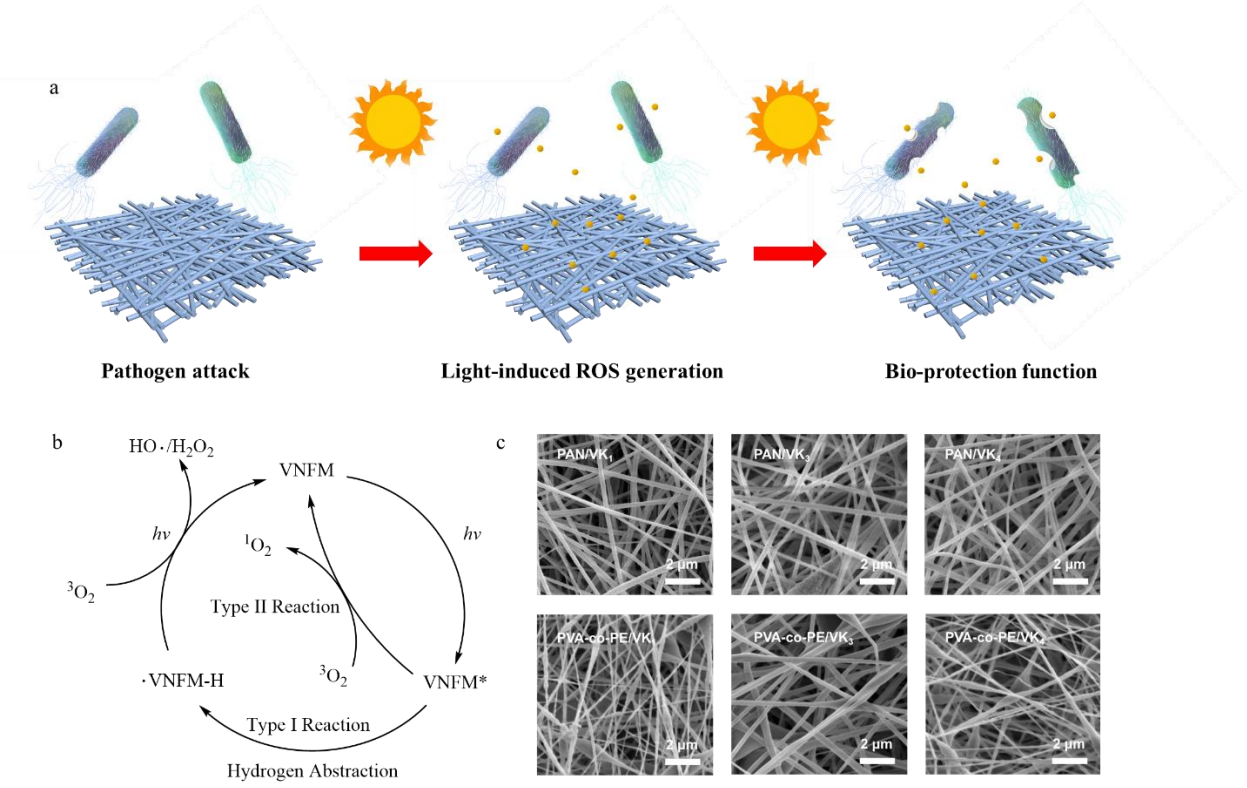

Figure 3.1. Fabrication and Biocidal Functions of VNFMs. (a) Schematic illustration of photoactivated biocidal function of VNFMs. (b) Mechanism of the photoactive ROS generation cycle of VNFMs. (c) Micro-structure of various VNFMs.

Both PAN and PVA-co-PE nanofibrous membranes have similar morphology. The scanning electron microscopy (SEM) images of the resulting VNFMs (Figure 3.1c) reveal the randomly oriented three-dimensional nanostructure of the electrospun nanofibrous materials, which provide ultrahigh fibrous surface areas for triggering the photo-reactions of the polymers with oxygen in air. The porous structures also provide the nanofibrous materials with desired air permeability and potential pathogen interception capacity. An average fiber diameter of 200-290 nm was found in the fibers in all membranes based on the SEM images (Figure 3.3), demonstrating the successful fabrication of the nano-scale fibrous materials. No apparent hierarchies are observed between the membranes containing or without containing VKs (Figure 3.2), implying good compatibility of the compounds with the polymers. To confirm that the structure of VKs in VNFM is not affected by the high voltage applied during electrospinning, Nuclear magnetic resonance (NMR) analyses of the VNFMs were conducted, and results are shown in Figure 3.4. No obvious structural change was found based on the NMR spectra, indicating that the chemical structures of the photoactive VKs are resistant to high electrical voltage. Furthermore, the photoactivity of the chemicals is therefore retained, and the fabricated VNFMs could possess the desired photo-induced biocidal functions and be applied in the biological protective PPEs.

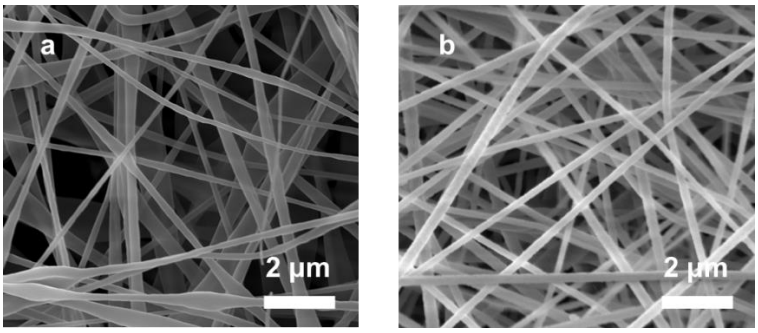

Figure 3.2. Microstructure of electrospun (a) PVA-co-PE and (b) PAN nanofibrous membranes.

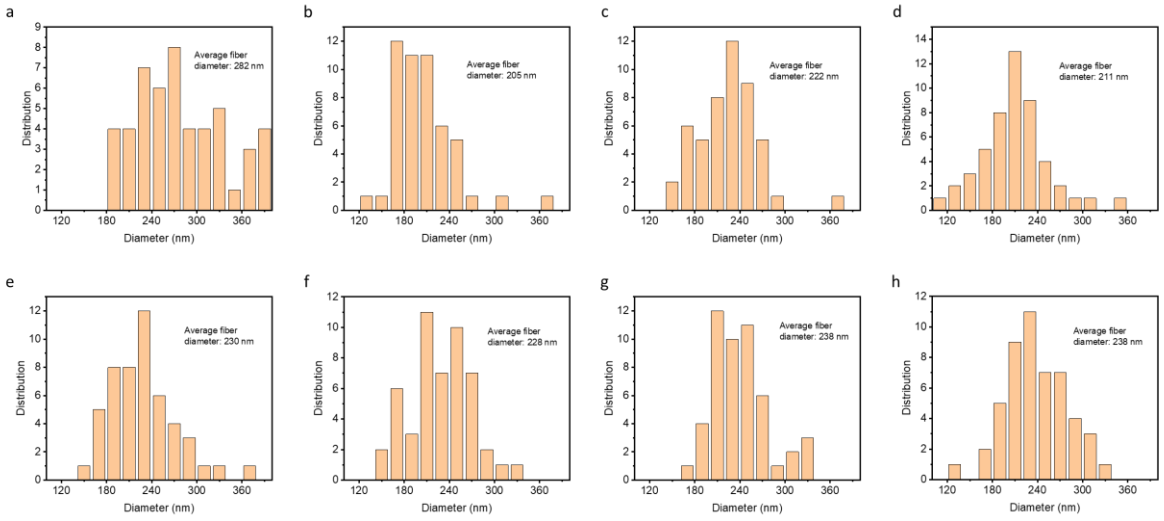

Figure 3.3. Fiber diameter distribution of electrospun nanofibrous membranes (n=50) (a) PVA-co-PE (b) PVA-co-PE/VK$_1$ (c) PVA-co-PE/VK$_3$ (d) PVA-co-PE/VK$_4$ (e) PAN (f) PAN/VK$_1$ (g) PAN/VK$_3$ (h) PAN/VK$_4$.

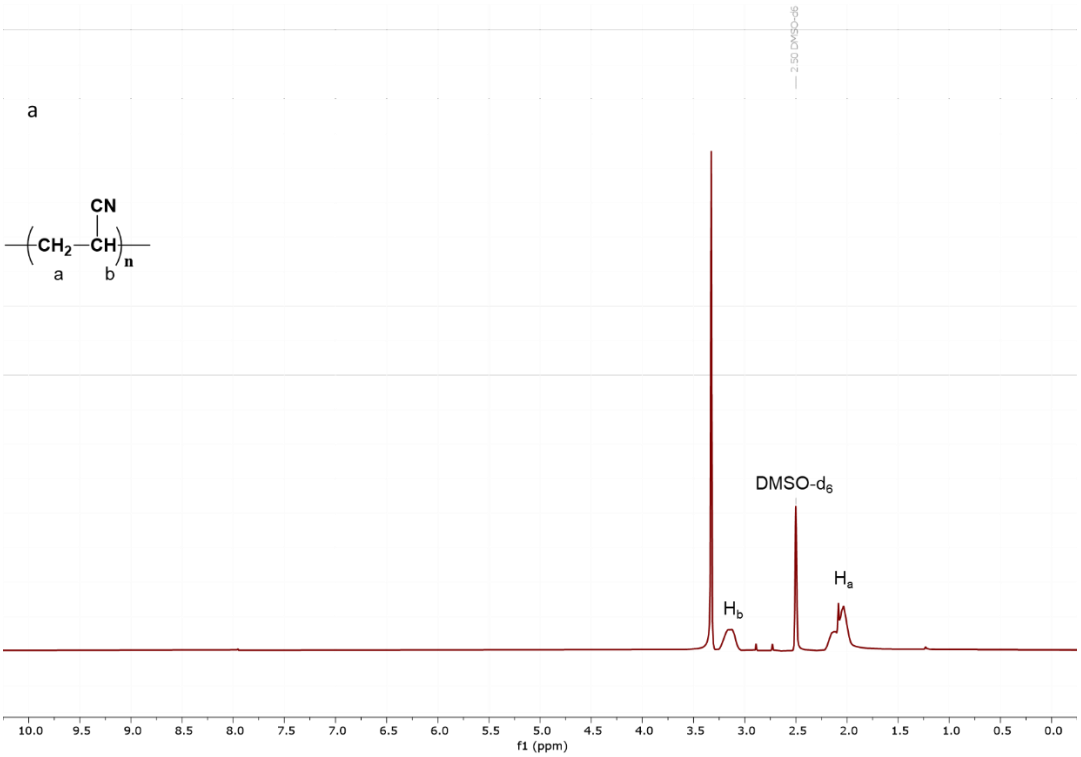
a
CN
CH2
CH
n
a
b
DMSO-d6
Ha
Hb
10.0 9.5 9.0 8.5 8.0 7.5 7.0 6.5 6.0 5.5 5.0 4.5 4.0 3.5 3.0 2.5 2.0 1.5 1.0 0.5 0.0
f1 (ppm)

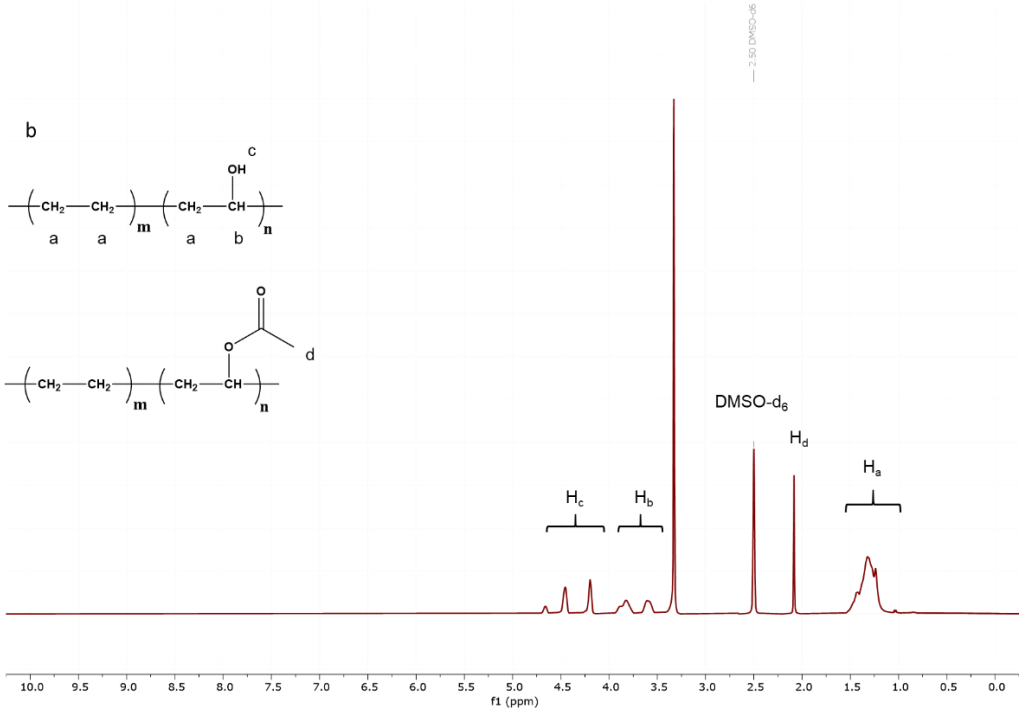
b
c
OH
CH2
CH
m
n
a
a
a
b
O
O
d
DMSO-d6
Hd
Ha
Hc
Hb
10.0 9.5 9.0 8.5 8.0 7.5 7.0 6.5 6.0 5.5 5.0 4.5 4.0 3.5 3.0 2.5 2.0 1.5 1.0 0.5 0.0
f1 (ppm)

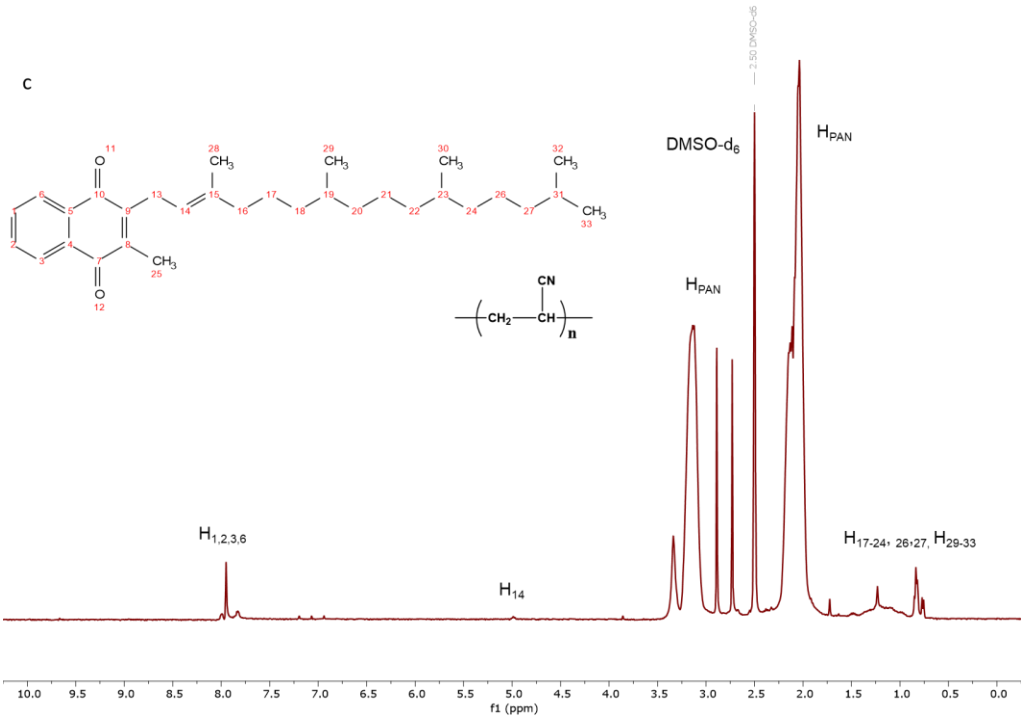
c
DMSO-d6
HPAN
HPAN
H1,2,3,6
H14
H17-24, 26,27, H29-33
f1 (ppm)

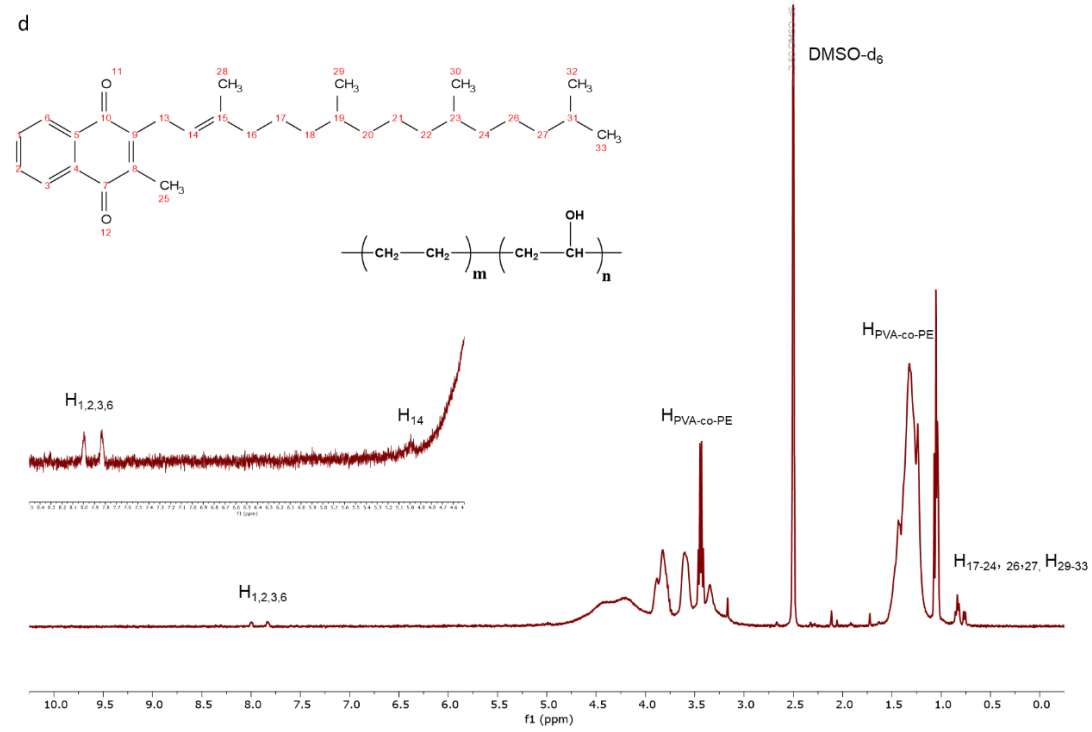
d
DMSO-d6
HPVA-co-PE
HPVA-co-PE
H1,2,3,6
H14
H1,2,3,6
H17-24, 26,27, H29-33
f1 (ppm)

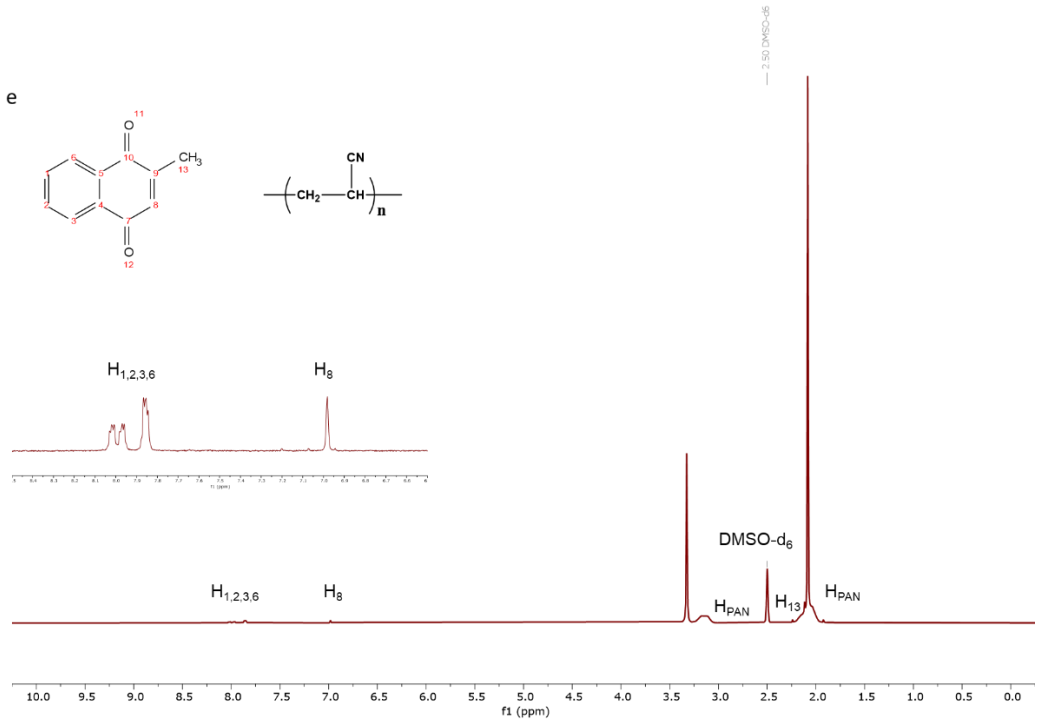
e
CN
CH2
CH
n
CH3
H1,2,3,6
H8
DMSO-d6
HPAN
H13
f1 (ppm)

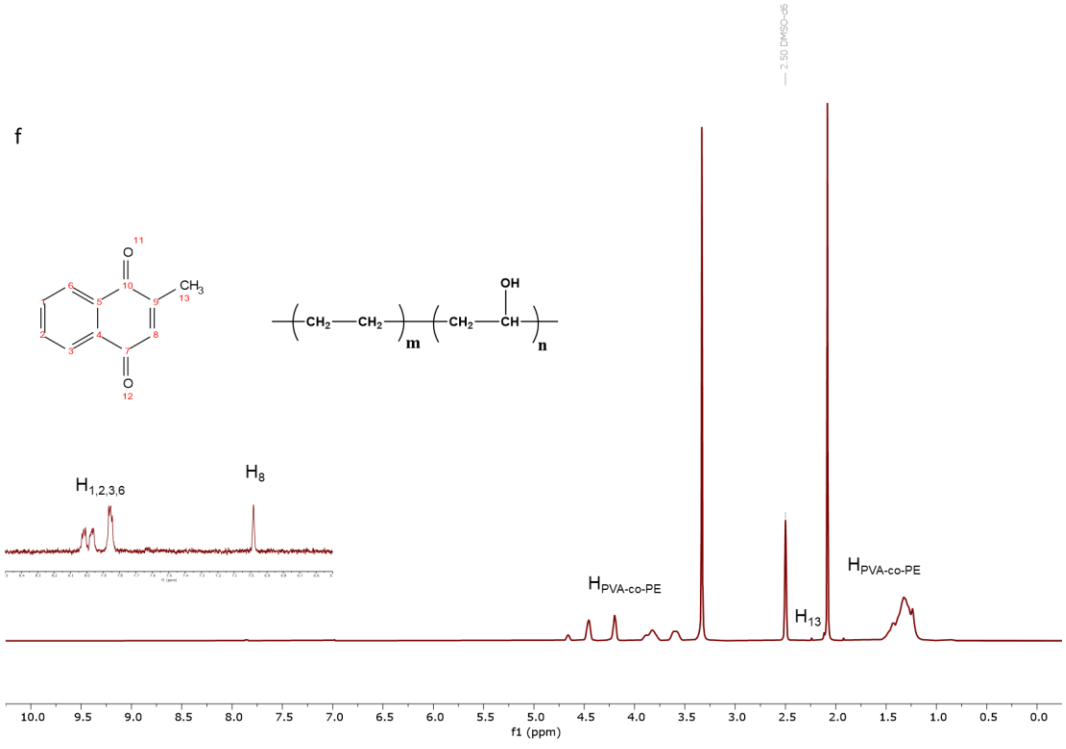
f
OH
CH2
CH
m
n
CH3
H1,2,3,6
H8
HPVA-co-PE
H13
f1 (ppm)

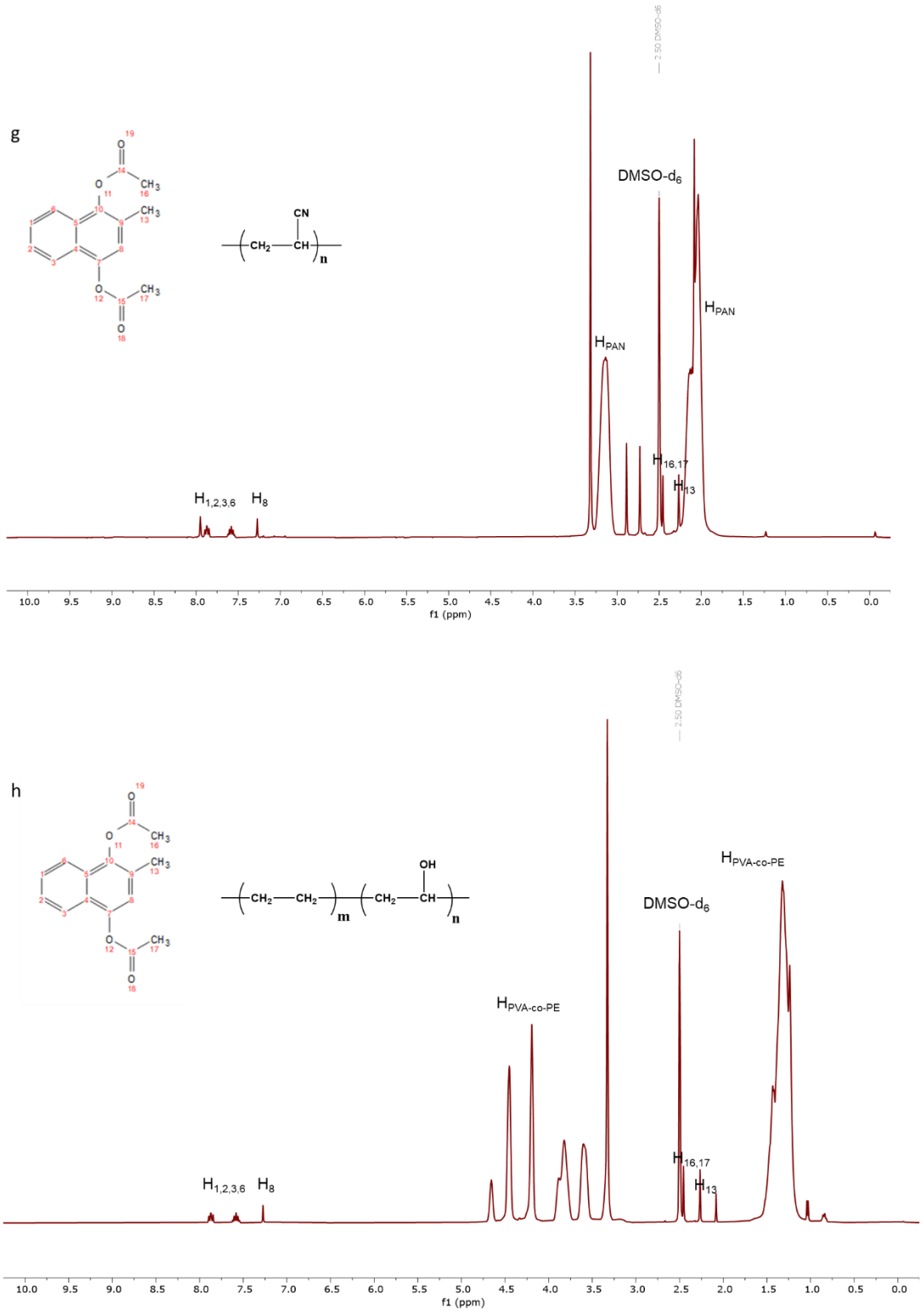

Figure 3.4. ^{1}H NMR spectrum of (a) PAN (b) PVA-co-PE (c) PAN/VK$_1$ (d) PVA-co-PE/VK$_1$ (e) PAN/VK$_3$ (f) PVA-co-PE/VK$_3$ (g) PAN/VK$_4$ (h) PVA-co-PE/VK$_4$.

3.3.2 Photoactivity and ROS generation efficiency of VNFMs

Diffuse reflection UV-visible (UV-vis) spectroscopy was employed to explore the excitation nature of the prepared VNFMs (Figure 3.5). The detailed excitation information was explored at the molecular level with the assistance of computational modeling using time-dependent density functional theory (TD-DFT). VK_1, VK_3, and VK_4 in polymer materials all show similar absorption wavelengths in solvent systems, indicating that the polymers do not affect the light absorption and excitation of the photoactive chemicals. The maximum excitation wavelengths for VK_1NFMs, VK_3NFMs, and VK_4NFMs are S_5 (339.30 nm), S_4 (343.74 nm), and S_1 (297.83 nm), respectively, according to the calculation results, which are all ππ* excitation. However, the triplet states for the three VNFMs are distinctly different, which are nπ* (35.59%), nπ* (95.68%), and ππ* (91.70%), respectively (Figure 3.5).

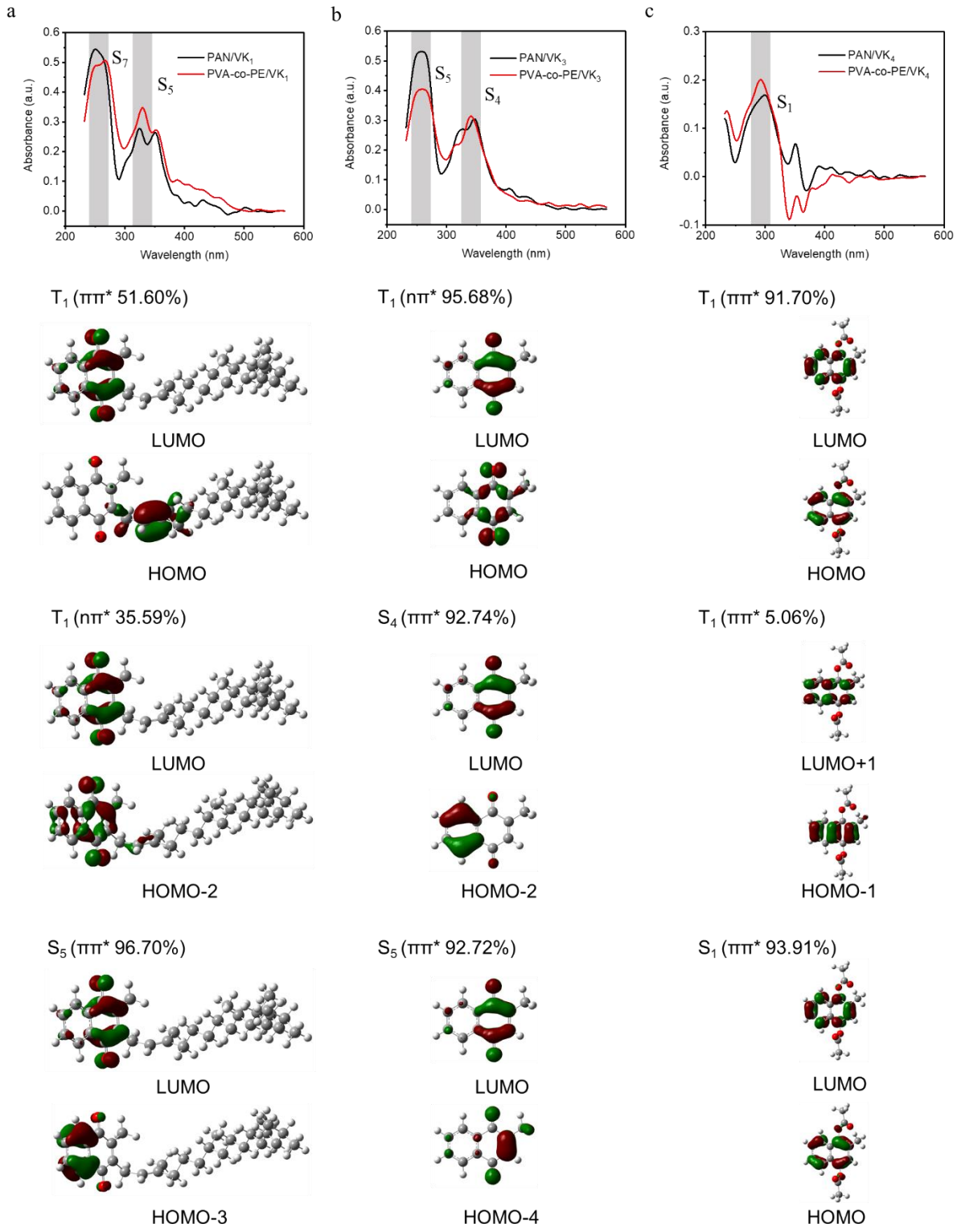

Figure 3.5. Diffuse reflection UV-vis spectra and excitation analysis of VNFMs. (a) VK_1NFMs, (b) VK_3NFMs, and (c) VK_4NFMs.

Based on our previous study, VK_3 should be the most efficient one in generating HO· and H_2O_2 via Type I photoreaction due to its highest nπ* ratio in the triplet state[44]. To demonstrate whether VKs have similar photoactivity as previously studied in the solvent systems, a photo-induced HO· production test of six VNFMs was carried out under three types of irradiation resources (daylight D65 300-800nm, UVA 365 nm, and UVB 312nm). Although the D65 can only provide VKs with necessary excitation wavelengths to a relatively small extent (Figure 3.6), it was employed in this study to mimic the daylight that is much more accessible in the practical situation.

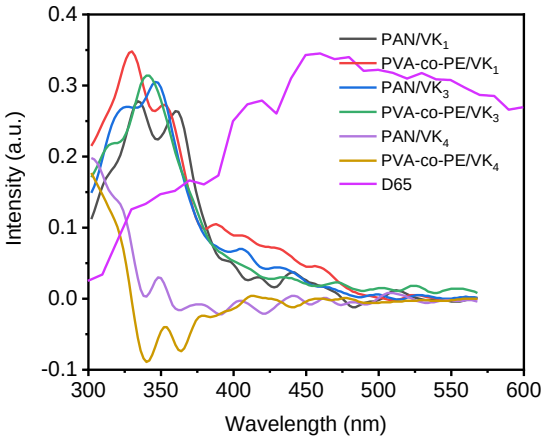

Figure 3.6. UV-DRS spectra of various VNFMs along with the emission spectrum of the D65 standard daylight source.

Under the D65 irradiation (Figure 3.7a), VK_3 is the most efficient one in generating HO· in either PVA-co-PE or in PAN matrix, whereas VK_1NFMs and VK_4NFMs are much less efficient. VK_1 shows higher HO· production via Type I photoreaction comparing to the VK_4, due to its higher contributions of nπ* featured triplet excited states and UVA-wavelength absorption[44]. Moreover, the PVA-co-PE/VK_3 VNFM reveals robust HO· generation capacity under D65 irradiation, reaching to 948 μg g^{-1} in one hour, which is more than ten times higher than that of

natural polyphenols or synthesized antibacterial materials reported in literatures[54-55]. In comparison to the D65 irradiation results, PVA-co-PE/VK_3 VNFM again produced more HO· under UVA and UVB irradiation (Figure 3.7b and 3.7c). The HO· production efficiency indicates that VK_3 is the most optimal in Type I photoreaction in the polymer materials under various photoirradiation resources, consistent with its photoactivity in the solvent system[44].

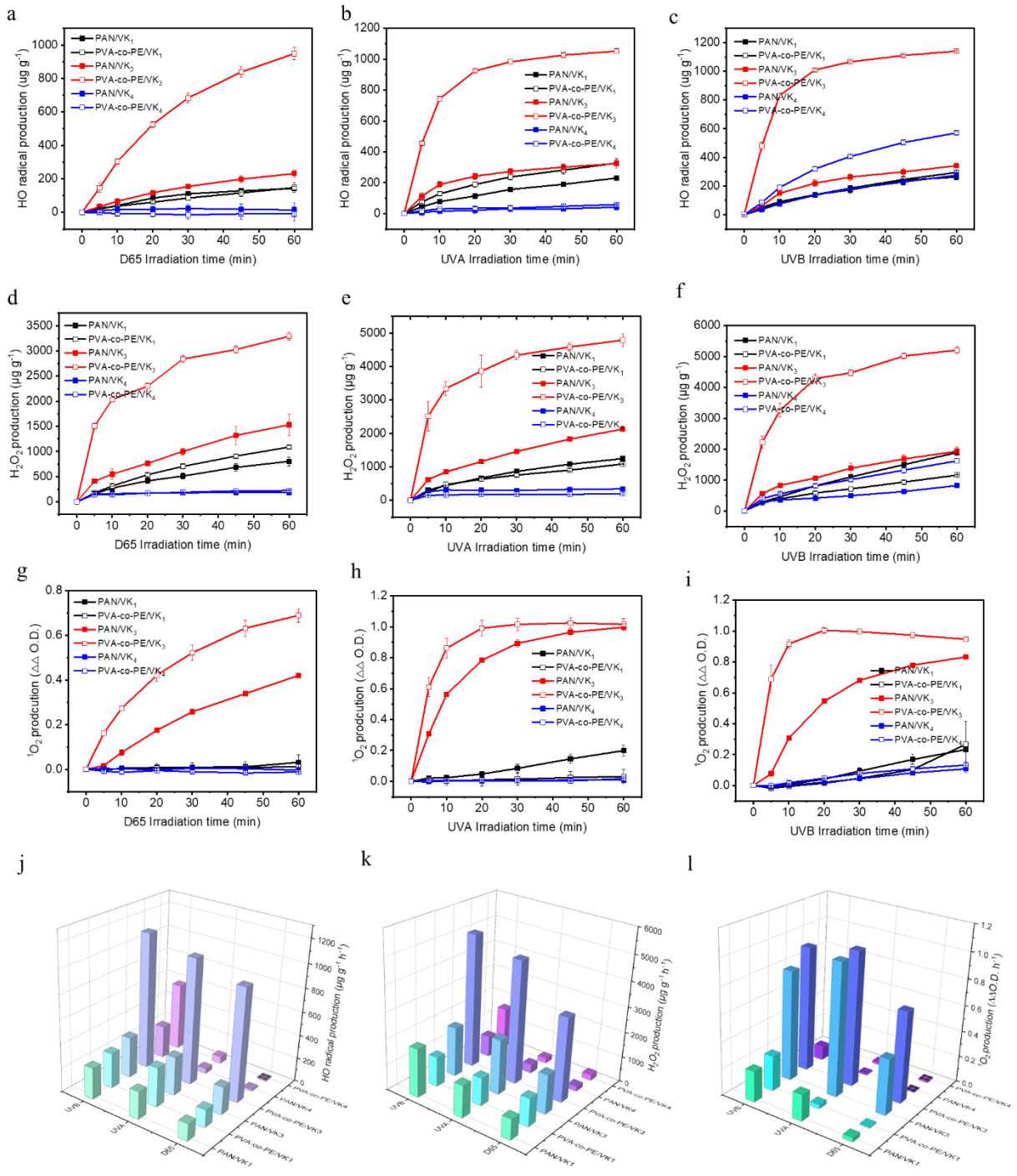

Figure 3.7. Production of reactive oxygen species by VNFMs under various photo-irradiation resources. Hydroxyl radical production of VNFMs under (a) D65, (b) UVA, and (c) UVB. Hydrogen peroxide production of VNFMs under (d) D65, (e) UVA, and (f) UVB. Singlet oxygen

production of VNFMs under (g) D65, (h) UVA, and (i) UVB. Summary of (j) hydroxyl radical production, (k) hydrogen peroxide production, and (l) singlet oxygen production of VNFMs.

To further demonstrate the Type I photoreactivity of the materials, the H_2O_2 production test was carried on the membranes, and the results are shown in Figure 3.7d, 3.7e, and 3.7f, respectively. Similarly, VK_3NFMs show the highest efficiency in generating H_2O_2 under all irradiation resources, which again proves that the VK_3 is the best one in Type I photoreaction in the polymer materials. Under the D65 irradiation, the PVA-co-PE/VK_3 VNFM exhibits highly efficient H_2O_2 production, reaching 3292 $\mu g\ g^{-1}\ h^{-1}$ which is three times more efficient than those of previous daylight-induced antibacterial nanofibrous materials[25]. Increased H_2O_2 productions under the UVA and UVB were noticed on the materials, consistent with their photoactivity in the HO· production test.

In addition to the Type I photoreaction, the VK compounds could undergo Type II reaction under light exposure[33, 56]. Our previous study indicates that VKs could generate $^1O_2$ via the Type II reaction in the solvent system[44]. Since the energies of the triplets are all high enough to produce $^1O_2$, Inter System Crossing (ISC) yield is considered as a main factor that can influence the singlet oxygen quantum yield. VK_1 and VK_3 are photoactive chemicals with high triplet quantum yield due to their quinone structure which is reported to have a 0.74 intersystem crossing yield in acetonitrile [57]. VK_4, however, does not have a high ISC quantum yield according to the computational calculation. Comparing to VK_1 and VK_3, VK_4 has a very limited ISC yield due to its high-ratio $\pi\pi^*$ featured S_1 and T_3 states, which is a violation of the El-Sayed's Rules in ISC process[58]. Although VK_1 has symmetry allowed excited states during the ISC process, however, according to literature, an intramolecular electron transfer competes with the ISC process, which lowers its singlet oxygen quantum yield to 0.02[59]. Thus, VK_1 or VK_4 containing VNFMs may

exhibit very low $^1O_2$ production. As a demonstration, the $^1O_2$ production by the membranes was also carried out, and the results are shown in Figure 3.7g, 3.7h, and 3.7i, respectively. All VK_1FNMs and VK_4NFMs showed much lower $^1O_2$ production rates under the photoirradiation, whereas VK_3NFMs are still the most efficient material under each irradiation condition, same as the results we got previously[44]. Moreover, it is worth mentioning that PVA-co-PE/VK_3 and PAN/VK_3 VNFMs generated comparable $^1O_2$ after one hour of photoirradiation, suggesting that the production of the $^1O_2$ of VK_3 may be independent on the matrix polymers.

Interestingly, we noticed that PVA-co-PE and PAN-based VNFMs were relatively similar in the production of ROS with the photosensitizers VK_1 and VK_4. However, the ROS production difference of PVA-co-PE and PAN VNFMs was obvious when VK_3 is employed. The detailed ROS production ratios of PVA-co-PE/VK_3 and PAN/VK_3 VNFMs are listed in Table 3.1.

ROS production ratio (PVA-co-PE : PAN)	$^1O_2$	HO·	H_2O_2
D65	1.64	4.10	2.61
UVA	1.02	3.25	2.25
UVB	1.14	3.34	2.70

Table 3.1. ROS production ratio of PVA-co-PE/VK_3 and PAN/VK_3 VNFMs.

According to Table 3.1, PVA-co-PE/VK_3 VNFM and PAN/VK_3 VNFM produced similar amounts of $^1O_2$ under D65, UVA, and UVB irradiation with ratios close to one, confirming that the generation of $^1O_2$ via the Type II photoreaction is independent on the polymer matrix material. However, PVA-co-PE/VK_3 VNFM shows significantly higher HO· and H_2O_2 production via the

Type I photoreaction comparing to PAN/VK_3 VNFM under all three types of irradiation conditions. The data confirms that polymer matrix material has an impact on the Type I photoreaction, especially on the hydrogen abstraction reaction (Figure 3.8, $\triangle G_1$) which is considered to be the critical step of the formation of HO· and H_2O_2[60]. To explore the Type I photoreaction tendency between VK and the polymers, the detailed reaction mechanism and Gibbs free energy change were calculated with results shown in Figure 3.8.

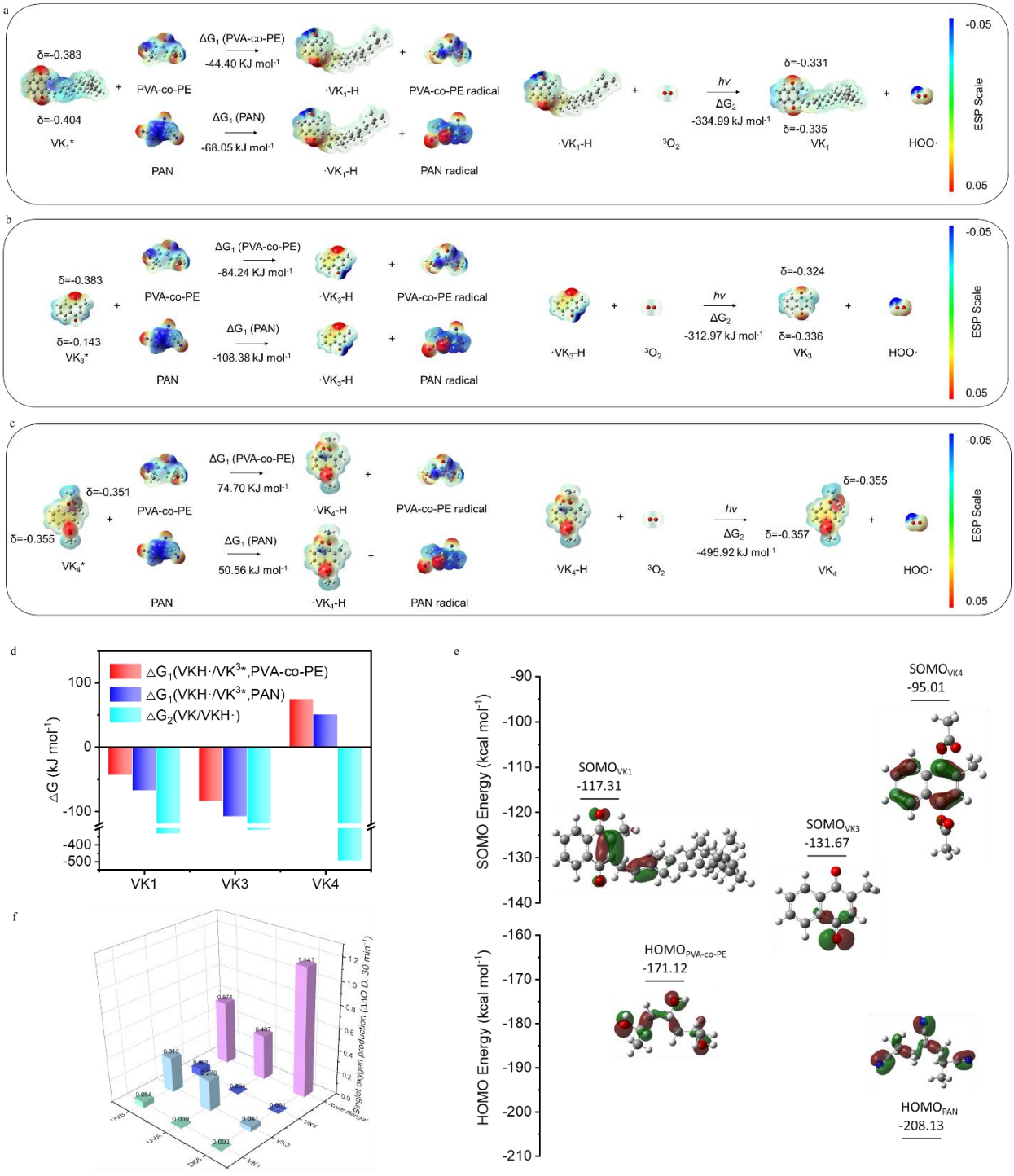

Figure 3.8. Gibbs free energy and frontier orbital analysis of the Type I photoreaction, and relative singlet oxygen production from the Type II photoreaction. Computed Type I photoreaction △G for (a) VK_1, (b)VK_3, and (c)VK_4 with PAN and PVA-co-PE. The color

represents the ESP-mapped electron density of the VKs and polymers. The δ is the ESP charge on the carbonyl oxygen in VKs. (d) Summarized △G for each step in the Type I photoreaction. (e) Orbital energy analysis on VKs and hydrogen donors. (f) Singlet oxygen production of VK_1, VK_3, VK_4, and Rose Bengal under D65, UVA, and UVB irradiation.

Two essential steps ($\triangle G_1$ and $\triangle G_2$) constitute the Type I reaction for the VK derivatives after the formation of their triplet excited states. Based on the calculation, the $\triangle G_1$, $\triangle G_2$, and total $\triangle G$ values of the VK_1 and VK_3 are negative in both two polymers, implying the feasibility of the Type I reaction for both VK_3NFMs and VK_1NFMs. Noticeably, the $\triangle G_1$ values of VK_3 are more negative than that of VK_1 in the two polymers, revealing that VK_3 is much more efficient in generating HO· or H_2O_2 via the Type I photoreaction due to the dominating nπ* triplet excited states. However, the $\triangle G_1$ values of VK_4 in the two polymers are both positive, indicating its low HO· or H_2O_2 generation efficiency in both polymer materials. Interestingly, we found that the $\triangle G_1$ value of VK_3 in PAN is more negative than that in PVA-co-PE, which indicates that PAN should be a better hydrogen donor comparing to PVA-co-PE and can consequently generate more HO· and H_2O_2. The calculation result is contradictory to the experimental data that in fact VK_3 produces much more HO· or H_2O_2 in PVA-co-PE. This difference can be attributed to a better orbital overlap between VK_3 and PVA-co-PE, which is shown in Figure 3.8e. A semi-occupied molecular orbital (SOMO) of oxidative triplet VKs (VK*) and the highest occupied molecular orbital (HOMO) of electron-rich hydrogen donors are depicted. Based on the orbital energy analysis, VK_3* has the lowest SOMO, followed by VK_1*, whereas VK_4* has the highest SOMO. As the hydrogen donor, PVA-co-PE has a higher HOMO than PAN. In this case, the electron-deficient VK_3* has a smaller orbital energy gap to PVA-co-PE comparing to PAN, meaning that VK_3* has a larger reactivity with PVA-co-PE via the Type I photoreaction. The energy gap order

of VK_1*, VK_3*, and VK_4* between the polymer hydrogen donors also proves that VK_3 is the best one in generating HO· and H_2O_2 comparing to the others. The configuration of SOMO also proves the triplet excited state computation of VKs in Figure 3.5. For VK_1, its triplet excited state is formed through a transition from the double bond in the side chain to the unoccupied carbonyl carbon forming a ππ* transition (51.60%), or through a transition of the none bonding lone pair electrons on the carbonyl oxygen to the unoccupied carbonyl carbon, forming an nπ* transition (35.59%). So, the SOMO of its triplet excited state locates on both side-chain double bond and carbonyl carbon, leading to very mild hydrogen abstraction reactivity. For VK_3, due to its high ratio of nπ* transition in the triplet state (95.68%) from carbonyl oxygen to carbonyl carbon, its SOMO merely locates on the carbonyl oxygen leading to its highest oxidative property and largest HO· and H_2O_2 production. This can be further confirmed by the electrostatic potential (ESP) mapped electron density in Figure 3.8. For VK_3, an obvious change on the ESP was noticed on the excited carbonyl carbon, whereas the other two VKs have no obvious ESP change during the excitation and triplet state formation process. Due to the nπ* transition, the carbonyl oxygen of VK_3* becomes extremely electron-deficient and oxidative, which enables the hydrogen abstraction between the VK_3* and matrix polymer. However, for VK_4, its SOMO is on the conjugated π system among the whole molecule, indicating its lowest HO· and H_2O_2 production, which is consistent with the obtained results. Based on the above analysis, we confirm that the polymer matrix material has little influence on the $^1O_2$ generation efficiency of VK_3 via the Type II photoreaction. Whereas for HO· and H_2O_2 formation, the polymer matrix has a significant impact because of its involvement in the hydrogen abstraction reaction. Specifically, based on this study, PVA-co-PE is a better hydrogen donor comparing to PAN, possibly because it has a higher-energy HOMO and electron-richer reaction site.

To further investigate the $^1O_2$ production of the prepared VNFMs, we compared the singlet oxygen quantum yield of VKs and Rose Bengal, the latter of which is a benchmark $^1O_2$ sensitizer with a known singlet oxygen quantum yield as 0.76[37, 61]. Under each light irradiation condition, the relative $^1O_2$ production rates are shown in Figure 3.8f and the relative singlet oxygen quantum yields are summarized in Table 3.2.

Relative $^1O_2$ Quantum Yield (Φ_r)	D65	UVA	UVB
VK_1	0.002	0.017	0.094
VK_3	0.027	0.519	0.417
VK_4	0.000	0.007	0.090

Table 3.2. Relative singlet oxygen quantum yield of VKs under D65, UVA, and UVB irradiation.

According to Figure 3.8f, both VK_1 and VK_4 show little $^1O_2$ production under D65, UVA, and UVB photo-irradiation, whereas VK_3 shows the highest $^1O_2$ production. By comparing the $^1O_2$ production rates of VK_3 and Rose Bengal, the VK_3 only shows comparable $^1O_2$ production and quantum yield to Rose Bengal under UVA and UVB irradiation, but not under daylight. Thus, VK_3 may not be an efficient $^1O_2$ sensitizer under D65 irradiation.

3.3.3 Photo-induced antibacterial function of VNFMs.

$^1O_2$, HO·, and H_2O_2 all could serve as biocides. The prepared VNFMs could provide desired antimicrobial functions under light exposure based on the above analyses. Thus, two model bacteria, Gram-negative *Escherichia coli* O157: H7 (*E. coli*) and Gram-positive *Listeria innocua*

(*L. innocua*), were applied on the surfaces of PVA-co-PE/VK_3 or PAN/VK_3 VNFM and exposed to D65 or UVA irradiation for a certain time of periods. For the time-dependent photo-induced antibacterial test, two control groups (pristine nanofibrous membranes without VK_3 under light irradiation and VK_3NFMs under dark condition) were also employed to evaluate the bacterial inactivation resulting from light irradiation or the presence of VK_3 itself. Figures 3.9a and 3.9b depict the daylight-induced time-dependent antibacterial function of PVA-co-PE/VK_3 and PAN/VK_3 VNFMs against *E. coli*.

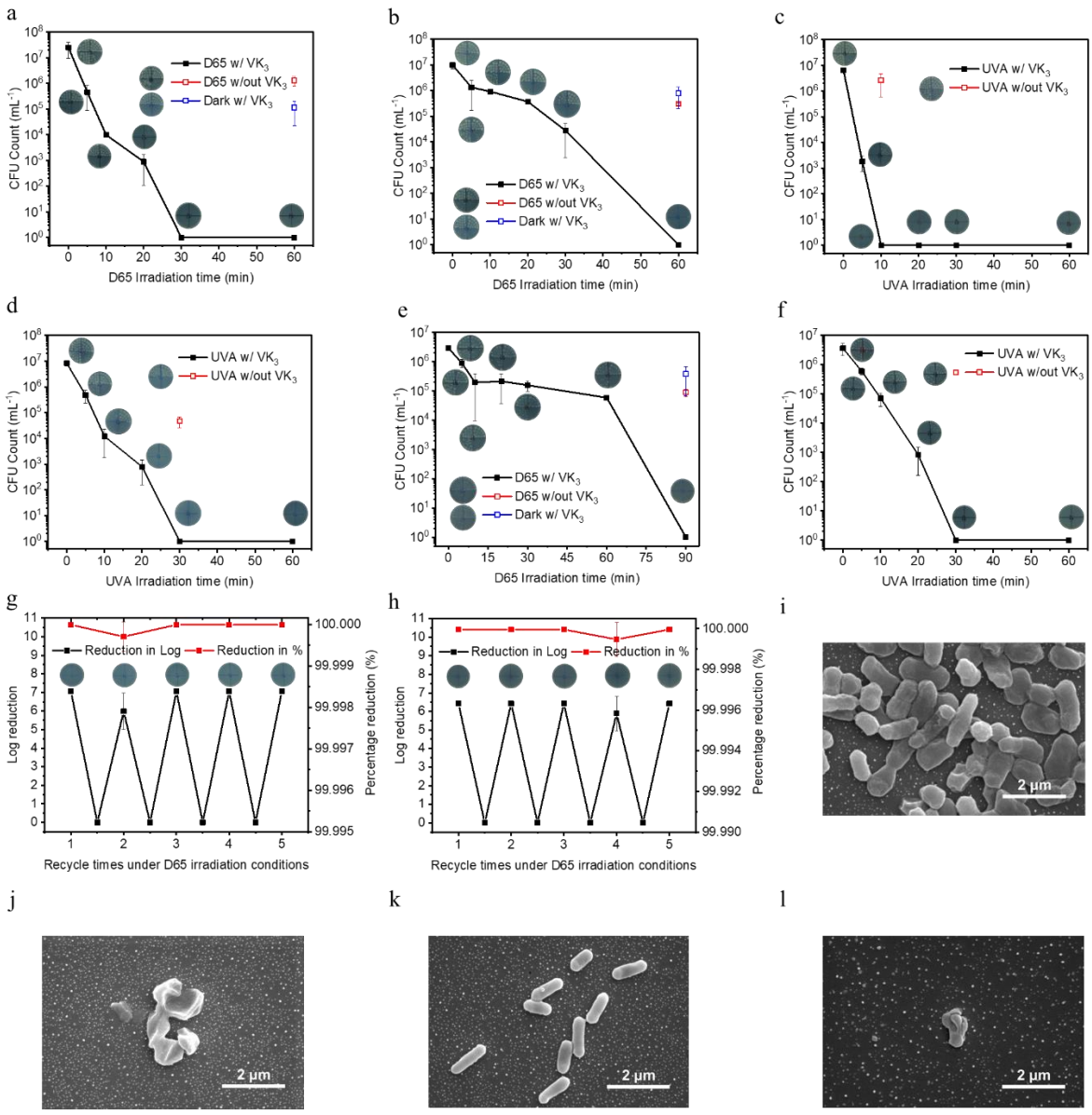

Figure 3.9. Photo-induced antibacterial function of VNFMs. Time-dependent bactericidal activity of (a) PVA-co-PE/VK_3 and (b) PAN/VK_3 VNFMs against *E. coli* under D65 and UVA (c and d) irradiation. Time-dependent bactericidal activity of PVA-co-PE/VK_3 VNFM against *L. innocua* under (e) D65 and (f) UVA irradiation. For (a-f), VNFM without light (Dark w/VK_3) and pristine nanofibrous membrane with light (UVA or D65 w/out VK_3) are used as controls. Five-time cycle bactericidal activity of PVA-co-PE/VK_3 VNFM against (g) *E. coli* and (h) *L. innocua*

under D65 irradiation. SEM morphology of (i) *E. coli* and (k) *L. innocua* without any treatment. SEM morphology of (j) *E. coli* and (l) *L. innocua* on PVA-co-PE/VK_3 VNFM after 60-min and 90-min D65 irradiation, respectively.

Both PVA-co-PE/VK_3 and PAN/VK_3 VNFMs can provide 7-log reduction (>99.99999%) of *E. coli* within 60 minutes under daylight irradiation. The control groups showed very little bacterial inactivation (around 1 log) after 60 minutes of the daylight irradiation, indicating that neither the daylight nor VK_3 itself is lethal to bacteria. Only the combination of daylight irradiation, VK_3, and polymer could demonstrate a significant antibacterial effect. Interestingly, we noticed that it only takes 30 minutes for PVA-co-PE/VK_3 VNFM to completely kill the *E. coli*. Yet, for PAN/VK_3 VNFM, it takes 60 minutes to achieve complete bacterial inactivation. Similar results were found in the UVA-induced time-dependent antibacterial tests of VK_3 NFMs against *E. coli*. In Figure 3.9c and 3.9d, UVA shows a stronger power than D65 to provide antibacterial functions on the VNFMs. For PVA-co-PE/VK_3 VNFM, the complete bactericidal timepoint is shortened to 10 minutes under UVA irradiation. Under the same condition, the PAN/VK_3 VNFM could achieve a complete kill in 30 minutes. The higher efficiency of UVA in triggering photoreactions is consistent with the previous formation of ROS by the materials, in which UVA exposure leads to production of more ROS. Meanwhile, under both D65 and UVA irradiations, the PVA-co-PE/VK_3 VNFM shows a higher bactericidal efficiency than that of the PAN/VK_3 VNFM, indicating that PVA-co-PE is a better hydrogen donor matrix polymer for preparing antimicrobial materials via the type I photoreaction to generate biocidal ROS.

To demonstrate the non-selective antibacterial function of the prepared PVA-co-PE/VK_3 VNFM, a time-dependent antibacterial test was also performed against Gram-positive *L. innocua* under D65 and UVA irradiation. Under daylight irradiation, PVA-co-PE/VK_3 VNFM achieved a

6-log reduction of *L. innocua* (>99.9999%) in 90 minutes of daylight exposure (Figure 3.9e), while UVA irradiation could shorten the kill time to 30 minutes (Figure 3.9f), again proving that UVA is more powerful than daylight. It is worth noting that, under both D65 and UVA irradiations, PVA-co-PE/VK_3 VNFM takes a longer time to achieve a complete inactivation against *L. innocua* than that of *E. coli*, even with a lower *L. innocua* concentration. This phenomenon is consistent with the antibacterial results of VK_3 in PBS buffer solvent system[44]. Gram-positive bacteria like *L. innocua* have a thicker cell wall compared with Gram-negative bacteria (*E. coli*), which will likely decrease the bactericidal efficiency of ROS, resulting in a stronger bacterial self-defense and slower bactericidal activity[62].

The PVA-co-PE/VK_3 VNFM could be reusable in the practical situation, according to the proposed photo-induced ROS generation mechanism. Thus, an antibacterial durability test was carried out under daylight irradiation to verify this putative function. Cyclic daylight-induced antibacterial tests against *E. coli* or *L. innocua* were applied on the PVA-co-PE/VK_3 VNFM for five times, and the results are shown in Figure 3.9g and 3.9h. The PVA-co-PE/VK_3 VNFM retains its robust antibacterial function even after five-time bacterial accumulations, leading to consistent 7-log reduction (>99.99999%) of *E. coli* and 6-log reduction (>99.9999%) of *L.innocua*, respectively. The antibacterial efficiency of the VNFMs after five repeated uses are basically the same as the freshly produced ones, proving that the VNFMs are durable and reusable antibacterial materials under daylight exposure.

To demonstrate that the bacteria are completely and irreversibly inactivated by the ROS produced by the PVA-co-PE/VK_3 VNFM under daylight irradiation, the morphological changes of the bacteria before and after contacting with the PVA-co-PE/VK_3 VNFM were investigated by using SEM shown in Figure 3.9i-3.9l. The cell structures of both *E. coli* and *L. innocua* in control

group without any treatment remain smooth and intact during the SEM capturing process. By sharp contrast, the cell walls of both *E. coli* and *L. innocua* on the PVA-co-PE/VK_3 VNFM after D65 irradiation are disrupted or broken into small fragments due to the attack by ROS[44], which again proves the daylight-induced bactericidal function of the prepared PVA-co-PE/VK_3 VNFM.

3.3.4 Daylight-induced antiviral function of VNFMs.

Inspired by the antibacterial results of the prepared VNFMs, several antiviral efficacy tests of the PVA-co-PE/VK_3 VNFMs were conducted. T7 bacteriophage (ATCCBAA-1025-B2), a non-enveloped double-stranded DNA virus that infects bacteria, was employed as a surrogate of mammalian viruses due to several distinguishing features including its rapid and relatively simple detection method and lack of pathogenicity to humans [25, 63-64]. Most importantly, the non-enveloped virus is widely considered to be less sensitive to photodynamic inactivation (PDI) in comparison to enveloped mammalian viruses such as Zika virus, Ebola virus, and coronavirus (SARS-CoV-2)[64-66]. As shown in Figure 3.10a, we challenged PVA-co-PE/VK_3 VNFM with a concentrated T7 phage suspension and placed the samples under daylight irradiation or dark condition for various durations to determine the material's time-dependent antiviral performance. Similar to the antibacterial tests, two control groups were designed to eliminate the effects caused by daylight irradiation or VK_3 itself. The results demonstrate that the T7 phage isolated from the control groups experienced only a slight reduction in phage count based on the activity assay assessed using plaque counts. In contrast to these findings, PVA-co-PE/VK_3 VNFM demonstrates a rapid and effective antiviral capacity, achieving 6 logs (>99.9999%) of PFU (plaque-forming units) reduction after 30-min daylight irradiation, revealing highly efficient antiviral activity compared to literature reported UV-induced antiviral materials[67]. The inactivation of the T7 phages can be attributed to the ROS oxidation of viral nucleic acids and lipid membranes[62]. Also, the ROS

were reported to crosslink the capsid protein of viruses, resulting in an inactivation of specific binding sites with virus hosts[63].

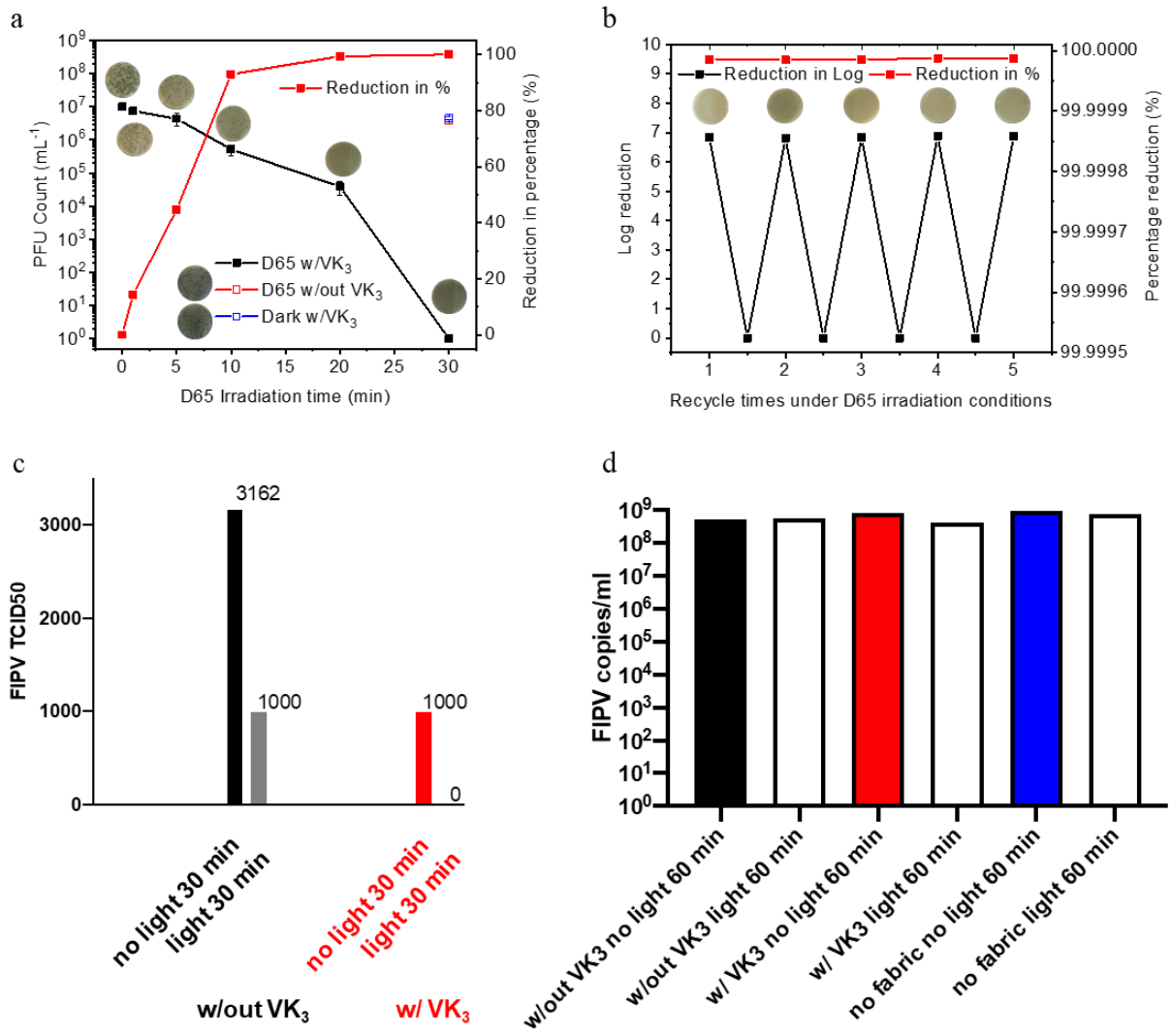

Figure 3.10. Daylight-induced antiviral function of PVA-co-PE/VK$_3$ VNFMs. (a) Time-dependent antiviral activity of PVA-co-PE/VK$_3$ VNFM against T7 bacteriophage under D65 irradiation (PVA-co-PE/VK$_3$ VNFM without daylight and pristine PVA-co-PE nanofibrous membrane with daylight as controls). (b) Five-time cycle antiviral activity of PVA-co-PE/VK$_3$ VNFM against T7 bacteriophage under D65 irradiation. (c) Antiviral results against FIPV of PVA-

co-PE/VK_3 VNFM and pristine PVA-co-PE nanofibrous membranes under daylight D65 irradiation. (d) RT-PCR results of the FIPV on the materials.

To further investigate the antiviral durability of the nanofibrous material, cyclic antiviral test was applied on the PVA-co-PE/VK_3 under daylight irradiation for five times. As shown in Figure 3.10b, the PVA-co-PE/VK_3 VNFM retains its robust antiviral function even after 5 times phage accumulation, achieving a 6 log of reduction (>99.9999%). The constant antiviral efficacy of the PVA-co-PE/VK_3 VNFM proves its durability and reusability as a potential antiviral PPE material under daylight exposure.

An *in vitro* cell culture system utilizing Crandell-Reese feline kidney cells (CRFK, ATCC) and feline infectious peritonitis virus (serotype II FIPV, WSU-79-1146, GenBank DQ010921) was utilized in order to assess the anti-coronaviral effect of the PVA-co-PE/VK_3 VNFM materials. Four thousand TCID50 (median tissue culture infectious dose) FIPV inoculated onto 1×2 cm^2 of the PVA-co-PE/VK_3 VNFM and then exposed to D65 irradiation for 30 minutes. No detectable FIPV was found in a viral infection assay, whereas the same membrane that was not exposed to light for 30 minutes had 1000 TCID50 FIPV. Pristine PVA-co-PE nanofibrous membrane (control sample) inoculated with FIPV showed 3000 or 1000 TCID50 FIPV, without or under the same D65 light exposure, respectively (Figure 3.10c). These results confirm the effective daylight-induced anticoronavirus functions of the PVA-co-PE/VK_3 VNFM materials. Interestingly, no significant reduction in viral RNA was identified as a result of any treatment when assessed by real-time RT-PCR (Figure 3.10d). This result suggests that the antiviral effect of the vitamin K derivatives is not a result of hyper-fragmentation of the viral genome.

3.4. Conclusion

Vitamin K derivatives in both PVA-co-PE (PVA-co-PE/VK_3) and PAN (PAN/VK_3) VNFMs could effectively produce large amounts of hydroxyl radicals, hydrogen peroxide, and singlet oxygen under photoirradiation following two different reaction paths. The two VNFMs are comparable in generating $^1O_2$, which proves the $^1O_2$ production is generally independent of the matrix polymer material via the Type II photoreaction. Interestingly, PVA-co-PE/VK_3 VNFM produces more HO· and H_2O_2 than PAN/VK_3 VNFM indicating that PVA-co-PE is a better hydrogen donor matrix polymer in the Type I photoreaction. The PVA-co-PE/VK_3 VNFM showed very high daylight-induced microbicidal efficiency against Gram-negative *E. coli* (>99.99999%), Gram-positive *L. innocua* (>99.9999%), T7 bacteriophage (>99.9999%) and feline infectious peritonitis virus (WSU-79-1146) (>99.9%), confirming the proposed photoreaction mechanism and robust biocidal functions. Moreover, the PVA-co-PE/VK_3 VNFM demonstrated great non-selective antimicrobial durability with constant microbicidal efficiency even after five times of repeated exposures to bacteria and T7 bacteriophages, revealing the excellent antimicrobial durability and reusability of the prepared VNFM under daylight irradiation. The membranes could serve as antibacterial and antiviral materials for face masks and other PPE with improved antimicrobial functionality.

3.5 Reference

(1) Metcalf, C. J. E.; Lessler, J. Opportunities and Challenges in Modeling Emerging Infectious Diseases. *Science* **2017,** *357* (6347), 149-152.

(2) Binder, S.; Levitt, A. M.; Sacks, J. J.; Hughes, J. M. Emerging Infectious Diseases: Public Health Issues for the 21st Century. *Science* **1999,** *284* (5418), 1311-1313.

(3) Morens, D. M.; Folkers, G. K.; Fauci, A. S. The Challenge of Emerging and Re-Emerging Infectious Diseases. *Nature* **2004,** *430* (6996), 242-249.

(4) Weatherall, D.; Greenwood, B.; Chee, H. L.; Wasi, P. Science and Technology for Disease Control: Past, Present, and Future. *Disease Control Priorities in Developing Countries* **2006,** *2*, 119-38.

(5) Holmes, E. C.; Dudas, G.; Rambaut, A.; Andersen, K. G. The Evolution of Ebola Virus: Insights from the 2013–2016 Epidemic. *Nature* **2016,** *538* (7624), 193-200.

(6) Leal, M. C.; Muniz, L. F.; Ferreira, T. S.; Santos, C. M.; Almeida, L. C.; Linden, V. V. D.; Ramos, R. C.; Rodrigues, L. C.; Neto, S. S. C. Hearing Loss in Infants with Microcephaly and Evidence of Congenital Zika Virus Infection—Brazil, November 2015–May 2016. *Morbidity and Mortality Weekly Report* **2016,** *65* (34), 917-919.

(7) Sohrabi, C.; Alsafi, Z.; O'Neill, N.; Khan, M.; Kerwan, A.; Al-Jabir, A.; Iosifidis, C.; Agha, R. World Health Organization Declares Global Emergency: A Review of the 2019 Novel Coronavirus (Covid-19). *International Journal of Surgery* **2020**.

(8) Mitchell, R.; Ogunremi, T.; Astrakianakis, G.; Bryce, E.; Gervais, R.; Gravel, D.; Johnston, L.; Leduc, S.; Roth, V.; Taylor, G. Impact of the 2009 Influenza a (H_1N_1) Pandemic on Canadian Health Care Workers: A Survey on Vaccination, Illness, Absenteeism, and Personal Protective Equipment. *American Journal of Infection Control* **2012,** *40* (7), 611-616.

(9) Moore, D.; Gamage, B.; Bryce, E.; Copes, R.; Yassi, A. Protecting Health Care Workers from Sars and Other Respiratory Pathogens: Organizational and Individual Factors That Affect Adherence to Infection Control Guidelines. *American Journal of Infection Control* **2005,** *33* (2), 88-96.

(10) Connor, T. H.; Leone, M. M.; McDiarmid, M. A.; Polovich, M.; Power, L. A.; Reed, L. D.; Whalen, J. J. Personal Protective Equipment for Health Care Workers Who Work with Hazardous Drugs. *DHHS Publication* **2008**.

(11) Borkow, G.; Zhou, S. S.; Page, T.; Gabbay, J. A Novel Anti-Influenza Copper Oxide Containing Respiratory Face Mask. *PLoS One* **2010,** *5* (6), e11295.

(12) Kim, Y. K. The Use of Polyolefins in Industrial and Medical Applications. *Polyolefin Fibres* **2017**, 135-155.

(13) Tomas, M. E.; Kundrapu, S.; Thota, P.; Sunkesula, V. C.; Cadnum, J. L.; Mana, T. S. C.; Jencson, A.; O'Donnell, M.; Zabarsky, T. F.; Hecker, M. T. Contamination of Health Care Personnel During Removal of Personal Protective Equipment. *JAMA Internal Medicine* **2015,** *175* (12), 1904-1910.

(14) Casanova, L.; Alfano-Sobsey, E.; Rutala, W. A.; Weber, D. J.; Sobsey, M. Virus Transfer from Personal Protective Equipment to Healthcare Employees' Skin and Clothing. *Emerging Infectious Diseases* **2008,** *14* (8), 1291.

(15) Livingston, E.; Desai, A.; Berkwits, M. Sourcing Personal Protective Equipment During the COVID-19 Pandemic. *JAMA* **2020**.

(16) World Health Organization (WHO). *Rational Use of Personal Protective Equipment for Coronavirus Disease (COVID-19) and Considerations During Severe Shortages: Interim Guidance*, WHO 2020, Interim guidance 6 April 2020.

(17) Gao, Y.; Cranston, R. Recent Advances in Antimicrobial Treatments of Textiles. *Textile Research Jjournal* **2008,** *78* (1), 60-72.

(18) Simoncic, B.; Tomsic, B. Structures of Novel Antimicrobial Agents for Textiles-a Review. *Textile Research Journal* **2010,** *80* (16), 1721-1737.

(19) Zhou, C.; Wang, M.; Zou, K.; Chen, J.; Zhu, Y.; Du, J. Antibacterial Polypeptide-Grafted Chitosan-Based Nanocapsules as an "Armed" Carrier of Anticancer and Antiepileptic Drugs. *ACS Macro Letters* **2013,** *2* (11), 1021-1025.

(20) Sun, G.; Worley, S. D. Chemistry of Durable and Regenerable Biocidal Textiles. *Journal of Chemical Education* **2005,** *82* (1), 60.

(21) Si, Y.; Li, J.; Zhao, C.; Deng, Y.; Ma, Y.; Wang, D.; Sun, G. Biocidal and Rechargeable N-Halamine Nanofibrous Membranes for Highly Efficient Water Disinfection. *ACS Biomaterials Science & Engineering* **2017,** *3* (5), 854-862.

(22) Si, Y.; Cossu, A.; Nitin, N.; Ma, Y.; Zhao, C.; Chiou, B. s.; Cao, T.; Wang, D.; Sun, G. Mechanically Robust and Transparent N-Halamine Grafted PVA-co-PE Films with Renewable Antimicrobial Activity. *Macromolecular Bioscience* **2017,** *17* (3), 1600304.

(23) Sun, G.; Xu, X.; Bickett, J. R.; Williams, J. F. Durable and Regenerable Antibacterial Finishing of Fabrics with a New Hydantoin Derivative. *Industrial & Engineering Chemistry Research* **2001,** *40* (4), 1016-1021.

(24) Sun, G.; Hong, K. H. Photo-Induced Antimicrobial and Decontaminating Agents: Recent Progresses in Polymer and Textile Applications. *Textile Research Journal* **2013,** *83* (5), 532-542.

(25) Si, Y.; Zhang, Z.; Wu, W.; Fu, Q.; Huang, K.; Nitin, N.; Ding, B.; Sun, G. Daylight-Driven Rechargeable Antibacterial and Antiviral Nanofibrous Membranes for Bioprotective Applications. *Science Advances* **2018,** *4* (3), eaar5931.

(26) Jalvo, B.; Faraldos, M.; Bahamonde, A.; Rosal, R. Antimicrobial and Antibiofilm Efficacy of Self-Cleaning Surfaces Functionalized by TiO_2 Photocatalytic Nanoparticles against Staphylococcus Aureus and Pseudomonas Putida. *Journal of Hazardous Materials* **2017,** *340*, 160-170.

(27) Kumar, R.; Umar, A.; Kumar, G.; Nalwa, H. S. Antimicrobial Properties of ZnO Nanomaterials: A Review. *Ceramics International* **2017,** *43* (5), 3940-3961.

(28) Gerischer, H. Photocatalysis in Aqueous Solution with Small TiO_2 Particles and the Dependence of the Quantum Yield on Particle Size and Light Intensity. *Electrochimica Acta* **1995,** *40* (10), 1277-1281.

(29) Zhang, Z.; Wang, C.-C.; Zakaria, R.; Ying, J. Y. Role of Particle Size in Nanocrystalline TiO_2-Based Photocatalysts. *The Journal of Physical Chemistry B* **1998,** *102* (52), 10871-10878.

(30) Kočí, K.; Obalová, L.; Matějová, L.; Plachá, D.; Lacný, Z.; Jirkovský, J.; Šolcová, O. Effect of TiO_2 Particle Size on the Photocatalytic Reduction of CO_2. *Applied Catalysis B: Environmental* **2009,** *89* (3-4), 494-502.

(31) Wu, J.; Liu, W.; Xue, C.; Zhou, S.; Lan, F.; Bi, L.; Xu, H.; Yang, X.; Zeng, F.-D. Toxicity and Penetration of TiO_2 Nanoparticles in Hairless Mice and Porcine Skin after Subchronic Dermal Exposure. *Toxicology Letters* **2009,** *191* (1), 1-8.

(32) Hong, K. H.; Sun, G. Photoactive Antimicrobial Agents/Polyurethane Finished Leather. *Journal of Applied Polymer Science* **2010,** *115* (2), 1138-1144.

(33) Tim, M. Strategies to Optimize Photosensitizers for Photodynamic Inactivation of Bacteria. *Journal of Photochemistry and Photobiology B: Biology* **2015,** *150*, 2-10.

(34) Tong, M.; Yuan, S.; Ma, S.; Jin, M.; Liu, D.; Cheng, D.; Liu, X.; Gan, Y.; Wang, Y. Production of Abundant Hydroxyl Radicals from Oxygenation of Subsurface Sediments. *Environmental Science & Technology* **2016,** *50* (1), 214-221.

(35) Zhuo, J.; Sun, G. Antimicrobial Functions on Cellulose Materials Introduced by Anthraquinone Vat Dyes. *ACS Applied Materials & Interfaces* **2013,** *5* (21), 10830-10835.

(36) Liu, N.; Sun, G.; Zhu, J. Photo-Induced Self-Cleaning Functions on 2-Anthraquinone Carboxylic Acid Treated Cotton Fabrics. *Journal of Materials Chemistry* **2011,** *21* (39), 15383-15390.

(37) Liu, N.; Sun, G. Production of Reactive Oxygen Species by Photoactive Anthraquinone Compounds and Their Applications in Wastewater Treatment. *Industrial & Engineering Chemistry Research* **2011,** *50* (9), 5326-5333.

(38) Hou, A.; Sun, G. Multifunctional Finishing of Cotton Fabrics with 3, 3′, 4, 4′-Benzophenone Tetracarboxylic Dianhydride: Reaction Mechanism. *Carbohydrate Polymers* **2013,** *95* (2), 768-772.

(39) Rhodes, M.; Bucher, J.; Peckham, J.; Kissling, G.; Hejtmancik, M.; Chhabra, R. Carcinogenesis Studies of Benzophenone in Rats and Mice. *Food and Chemical Toxicology* **2007,** *45* (5), 843-851.

(40) Booth, S. L. Vitamin K: Food Composition and Dietary Intakes. *Food & Nutrition Research* **2012,** *56* (1), 5505.

. Vitamin K: Food Composition and Dietary Intakes. *Food & Nutrition Research* **2012,** *56* (1), 5505.

(41) van Hylckama Vlieg, J. E.; Veiga, P.; Zhang, C.; Derrien, M.; Zhao, L. Impact of Microbial Transformation of Food on Health—from Fermented Foods to Fermentation in the Gastro-Intestinal Tract. *Current Opinion in Biotechnology* **2011,** *22* (2), 211-219.

(42) Shearer, M. J.; Newman, P. Recent Trends in the Metabolism and Cell Biology of Vitamin K with Special Reference to Vitamin K Cycling and MK-4 Biosynthesis. *Journal of Lipid Research* **2014,** *55* (3), 345-362.

(43) Ferland, G. The Discovery of Vitamin K and Its Clinical Applications. *Annals of Nutrition and Metabolism* **2012,** *61* (3), 213-218.

(44) Zhang, Z.; Si, Y.; Sun, G. Photoactivities of Vitamin K Derivatives and Potential Applications as Daylight-Activated Antimicrobial Agents. *ACS Sustainable Chemistry & Engineering* **2019,** *7* (22), 18493-18504.

(45) Xu, F.; Vostal, J. G. Inactivation of Bacteria via Photosensitization of Vitamin K_3 by UV-A Light. *FEMS Microbiology Letters* **2014,** *358* (1), 98-105.

(46) Bors, W.; Michel, C.; Saran, M. On the Nature of Biochemically Generated Hydroxyl Radicals Studies Using the Bleaching of p-Nitrosodimethylaniline as a Direct Assay Method. *European Journal of Biochemistry* **1979,** *95* (3), 621-627.

(47) Kraljić, I.; Mohsni, S. E. A New Method for the Detection of Singlet Oxygen in Aqueous Solutions. *Photochemistry and Photobiology* **1978,** *28* (4-5), 577-581.

(48) Ramakrishnan, M. A. Determination of 50% Endpoint Titer Using a Simple Formula. *World Journal of Virology* **2016,** *5* (2), 85-86.

(49) Murphy, B. G.; Perron, M.; Murakami, E.; Bauer, K.; Park, Y.; Eckstrand, C.; Liepnieks, M.; Pedersen, N. C. The Nucleoside Analog GS-441524 Strongly Inhibits Feline Infectious Peritonitis

(FIP) Virus in Tissue Culture and Experimental Cat Infection Studies. *Veterinary Microbiology* **2018,** *219*, 226-233.

(50) Ahmed, F. E.; Lalia, B. S.; Hashaikeh, R. A Review on Electrospinning for Membrane Fabrication: Challenges and Applications. *Desalination* **2015,** *356*, 15-30.

(51) Fang, F. C. Antimicrobial Reactive Oxygen and Nitrogen Species: Concepts and Controversies. *Nature Reviews Microbiology* **2004,** *2* (10), 820-832.

(52) Pan, X.; Zhou, G.; Wu, J.; Bian, G.; Lu, P.; Raikhel, A. S.; Xi, Z. Wolbachia Induces Reactive Oxygen Species (ROS)-Dependent Activation of the Toll Pathway to Control Dengue Virus in the Mosquito *Aedes Aegypti*. *Proceedings of the National Academy of Sciences* **2012,** *109* (1), E23-E31.

(53) DeRosa, M. C.; Crutchley, R. J. Photosensitized Singlet Oxygen and Its Applications. *Coordination Chemistry Reviews* **2002,** *233*, 351-371.

(54) Zhuo, J. Photoactive Chemicals for Antimicrobial Textiles. In *Antimicrobial Textiles* **2016,** 197-223.

(55) Nakamura, K.; Yamada, Y.; Ikai, H.; Kanno, T.; Sasaki, K.; Niwano, Y. Bactericidal Action of Photoirradiated Gallic Acid via Reactive Oxygen Species Formation. *Journal of Agricultural and Food Chemistry* **2012,** *60* (40), 10048-10054.

(56) Hynek, J.; Rathouský, J.; Demel, J.; Lang, K. Design of Porphyrin-Based Conjugated Microporous Polymers with Enhanced Singlet Oxygen Productivity. *RSC Advances* **2016,** *6* (50), 44279-44287.

(57) Amada, I.; Yamaji, M.; Sase, M.; Shizuka, H. Laser Flash Photolysis Studies on Hydrogen Atom Abstraction from Phenol by Triplet Naphthoquinones in Acetonitrile. *Journal of the Chemical Society, Faraday Transactions* **1995,** *91* (17), 2751-2759.

(58) Dormán, G.; Nakamura, H.; Pulsipher, A.; Prestwich, G. D. The Life of Pi Star: Exploring the Exciting and Forbidden Worlds of the Benzophenone Photophore. *Chemical Reviews* **2016,** *116* (24), 15284-15398.

(59) Görner, H. Photoprocesses of p-Naphthoquinones and Vitamin K_1: Effects of Alcohols and Amines on the Reactivity in Solution. *Photochemical & Photobiological Sciences* **2004,** *3* (1), 71-78.

(60) Michelin, C.; Hoffmann, N. Photosensitization and Photocatalysis—Perspectives in Organic Synthesis. *ACS Catalysis* **2018,** *8* (12), 12046-12055.

(61) Gollnick, K.; Schenck, G. Mechanism and Stereoselectivity of Photosensitized Oxygen Transfer Reactions. *Pure and Applied Chemistry* **1964,** *9* (4), 507-526.

(62) Mai-Prochnow, A.; Clauson, M.; Hong, J.; Murphy, A. B. Gram Positive and Gram Negative Bacteria Differ in Their Sensitivity to Cold Plasma. *Scientific Reports* **2016,** *6*, 38610.

(63) Cossu, A.; Ercan, D.; Tikekar, R. V.; Nitin, N. Antimicrobial Effect of Photosensitized Rose Bengal on Bacteria and Viruses in Model Wash Water. *Food and Bioprocess Technology* **2016,** *9* (3), 441-451.

(64) Costa, L.; Faustino, M. A. F.; Neves, M. G. P.; Cunha, Â.; Almeida, A. Photodynamic Inactivation of Mammalian Viruses and Bacteriophages. *Viruses* **2012,** *4* (7), 1034-1074.

(65) Siddharta, A.; Pfaender, S.; Vielle, N. J.; Dijkman, R.; Friesland, M.; Becker, B.; Yang, J.; Engelmann, M.; Todt, D.; Windisch, M. P. Virucidal Activity of World Health Organization–Recommended Formulations against Enveloped Viruses, Including Zika, Ebola, and Emerging Coronaviruses. *The Journal of Infectious Diseases* **2017,** *215* (6), 902-906.

(66) Wiehe, A.; O'Brien, J. M.; Senge, M. O. Trends and Targets in Antiviral Phototherapy. *Photochemical & Photobiological Sciences* **2019,** *18* (11), 2565-2612.

(67) Ercan, D.; Cossu, A.; Nitin, N.; Tikekar, R. V. Synergistic Interaction of Ultraviolet Light and Zinc Oxide Photosensitizer for Enhanced Microbial Inactivation in Simulated Wash-Water. *Innovative Food Science & Emerging Technologies* **2016,** *33*, 240-250.

Chapter 4. Photoactive Water-soluble Vitamin K: A Novel Amphiphilic Photo-induced Antibacterial Agent

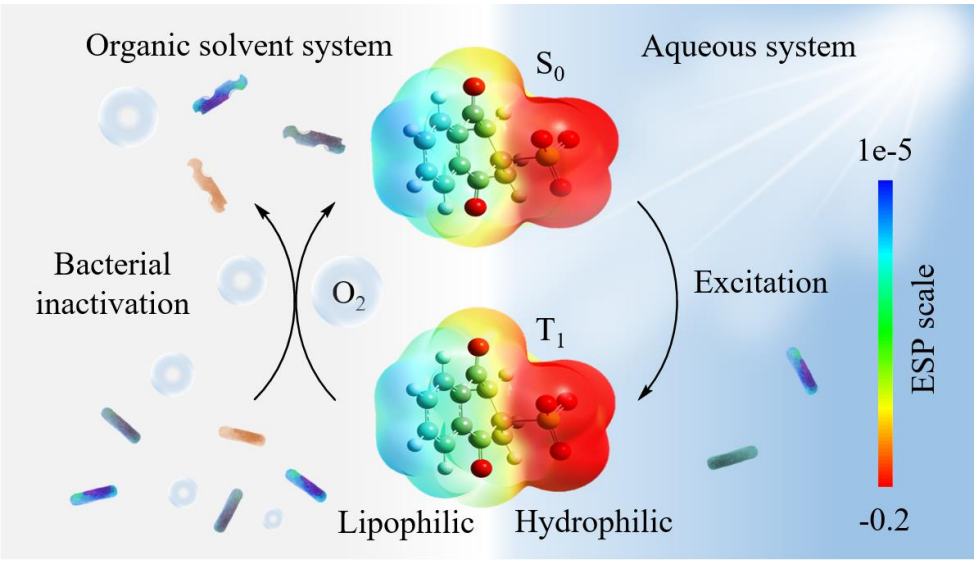

Abstract

Menadione sodium bisulfite (MSB), also known as water-soluble vitamin K_3, are widely used as an animal food additive due to its low toxicity and low cost. MSB is for the first time proven to be photoactive and antibacterial under various photoirradiation sources, evidenced by computational modeling method and well-designed experiments. MSB demonstrates its robust photoactivity and application potential under ultra-violet A (UVA, 315-400 nm) irradiation. The results reveal that MSB could effectively generate reactive oxygen species (ROS) under UVA irradiation due to the formation of its oxidative triplet excited state. The photo-induced antibacterial tests also demonstrate the non-selective bacterial inactivation functions of MSB under proper photo-irradiation. MSB was challenged against Gram-negative *Escherichia coli* (*E. coli*) and Gram-positive *Listeria innocua* (*L. innocua*) under UVA irradiation and exhibited excellent antibacterial performance (99.999% bacterial inactivation in 30 min of UVA exposure) in PBS. The antibacterial performance of MSB does not decay after five-times of repeated exposures to

bacteria and UVA irradiation, indicating the photostability and durability of MSB as a photo-induced antibacterial agent. More interestingly, solvents played a significant impact on photo-induced antibacterial properties but not on the generation of ROS of MSB, indicating that the solvents may serve as contact media between MSB and bacteria cells. Intimate contact of MSB and microorganisms is thought to determine the bacterial inactivation by ROS or triplet excited states due to their relatively short lifetimes and limited diffusion and function radius.

4.1 Introduction

Vitamin K derivatives are a series of photoactive compounds sharing similar aromatic ketone structures with different side chains. They play essential roles in human bodies in blooding coagulation and bone metabolism processes[1-2]. Both vitamin K_1 and K_2 are naturally based[2-4] and nontoxic[5-7] but less photoactive in generating cell-lethal ROS due to the electron transfer from the side chain to the carbonyl oxygen during the photoexcitation process, which lowers the intersystem crossing (ISC) and triplet state quantum yields[8-9]. Vitamin K_3 (VK_3), which is also known as menadione and used in animal foods, is however organically synthesized and harmful to human due to its active role in cell-mediated electron transfer and consequently severe cell oxidative stress[10]. High photo reactivity of VK_3 was demonstrated in previous works[8, 11], and therefore, excellent photo-induced antimicrobial performance of VK_3 was found and applied in the fabrication of daylight-induced reusable antimicrobial materials for face masks[12].

Inspired by the strong photoactivity of VK_3, a water-soluble vitamin K_3 derivative, menadione sodium bisulfite (MSB), attracted our attention due to its aromatic ketone structure similar to VK_3. MSB is derivatized from VK_3 by addition of a sulfonate group and hydrogen to the conjugated double bond. The compound was found non-fluorescent with a high ISC yield[13], which reveals its potential in forming the triplet excited state, a key structure in certain photoreactions[14],

especially the formation of ROS under photoirradiation[8, 15-16]. Meanwhile, MSB is less cytotoxic than VK_3 due to its stable intracellular electron transfer function and less production of superoxide radical anion and hydrogen peroxide during the metabolism[17].

MSB has been widely used as an animal feed additive in Europe for a long time without a time limit[18]. It is considered as an adequate vitamin K resource to prevent animals' vitamin K deficiency. Besides, MSB is also intended for use in drinking water[18]. No acute toxicity of MSB was found at levels as high as 1000 times of the dietary requirements[18]. Meanwhile, there is no danger to humans when MSB is used as a nutritional additive in animal feed[18]. Also, the use of MSB in animal feed does not put the environment at risk. The U.S. Food & Drug Administration also lists MSB as a legal animal food additive to prevent vitamin K deficiency of animals[19]. A long history of using MSB in poultry food in the U.S. can be traced back to 1958, demonstrating the safety of the MSB utilization[19]. Except for being used as animal food additives, MSB was also employed as a plant defender to inactivate various pathogens[20-21] or as a detoxifier against some carcinogens[22]. Despite the multi functionalities mentioned above, few literature reveals the photoactivity of MSB and its potential to be used as a photo-induced antibacterial agent, though it shares a similar basic aromatic ketone structure as other photoactive quinone derivatives, such as benzophenones and anthraquinones. Thus, we took the lead in predicting and explaining the photo reactivity and photo-induced antibacterial property of MSB. More interestingly, we noticed that some solvents could significantly impact the photo-induced bacterial inactivation activity of MSB by providing intimate interactions between the short-lived reactive species and bacteria cells.

4.2 Experimental Methods

4.2.1 Materials

Menadione (VK_3) was purchased from Chem-Impex International Inc. p-Nitroso-N, N-dimethylaniline (p-NDA) was purchased from TCI Co. LTD. Menadione sodium bisulfite (MSB), ethyl alcohol (EtOH), ethyl acetate (EtOAc), chloroform ($CHCl_3$), L-histidine, potassium iodide, sodium hydroxide, ammonium molybdate tetrahydrate, potassium hydrogen phthalate, sodium phosphate dibasic, potassium phosphate monobasic, sodium chloride, potassium chloride, propidium iodide dye (PI dye), SYBR green dye (SG dye), and Reactive Black 5 (RB) were purchased from Sigma-Aldrich. Luria-Bertani (LB) broth, LB agar, Tryptic soy broth (TSB), and Tryptic soy agar (TSA) were purchased from Thermo Fisher Scientific. All of the chemicals or supplies were used as received without any further purification.

4.2.2 Computational details

All computations were performed in a computational software package Gaussian 09 ver. 08. The ground-state and triplet-state geometries of ionic MSB and ionic hydro-MSB (MSB-H) radical were optimized at the unrestricted DFT-B3LYP/6-31G+ (d,p) level of theory in the polarizable continuum model (PCM) using the integral equation formalism variant (IEFPCM) in H_2O solvent. The ground-state geometries of neutral molecules were optimized at the unrestricted DFT-B3LYP/6-31G (d,p) level of theory in the IEFPCM in H_2O solvent. The ionic MSB excitation was further obtained at the restricted TDDFT-B3LYP/6-31G+ (d,p) level of theory in the IEFPCM-H_2O solvent model based on the optimized ground-state MSB structures. The Gibbs free energies of the anions were obtained by frequency calculations at the DFT-B3LYP/6-31G+ (d,p) level of theory in the IEFPCM-H_2O solvent based on the optimized geometries. The Gibbs free energies of neutral molecules were obtained by frequency calculations at the DFT-B3LYP/6-31G (d,p) level of theory in the IEFPCM-H_2O solvent based on the optimized geometries. The ESP-mapped electron densities of the ground-state and triplet-state MSB were obtained at the DFT-

B3LYP/6-31G+ (d,p) level of theory in the IEFPCM-H_2O solvent model. The total electron density was plotted and mapped with ESP-derived charges to show the molecular out-shell charge distributions.

4.2.3 Measurements of UV-vis spectra of MSB, VK_3, and Reactive Black 5 (RB)

The photostability of MSB under the UVA irradiation was obtained using a UV-vis spectrometer (Evolution 600, Thermo Fisher Scientific). 20 μM MSB in H_2O was placed under the UVA (365 nm) irradiation. The UV-vis absorption of MSB in H_2O was recorded every 10 min. The photostability of MSB in 10% EtOH/H_2O under UVA irradiation was also determined. The UV-vis absorption spectrum of 0.2 mM MSB in the presence of hydrogen donor (EtOH) was recorded after 20-min and 60-min UVA exposure. The decomposition of RB by MSB was recorded using the UV-vis spectrometer. 20 μM of RB was dissolved in various solutions with or without 0.2 mM MSB. The solution was then placed under the UVA irradiation. The degradation of RB was recorded according to the absorbance at 598 nm with λ_{max}. The light transmittance of 2 mM VK_3 in 8% EtOH/PBS or 8% EtOAc/PBS solution was also determined by UV-vis spectrometer. The transmittance rate of the VK_3 suspensions at 660 nm was recorded after 10-min, 20-min, and 30-min placement at room temperature.

4.2.4 Measurements of hydroxyl radicals

The hydroxyl radicals produced from MSB in the solution under the UVA irradiation were quantitively measured by p-NDA, a specific hydroxyl radical quencher that is widely used in the hydroxyl radical related tests[15, 23]. A photo-irradiation crosslinker box (Spectrolinker XL-1500, Spectronics Corporation) equipped with six 15-Watt cool white (CW) fluorescent lamps (General Electric F15T8-CW) was employed in this experiment. The irradiance distance between lamps and

test samples is 16 cm. The UV irradiance power of the cool white fluorescence lamps were detected by an Ultra-Violet Radiometer (Fisher Scientific) as 50 μW/cm^2.Photo-irradiation crosslinker box (Spectrolinker XL-1000, Spectronics Corporation) equipped with five 8-Watt 365 nm (UVA) lamps (Spectroline BLE-8T365) or 312 nm (UVB) lamps (Spectroline BLE-8T312) was also employed to supply UV irradiance. The irradiance distance between UV lamps and samples is 12 cm. The UV irradiance power was detected as 3.0 mW/cm^2. MSB (or VK_3) and p-NDA (50 μM) were dissolved in various solutions and exposed under photoirradiation or dark conditions for a certain time. The amount of the residual p-NDA in the solution was quantitively measured by the UV-vis spectrometer according to the absorbance at 440 nm with λ_{max}.

4.2.5 Measurements of hydrogen peroxide

The production of hydrogen peroxide was quantified by an indirect photometric method, according to the literature[15]. MSB (or VK_3) was dissolved in 5 mL of various solutions and placed under photoirradiation sources or dark condition. After that, 1 mL of the sample solution was mixed with 1 mL of the reagent A [Potassium iodide (66 g L^{-1}), sodium hydroxide (2g L^{-1}), and ammonium molybdate tetrahydrate (0.2 g L^{-1}) in water] and 1mL of the reagent B [Potassium hydrogen phthalate (20g L^{-1}) in water]. The mixture was vortexed for 10 seconds to mix homogeneously and sufficiently. The mixture was then placed in a dark environment for 5 min to fully react. The accumulated hydrogen peroxide in the sample solution could be quantified by the UV-vis spectrometer according to the absorbance at 351 nm with λ_{max}.

4.2.6 Measurements of singlet oxygen

The generated singlet oxygen was measured by a widely used method in literature[24-25]. MSB (20 μM) and p-NDA (50 μM) were dissolved in 0.01 M PBS solution (or 20 μM VK_3 in 10%

EtOH/PBS solution). L-histidine (0.01 M) was also added to detect the singlet oxygen. Under the photoirradiation, the formed singlet oxygen could first react with L-histidine and subsequently form a transannular intermediate, which could oxidize the p-NDA leading to an extra p-NDA consumption, comparing to the system without L-histidine. The additional p-NDA consumption caused by singlet oxygen was recorded as the singlet oxygen formation.

4.2.7 Bacterial culture

Two types of generic bacteria, Gram-negative *E. coli* and Gram-positive *L. innocua*, were incubated and used in the photo-induced antibacterial tests in this work. A colony of *E. coli* was inoculated in 10 mL of LB broth at 37 ℃ for 18 h. A bacterial culture of around 1×10^9 CFU mL^{-1} was obtained accordingly. The *E. coli* suspension was diluted to around 1×10^7 CFU mL^{-1} for the following antibacterial tests. Similarly, a colony of *L. innocua* was inoculated in 10 mL of TSB broth at 37℃ for at least 24 h. After that, a bacterial culture of around 1×10^8 CFU mL^{-1} was obtained. The *L. innocua* suspension was diluted to around 1×10^7 CFU mL^{-1} for the following antibacterial tests.

4.2.8 Antibacterial tests

MSB stock solution (50 mM) was freshly prepared in PBS. Similarly, VK_3 stock solution (50 mM) was also freshly prepared in EtOH, EtOAc, or $CHCl_3$ for the photo-induced antibacterial tests. 10 μL of the 1×10^7 CFU mL^{-1} *E. coli* or *L. innocua* suspension, a certain amount of MSB or VK_3 stock solution, and a certain amount of EtOH, EtOAc, or $CHCl_3$ solvent were also added into the PBS to obtain 1 mL of finalized bacterial suspension with a concentration of 1×10^5 CFU mL^{-1}. The bacterial suspension was placed under photoirradiation sources for a certain time. Then the bacteria suspension was serially diluted ($\times10^0$, $\times10^1$, $\times10^2$, and $\times10^3$) and plated on LB agar (*E.*

coli) or TSA agar (*L. innocua*) for the bacterial enumeration. For the antibacterial durability test, 5 groups of MSB/bacteria suspension were placed under UVA (365 nm) irradiation for a certain time. After the first cycle, the bacteria in group 1 were collected and plated on the agar plates. Another fresh 10 μL of the 1×10^7 CFU mL^{-1} bacterial suspension was added to the remaining four groups, which were subsequently placed under the UVA irradiation for the second cycle. Same operations were performed until the five cycles were finished. The LA agars with *E. coli* were incubated at 37℃ for 18 h. The TSA agars with *L. innocua* were incubated at 37℃ for at least 24 h. The bacterial viability was assessed by the plate counting assay.

4.2.9 Live/dead bacterial viability assay

10 μL of the 1×10^9 CFU mL^{-1} bacterial suspension and 40 μL of the MSB stock solution were added into 950 μL of PBS to obtain an MSB/bacteria suspension with a final bacterial concentration of 1×10^7 CFU mL^{-1}. The bacterial suspension was placed under UVA irradiation for 60 min. Bacteria in PBS without MSB under dark conditions were used as the control group. PI and SG dye were added to the bacterial suspension with a concentration of 10 μg mL^{-1}. The bacteria were washed and re-diluted with PBS after 20-min staining. The bacteria suspension was subsequently dropped on a microscope slide, and the fluorescence signals were detected on a laser scanning confocal microscope (Olympus FV1000).

4.2.10 Surface tension test

Surface tension was measured using a SensaDyne surface tensiometer (SensaDyne Instrument Division, Mesa, AZ) attached with 0.5 and 4 mm non-inverted probes. Prior to calibration, N_2 gas bubble frequency of the smaller probe (0.5 mm) was set slightly faster than the larger probe (4 mm). Calibration was then completed with water (around 72 mN/m) and ethanol

(around 22 mN/m) at room temperature. Probes were inserted into a beaker containing a sample until fully submerged. After readings stabilized (around 1 min), surface tension was recorded from display.

4.2.11 Bacterial affinity to organic solvents

The affinity between the bacteria and organic solvent was quantitatively determined by using an extraction method, according to the literature[26]. 1 mL of the 1×10^9 CFU mL^{-1} *E. coli* suspension was added to 9 mL of PBS solution, resulting in a bacterial suspension with a concentration of 1×10^8 CFU mL^{-1}. The absorbance of the bacterial suspension was measured at 600 nm and recorded as A_0. 3 mL of 1×10^8 CFU mL^{-1} *E. coli* suspension was mixed with 1 mL of PBS, EtOAc, or $CHCl_3$. After 10 min of incubation at room temperature, the two-phase system was vigorously vortexed for 2 min to mix them homogeneously. The mixture was further incubated for 20 min at room temperature to let the bacterial extraction sufficient. After that, the aqueous phase was removed, and its absorbance at 600 nm was measured and recorded as A_1. The percentage of the bacterial concentration reduction by the solvent extraction was calculated as $(1-A_1/A_0)\times100$.

4.3 Results and Discussion

4.3.1 Photo-reactivity of MSB

The photoactivity of VK_3 comes from the aromatic ketone structure, which has been confirmed in a previous research[8]. The unique aromatic ketone structure shows a high ISC yield with minimal fluorescence emission[27-28], which is also the unique feature found in MSB during its excitation process[13]. MSB therefore possesses potential photoactivity due to the aromatic ketone structure. In this case, we infer that MSB shares the typical photoreaction mechanism as VK_3.

Under proper photo-irradiation, the ground-state MSB can be excited to the singlet state followed by the ISC and the formation of triplet state (Figure 4.1a), the latter of which is widely thought of as the starting material in various photoreactions due to its relatively long lifetime and oxidative property[22, 29]. Several subsequent reactions could occur to MSB after the formation of the triplet state, such as the electron transfer[30] or hydrogen abstraction reaction from substrates[31], the singlet oxygen sensitization[32], and the microbial oxidation and disruption[15]. A UV-vis absorption spectrum of MSB was obtained to determine its proper excitation light resource. According to Figure 4.1b, MSB mainly absorbs light in the ultra-violet B (UVB) region (280-315 nm) with weak absorption peaks in the UVA region (315-400 nm). The prominent absorption peaks of MSB in the UVB region can be attributed to its multiple singlet excited states, such as S_5 (279.86 nm) and S_{13} (235.76 nm), based on the computational modeling. However, a weak absorption shoulder at around 350 nm (Figure 4.1b, inset) noticed under a higher MSB concentration can be attributed to excited states of S_1-S_3 (335.69 nm- 328.71 nm), revealing a weaker photo reactivity of MSB under UVA irradiation compared with that under UVB irradiation. The detailed computational excitation information can be found in Table 4.1. A good coincidence between the computed and experimental spectra is found (Figure 4.2), which proves the accuracy of the modeling used in this work.

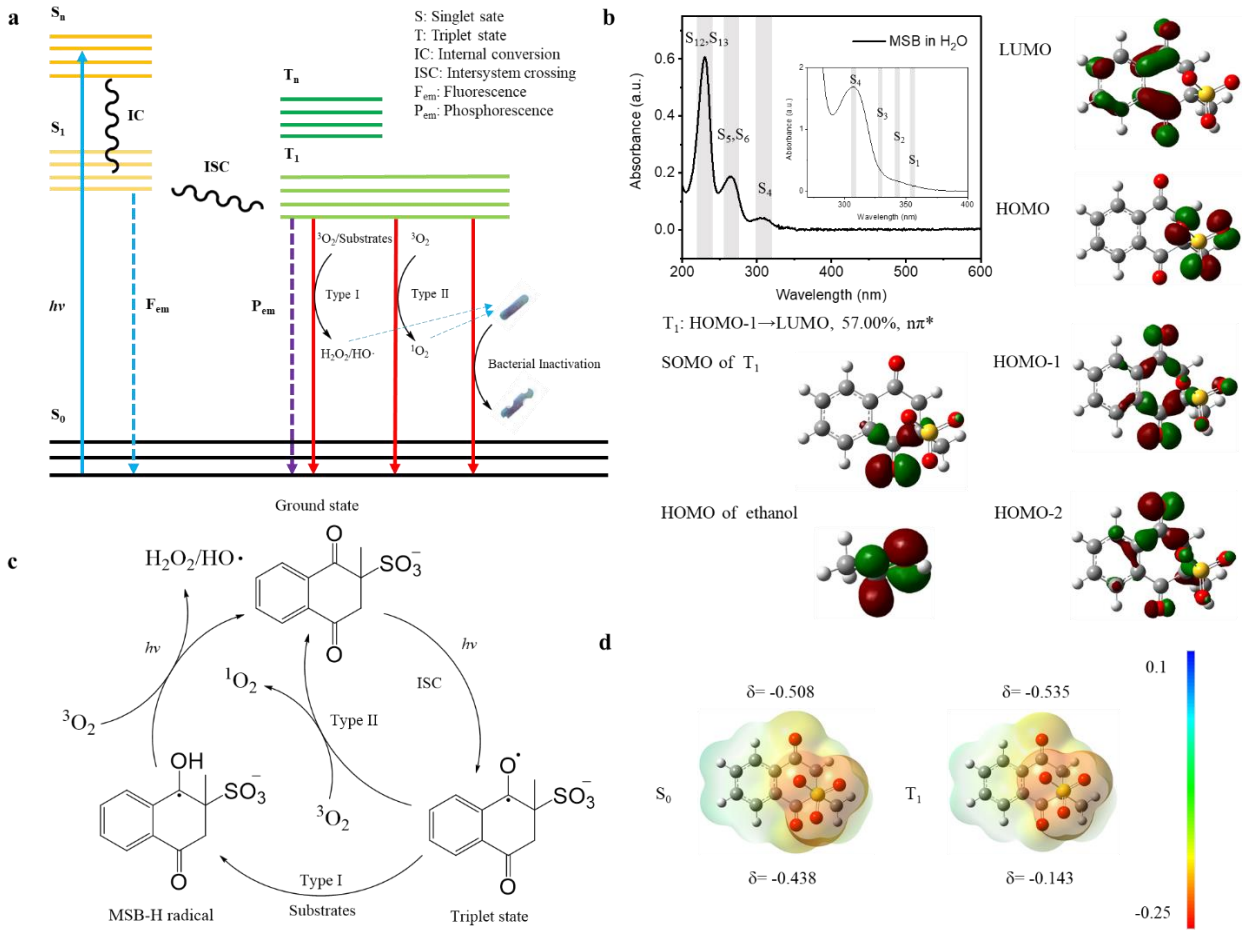

Figure 4.1. Photo reactivity of MSB. (a) Schematic Jablonski diagram describing the photoexcitation process of MSB and following photoreactions. (b) UV-vis absorption spectrum of 20 μM MSB in H_2O (Inset: UV-vis spectrum of 1 mM MSB in H_2O) and computational frontier molecular orbitals of MSB. HOMO: highest occupied molecular orbital; LUMO: lowest unoccupied molecular orbital; SOMO: semi occupied molecular orbital. (c) Proposed photoreaction mechanism of MSB in aerobic environment. (d) ESP-mapped electron density of ground-state and triplet-state MSB. The δ is the ESP charge on the carbonyl oxygen of MSB in each state.

Singlet state	[a]f	[b]λ_{max} (nm)
S_1	0.0049	355.69
S_2	0.0031	339.72
S_3	0.0022	328.71
S_4	0.0502	292.29
S_5	0.0461	279.86
S_6	0.0693	276.78
S_{12}	0.1974	239.27
S_{13}	0.2396	235.76

[a]Oscillator strength and [b]theoretical excitation wavelength of corresponding singlet state.

Table 4.1. Computation details of singlet states of MSB.

Based on the frontier molecular orbitals obtained from the computation, the triplet-state configuration of MSB is mainly nπ* with electron excitation from HOMO-1 to LUMO, which is highly active in abstracting an electron or hydrogen from substrates[33]. During the photoexcitation, the electrons are excited from the lone-pair electrons of the carbonyl oxygen to the anti-bonding orbital on the carbonyl carbon (Figure 4.1b). The SOMO of the MSB triplet, which locates at the carbonyl oxygen, also confirms the electron excitation process. The electron migrates from the carbonyl oxygen's lone pair, leaving a partially unoccupied site on the carbonyl oxygen. The HOMO of the hydrogen donor used in this project, ethanol (EtOH), is also depicted in Figure 4.1b. The computation result shows that the electron-rich sites in EtOH are the lone-pair electrons in the hydroxyl group and the α C-H bond, which also coincides with the literature[34]. The formed MSB triplet state is much more oxidative, verified by the computed Electrostatic Surface Potential (ESP)-mapped electron density difference between the ground-state and triplet state of MSB. Figure 4.1d shows that the carbonyl oxygen is relatively electron sufficient in the ground state. After the triplet state formation, the electron charge on the carbonyl oxygen changes from -0.438

to -0.143. The less negative value proves the electron deficiency on the carbonyl oxygen after the photoexcitation. The oxidative triplet MSB provides the potential for type I and type II photoreactions. Typically, both type I and type II photoreactions start from the triplet MSB (Figure 4.1a and 4.1c) after the photoexcitation and ISC processes. In the presence of a hydrogen donor or electron donor, the type I photoreaction with an electron/hydrogen transfer can happen from electron-rich substrates to electron-deficient triplet MSB. The formed hydroquinone radical (MSB-H radical) can then react with oxygen to form hydroxyl radical (HO·) and hydrogen peroxide (H_2O_2) with the accompanied formation of ground-state MSB. Meanwhile, a type II photoreaction can simultaneously happen between the triplet MSB and ground-state triplet oxygen ($^3O_2$) via energy exchange, after which a more oxidative singlet oxygen ($^1O_2$) and ground-state MSB can be generated. The formed HO·, H_2O_2, and $^1O_2$ are known as ROS, which are lethal to microbes[35]. Based on the photoreaction mechanisms, no MSB is consumed after the reaction cycles. Interestingly, we noticed that the triplet excited state of MSB could also efficiently kill the bacteria even with no hydrogen-donating substrates existed in the system, which will be discussed in the latter sections.

	Hansen Solubility Parameters			
	δD	**δP**	**δH**	**$\delta_{VK3\text{-}Solvent}$**
H_2O	15.5	16.0	42.3	37.4
EtOH	15.8	8.8	19.4	16.0
EtOAc	15.8	5.3	7.2	10.8
$CHCl_3$	17.8	3.1	5.7	10.0
VK_3	19.9	12.2	6.1	-

Table 4.2. Hansen Solubility parameters of VK_3 (structure shown below) to various solvents.

Hansen Solubility Parameters				
	δD	**δP**	**δH**	**$\delta_{AK\text{-}Solvent}$**
H_2O	15.5	16.0	42.3	38.4
EtOH	15.8	8.8	19.4	16.6
EtOAc	15.8	5.3	7.2	10.5
$CHCl_3$	17.8	3.1	5.7	9.80
AK	19.6	12.2	5.0	-

Table 4.3. Hansen Solubility parameters of the aromatic ketone structure of MSB (AK, structure shown below) to various solvents.

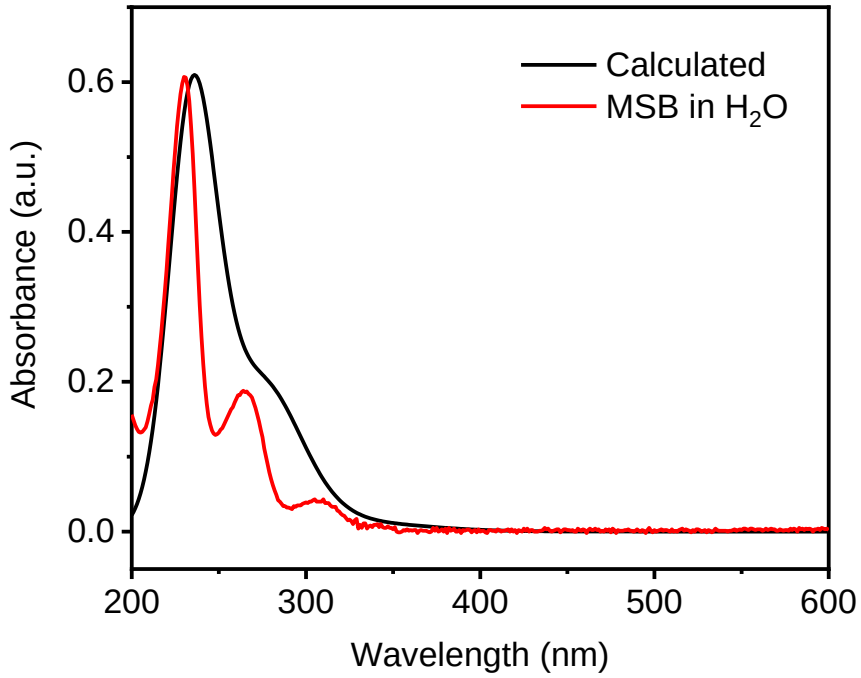

Figure 4.2. Computational and experimental UV-vis spectra of MSB in H_2O (The calculated spectrum was fixed to have the same absorbance peak height as the experimental spectrum).

4.3.2 Photo reactivity of the type I and type II reactions of MSB

To further investigate the type I and type II photoreaction potentials of MSB under photoirradiation, the Gibbs free energy changes (△G) of the two reactions were computed by the Gaussian modeling package[15]. In the type I photoreaction, the hydrogen abstraction reaction is regarded as the critical step determining the photoreaction rate[36]. The △G of the hydrogen abstraction step in type I reaction of MSB was calculated and depicted in Figure 4.3a using EtOH as a hydrogen donor. According to the modeling, the △G of the hydrogen abstraction step is -54.66 kJ/mol, which indicates the feasibility of the hydrogen abstraction reaction between the α C-H of EtOH and the triplet MSB. The electron charges of the carbonyl oxygen before and after the hydrogen abstraction step were also computed as -0.143 and -0.452, respectively. The increased electron charge after the hydrogen abstraction proves that the carbonyl oxygen becomes less electron-deficient due to the addition of the hydrogen atom with a relatively low electronegativity. The △G of the type II reaction of MSB was also computed to be negative, which is -96.93 kJ/mol, indicating that the MSB is a potential singlet oxygen sensitizer under proper photoirradiation.

Based on the proposed photoreaction mechanisms, the MSB should be regenerated after the photoreactions with no consumption regardless of the hydrogen abstraction reaction or the singlet oxygen sensitization. The photostability of 20 μM MSB in H_2O is shown in Figure 4.3b. After UVA (365 nm) irradiation for 60 min, no noticeable change was found in UV-vis spectra, which shows its excellent photostability compared to other vitamin derivatives[37-39]. With increased concentration of MSB (0.2 mM) and the addition of hydrogen donors (EtOH), no apparent absorption peak change was noticed until after 60 min of the UVA exposure. A slight absorption increase shows at around 340 nm was found in Figure 4.4, which can be attributed to the formation of some light-absorbing transient (LAT) structures that can be efficiently quenched by reducing agents or oxygen accompanied with re-formation of aromatic ketone structures, according to

literature[15, 40-41]. Meanwhile, a slight decrease in absorption intensity was noticed at around 270 nm, which can be attributed to the reduction of carbonyl oxygens to alcohol structures that are structurally irreversible to ketones under photoirradiation[15]. These slight changes revealed that only a minority of them could transform to other structures irreversibly, additional evidence of the photostability of MSB.

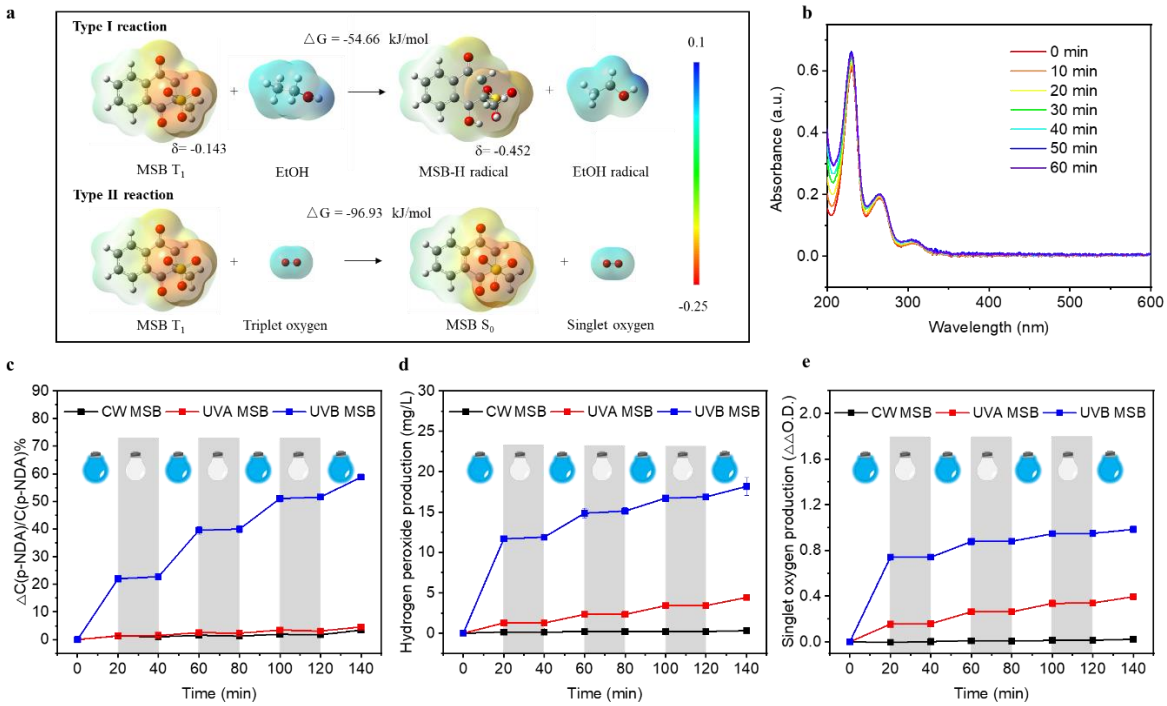

Figure 4.3. Photo-reactivity of type I and type II reactions of MSB. (a) Computed Gibbs energy changes (△G) for the type I and type II photoreactions. (b) UV-vis spectra of 20 μM MSB in H_2O under UVA (365 nm) irradiation after various time durations. Productions of (c) hydroxyl radical and (d) hydrogen peroxide from 20 μM MSB in 10% EtOH/H_2O solution, and I singlet oxygen production from 20 μM MSB in 0.01M PBS solution under UVB (312 nm), UVA (365 nm) and cool white (CW, 370-750 nm) photoirradiation or dark conditions (irradiation in white and dark periods in gray).

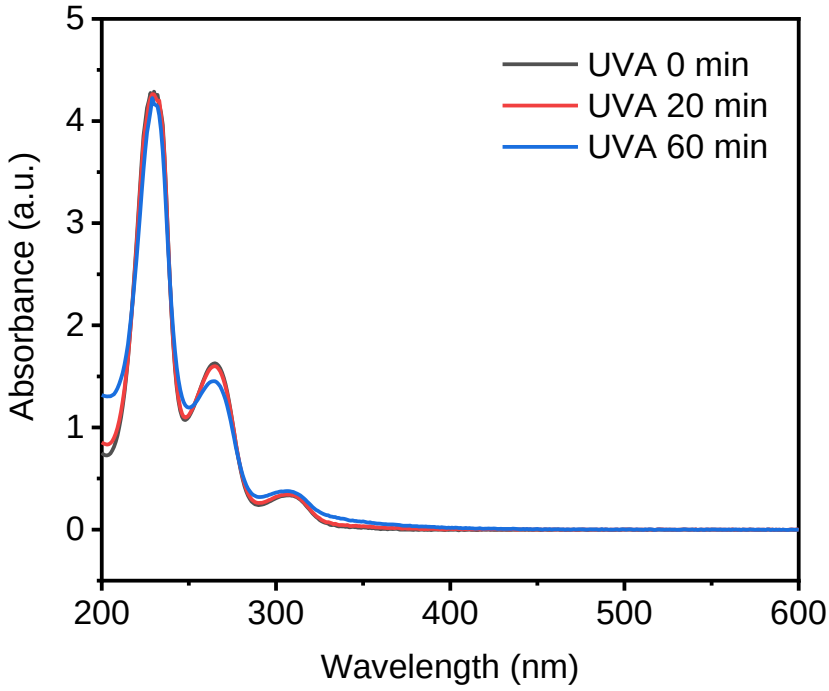

Figure 4.4. UV-vis absorption spectra of 0.2 mM MSB in 10% EtOH/H2O under UVA (365 nm) irradiation.

To demonstrate the photoactivity of MSB predicted by the theoretical modeling, the amounts of reactive oxygen species (hydroxyl radical, hydrogen peroxide, and singlet oxygen) generated by 20 μM MSB in 10% EtOH/PBS solution under irradiations of cool white (CW, 370–750 nm), UVA (365 nm), and UVB (312 nm) lighting sources are depicted in Figures 4.3(c-e). Hydroxyl radicals are generated effectively under the UVB light irradiation, whereas no hydroxyl radical is produced when the light source is removed (Figure 4.3c). MSB shows the strongest photoactivity under the UVB irradiation because of its prominent absorption peaks in the region. Less hydroxyl radical production from MSB is found under the UVA irradiation, and the least under the CW irradiation, which are consistent with the MSB UV-vis spectra with fewer absorption peaks in the UVA region and almost no absorption in the CW region. As comparison tests, the

decomposition of 50 μM p-NDA solution under CW, UVA, and UVB irradiation was studied and shown in Figure 4.5a. No obvious p-NDA decomposition was noticed in these experiments, which demonstrates the photostability of p-NDA under the photoirradiation. The UVB-induced decomposition of 50 μM p-NDA in 20 μM MSB solutions was also studied and shown in Figure 4.5b. No obvious p-NDA decomposition was found in either normal or deoxygenated solution, indicating that the triplet MSB could not chemically react with p-NDA.

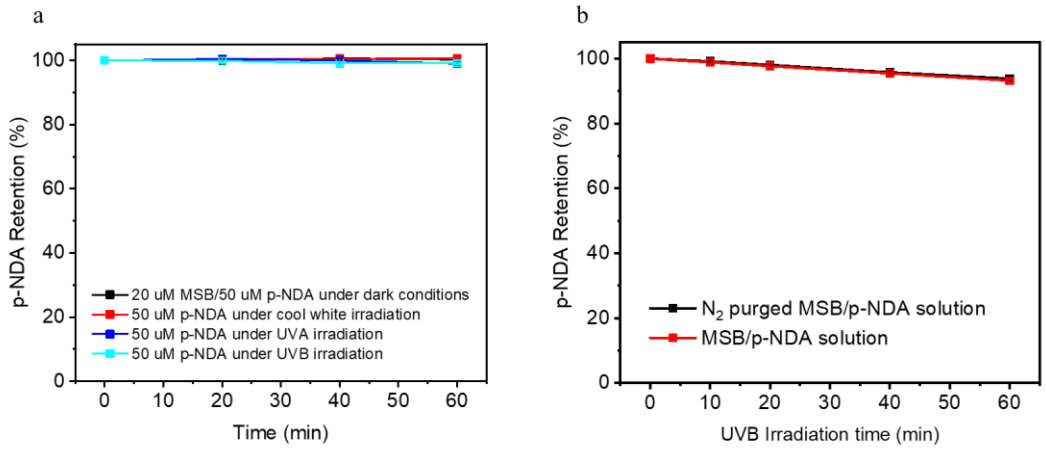

Figure 4.5. (a) p-NDA Photostability under CW, UVA, and UVB irradiation. (b) p-NDA decomposition in MSB solution under UVB irradiation.

Similar results are found in the generations of hydrogen peroxide (Figure 4.3d) and singlet oxygen (Figure 4.3e). UVB (312 nm) always gives the highest amount of ROS production, followed by the UVA (365 nm) irradiation. The CW is the least effective light source in terms of ROS production from MSB. Interestingly, the ROS production from MSB under the UVB irradiation was reduced as testing time prolonged, different from the predicted photo-stability of MSB. Such a phenomenon maybe caused by consumption of the hydrogen donors and ROS detectors in the systems. The formation of irreversible alcohol structures under the robust UVB irradiation could also be one of the possible reasons causing the reduction in ROS production.

According to the proposed photoreaction mechanism, MSB should be capable of generating hydroxyl radical, hydrogen peroxide, and singlet oxygen under photoirradiation via type I and type II reaction without any MSB consumption. The unchanged ROS production slopes (red lines in Figures 4.3c, 4.3d, and 4.3e) during the irradiation periods demonstrate the photostability and reusability of MSB under the UVA photoirradiation.

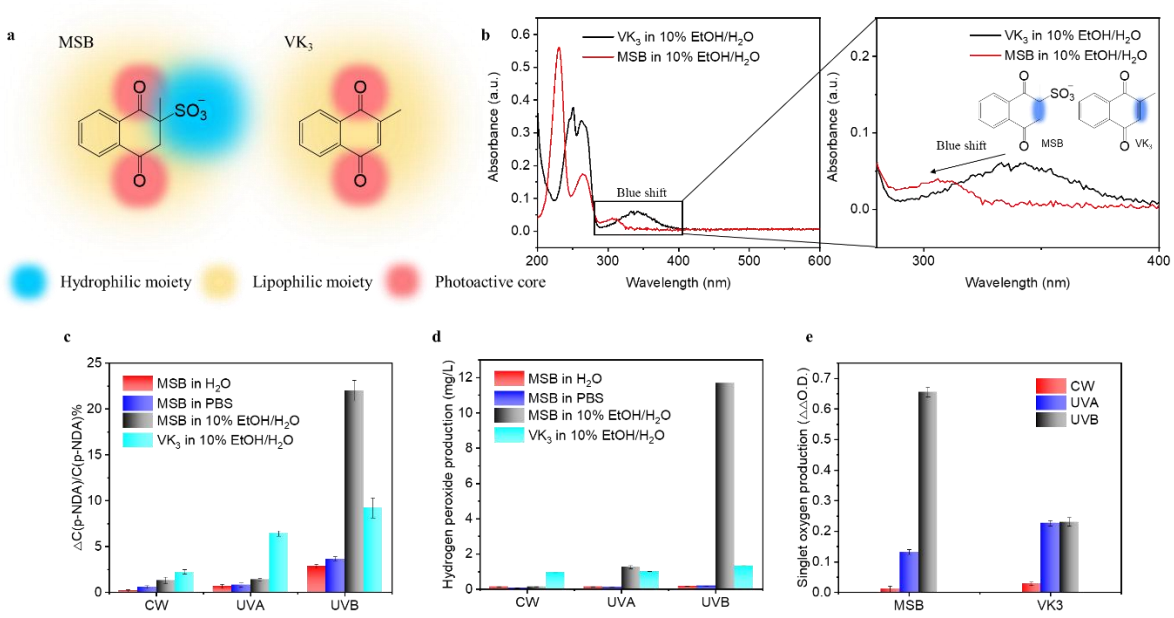

Figure 4.6. ROS production from MSB and VK_3. (a) Chemical structures of MSB and VK_3. (b) UV-vis spectra of 20 μM MSB or VK_3 in 10% $EtOH/H_2O$ solution. Production of (c) hydroxyl radical and (d) hydrogen peroxide from 20 μM MSB or VK_3 in H_2O, PBS, and 10% $EtOH/H_2O$ solutions under the same photoirradiation conditions after 20-min exposure. (e) Singlet oxygen production from 20 μM MSB or VK_3 in 10% EtOH/PBS under the photoirradiation conditions after 20-min exposure.

The ROS production from MSB in various solvent systems was also determined to evaluate the hydrogen donor functions of the chemicals in the type I photoreaction. As a comparison, VK_3 (structure shown in Figure 4.6a) was employed as a reference due to its demonstrated excellent antimicrobial function under various photoirradiation conditions in photo dynamic therapy[11-12]. Figures 4.5c to 4.5e depict the hydroxyl radical, hydrogen peroxide, and singlet oxygen production from 20 μM MSB or VK_3 in several solvent systems. UVB (312 nm) is proven most effective in generating ROS during the photoreaction of both MSB and VK_3, followed by UVA (365 nm). Cool white light (CW) is less effective in triggering the photoreactions for both MSB and VK_3. Almost no ROS is produced from MSB and a small amount from VK_3 under the CW irradiation. The results indicate that very limited triplet states of MSB or VK_3 were formed in a CW exposure environment. MSB shows the highest hydroxyl radical and hydrogen peroxide production in the presence of EtOH, which is employed as a hydrogen donor under the three photoirradiation sources. Much less hydroxyl radical and hydrogen peroxide is produced from MSB when it is in the aqueous systems, for example, water and PBS solutions, proving the mandatory role of the hydrogen donors in the type I photoreaction. VK_3 is more photoactive under the UVA and CW irradiation than MSB, which is because of its higher-conjugated system that enables it to absorb more lights in the UVA and CW regions. The removal of the double bond in VK_3 makes UV absorption of MSB blue shifted, resulting in reduced photo reactivity under the UVA or CW irradiation (Figure 4.6b). Interestingly, under the UVB irradiation, MSB seems to be more reactive than VK_3, leading to much more ROS production. The reason may be that the energy level of the triplet excited state of MSB is higher than that of VK_3 because that the shorter-wavelength excitation light has higher energy. Therefore, the MSB shows excellent potential to be employed in photo-induced antibacterial application in the UVB region due to the produced ROS that are lethal to bacteria.

4.3.3 Photo-induced antibacterial function of MSB.

Gram-negative *Escherichia coli* (*E. coli*) and Gram-positive *Listeria innocua* (*L. innocua*) were employed as the representative microbes to demonstrate the non-selective photo-induced antibacterial functions of MSB, according to literature[15]. Based on the previous analysis, MSB should show the strongest photo reactivity under the UVB irradiation. Therefore, we challenged 2 mM MSB with *E. coli* in 4% EtOH/PBS solution under the UVB irradiation for specific periods. *E. coli* in 4% EtOH/PBS with MSB under dark conditions or in 4% EtOH/PBS without MBS under the UVB irradiation were employed as control groups to exclude any effect caused by the dark toxicity of MBS or the cell-lethality of the UVB irradiation itself. The 4% EtOH/PBS solution causes no bacterial inactivation based on our previous research[8]. According to the Figure 4.7, *E. coli* in 4% EtOH/PBS without MSB under the UVB were completely killed only after 5 min of exposure. However, *E. coli* in PBS with MSB under the UVB remains partially alive after 5 min of irradiation. The complete bacterial inactivation time is delayed to 20 min in the MSB/PBS/UVB group. We infer that the UVB irradiation itself is exceptionally lethal to bacteria in this case. MSB in PBS plays a shielding role like “sunscreen” to protect the bacteria from the UVB irradiation. Although a certain amount of MSB triplet and ROS were produced during the UVB irradiation, their lethality to *E. coli* is much weaker than the direct UVB irradiation. Thus, the addition of MSB in PBS under the UVB actually slows down the inactivation of the bacteria.

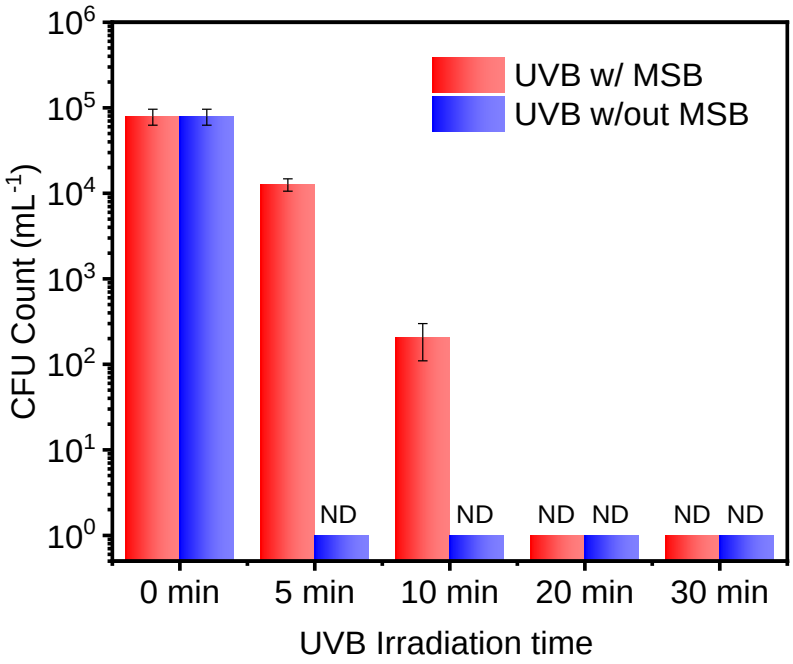

Figure 4.7. UVB (312 nm) induced antibacterial performance of 2 mM MSB in 4% EtOH/PBS against *E. coli*.

Inspired by the ROS production tests mentioned above, the UVA irradiation should also be effective in triggering the photoreactions for MSB to inactivate bacteria due to the ROS formed via the photoreactions. The ROS are reported to be lethal to pathogens by damaging cellular components, such as lipid bilayer membranes, proteins and nuclei acids, through oxidation reactions[35, 42]. Therefore, we challenged 2 mM MSB with *E. coli* and *L. innocua* under the UVA irradiation in 4% EtOH/PBS solution to demonstrate its non-selective antibacterial function. Similarly, bacteria in 4% EtOH/PBS with MSB under dark conditions or in 4% EtOH/PBS without MSB under the UVA irradiation were taken as control groups. Figures 4.7a and 4.7b indicate MSB shows non-selective bacterial inactivation function against both *E. coli* and *L. innocua* under the UVA irradiation. *E. coli* shows a stronger resistance to MSB than *L. innocua* under the UVA

irradiation. In the 4% EtOH/PBS system, around 5-log reduction (99.999%) of *E. coli* bacteria was achieved after 90 min of the UVA irradiation. Meanwhile, it only takes 60 min to completely kill *L. innocua* bacteria under the same circumstance. No dark toxicity of MSB was noticed in these two cases since no apparent bacterial inactivation was found even after 90 min of incubation in a dark environment (the blue bar). Whereas the UVA irradiation shows lethality to bacteria cells to some extend (the red bar). The bacterial inactivation function of the UVA irradiation is not evident until after 60 min of incubation. Bacterial accumulation tests were also performed to show the photostability and reusability of MSB under the UVA irradiation. Figures 4.7c and 4.7d depict the durability of MSB against *E. coli* and *L. innocua* under UVA irradiation in 4% EtOH/PBS solution, respectively. No bacterial inactivation activity decay was found in either *E. coli* or *L. innocua* group, indicating the excellent photo durability of MSB with a constant 99.999% bacterial inactivation efficacy in the presence of hydrogen donors, even after five times of repeated 90-min UVA exposure. To demonstrate the CW-induced bactericidal function of MSB, time-dependent antibacterial tests were also performed. Figures 4.7e and 4.7f depict the bacterial inactivation efficacy of MSB in 4% EtOH/PBS solution under CW irradiation against both *E. coli* and *L. innocua*, respectively. After 90 min of CW irradiation, only a little bacteria inactivation (less than 1-log bacterial reduction) was found in both *E. coli* and *L. innocua* groups, which is much ineffective than that of the UVA-irradiated groups, coinciding with the ROS production tests mentioned in the previous section.

It is worth of noting that MSB is photo-sensitive under UVA irradiation, which is safer than UVB to biomolecules but still could cause damages to tissues and cells, especially under long exposure time. Proper applications of the photo-sensitivity of MSB should be emphasized.

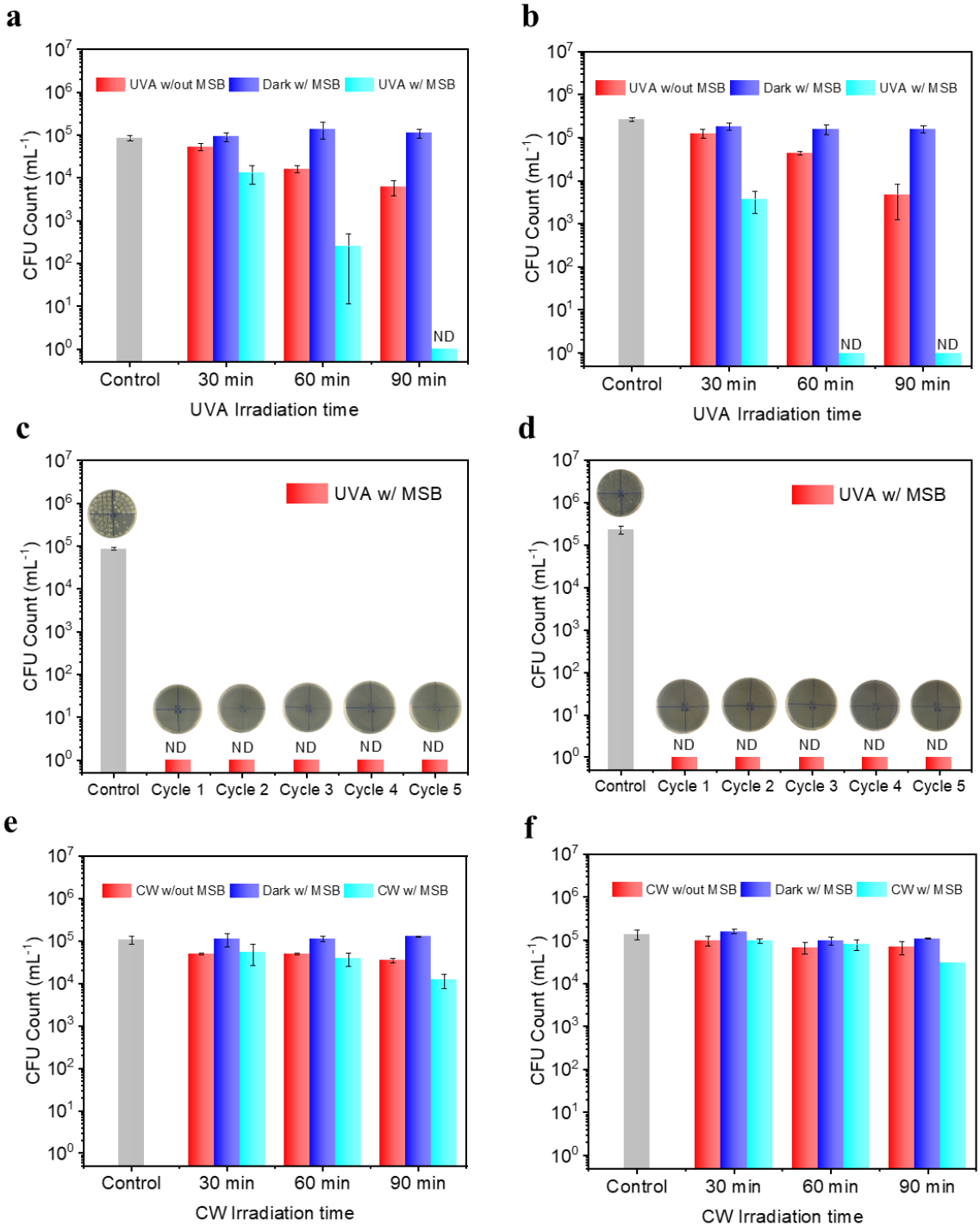

Figure 4.8. Photo-induced antibacterial function of MSB in 4% EtOH/PBS solution. UVA (365 nm) induced antibacterial activity of 2 mM MSB in 4% EtOH/PBS against (a) *E. coli* and (b) *L. innocua*. Five-time cycle bactericidal activity of 2 mM MSB against (c) *E. coli* and (d) *L.*

innocua in 4% EtOH/PBS under UVA (365 nm) irradiation for 90 min. Cool white light (CW) induced antibacterial activity of 2 mM MSB in 4% EtOH/PBS against (e) *E. coli* and (f) *L. innocua***.**

We performed another series of antibacterial tests in PBS solution without addition of any organic solvent to exclude the hydrogen donor effect on the photo-induced antibacterial functions of MSB. Figures 4.8a and 4.8b depict the antibacterial results of MSB in PBS solution against *E. coli* and *L. innocua* under the UVA irradiation, respectively. Interestingly, we found a faster bactericidal rate of MSB in the absence of EtOH, which is a potent hydrogen donor, in PBS under the UVA light. The complete bacterial inactivation time was shortened to 30 min against both *E. coli* and *L. innocua*. Similar phenomena were found in the bacterial accumulation tests, which are shown in Figures 4.8c and 4.8d. The UVA irradiation time in each cycle of the test was shortened from 90 min in the 4% EtOH/PBS solution (Figure 4.8c and 4.8d) to 60 min. The results show that the shortening of the UVA irradiation time does not affect the antibacterial efficacy of MSB in PBS solution. No bacterial function decay was noticed after five times of repeated 60-min of the UVA exposure, indicating a better bacterial inactivation activity of MSB in PBS without existence of hydrogen donors. Since the existence of EtOH in the system could increase production of biocidal ROS, the reduced antimicrobial function in the 4% EtOH solution system is quite strange. According to the literature, such a result may be because that the triplet excited state of MSB could directly damage and degrade proteins or DNAs via direct oxidation reactions or hydrogen abstraction[43]. Effective electron transfer or hydrogen transfer could happen from amino acids and nucleic acids to triplet excited quinones[30, 44-46]. The EtOH in the PBS solution can effectively quench the triplet excited MSB via the type I photoreaction with production of hydroxyl radicals. Coincidently, EtOH is a very good hydroxyl radical quencher as well which can react with both the triplet-state MSB and hydroxyl radicals in the system[47-48]. Therefore, the triplet excited state

of MSB could be a dominant biocide if the generated hydroxyl radicals are not in the vicinity of microorganisms. The CW induced antibacterial performance of MSB in PBS solution also supports this hypothesis. Figures 4.8e and 4.8f depict the bacteria inactivation function of MSB in PBS under CW irradiation. More than one log of bacterial reduction (>90%) was found against both *E. coli* and *L. innocua* in the tests of MSB under the CW irradiation. The bacterial inactivation effect of MSB in PBS is more robust than that of MSB in 4% EtOH/PBS solution after 90 min of CW irradiation. Only a limited amount of ROS is generated from MSB even though in the presence of EtOH in the PBS solution under CW irradiation, indicating the bactericidal function of MSB because of the formation of the triplet excited state. These results indicated that the solvent system may play a significant role in the photo-induced antibacterial process. We thus employed additional organic solvents in the photo-induced antibacterial tests to study the solvent effect in the next section.

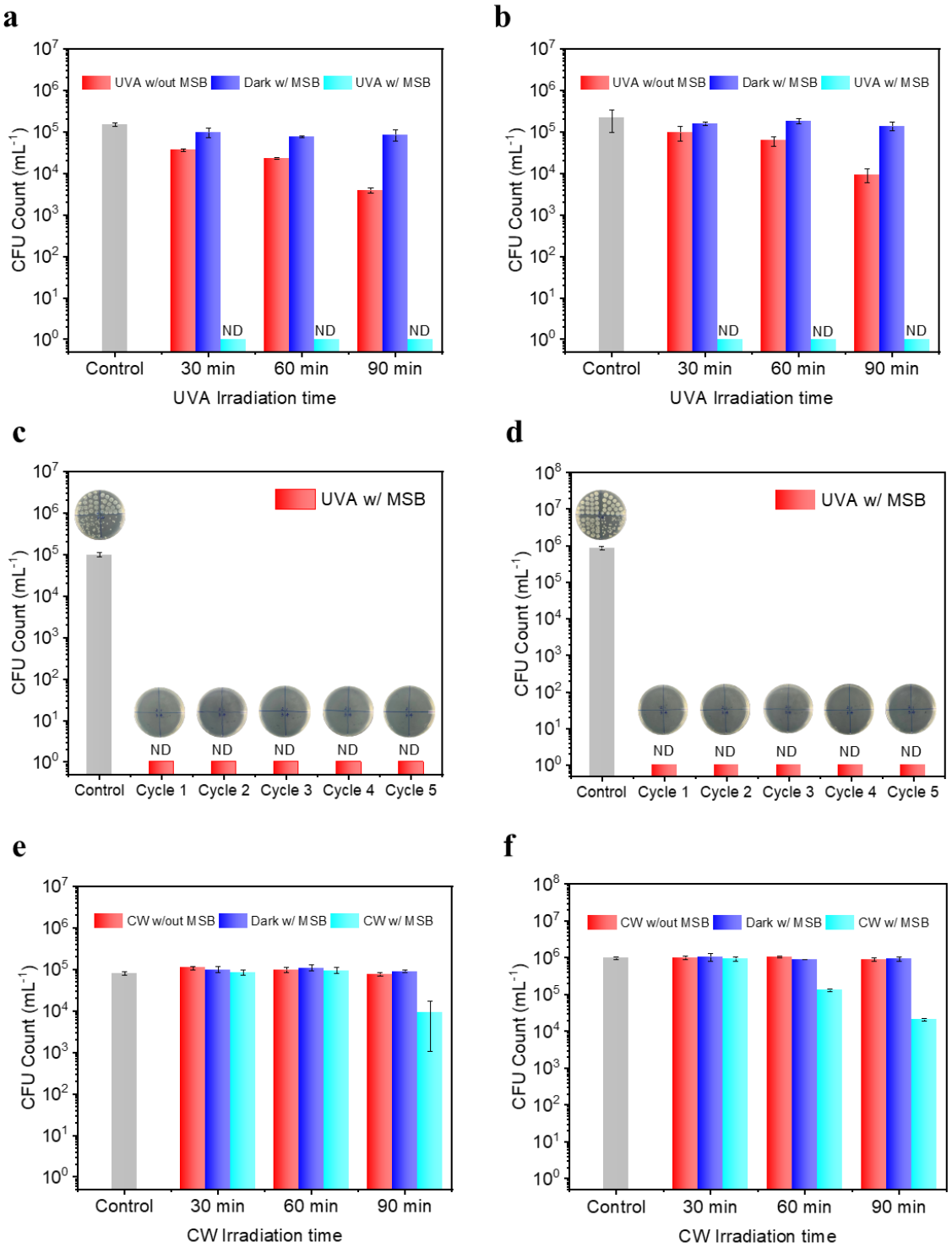

Figure 4.9. Photo-induced antibacterial function of MSB in PBS solution. UVA (365 nm) induced antibacterial activity of 2 mM MSB in PBS against (a) *E. coli* and (b) *L. innocua*. Five-

time cycle bactericidal activity of 2 mM MSB against (c) *E. coli* and (d) *L. innocua* in PBS under UVA (365 nm) irradiation for 60 min. Cool white light (CW) induced antibacterial activity of 2 mM MSB in PBS against (e) *E. coli* and (f) *L. innocua***.**

A live/dead bacterial fluorescence staining assay was employed to demonstrate the bacteria inactivation function of MSB in PBS under the UVA irradiation[15]. The bacteria in PBS with no MSB under dark conditions or in PBS with MSB under the UVA irradiation were first stained with a cell-nonpermeant propidium iodide (PI) red dye, which is only capable of penetrating dead bacteria without intact cell wall structures. The bacteria were then counterstained with a cell-permeant SYBR Green (SG) green dye, which can penetrate both alive and dead bacterial cell walls regardless of the cell wall structures. As shown from Figures 4.9, *E. coli* (4.9a and 4.9b) and *L. innocua* (4.9c and 4.9d) in PBS without MSB nor UVA irradiation remain mostly in green color whereas little in red color, indicating that the majority of the bacteria cells are alive. In sharp contrast, after the UVA irradiation for 60min, *E. coli* (4.9e and 4.9f) and *L. innocua* (4.9g and 4.9h) in PBS with MSB were all stained by the PI dye that is only capable of staining dead bacteria cell, indicating that the bacterial cells in the MSB/UVA group were disrupted by the attack from the ROS and MSB triplet excited states during the UVA irradiation process.

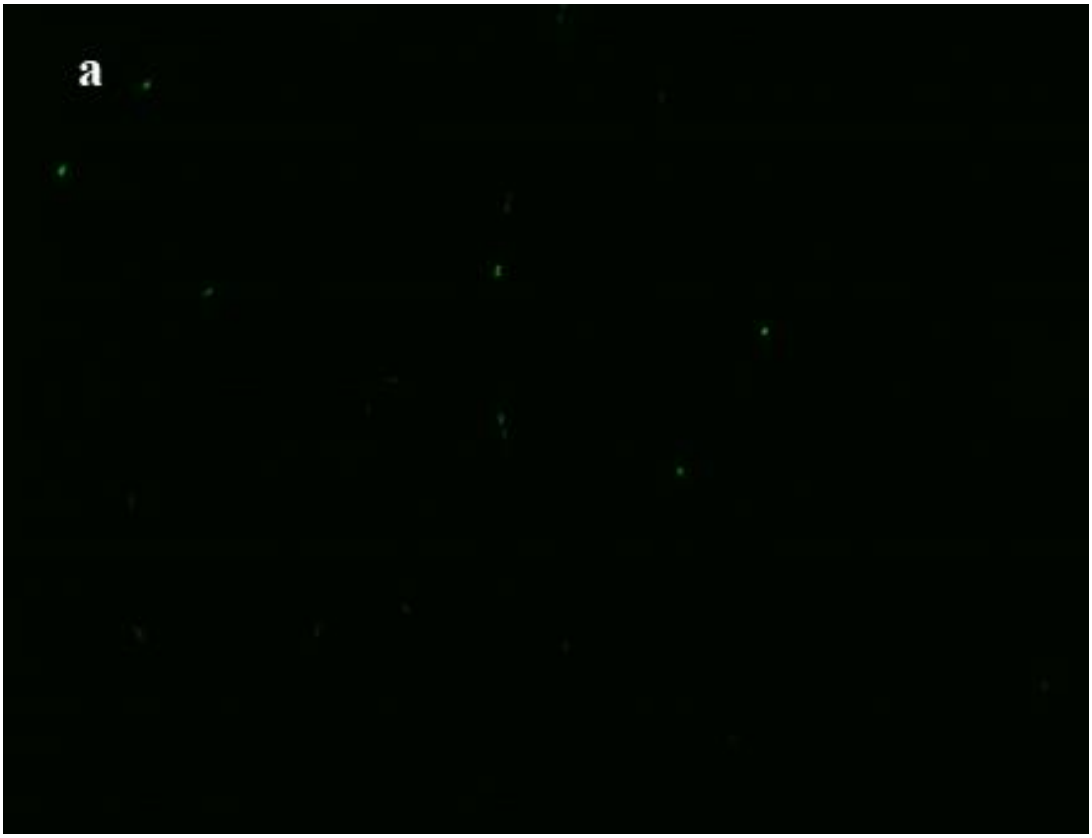
a


b

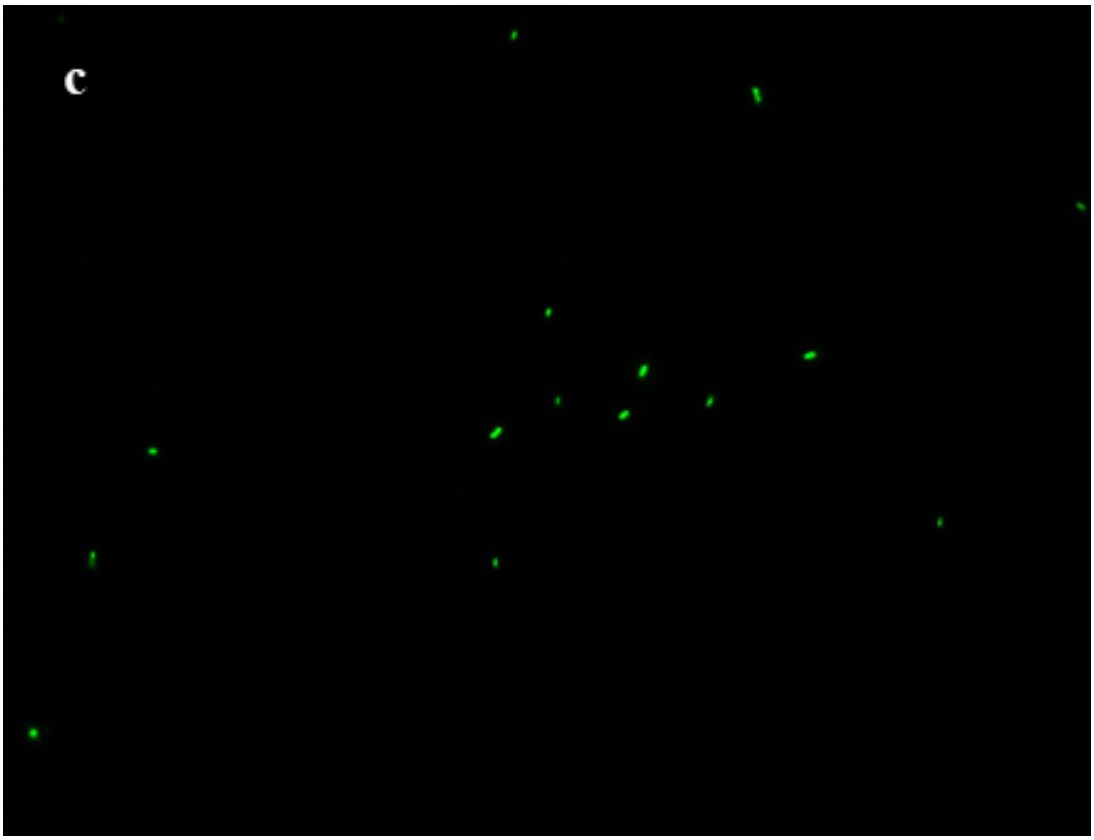
c


d

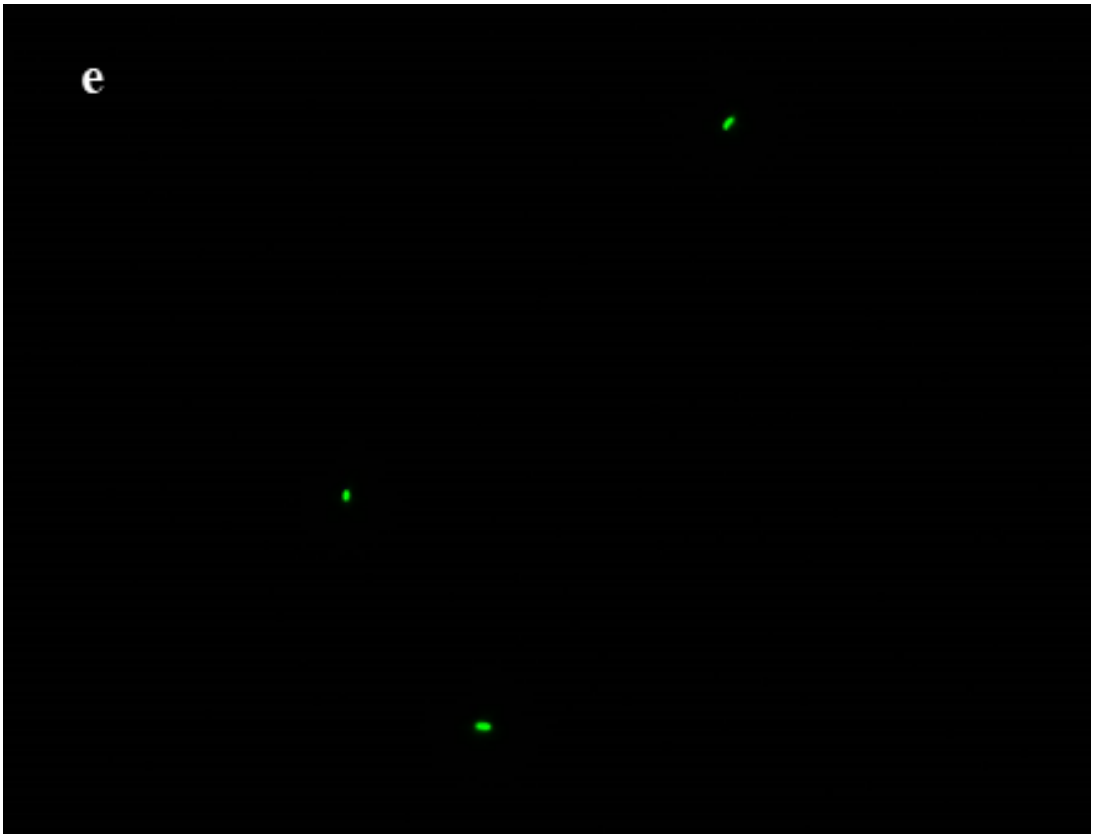
e

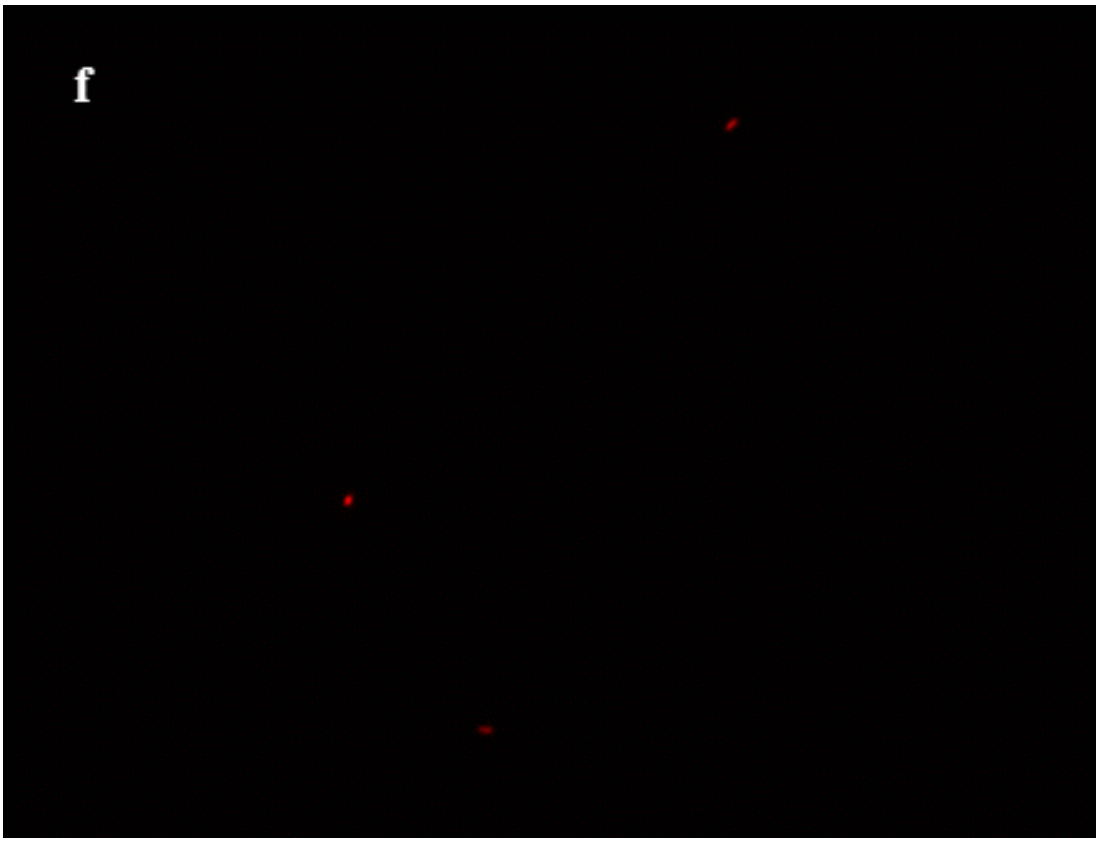
f

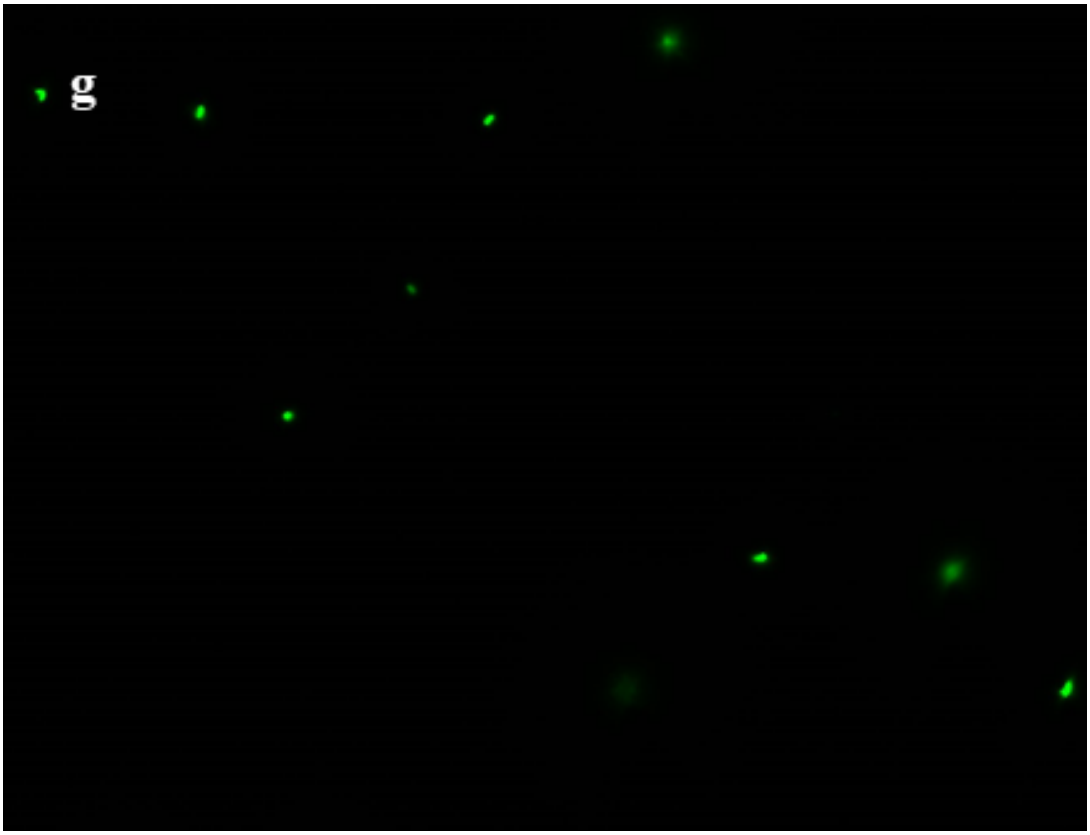
g

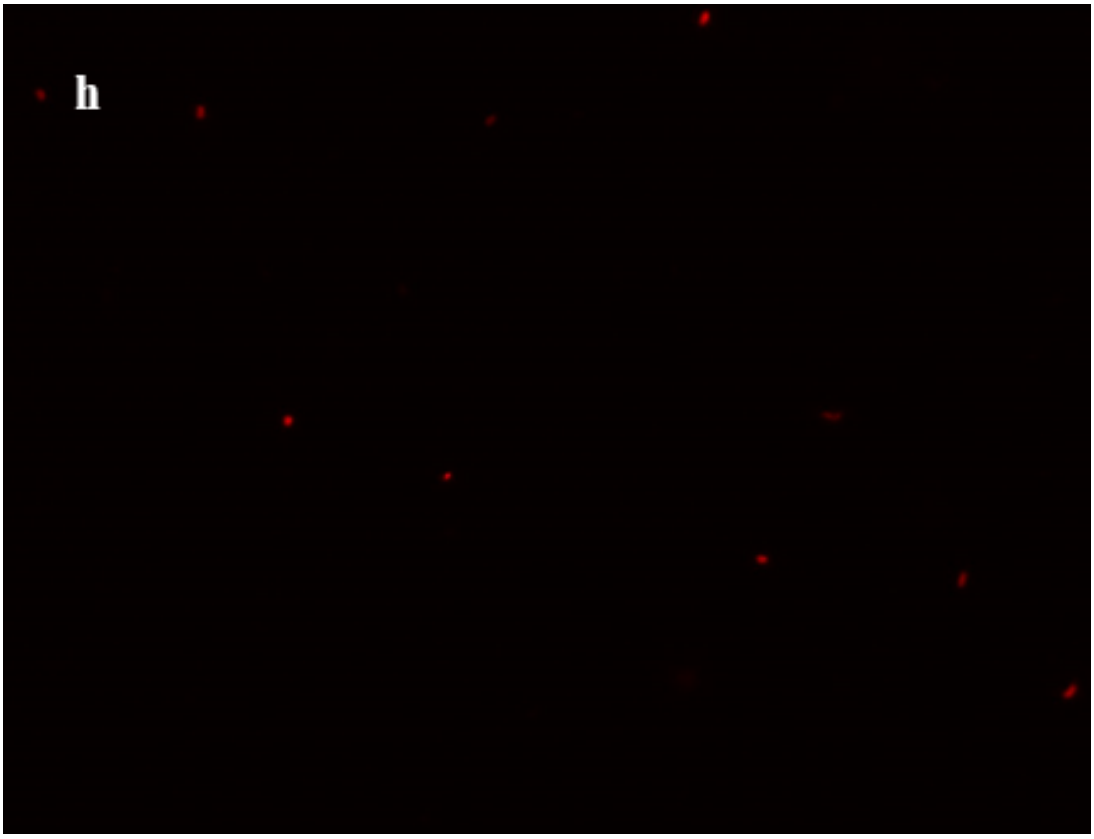
h

Figure 4.10. Fluorescent live/dead bacterial viability assay of *E. coli* (a, b, e, and f) and *L. innocua* (c, d, g, and h) cells in PBS without MSB under dark conditions (a to d) or in PBS with 2 mM MSB (e to h) under UVA (365 nm) irradiation for 60 min.

4.3.4 Solvent effect on the photo-induced function of MSB.

Based on the above analysis, the solvent medium may significantly impact the antibacterial function of MSB during the photo irradiation process. The addition of EtOH in MSB/PBS solution reduced the bactericidal efficacy of MSB under the photoirradiation. A potential question is that whether ethanol is a good triplet state and hydroxyl radical quencher in the system, which lowers the biocide concentration in the solution. Therefore, we employed ethyl acetate (EtOAc) as a substitution for EtOH to perform the same photo-induced antibacterial test. According to Figure 4.11a, MSB in 4% EtOAc/PBS solution gives a faster bacteria inactivation rate than in water or PBS solution without any organic solvent. No apparent difference in bacteria inactivation rate was found on MSB in either water or PBS system, in which most of the bacteria can be efficiently inactivated within 30 min of the UVA exposure, much quicker than that in the 4% EtOH/PBS system. To investigate the triplet states or hydroxyl radical quenching function of EtOH and EtOAc, an organic dye, namely Reactive black 5 (RB, structure is shown in Figure 4.12), was used as a non-specific quencher of triplet excited states and hydroxyl radicals, according to the literature[24]. RB can be non-selectively oxidized by the triplet states or hydroxyl radicals with a color fading that can be quantitively detected by the UV-vis spectrometer. Any addition of organic solvent that can promote the production of hydroxyl radicals could accelerate the decomposition of RB under the photo-irradiation. RB and MSB were dissolved in pure water, PBS, 4% EtOH/PBS solution, or 4% EtOAc/PBS solution to prove the radical quenching effect caused by EtOH or EtOAc. As control groups, RB in pure water, PBS, 4% EtOH/PBS, or 4% EtOAc/PBS without any MSB were

employed to eliminate any photo-bleaching effect from RB itself. As shown in Figure 4.11b, no RB decomposition was found in the absence of MSB, revealing that RB is relatively stable under the UVA irradiation. With the presence of MSB, the UVA-induced decomposition rate of RB is apparently accelerated but remains similar in water, PBS, and 4% EtOAc/PBS systems. A low RB decomposition rate was noticed in 4% EtOH/PBS solution in the presence of MSB under the UVA irradiation, which coincides with the photo-induced antibacterial tendencies shown in Figure 4.11a, and the rate is actually lower than that in the pure water or PBS system, in which the triplet states are dominant biocides due to the limited production of ROS. This result also suggests that the triplet states of MSB in the 4% EtOH/PBS system could be consumed due to the presence of EtOH. The production of hydroxyl radical (Figure 4.11c) and hydrogen peroxide (Figure 4.11d) from MSB in various solvent systems reveal that EtOH is a suitable hydrogen donor and MSB triplet state quencher. In contrast, EtOAc shows very low hydrogen-donating or triplet state quenching capacity, leading to the low production of hydroxyl radicals and hydrogen peroxides in the 4% EtOAc/PBS group. Therefore, the reduced antimicrobial effect of EtOH in PBS solution comes from its quenching capacity to hydroxyl radicals and triplet states, reducing the bactericidal species formed by photo-irradiation of MSB.

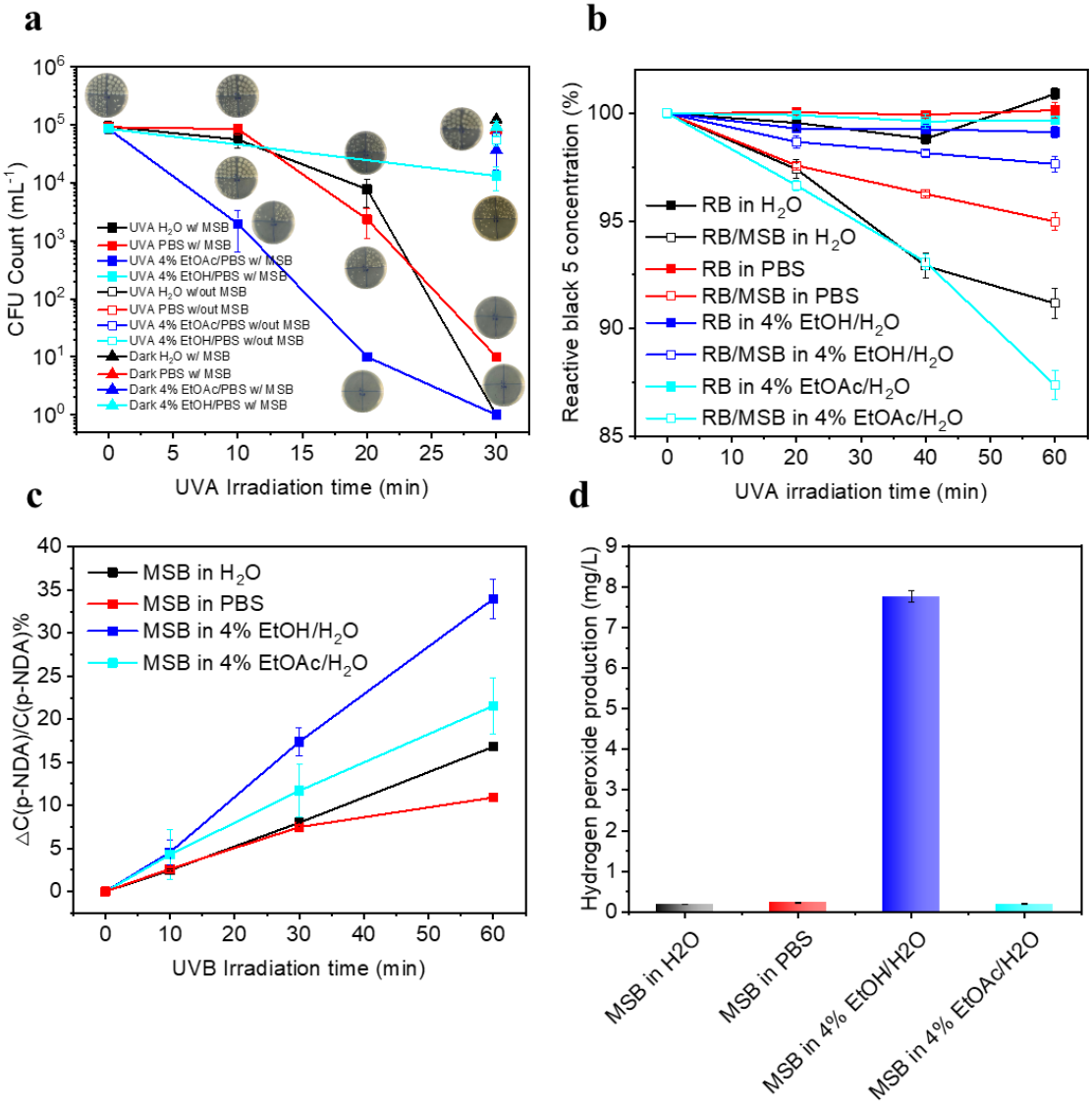

Figure 4.11. Solvent effect on the photo-induced antibacterial function of MSB. (a) UVA (365 nm) induced antibacterial activity of 2 mM MSB in various solvent systems. (b) UVA (365 nm) induced degradation of 20 μM Reactive Black 5 by 0.2 mM MSB in various solvent systems. (c) Hydroxyl radical production from 50 μM MSB in various solvent systems under UVB (312 nm) irradiation. (d) Hydrogen peroxide production from 50 μM MSB in various solvent systems after 20-min UVB (312 nm) irradiation.

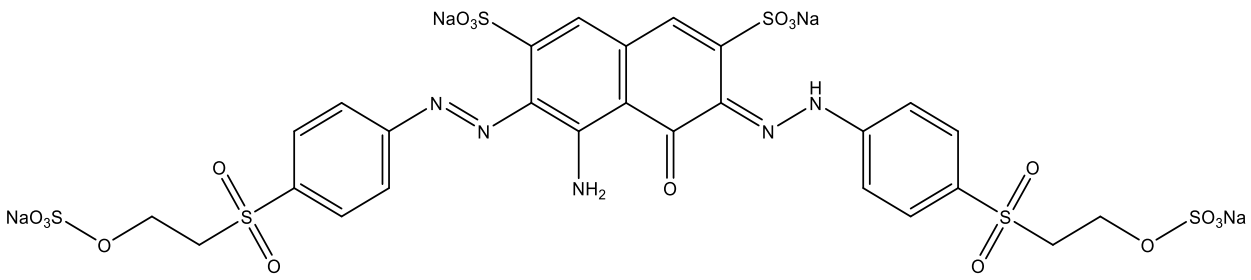

Figure 4.12. Chemical structure of Reactive Black 5.

The evident acceleration effect of EtOAc in the system is another issue to be investigated. According to the literature, organic solvents could improve conversion yields and selectivity of chemical reactions by increasing interactions between reactants and catalyst surfaces[49]. We speculate that the accelerated antimicrobial function of EtOAc in the solution systems is caused by its good affinity with both MSB and *E. coli* bacteria cells, which could serve as a good media by shortening the distance between the bacterial cells and the photoactive aromatic ketones (marked in red in Figure 4.6a) and promoting contacts between the short-lived triplets or ROS with the bacteria cells. The shortened distance enables the biocidal ROS and oxidative triplet states to diffuse effectively to the target microbes[50-52], resulting in more efficient microbial inactivation. Although MSB is known as a water-soluble vitamin K bearing a hydrophilic sulfonate group (marked in blue in Figure 4.6a), MSB was recorded as an amphiphilic compound due to its lipophilic aromatic ketone structure (marked in yellow and red in Figure 4.6a)[53]. As shown in Figure 4.13a, MSB shows an apparent surface tension reduction effect with its concentration gradually increased in solutions. Based on its surface-active feature, the sulfonate group in MSB is hydrophilic, whereas the aromatic ketone part is hydrophobic and prefers to stay in the EtOAc moiety in the solution system. As an evidence of the proposed affinity hypothesis, lipophilic VK_3 was dispersed in 8% EtOH/PBS or 8% EtOAc/PBS solution. Figure 4.13d depicts the solubility and stability of the lipophilic VK_3 in these EtOH and EtOAc solution systems, respectively. VK_3

was dispersed evenly in the EtOH and EtOAc systems at the very initial time without noticeable phase separation or VK_3 aggregation. After 30 min of placement at room temperature, VK_3 in the EtOH system became aggregated and precipitated, while no evident VK_3 precipitation was found in the EtOAc group. The light transmittances of the VK_3/EtOH/PBS and VK_3/EtOAc/PBS systems were also determined and shown in Figure 4.13b. PBS solution without presence of organic solvent nor VK_3 is clear with a 100% transmittance as a reference. The VK_3/EtOAc/PBS system remains clear and has a higher transmittance rate than the VK_3/EtOH/PBS system after 30 min of placement at room temperature, indicating a better affinity between EtOAc and the aromatic ketone structure. Additionally, Hansen Solubility Parameters (HSP) theory was also employed to evaluate the affinity between two substances[54-55]. HSP is widely used to understand the solubility of a chemical in various organic solvents by three parameters, δD for dispersion (van der Waals), δP for polarity (related to dipole moment), and δH for hydrogen bonding. The solubility parameter distance is calculated as the square root of $4\triangle\delta D^2+\triangle\delta P^2+\triangle\delta H^2$, which is a theoretical parameter to evaluate the solubility of a solute in a specific solvent. The HSP results also support the experimental phenomena, which can be referred to in Tables 4.2 and 4.3, in which EtOAc shows better affinity to both VK_3 and the aromatic ketone structure of MSB than EtOH. Accordingly, the accelerated antimicrobial effect of EtOAc was partially proven to be its good affinity to the lipophilic aromatic ketone structure. This can also be demonstrated in the UVA-induced antibacterial test of VK_3 against *E. coli* in 4% EtOH/PBS and 4% EtOAc/PBS solution systems, which could reveal similar tendencies as those in MSB solutions. As shown in Figure 4.13c, EtOH apparently reduces the photo-induced antibacterial efficacy of VK_3 to a large extent, which confirms the radical quenching effect of EtOH. VK_3 in 4% EtOAc/PBS clearly shows a much quicker bacterial inactivation efficacy due to the better stabilization and homogenization function of EtOAc.

Moreover, VK_3 reveals a higher photoactivity than MSB under the UVA irradiation, which coincides with the previous study that VK_3 generates more considerable ROS than MSB, and accordingly, more triplet excited states. The higher antibacterial efficacy of MSB and VK_3 in EtOAc/PBS systems demonstrates the excellent affinity between the EtOAc and aromatic ketone structures.

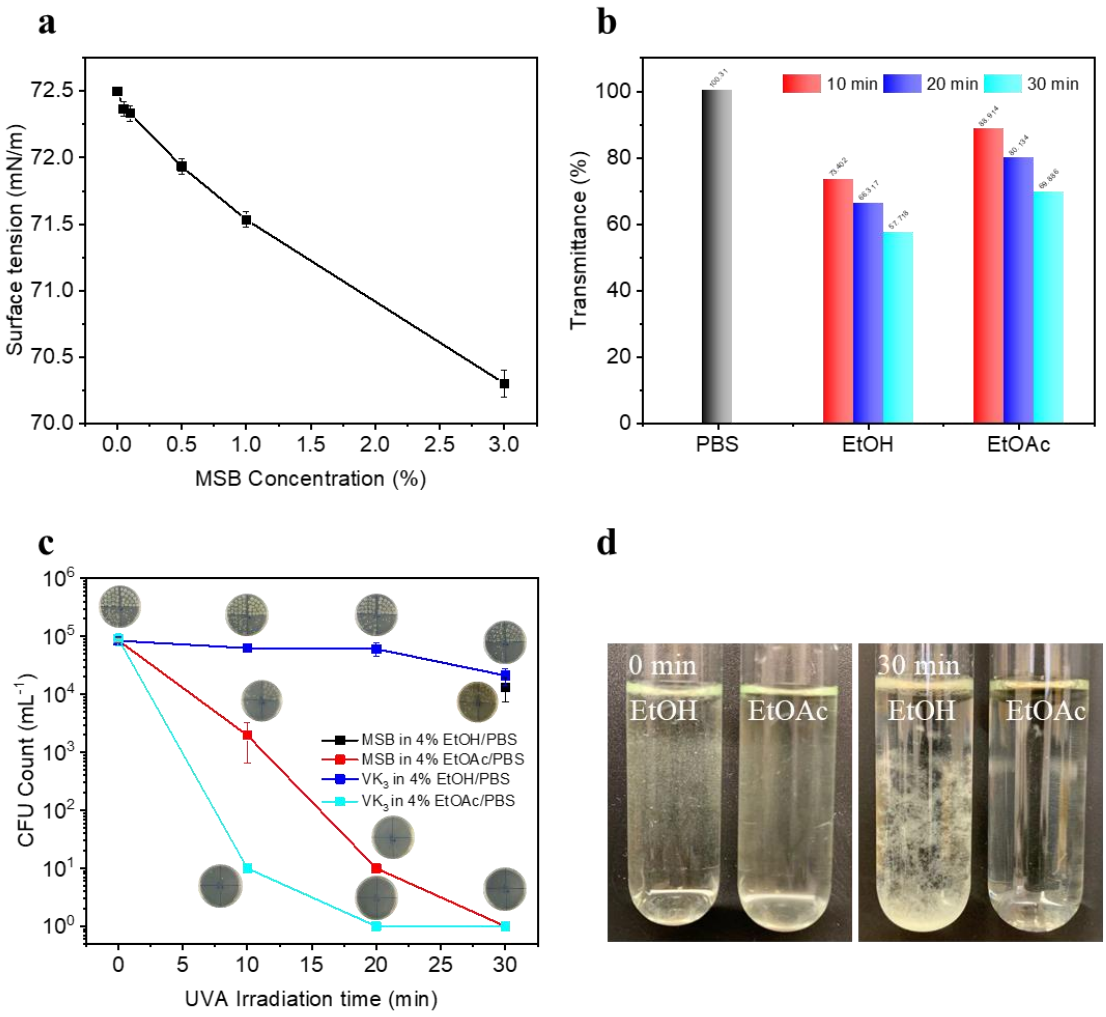

Figure 4.13. Amphiphilicity of MSB and solubility of VK_3 in ethanol and ethyl acetate. (a) Surface tension test with various MSB concentrations in deionized (DI) water. (b) Light transmittance of 2 mM VK_3 in 8% EtOH/PBS and 8% EtOAc/PBS solution systems at 660 nm

after 10 min, 20 min, and 30 min of placement at room temperature. (c) UVA (365 nm) induced antibacterial activities of 2 mM VK_3 and 2 mM MSB in 4% EtOAc/PBS and 4% EtOH/PBS solution systems against *E. coli.* (d) Clarity of 2 mM VK_3 in 8% EtOH/PBS and 8% EtOAc/PBS solution systems at 0 min and 30 min of replacement at room temperature, respectively.

To prove the affinity between bacteria cells and the organic solvent, a bacteria extraction test was performed using either chloroform ($CHCl_3$) or EtOAc as an electron-deficient or an electron-rich solvent, respectively[56-57]. The affinity between the organic solvent and bacteria cells mainly comes from the electrostatic attraction of bacteria cells with a solvent in an oil-water system, according to the literature[58]. The bacteria concentration before and after the extraction by the organic solvent was recorded and converted to a bacteria concentration reduction in percentage. Figure 4.14a depicts the bacteria concentration reduction after mixing *E. coli* in PBS suspension with equal amount of PBS, $CHCl_3$, and EtOAc, respectively. The results show that $CHCl_3$ extracts most of the *E. coli* bacteria cells from PBS, whereas EtOAc shows a weaker extraction effect, indicating that *E. coli* is an electron donor and, therefore, electron-rich. EtOAc shows a slightly better bacterial extraction and bacterial concentration reduction effect than a direct bacterial concentration dilution effect by mixing equal amount of PBS solutions, indicating that *E. coli* has no preference to stay in PBS or EtOAc. The accelerated antimicrobial effect of EtOAc in the MSB systems may be merely due to the better affinity between the organic solvent and photoactive aromatic ketone, which provides closer distance between the bacteria cells and photoactive sites. The dark toxicity of MSB and VK_3 in 4% EtOH/PBS or 4% EtOAc/PBS solutions toward *E. coli* cells also proves the hypothesis. According to the literature, both MSB and VK_3 are capable of penetrating the cell membranes due to the lipophilic aromatic ketone structure they possess[53, 59]. After the cell membrane penetration, MSB or VK_3 can cause an impact on cell metabolism by

engaging in the intracellular redox reaction as redox mediators[17]. Production of various ROS, such as superoxide radical anion and hydrogen peroxide, or oxidation of the NAD(P)H can happen during the redox reaction, resulting in oxidative stress to cell activity. Especially, VK_3 is considered more toxic than MSB because of its stronger promotion effect on the oxidation of NAD(P)H and production of ROS[17]. Figure 4.15 shows less dark toxicity and less bacterial reduction of MSB than VK_3 regardless of in 4% EtOH/PBS or 4% EtOAc/PBS systems. Remarkably, both MSB and VK_3 are more toxic in the 4% EtOAc/PBS than in the 4% EtOH/PBS, leading to more bacterial reduction, which may be because of the better affinity between the *E. coli* bacterial cells and aromatic ketone structures in EtOAc than in EtOH.

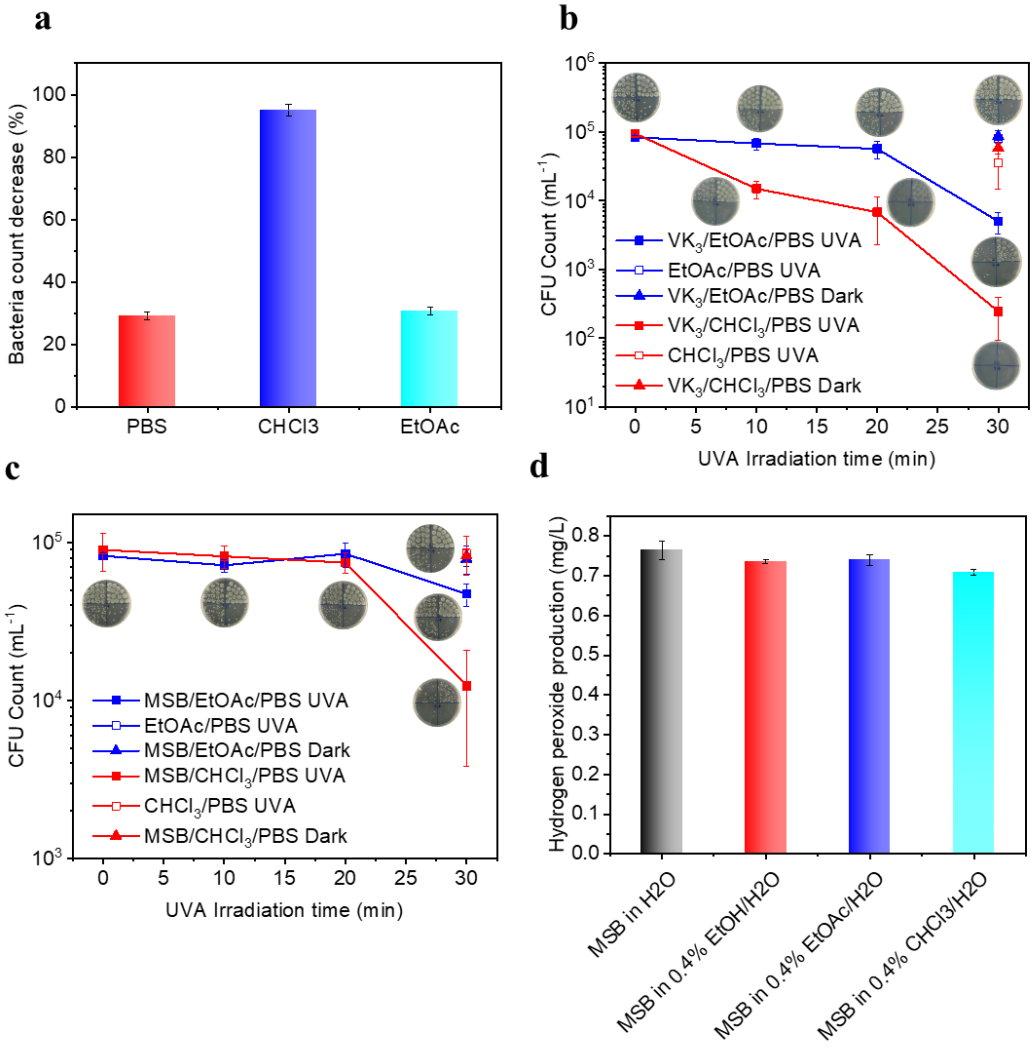

Figure 4.14. The acceleration effect of $CHCl_3$ on MSB antibacterial function. (a) *E. coli* affinity to PBS, $CHCl_3$, and EtOAc. (b) UVA (365 nm) induced antibacterial activity of 0.25 mM VK_3 in 0.4% $CHCl_3$/PBS and 0.4% EtOAc/PBS solution systems. (c) UVA (365 nm) induced antibacterial activity of 0.25 mM MSB in 0.4% $CHCl_3$/PBS and 0.4% EtOAc/PBS solution systems. (d) Hydrogen peroxide production from 0.25 mM MSB in various solvent systems after 20-min UVA (365 nm) irradiation.

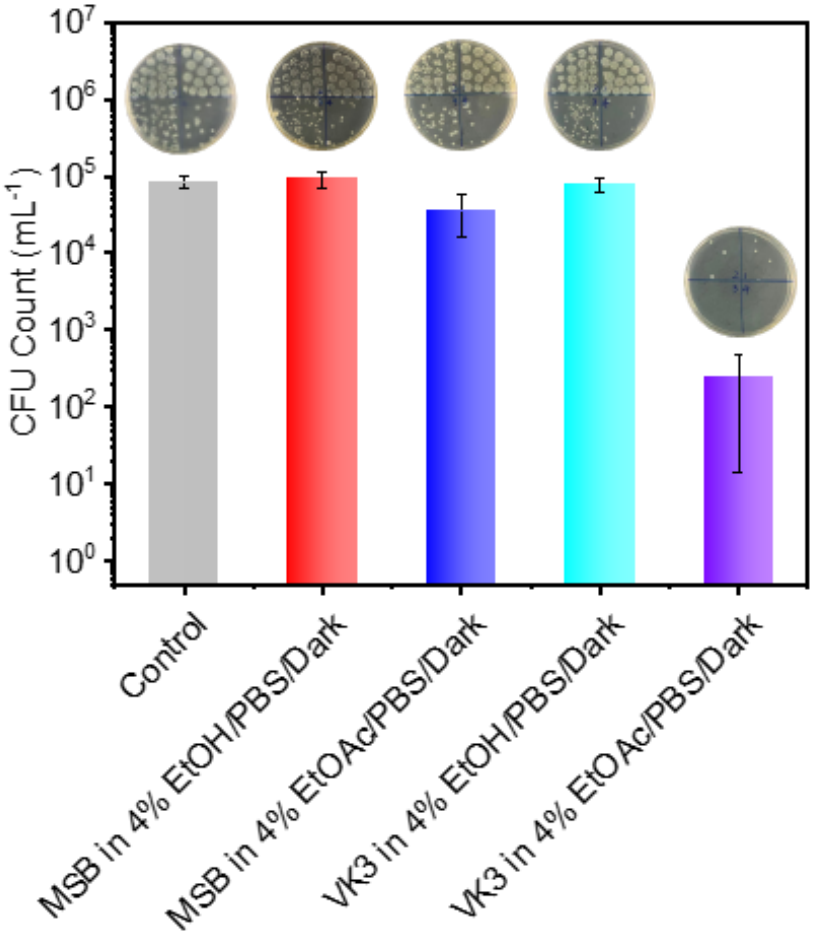

Figure 4.15. Dark toxicity of 2 mM MSB or VK3 toward E. coli in 4% EtOH/PBS and 4% EtOAc/PBS solution systems after 30-min incubation.

Based on the above analysis, $CHCl_3$ should be a better organic solvent than EtOAc, in which the distance between photoactive aromatic ketones and bacteria cells is further closer. Table 4.2 and 4.3 show $CHCl_3$ has a slightly better affinity to aromatic ketone structures than EtOAc. Figure 4.14a also indicates that *E. coli* extremely prefers to stay in $CHCl_3$ than in EtOAc or PBS. In this case, the addition of $CHCl_3$ in PBS should further accelerate the antibacterial rate of MSB and VK_3 under photoirradiation. Figure 4.14b shows an exact accelerating effect of $CHCl_3$ than EtOAc on VK_3 in PBS under the UVA irradiation. In order to eliminate the influence of the dark

toxicity of MSB and VK_3, their concentration was lowered from 2 mM to 0.25 mM. The percentage of chloroform and ethyl acetate in PBS solution was decreased to 0.4% due to the limited solubility of chloroform in water. No pronounced bacterial inactivation was found in the $VK_3/CHCl_3$/PBS solution under dark conditions. Similar accelerating effect of $CHCl_3$ on MSB was also found and depicted in Figure 4.14c. 0.25 mM MSB in 0.4% $CHCl_3$/PBS shows a quicker bacterial inactivation rate than that in 0.4% EtOAc/PBS, which again proves the better affinity between bacteria cells and photoactive aromatic ketone structures in the $CHCl_3$. To get rid of the hydrogen-donating effect of $CHCl_3$, due to its weak C-H bond, hydrogen peroxide production from 0.25 mM MSB in various solvent systems was determined under the UVA irradiation. As shown in Figure 4.14d, no additional hydrogen peroxide production was found in the $CHCl_3$ group, which excludes the hydrogen donating function of $CHCl_3$. The test result coincides with the literature in which $CHCl_3$ is regarded as a lousy hydrogen donor and can hardly quench triplet benzophenone or triplet decafluoro-benzophenone[60]. The latter one is recognized as one of the most oxidative triplet excited states. Herein, we conclude that $CHCl_3$ and EtOAc can tremendously accelerate the photo-induced antibacterial function of MSB by shortening the diffuse distance between the short-lived biocidal active species to bacterial cells, resulting in a more effective bacterial inactivation.

4.4 Conclusion

MSB, a water-soluble vitamin K_3 derivative with low dark toxicity, was proven to be photoactive under various photoirradiation sources. Although UVB is a more powerful source of excitation of MSB, UVA irradiation could primally provide desired triggering force in generating MSB triplets and ROS to inactivate bacteria. MSB showed highly non-selective bacterial inactivation efficacy against both Gram-negative *E. coli* and Gram-positive *L. innocua* (99.999% bacterial reduction) within 30 min of UVA exposure in PBS solution. The bacterial inactivation

function of MSB is durable and can survive five repeated exposures to concentrated bacterial cells and UVA irradiations. More interestingly, organic solvents could significantly affect the photo-induced antibacterial efficacy of MSB. Both $CHCl_3$ and EtOAc could accelerate antimicrobial effects of MSB with the former one apparently better in performance. This effect was proven to be a function of the organic solvent serving as medium for close contacts of MSB and microorganisms, assisting the short-lived ROS and triplet MSB to inactivate the bacterial cells. This work may provide a platform for seeking new sustainable photo-induced antibacterial agents applied in medical and food-related aspects. Meanwhile, the solvent effect may offer some new insights into optimizing antibacterial functions of photo-sensitizers in the practical applications.

4.5 Reference

(1) Vermeer, C. V. Vitamin K: The Effect on Health Beyond Coagulation–an Overview. *Food & Nutrition Research* **2012,** *56* (1), 5329.

(2) Halder, M.; Petsophonsakul, P.; Akbulut, A. C.; Pavlic, A.; Bohan, F.; Anderson, E.; Maresz, K.; Kramann, R.; Schurgers, L. Vitamin K: Double Bonds Beyond Coagulation Insights into Differences between Vitamin K_1 and K_2 in Health and Disease. *International Journal of Molecular Sciences* **2019,** *20* (4), 896.

(3) Booth, S. L. Vitamin K: Food Composition and Dietary Intakes. *Food & Nutrition Research* **2012,** *56* (1), 5505.

. Vitamin K: Food Composition and Dietary Intakes. *Food & Nutrition Research* **2012,** *56* (1), 5505.

(4) van Hylckama Vlieg, J. E.; Veiga, P.; Zhang, C.; Derrien, M.; Zhao, L. Impact of Microbial Transformation of Food on Health—from Fermented Foods to Fermentation in the Gastro-Intestinal Tract. *Current Opinion in Biotechnology* **2011,** *22* (2), 211-219.

(5) Refolo, M. G.; D'Alessandro, R.; Lippolis, C.; Carella, N.; Cavallini, A.; Messa, C.; Carr, B. I. IGF-1R Tyrosine Kinase Inhibitors and Vitamin K_1 Enhance the Antitumor Effects of Regorafenib in HCC Cell Lines. *Oncotarget* **2017,** *8* (61), 103465.

(6) Plaza, S. M.; Lamson, D. W. Vitamin K_2 in Bone Metabolism and Osteoporosis. *Alternative Medicine Review* **2005,** *10* (1), 24-35.

(7) Akbulut, A. C.; Pavlic, A.; Petsophonsakul, P.; Halder, M.; Maresz, K.; Kramann, R.; Schurgers, L. Vitamin K_2 Needs an RDI Separate from Vitamin K_1. *Nutrients* **2020,** *12* (6), 1852.

(8) Zhang, Z.; Si, Y.; Sun, G. Photoactivities of Vitamin K Derivatives and Potential Applications as Daylight-Activated Antimicrobial Agents. *ACS Sustainable Chemistry & Engineering* **2019,** *7* (22), 18493-18504.

(9) Görner, H. Photoprocesses of p-Naphthoquinones and Vitamin K_1: Effects of Alcohols and Amines on the Reactivity in Solution. *Photochemical & Photobiological Sciences* **2004,** *3* (1), 71-78.

(10) Thor, H.; Smith, M.; Hartzell, P.; Bellomo, G.; Jewell, S.; Orrenius, S. The Metabolism of Menadione (2-Methyl-1, 4-Naphthoquinone) by Isolated Hepatocytes. A Study of the Implications of Oxidative Stress in Intact Cells. *Journal of Biological Chemistry* **1982,** *257* (20), 12419-12425.

(11) Xu, F.; Vostal, J. G. Inactivation of Bacteria via Photosensitization of Vitamin K_3 by UV-A Light. *FEMS Microbiology Letters* **2014,** *358* (1), 98-105.

(12) Zhang, Z.; El-Moghazy, A. Y.; Wisuthiphaet, N.; Nitin, N.; Castillo, D.; Murphy, B. G.; Sun, G. Daylight-Induced Antibacterial and Antiviral Nanofibrous Membranes Containing Vitamin K Derivatives for Personal Protective Equipment. *ACS Applied Materials & Interfaces* **2020,** *12* (44), 49416-49430.

(13) Hakli, Ö.; Karapire, C.; Posokhov, Y.; Içli, S. A Study on Photophysical Properties of Some Vitamin K_3 Derivatives. *Journal of Photochemistry and Photobiology A: Chemistry* **2004,** *162* (2-3), 283-288.

(14) Lamola, A. A.; Hammond, G. S. Mechanisms of Photochemical Reactions in Solution. XXXIII. Intersystem Crossing Efficiencies. *The Journal of Chemical Physics* **1965,** *43* (6), 2129-2135.

(15) Si, Y.; Zhang, Z.; Wu, W.; Fu, Q.; Huang, K.; Nitin, N.; Ding, B.; Sun, G. Daylight-Driven Rechargeable Antibacterial and Antiviral Nanofibrous Membranes for Bioprotective Applications. *Science Advances* **2018,** *4* (3), eaar5931.

(16) Zhuo, J.; Sun, G. Antimicrobial Functions on Cellulose Materials Introduced by Anthraquinone Vat Dyes. *ACS Applied Materials & Interfaces* **2013,** *5* (21), 10830-10835.

(17) Yamashoji, S. Different Characteristics between Menadione and Menadione Sodium Bisulfite as Redox Mediator in Yeast Cell Suspension. *Biochemistry and Biophysics Reports* **2016,** *6*, 88-93.

(18) EFSA FEEDAP Panel (EFSA Panel on Additives and Products or Substances used in Animal Feed). Scientific Opinion on the Safety and Efficacy of Vitamin K_3 (Menadione Sodium Bisulphite and Menadione Nicotinamide Bisulphite) as a Feed Additive for All Animal Species. *EFSA Journal* **2014,** *12* (1), 3532.

(19) Pillai, P. B.; Alewynse, M. G.; Benz, S. A. Vitamin K Substances and Animal Feed. https://www.fda.gov/animal-veterinary/safe-feed/vitamin-k-substances-and-animal-feed. (accessed 27 February 2021).

(20) Borges, A. A.; Borges-Perez, A.; Fernandez-Falcon, M. Effect of Menadione Sodium Bisulfite, an Inducer of Plant Defenses, on the Dynamic of Banana Phytoalexin Accumulation During Pathogenesis. *Journal of Agricultural and Food Chemistry* **2003,** *51* (18), 5326-5328.

(21) Jo, Y. S.; Park, H. B.; Kim, J. Y.; Choi, S. M.; Lee, D. S.; Kim, D. H.; Lee, Y. H.; Park, C.-J.; Jeun, Y.-C.; Hong, J. K. Menadione Sodium Bisulfite-Protected Tomato Leaves against Grey Mould via Antifungal Activity and Enhanced Plant Immunity. *The Plant Pathology Journal* **2020,** *36* (4), 335-345.

(22) Guo, X.-Q.; Zhao, Y.-B.; Xu, J.-G. Study on Sensitized Photochemical Fluorescence of Menadione Sodium Bisulfite and Its Application in Pharmaceutics Analysis. *Analytica Chimica Acta* **1997,** *343* (1-2), 109-116.

(23) Sheng, L.; Zhang, Z.; Sun, G.; Wang, L. Light-Driven Antimicrobial Activities of Vitamin K_3 against *Listeria Monocytogenes*, *Escherichia Coli* O157: H7 and *Salmonella Enteritidis*. *Food Control* **2020,** *114*, 107235.

(24) Liu, N.; Sun, G. Production of Reactive Oxygen Species by Photoactive Anthraquinone Compounds and Their Applications in Wastewater Treatment. *Industrial & Engineering Chemistry Research* **2011,** *50* (9), 5326-5333.

(25) Kraljić, I.; Mohsni, S. E. A New Method for the Detection of Singlet Oxygen in Aqueous Solutions. *Photochemistry and Photobiology* **1978,** *28* (4-5), 577-581.

(26) MladenoviĆ, K. G.; GrujoviĆ, M. Ž.; D NIKODIJEVIĆ, D.; ČomiĆ, L. R. The Hydrophobicity of Enterobacteria and Their Co-Aggregation with Enterococcus Faecalis Isolated from Serbian Cheese. *Bioscience of Microbiota, Food and Health* **2020,** *39* (4), 227-233.

(27) Amada, I.; Yamaji, M.; Sase, M.; Shizuka, H. Laser Flash Photolysis Studies on Hydrogen Atom Abstraction from Phenol by Triplet Naphthoquinones in Acetonitrile. *Journal of the Chemical Society, Faraday Transactions* **1995,** *91* (17), 2751-2759.

(28) Fisher, G. J.; Land, E. J. Photosensitization of Pyrimidines by 2-Methylnaphthoquinone in Water: A Laser Flash Photolysis Study. *Photochemistry and Photobiology* **1983,** *37* (1), 27-32.

(29) Mccormick, M. L.; Denning, G. M.; Reszka, K. J.; Bilski, P.; Buettner, G. R.; Rasmussen, G. T.; Railsback, M. A.; Britigan, B. E. Biological Effects of Menadione Photochemistry: Effects of Menadione on Biological Systems May Not Involve Classical Oxidant Production. *Biochemical Journal* **2000,** *350* (3), 797-804.

(30) Görner, H. Electron Transfer from Aromatic Amino Acids to Triplet Quinones. *Journal of Photochemistry and Photobiology B: Biology* **2007,** *88* (2-3), 83-89.

(31) Andreu, I.; Palumbo, F.; Tilocca, F.; Morera, I. M.; Boscá, F.; Miranda, M. A. Solvent Effects in Hydrogen Abstraction from Cholesterol by Benzophenone Triplet Excited State. *Organic letters* **2011,** *13* (15), 4096-4099.

(32) de Lucas, N. C.; Corrêa, R. J.; Garden, S. J.; Santos, G.; Rodrigues, R.; Carvalho, C. E. M.; Ferreira, S. B.; Netto-Ferreira, J. C.; Ferreira, V. F.; Miro, P. Singlet Oxygen Production by Pyrano and Furano 1, 4-Naphthoquinones in Non-Aqueous Medium. *Photochemical & Photobiological Sciences* **2012,** *11* (7), 1201-1209.

(33) Demeter, A.; Horváth, K.; Böőr, K.; Molnár, L.; Soós, T.; Lendvay, G. r. Substituent Effect on the Photoreduction Kinetics of Benzophenone. *The Journal of Physical Chemistry A* **2013,** *117* (40), 10196-10210.

(34) Chen, X.; Wu, F.; Yan, M.; Li, H.-B.; Tian, S. X.; Shan, X.; Wang, K.; Li, Z.; Xu, K. Hyperconjugative Effect on the Electronic Wavefunctions of Ethanol. *Chemical Physics Letters* **2009,** *472* (1-3), 19-22.

(35) Ezraty, B.; Gennaris, A.; Barras, F.; Collet, J.-F. Oxidative Stress, Protein Damage and Repair in Bacteria. *Nature Reviews Microbiology* **2017,** *15* (7), 385.

(36) Michelin, C.; Hoffmann, N. Photosensitization and Photocatalysis—Perspectives in Organic Synthesis. *ACS Catalysis* **2018,** *8* (12), 12046-12055.

(37) Liang, J.-Y.; Yuann, J.-M. P.; Hsie, Z.-J.; Huang, S.-T.; Chen, C.-C. Blue Light Induced Free Radicals from Riboflavin in Degradation of Crystal Violet by Microbial Viability Evaluation. *Journal of Photochemistry and Photobiology B: Biology* **2017,** *174*, 355-363.

(38) Cardoso, D. R.; Libardi, S. H.; Skibsted, L. H. Riboflavin as a Photosensitizer. Effects on Human Health and Food Quality. *Food & Function* **2012,** *3* (5), 487-502.

(39) Guneser, O.; Yuceer, Y. K. Effect of Ultraviolet Light on Water-and Fat-Soluble Vitamins in Cow and Goat Milk. *Journal of Dairy Science* **2012,** *95* (11), 6230-6241.

(40) Du, Y.; Ma, C.; Kwok, W. M.; Xue, J.; Phillips, D. L. Time-Resolved Resonance Raman Identification and Structural Characterization of a Light Absorbing Transient Intermediate in the Photoinduced Reaction of Benzophenone in 2-Propanol. *The Journal of Organic Chemistry* **2007,** *72* (19), 7148-7156.

(41) Barboiu, V.; Avadanei, M. I. Chemical Reactions of Benzophenone Photoirradiated in 1, 2-Polybutadiene. *Journal of Photochemistry and Photobiology A: Chemistry* **2011,** *222* (1), 170-179.

(42) Zaid, A.; Mohammad, F. Methyl Jasmonate and Nitrogen Interact to Alleviate Cadmium Stress in *Mentha Arvensis* by Regulating Physio-Biochemical Damages and ROS Detoxification. *Journal of Plant Growth Regulation* **2018,** *37* (4), 1331-1348.

(43) Teixeira, R. I.; Goulart, J. S.; Corrêa, R. J.; Garden, S. J.; Ferreira, S. B.; Netto-Ferreira, J. C.; Ferreira, V. F.; Miro, P.; Marin, M. L.; Miranda, M. A. A Photochemical and Theoretical Study of the Triplet Reactivity of Furano-and Pyrano-1, 4-Naphthoquionones Towards Tyrosine and Tryptophan Derivatives. *RSC Advances* **2019,** *9* (24), 13386-13397.

(44) Ma, J.-H.; Lin, W.-Z.; Wang, W.-F.; Han, Z.-H.; Lin, N.-Y. Triplet State Mechanism for Electron Transfer Oxidation of DNA. *Journal of Photochemistry and Photobiology B: Biology* **2000,** *57* (1), 76-81.

(45) Ly, D.; Kan, Y.; Armitage, B.; Schuster, G. B. Cleavage of DNA by Irradiation of Substituted Anthraquinones: Intercalation Promotes Electron Transfer and Efficient Reaction at GG Steps. *Journal of the American Chemical Society* **1996,** *118* (36), 8747-8748.

(46) Wagner, J.; Lier, J. E. V.; Johnston, L. Quinone Sensitized Electron Transfer Photooxidation of Nucleic Acids: Chemistry of Thymine and Thymidine Radical Cations in Aqueous Solution. *Photochemistry and Photobiology* **1990,** *52* (2), 333-343.

(47) Das, K. C.; Das, C. K. Curcumin (Diferuloylmethane), a Singlet Oxygen ($^1O_2$) Quencher. *Biochemical and Biophysical Research Communications* **2002,** *295* (1), 62-66.

(48) Green, P.; Green, W. A.; Harriman, A.; Richoux, M.-C.; Neta, P. The Dehydrogenation of Ethanol in Dilute Aqueous Solution Photosensitised by Benzophenones. *Journal of the Chemical Society, Faraday Transactions 1: Physical Chemistry in Condensed Phases* **1988,** *84* (6), 2109-2127.

(49) Paunovic, V.; Ordomsky, V. V.; Sushkevich, V. L.; Schouten, J. C.; Nijhuis, T. A. Direct Synthesis of Hydrogen Peroxide over Au-Pd Catalyst—the Effect of Co-Solvent Addition. *ChemCatChem* **2015,** *7* (7), 1161-1176.

(50) Murai, H.; Jinguji, M.; Obi, K. Activation Energy of Hydrogen Atom Abstraction by Triplet Benzophenone at Low Temperature. *The Journal of Physical Chemistry* **1978,** *82* (1), 38-40.

(51) Maisch, T. Resistance in Antimicrobial Photodynamic Inactivation of Bacteria. *Photochemical & Photobiological Sciences* **2015,** *14* (8), 1518-1526.

(52) Xing, C.; Xu, Q.; Tang, H.; Liu, L.; Wang, S. Conjugated Polymer/Porphyrin Complexes for Efficient Energy Transfer and Improving Light-Activated Antibacterial Activity. *Journal of the American Chemical Society* **2009,** *131* (36), 13117-13124.

(53) Šilkūnas, M.; Saulė, R.; Batiuškaitė, D.; Saulis, G. The Electroporation as a Tool for Studying the Role of Plasma Membrane in the Mechanism of Cytotoxicity of Bisphosphonates and Menadione. *The Journal of Membrane Biology* **2016,** *249* (5), 611-621.

(54) Aghanouri, A.; Sun, G. Hansen Solubility Parameters as a Useful Tool in Searching for Solvents for Soy Proteins. *RSC Advances* **2014,** *5* (3), 1890-1892.

(55) Tamizifar, M.; Sun, G. Control of Surface Radical Graft Polymerization on Polyester Fibers by Using Hansen Solubility Parameters as a Measurement of the Affinity of Chemicals to Materials. *RSC Advances* **2017,** *7* (22), 13299-13303.

(56) Kos, B.; Šušković, J.; Vuković, S.; Šimpraga, M.; Frece, J.; Matošić, S. Adhesion and Aggregation Ability of Probiotic Strain *Lactobacillus Acidophilus* M92. *Journal of Applied Microbiology* **2003,** *94* (6), 981-987.

(57) Semião, A. J.; Habimana, O.; Casey, E. Bacterial Adhesion onto Nanofiltration and Reverse Osmosis Membranes: Effect of Permeate Flux. *Water Research* **2014,** *63*, 296-305.

(58) Hamada, T.; Sameshima, Y.; Honda, K.; Omasa, T.; Kato, J.; Ohtake, H. A Comparison of Various Methods to Predict Bacterial Predilection for Organic Solvents Used as Reaction Media. *Journal of Bioscience and Bioengineering* **2008,** *106* (4), 357-362.

(59) Rawson, F. J.; Downard, A. J.; Baronian, K. H. Electrochemical Detection of Intracellular and Cell Membrane Redox Systems in *Saccharomyces Cerevisiae*. *Scientific Reports* **2014,** *4* (1), 1-9.

(60) Nau, W. M.; Adam, W.; Scaiano, J. Fluorescence Quenching of Azoalkanes by Solvent-Assisted Radiationless Deactivation Involving C-H Bonds. *Chemical Physics Letters* **1996,** *253* (1-2), 92-96.

Chapter 5. Photoactivities of Two Vitamin B Derivatives and Their Applications in the Perpetration of Photo-induced Antibacterial Nanofibrous Membranes

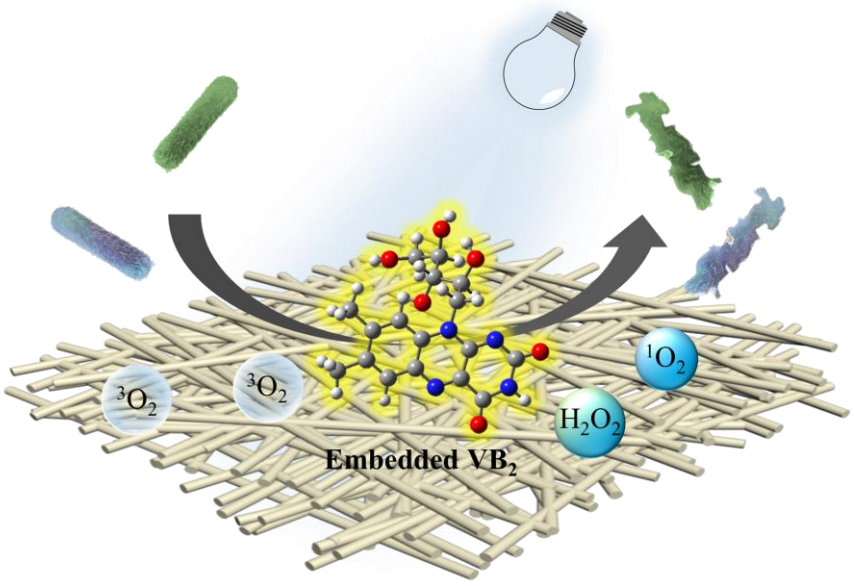

Abstract

Photoactivities of two vitamin B_2 (VB_2) derivatives, riboflavin (RF) and flavin mononucleotide (FMN), were investigated by computational modeling and experiments. Under photoirradiation, the ground-state of both VB_2 derivatives could be excited to their lowest singlet excited states (S_1) that could subsequently transform to the lowest triplet excited states (T_1) via an efficient intersystem crossing (ISC) process. The generated T_1 was oxidative and could undergo type I photoreaction with the accompanied formation of hydroxyl radicals (HO·) and hydrogen peroxide (H_2O_2), or type II photoreaction with the generation of singlet oxygen ($^1O_2$). Especially, the photoreactive site on both VB_2 derivatives was proven to be the nitrogen atoms in the imine (-C=N-) functional group in the isoalloxazine ring. The formed reactive oxygen species (ROS) could non-selectively inactivate microorganisms. However, RF and FMN exhibited negligible

photoinduced antimicrobial activity in PBS solution even at high concentrations. Therefore, a poly (vinyl alcohol-co-ethylene) (PVA-co-PE) nanofibrous membrane blended with RF or FMN was prepared through electrospinning technique and challenged by Gram-negative *Escherichia coli* (*E. coli*) and Gram-positive *Listeria innocua* (*L. innocua*) under UVA (365 nm) irradiation. The fabricated nanofibrous membranes containing VB_2 (VBNFMs) showed great photoinduced antibacterial activity against *E. coli* (99.999% in 20-min UVA irradiation) and *L. innocua* (99% in 20-min UVA irradiation). The photoinduced antimicrobial performance of RF/PVA-co-PE and FMN/PVA-co-PE nanofibrous membranes were comparable. Interestingly, the durability of the photoinduced antibacterial function of the prepared VBNFM was questionable, which might be caused by the photodegradation of VB_2 when presenting in nanomaterials.

5.1 Introduction

Riboflavin (RF), which is also known as vitamin B_2, is a naturally occurring water-soluble vitamin and plays an essential role in human health[1]. Riboflavin is vital in the human body as an antioxidant nutrient that may prevent lipid peroxidation and reperfusion oxidative injury. The insufficient intake of riboflavin may increase the risk of certain cancers such as cervical cancer by inducing its precursor condition[2]. Moreover, riboflavin may exhibit neuroprotective effects in some neurological disorders[3]. It widely exists in diverse food sources, such as milk, cereals, meats, fatty fish, and fruits and vegetables, especially dark-green vegetables[1]. Flavin mononucleotide (FMN) is another vitamin B_2 derivative that is produced enzymatically from riboflavin as a precursor[4]. Unlike RF that is sparingly soluble in water, FMN is highly water-soluble due to the ionic phosphate group in the side chain. Flavin adenine dinucleotide (FAD) is also derivatized from RF as a precursor with the assistance of FAD synthetase[1].

All three vitamin B_2 derivatives have been proven to be photoactive under UVA (330 nm or 370 nm) and UVB irradiation (308 nm) and are capable of generating singlet oxygen ($^1O_2$) with distinctive quantum yields[5]. The photoactivity of vitamin B_2 derivatives is attributed to the isoalloxazine ring that shows strong absorption in both UVA and visible light regions. However, the $^1O_2$ quantum yield of FAD (0.12) is much smaller than that of RF (0.64) and FMN (0.64)[5]. Therefore, FAD should not be an effective photosensitizer under photoirradiation and is thus excluded from this work. Except for the $^1O_2$ generation from RF and FMN via type II photoreaction, some literature reveals the type I photoreaction in RF and FMN through a one-electron transfer or a hydrogen atom abstraction reaction[6]. After the electron transfer or hydrogen abstraction reaction, the reduced VB_2 could be oxidized by ground-state oxygen ($^3O_2$) and generates superoxide radical anion ($\cdot O_2^-$) and H_2O_2. The formed ROS may lead to many lethal effects to live cells including cell-membrane peroxidation and nucleic acid degradation[7]. Unlike vitamin K derivatives, vitamin B_2 derivatives do not have the aromatic ketone structure yet still possess photoactivity in generating ROS, which should be attributed to the nitrogen atoms in the imine group in the isoalloxazine ring[7]. The goal of this work was to further explore and identify the photochemistry of VB2 derivatives. The detailed photochemistry of vitamin B_2 derivatives is discussed in this work, and the carbonyl group in the structure is shown not to be the photoactive center based on the computational modeling.

Inspired by the ROS production from vitamin B_2 derivatives, they have been applied in the fabrication of food-packaging materials to prevent oxygen or to inactive microorganisms under photoirradiation[8]. Some transition metal nanoparticles are synthesized with RF to prepare up-conversion photoactive functional materials to kill tumor cells in photodynamic therapy (PDT)[9]. Likely, free RF or FMN was dissolved in PBS solution to inactivate Gram-negative *E. coli* and

Gram-positive *L. innocua* under UVA irradiation in this work. Interestingly, no apparent bacterial reduction was found after long-period UVA exposure, which could be attributed to the long distance between the bacteria and the isoalloxazine ring in the solution weakening the diffusion and function of the short-lived ROS. In this case, RF or FMN was further blended in PVA-co-PE nanofibrous membrane and challenged by the bacteria. Certain bacterial inactivation was found after 20-min UVA irradiation. The distinct photoinduced antibacterial tests reveal that the diffusion of ROS to target microbes is the predominant factor that could affect the antibacterial efficacy of both Rf and FMN. A contact antibacterial method is needed for the vitamin B_2 derivatives, which is contradicted to the vitamin K derivatives that could inactive microbes either in solutions or in materials. This work may provide some insights into developing vitamin B_2 containing photoactive materials in photoinduced antimicrobial related applications.

5.2 Experimental Methods

5.2.1 Materials

Riboflavin (RF), menadione sodium bisulfite (MSB), ethyl alcohol (EtOH), ethyl acetate (EtOAc), L-histidine, potassium iodide, sodium hydroxide, ammonium molybdate tetrahydrate, potassium hydrogen phthalate, sodium phosphate dibasic, potassium phosphate monobasic, sodium chloride, potassium chloride, methylene blue (MB), poly (vinyl alcohol-co-ethylene) (PVA-co-PE, ethylene content of 27 mol%), isopropanol, and 2% osmium tetroxide (OsO_4) aqueous solution were purchased from Sigma-Aldrich (St. Louis, MO, USA). Flavin mononucleotide (FMN) was purchased from Spectrum Chemical (New Brunswick, NJ, USA). p-Nitroso-N, N-dimethylaniline (p-NDA) was purchased from TCI Co. LTD (Tokyo, Japan). Luria-Bertani (LB) broth, LB agar, tryptic soy broth (TSB), and tryptic soy agar (TSA) were purchased

from Thermo Fisher Scientific (Waltham, MA, USA). All the chemicals and supplies were used as received without any further purification.

5.2.2 Computational details

The computational modeling was carried on a computational platform using the software package Gaussian 09 ver. 08. The ground-state and triplet-state geometries of anionic FMN, hydro-FMN radical (FMN-H·), and reduced dihydroflavin ($FMNH_2$) were optimized at the unrestricted DFT-B3LYP/6-31G+ (d,p) level of theory in the polarizable continuum model (PCM) using the integral equation formalism variant (IEFPCM) in H_2O solvent model. The ground-state or triplet-state geometry of neutral molecules (ethanol, ethanol radical, lumichrome, lumiflavin, RF, RF-H·, and RFH_2) was optimized at the unrestricted DFT-B3LYP/6-31G (d,p) level of theory in the PCM-IEFPCM in H_2O model. The excited anionic FMN and excited RF were further computed at the restricted TDDFT-B3LYP/6-31G+ (d,p) level and the restricted TDDFT-B3LYP/6-31G (d,p) level of theory in the IEFPCM-H_2O solvent model, respectively. The Gibbs free energies of anionic and neutral molecules were obtained by frequency calculations at the DFT-B3LYP/6-31G+ (d,p) and the DFT-B3LYP/6-31G (d,p) level of theory in the IEFPCM-H_2O solvent, respectively. The ESP-mapped electron densities of the ground-state and triplet-state anionic FMN (or FMN-H·) and RF (or RF-H·) were obtained at the DFT-B3LYP/6-31G+ (d,p) level and the DFT-B3LYP/6-31G (d,p) of theory in the IEFPCM-H_2O solvent model, respectively. The total electron density was further plotted and mapped with ESP-derived charges to reveal the electron distribution of the out layer of the molecules.

5.2.3 Measurement of UV-vis spectra of RF and FMN

The UV-vis spectra of 20 μM RF or FMN in water was obtained from a UV-vis spectrometer (Evolution 600, Thermo Fisher Scientific). The photostability of RF and FMN was also measured by using the UV-vis spectrometer. Twenty micromolar (μM) RF or FMN in H_2O was placed under UVA (365 nm) or cool white (CW, 370-750 nm) irradiation. The UV-vis absorption spectra of RF or FMN under one-hour photo irradiation were recorded after every 10 min.

5.2.4 Measurement of hydrogen peroxide

The hydrogen peroxide produced by RF and FMN was quantitively measured by an indirect method reported in the literature[10]. Twenty micromolar (μM) RF or FMN was dissolved in H_2O and placed under photoirradiation or dark conditions. After each specific duration, 1 mL of sample solution was mixed with 1 mL of reagent A [Potassium iodide (66 g L^{-1}), sodium hydroxide (2g L^{-1}), and ammonium molybdate tetrahydrate (0.2 g L^{-1}) in water] and 1mL of reagent B [Potassium hydrogen phthalate (20g L^{-1}) in water]. The mixture was vigorously vortexed for 10 seconds to make the mixture homogeneous. The mixture was then placed in a dark environment to allow the reaction to complete. The accumulated hydrogen peroxides produced by RF or FMN were quantified by referring to the UV-vis absorption spectrum with a maximum absorption peak at 351 nm. As a reference, 1 mL of the sample solution was mixed with 2 mL of H_2O to eliminate the color influence on the H_2O_2 absorption caused by the inherent color of VB_2 derivatives.

5.2.5 Measurement of singlet oxygen

The singlet oxygen generated by RF or FMN was measured by using a widely used singlet oxygen quenching method reported in the literature[11-12]. Two μM RF or FMN was dissolved in 5 mL of 0.01 M PBS solution. Ten millimolar (mM) L-histidine was also dissolved in the solution

to quench the generated singlet oxygen by forming a transannular intermediate that could subsequently react with p-NDA (50 μM), leading to a color fading that could be detected at 440 nm by UV-vis spectrometer. The additional p-NDA consumption in the L-histidine-containing solution comparing to the L-histidine-free solution was taken as the singlet oxygen production. The singlet oxygen production comparison between FMN and methylene blue (MB) was also performed. Twenty μM FMN or MB was dissolved in 5 mL of 0.01 M PBS solution with 0.01 M L-histidine. The singlet oxygen production from FMN or MB was recorded after 20, 40, and 60 min of UVA or CW irradiation.

5.2.6 Fabrication of RF/PVA-co-PE and FMN/PVA-co-PE nanofibrous membranes

The photoactive VBNFMs were prepared by using the electrospinning technique. PVA-co-PE polymer particles were dissolved in a mixture solvent of isopropanol and water (weight ratio=7:3) at 85 °C with stirring for 6 hours to obtain a PVA-co-PE polymer solution in a concentration of 7% in weight. RF (0.5 wt% of the polymer) was then added into the polymer solution and mixed thoroughly. Similarly, FMN (same mole content as RF) was added to the polymer solution to obtain FMN blended PVA-co-PE polymer solution. The VB_2/PVA-co-PE polymer solution was filled in four 20-mL syringes with metallic needles. The solution feeding rate was controlled by a syringe pump (Kent Scientific) and set up at the speed of 2 mL h^{-1}. A high voltage electrostatic source of 28 kV (EQ30, Matsusada Inc.) was applied to the metallic needles. The formed electrospun nanofibrous membrane was collected on a roller covered by wax paper. The tip-to-roller distance was controlled at 15 cm. Fabricated membranes were then directly used in the following tests.

5.2.7 Bacterial culture

Two types of generic bacteria, Gram-negative *Escherichia coli* (LJH-1247) and Gram-positive *Listeria innocua* (ATCC 33090), were used in this study to demonstrate the photoinduced non-selective antibacterial activity of RF and FMN. An *E. coli* colony was cultivated in 10 mL of LB broth at 37 ℃ for 18 h. A bacterial suspension of approximately 1×10^9 CFU mL^{-1} was obtained accordingly. The *E. coli* suspension was further diluted to around 1×10^7 CFU mL^{-1} as stock bacterial suspension for the following antibacterial tests. Similarly, an *L. innocua* colony was cultivated in 10 mL of TSB broth at 37℃ for at least 24 h. A bacterial suspension of around 1×10^9 CFU mL^{-1} was obtained. The *L. innocua* suspension was diluted to around 1×10^8 CFU mL^{-1} as stock bacterial suspension for the following photoinduced antibacterial tests.

5.2.8 Antibacterial tests

A stock solution of FMN (50 mM), RF (10 mM), or methylene blue (10 mM) was freshly prepared before the photoinduced antibacterial test. The stock solution should be kept in dark and at a low temperature to avoid any photooxidation. To determine the concentration effect of VB_2 on the photoinduced antibacterial activity, RF or FMN stock solution was first diluted to following concentrations of 0, 0.1, 0.25, 0.5, 1, 2, and 4 mM in PBS solution. After that, 10 μL of *E. coli* stock suspension was added to RF or FMN solutions of different concentrations and placed under UVA irradiation for 30 min. The surviving bacteria were enumerated by serial dilatation and plating on LB agar. Colonies were counted after 24 hours of incubation at 37 °C. To determine the impact of different solvent medium, 10 μL of *E. coli* or *L. innocua* suspension was added to 2 mM FMN in 1 mL PBS solution or 4% EtOH/PBS solution and placed under UVA irradiation or dark conditions for 30 min, 60 min, and 90 min. Then the bacteria suspension was serially diluted and plated on LB agar (for *E. coli*) or TSA agar (for *L. innocua*) for the bacterial enumeration.

To evaluate the electro-static effect between the antimicrobial agent and bacteria, 2 mM Methylene blue in 1 mL PBS solution was also challenged by 10 μL of *E. coli or L. innocua* stock suspension under UVA or CW irradiation for 60-min. The bacteria suspension after photoirradiation or dark reservation was serially diluted and plated on LB agar (for *E. coli*) or TSA agar (*L. innocua*) for the bacterial enumeration. 10 μL of *E. coli* stock suspension was added to 2 mM FMN, 2 mM MB, and 2 mM FMN+2 mM MB in PBS solution and placed under UVA irradiation for 30 min. The bacteria suspension was serially diluted and plated on LB agar for the bacterial enumeration.

Ten microliters (μL) of *E. coli or L. innocua* stock suspension was uniformly applied on the surface of 2×2 cm^2 RF/PVA-co-PE or FMN/PVA-co-PE nanofibrous membranes and placed under UVA or CW irradiation for 5, 10, 15, or 20 min. After each time point, samples were washed with 1 mL of PBS solution and vortexed vigorously for 1 min to harvest the bacteria from the membranes. The collected bacteria were serially diluted and plated on LB agar (for *E. coli*) or TSA agar (*L. innocua*) for the bacterial enumeration.

For the UVA-induced antibacterial durability test, 10 μL of the *E. coli* stock suspension was uniformly applied on the surface of five-group RF/PVA-co-PE or FMN/PVA-co-PE nanofibrous membranes in the size of 2 × 2 cm^2. After the first-round 20-min UVA irradiation, the bacteria on the first-group nanofibrous membranes were harvested and cultivated on LB agar plates for further plate counting assay. Another fresh 10 μL bacteria stock suspension was applied to the remaining four groups to carry on the second-round UVA irradiation. The same process was performed another 3 times to complete the antibacterial durability test. After each round, the bacteria collected from nanofibrous membranes were serially diluted ($\times 10^0$, $\times 10^1$, $\times 10^2$, and $\times 10^3$) and plated on LB agar for the bacterial enumeration. The agar plates were further cultured at 37 ℃

for 18 h. The bacterial inactivation durability of the VB_2 containing PVA-co-PE nanofibrous membranes was accessed by plate counting assay.

5.2.9 SEM images of nanofibrous membranes

The SEM images of PVA-co-PE, RF/PVA-co-PE, FMN/PVA-co-PE nanofibrous membranes were obtained from a Quattro S SEM (Thermo Scientific). The nanofibrous membranes were placed on copper tape and then coated with gold before SEM images capture.

5.2.10 SEM images of bacteria

10 μL of 1×10^9 CFU mL^{-1} *E. coli* or *L. innocua* suspension was evenly applied to the VBNFMs in a size of 2×2 cm^2. The samples were placed under UVA irradiation for 30 min. After that, the bacteria on the sample nanofibrous membranes were firstly harvested by vigorous vortex for 3 min. The bacteria suspension was then centrifuged at 8,000 rpm for 10 min to deposit the bacteria for the following steps. Precipitated bacteria were then treated with 100 μL of 1 % (wt) OsO_4 aqueous solution for 30 min in dark. The bacteria were then washed with PBS solution two times to remove any residual OsO_4. The bacteria were subsequently dehydrated by ethanol. After that, 10 μL of the bacterial ethanol suspension was dropped on a copper tape and coated with gold before SEM analysis.

5.3 Results and Discussion

5.3.1 Photoreactivity of RF and FMN

Vitamin B_2 derivatives do not have an aromatic ketone structure that is known for its high photoreactivity in type I and type II photoreactions. The photoactivity of VB_2 is due to the isoalloxazine moiety that absorbs light with maxima wavelengths at around 365 nm and 445 nm[6].

As shown in Figure 5.1a, under UVA or blue light irradiation, the ground-state VB_2 was excited to multiple singlet excited states (S_n) or the lowest singlet excited state (S_1) via a spin-allowed excitation process. The S_1 can be formed by S_n via the internal conversion (IC) process as well. The S_1 of flavins is highly fluorescent with a very short lifetime (around 5 ns in water at ambient temperature)[13]. Meanwhile, the S_1 of VB_2 can transform to the lowest triplet excited state (T_1) via a rapid intersystem crossing (ISC) process with a quantum yield of 0.67[6], which is relatively high although still lower than aromatic ketones. The T_1 was reported relatively long-lived with a lifetime of 15 μs in water at ambient temperature[14]. The T_1 was also recorded as a bi-radical that is much more oxidative compared with the ground-state VB_2[6]. Therefore, many biomolecules are reported to be oxidized by the T_1 of the VB_2[6]. As shown in Figures 5.1a and 5.1b, the triplet VB_2 could proceed with either type I photoreaction by abstracting a hydrogen or an electron from substrates or type II photoreaction by transferring its energy to the ground-state molecular oxygen ($^3O_2$). According to the literature, the energy transfer process between VB_2 T_1 and the oxygen to generate more oxidative singlet oxygen is highly efficient and almost diffusion controlled[6]. The singlet oxygen quantum yield of RF and FMN is similar, reaching 0.64 under UVA irradiation[5]. The T_1 of VB_2 can abstract hydrogen or an electron from substrates through the direct interaction via type I photoreaction, leading to the generation of radicals (Figure 5.1b). $RF\cdot^-$ ($FMN\cdot^-$) or RF-H· (FMN-H·) can be produced after electron abstraction or hydrogen abstraction process, respectively. The formed $RF\cdot^-$ ($FMN\cdot^-$) or RF-H· (FMN-H·) can be further oxidized by $^3O_2$ to superoxide radical anion ($\cdot O_2^-$)[6, 15-16]. The $\cdot O_2^-$ could further transform to HO· and H_2O_2. Also, after the first hydrogen abstraction, the RF-H· (or FMN-H·) could further abstract hydrogen from substrates to form the reduced flavin in the dihydroflavin form (RFH_2/$FMNH_2$), which can subsequently be oxidized by $^3O_2$ to the ground-state VB_2 accompanied with the formation of

H_2O_2[16]. The formed HO·, H_2O_2, and $^1O_2$ could oxidize biomolecules and inactivate microbes via cell wall peroxidation or nucleic acid cleavage. To better understand the photoactivity of VB_2 derivatives, their frontier molecular orbitals were computed and presented in Figures 5.1c and 5.1d.

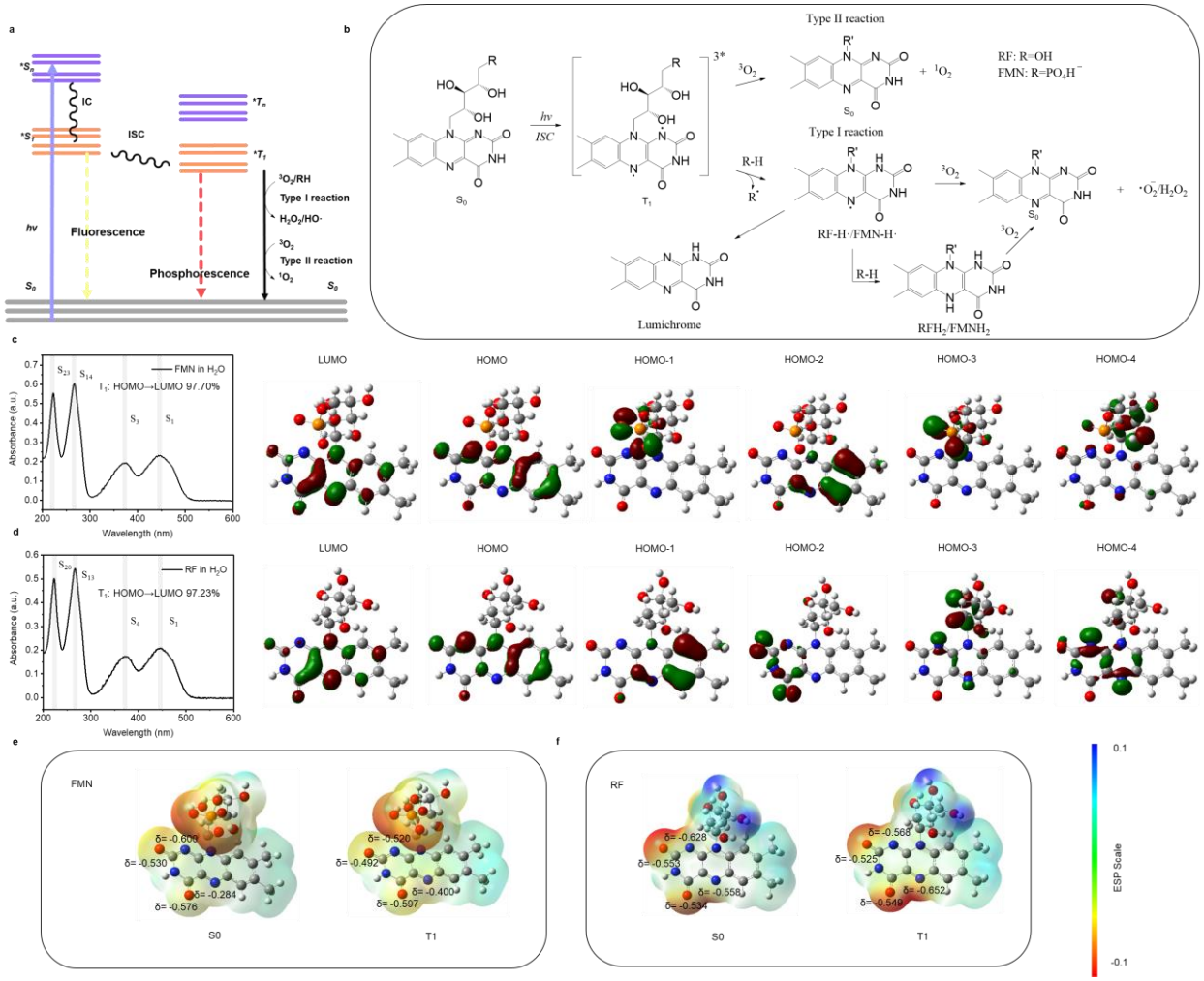

Figure 5.1. Photoreactivity of RF and FMN. (a) Schematic Jablonski diagram illustrating the photoexcitation process and following photoreactions of VB_2 derivatives. (b) Type I and type II photoreactions of VB_2 derivatives after the formation of the lowest triplet excited state. (c) UV-vis absorption spectrum of 20 μM FMN in H_2O and computational frontier molecular orbitals of FMN. HOMO: highest occupied molecular orbital; LUMO: lowest unoccupied molecular orbital. (d) UV-vis absorption spectrum of 20 μM RF in H_2O and computational frontier molecular orbitals

of RF. ESP-mapped electron density of ground-state and triplet-state (e) FMN and (f) RF. The δ is the ESP charge on the carbonyl oxygen of RF or FMN in each state.

According to Figures 5.1c and 5.1d, both FMN and RF exhibit high absorption in the UVA and blue light region (300-500 nm). Based on computation, the predominate excitation is $S_0 \rightarrow S_1$ (430.39 nm) and $S_0 \rightarrow S_3$ (357.53 nm) for FMN, and $S_0 \rightarrow S_1$ (422.97 nm) and $S_0 \rightarrow S_4$ (356.33 nm) for RF. Unlike vitamin K derivatives, the direct excitation from S_0 to S_1 reveals the high absorption of the two VB_2 derivatives under photoirradiation. The computational UV-vis spectra of FMN and RF are highly consistent with the experimental spectra (Figures 5.2a and 5.2b), which proves the accuracy of the computation method employed in this work.

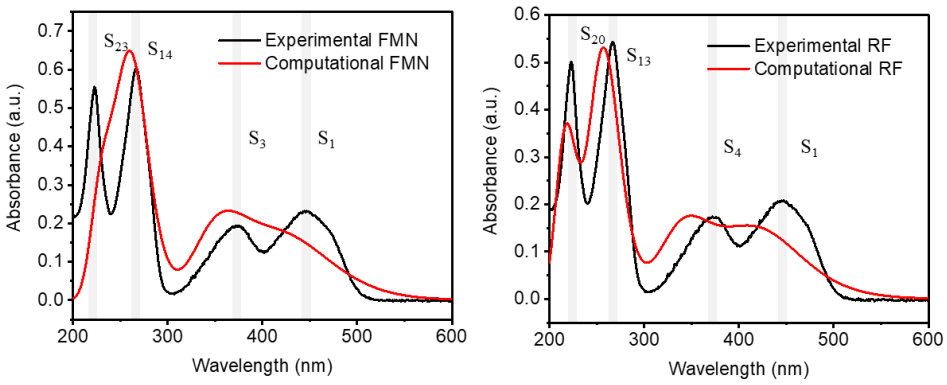

Figure 5.2. Computational UV-vis spectra of (a) FMN and (b) RF in H_2O.

Based on the computational frontier molecular orbital information (Figure 5.1c and 5.1d), the FMN T_1 was computed and proven to be formed via an electron transition from HOMO to LUMO. The electron in the nitrogen atom of the imine group (-C=N-) was excited to the π antibonding orbital, forming a bi-radical as shown in Figure 5.1b. Similarly, the RF T_1 was formed by an electron transition from the nitrogen atom of -C=N- to the carbon π antibonding orbital. Therefore, the N atom of the -C=N- in the triplet VB_2 is oxidative and active to abstract an electron

or a hydrogen from substrates, which is consistent with the literature[16-18]. Based on the computed frontier molecular orbitals, the carbonyl group does not engage in the excitation and the formation of the T_1 process, indicating that the carbonyl group may be photoinactive during the photoreaction. The oxidative property of the formed T_1 of two VB_2 derivatives was further confirmed by the ESP-mapped electron distribution of the ground state and the triplet state (shown in Figure 5.1e). The electron density of the carbonyl oxygen in the ground state and triplet state does not change much, proving the inactivity of the carbonyl group during the photoirradiation and photoreaction process. The electron density of the nitrogen atom in -C=N- in FMN changes from -0.600 to -0.520, indicating the electron deficiency on the nitrogen atom in the -C=N- functional group. Similarly, the electron density of the nitrogen atom in the -C=N- group in RF changes from -0.628 to -0.568. The less negative electron density tendency of the nitrogen atom in the -C=N- group from the ground state to triplet state proves the oxidative property of the formed triplet VB_2. However, compared with the water-soluble vitamin K_3 (menadione sodium bisulfite, MSB) with an $n\pi^*$ excited T_1 in the carbonyl group (electron density from -0.438 to -0.143), the electron deficiency change in the triplet VB_2 is not significant, which indicates that the triplet VB_2 is not as oxidative as the triplet MSB.

5.3.2 Photoreactivity of the type I and type II photoreactions of FMN and RF

Based on the above analysis, FMN and RF should be able to generate H_2O_2 via type I photoreaction or produce $^1O_2$ via type II photoreaction. To investigate the H_2O_2 generation efficiency of the VB_2 derivatives, 20 μM of FMN or RF in water was placed under irradiations of CW or UVA lighting source or kept in dark. As shown in Figure 5.3a, H_2O_2 was merely produced from FMN and RF under photoirradiation (white area), whereas no H_2O_2 production was found in the dark period (the grey area). As photo exposure duration prolonged, H_2O_2 production was found

to decrease in both RF and FMN, which indicated that FMN and RF might be degraded under long-term photoirradiation. The singlet oxygen production from 2 μM of FMN or RF was also determined and shown in Figure 5.3b. No $^1O_2$ was produced in dark. As the photoirradiation duration increased, the $^1O_2$ production decreased but to a smaller degree comparing to the H_2O_2 production. For example, the H_2O_2 production reduction of FMN compared between the first 20-min and the last 20-min irradiation under CW and UVA were determined as 93.2% and 94.2%, respectively. The $^1O_2$ production reduction of FMN under CW and UVA were measured as 75.6% and 86.2%, respectively. According to the literature, RF and FMN could self-degrade to toxic lumichrome by the intramolecular hydrogen abstraction happened on the side chain[16, 19-21]. Some other byproducts such as lumiflavin could also be formed at higher pH values[21]. Comparing to RF and FMN, the produced lumichrome is a more photostable and efficient $^1O_2$ generator, whereas with a lower solubility in water[22]. Moreover, the type I photoreaction of lumichrome was proven to be not as efficient as that of RF or FMN, indicating that lumichrome was not a good generator of H_2O_2 under photoirradiation[21]. Thus, it could be explained that the pro-longed photo exposure largely decreases the production of H_2O_2 and leads to a less reduction in the $^1O_2$ production, which could be attributed to the better $^1O_2$ generation efficacy yet the worse H_2O_2 generation efficacy of the degradation product. Interestingly, although the photoreactivity of RF and FMN are reported comparable, FMN clearly exhibits more H_2O_2 and $^1O_2$ production under photoirradiation, which may partially due to the better water solubility of FMN than RF, leading to a more intimate contact between ROS detectors and the photoactive site. To further explore the photodegradation via the intramolecular hydrogen abstraction, the effect of hydrogen donor on VB_2 derivatives was determined and is shown in Figures 5.3c and 5.3d. Twenty μM of RF or FMN in water (not a hydrogen donor), ethyl acetate (EtOAc, poor hydrogen donor), and ethanol (EtOH, good hydrogen

donor) were placed under CW and UVA irradiation to detect their H_2O_2 production via the hydrogen abstraction reaction. Under CW irradiation, the H_2O_2 production of RF and FMN was identical regardless of the hydrogen donors (water, EtOAc, or EtOH). Similarly, the H_2O_2 production of RF and FMN in these solutions were the same under UVA irradiation, which proved that the hydrogen donors in the system caused a negligible impact on the hydrogen abstraction reaction. The H_2O_2 was generated from RF or FMN by the intramolecular hydrogen abstraction from the side chain, and most likely, from the α C-H next to the hydroxyl groups. The abstraction of the C-H from the side chain induces a side-chain cleavage and the isoalloxazine ring rearrangement, leading to the photodegradation and the formation of lumichrome or lumiflavin.

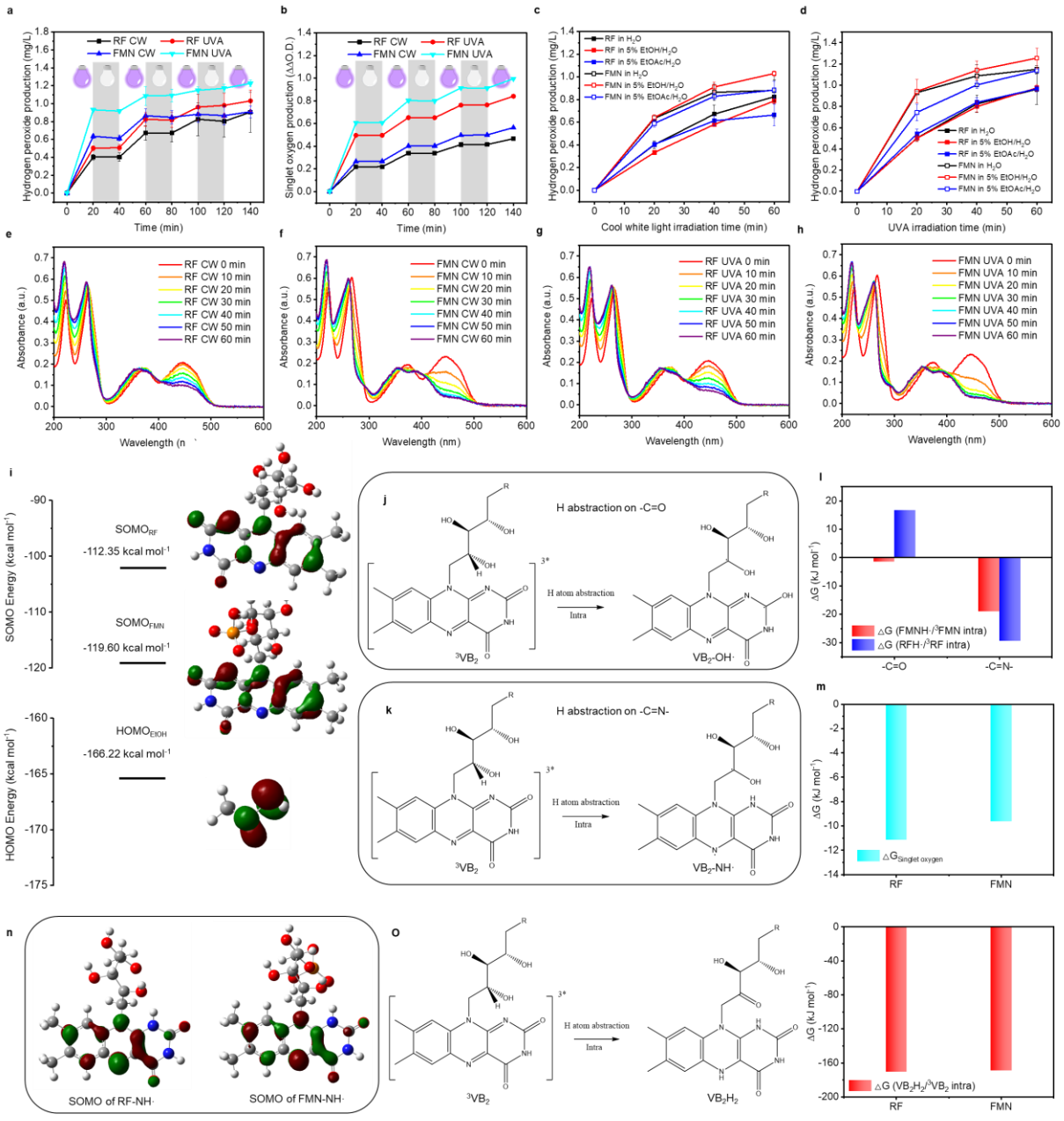

Figure 5.3. Photoreactivity of the type I and type II photoreactions of FMN and RF. (a) Hydrogen peroxide production from 20 μM of RF or FMN in H_2O and (b) singlet oxygen production from 2 μM of RF or FMN in 0.01M PBS solution under CW and UVA (365 nm) photoirradiation or dark conditions (irradiation in white and dark periods in gray). The effect of hydrogen donors on the hydrogen abstraction reaction on 20 μM of RF or FMN in various solution

systems under (c) CW and (d) UVA (365 nm) photoirradiation. Photostability of 20 μM (e and g) RF or (f and h) FMN under (e and f) CW and (g and h) UVA (365 nm) photoirradiation. (i) Orbital energy analysis on RF, FMN, and hydrogen donor (take EtOH as an example). Photoinduced hydrogen abstraction reaction on (j) carbonyl and (k) imine groups in the triplet VB_2 derivatives. (l) Gibbs free energy change of the intramolecular hydrogen abstraction reactions in the triplet VB_2 derivatives. (m) Gibbs free energy change of the singlet oxygen photosensitization reaction. (n) SOMO of the VB_2-NH·. (o) Intramolecular hydrogen abstraction in the triplet VB_2 derivatives and the Gibbs free energy change of the formed dihydroflavin (VB_2H_2).

The photostability of RF and FMN was also determined, and the results are illustrated in Figures 5.3e, 5.3f, 5.3g, and 5.3h. Both RF and FMN could be degraded under either CW or UVA (365 nm) irradiation to a large extent, even after only 10-min light exposure. UVA is a stronger trigger force on the VB_2 degradation because of the higher photoactivity of the VB_2 in generating ROS via type I or type II photoreaction under UVA irradiation (Figure 5.1a and 5.1b). Besides the intramolecular hydrogen reaction in the side chain that leads to the generation of H_2O_2, the production of $^1O_2$ could also lead to the oxidation and degradation of VB_2 derivatives[23]. Under photoirradiation, an absorption decrease was clearly noticed in the 400-500 nm region in both RF and FMN solutions. The decrease could be attributed to the photodegradation of VB_2 derivatives and the formation of the major product, lumichrome. Due to the poor water solubility of the lumichrome, its UV-vis absorption spectrum was computed and shown in Figure 5.4a. The absorption peak in the 400-500 nm region of the lumichrome disappeared due to the isoalloxazine ring rearrangement after the hydrogen abstraction on the side chain. Meanwhile, a little absorption peak increase was found in the 300-400 nm region (Figures 5.3e to 5.3h) after photoirradiation, which could be attributed to the formation of the lumiflavin that still possesses the isoalloxazine

ring and has an absorption peak at around 342.97 nm. Interestingly, RF exhibits a better photostability than FMN in water regardless of the irradiation lights (CW or UVA). This may be because that the phosphate group in FMN probably engaged in the excitation and photoreaction processes, as shown in Figures 5.1c and 5.1d. The HOMO-1 of FMN mainly locates at the phosphate group in the side chain, indicating that some electron transfer may happen from the phosphate group to the antibonding orbitals, leading to a photodegradation. Comparing to FMN, a HOMO-3 orbital on the side chain of RF was found, which means that larger light energy is needed to excite the electron in the RF side chain to transfer to the antibonding orbital. Another possible reason is that FMN has a better water solubility than RF, which enables FMN to disperse evenly and homogeneously in water, decreasing the triplet annihilation effect caused by the aggregation. In contrast, RF may self-aggregate because of its limited water solubility, which results in a triplet annihilation and a subsequent weaker photoreactivity in the water.

The semi-occupied molecular orbital (SOMO) of the triplet VB_2 derivatives and the HOMO of the hydrogen donor (EtOH) were also computed to determine the photoinduced hydrogen abstraction activity of RF and FMN (Figure 5.3i). The SOMO of RF and FMN locates at the nitrogen atom in the -C=N- because of the electron excitation from the N atom to the C atom, leaving an unoccupied site on the nitrogen atom in the -C=N- moiety. The HOMO of EtOH locates at the hydroxyl group and the α C-H, indicating the α C-H is the most electron-rich and could be most possibly abstracted by the oxidative triplet VB_2. The energy of the SOMO of triplet FMN and RF, as well as the energy of the HOMO of EtOH, were computed and depicted in Figure 5.3i. The energy gap between triplet FMN and EtOH is smaller than that between triplet RF and EtOH, indicating that the hydrogen abstraction reaction between FMN and hydrogen donors is more favorable than that between RF and hydrogen donors. This is also consistent with the H_2O_2

production of FMN and RF under photoirradiation (Figure 5.3a). In this case, the worse photostability of FMN compared with RF could be attributed to its higher photoactivity in the hydrogen abstraction reaction. Also, FMN may be a better photoinduced antimicrobial agent due to its higher ROS production comparing to RF.

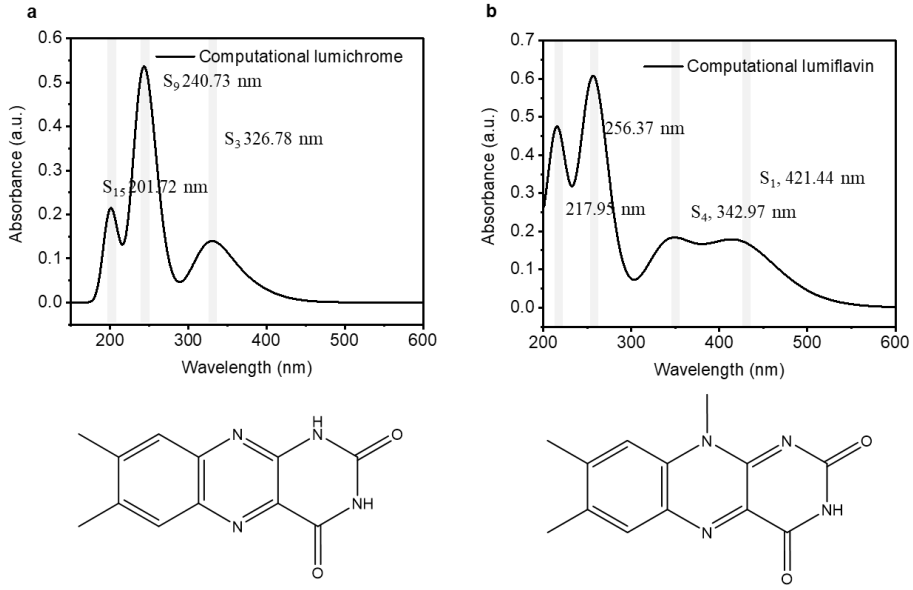

Figure 5.4. Computational UV-vis spectra of (a) lumichrome and (b) lumiflavin in H_2O.

The Gibbs free energy change of the intramolecular hydrogen abstraction reaction and singlet oxygen photosensitization was computed to demonstrate the above analysis. As shown in Figures 5.3j and 5.3k, hydrogen abstraction could potentially happen on the triplet carbonyl group or the triplet imine group. Based on the computational information in Figures 5.1c and 5.1d, the carbonyl group does not engage in the excitation and formation of the triplet VB_2 derivatives. Therefore, the hydrogen abstraction reaction on the carbonyl group or the imine group was computed and the Gibbs free energy change was concluded in Figure 5.3l to further prove the photo inactivity of the carbonyl group in VB_2 derivatives. It turned out that the carbonyl group in the triplet RF or triplet FMN was inactive to abstract hydrogen from the side chain due to the

positive or negligible negative △G (VB_2-OH·/$^3VB_2$). On the contrary, the imine group in both triplet RF and triplet FMN reveals great potential in the intramolecular hydrogen abstraction because of the negative △G (VB_2-NH·/$^3VB_2$). The computed Gibbs free energy change results are consistent with the previous conclusion that the photoactive site is the imine group in the VB_2 derivatives. The hydrogen abstraction reaction on the imine group may lead to ROS generation and photodegradation via the following reactions. As shown in Figure 5.3n, the oxidative SOMO of the formed VB_2-NH· is on the N atom in the other imine group, which is active to further abstract hydrogen intramolecularly followed by the formation of the reduced riboflavin, dihydroflavin (VB_2H_2, including RFH_2 and $FMNH_2$), which can be avidly oxidized by molecular oxygen and regenerate VB_2 derivatives with the accompanied formation of H_2O_2[15, 24-25]. The Gibbs free energy change of the VB_2H_2 formation process was computed and depicted in Figure 5.3o. The △G (VB_2H_2/$^3VB_2$) for both RF and FMN was negative, which proves the spontaneity of the intramolecular hydrogen abstraction reaction and the formation of the reduced flavin compound, as well as the H_2O_2. Moreover, the type II reaction of the triplet RF and FMN was confirmed by calculating the Gibbs free energy change of the photosensitization reaction. As shown in Figure 5.3m, both RF and FMN give a negative △G of the type II photoreaction, indicating the spontaneity of the singlet oxygen photosensitization process in the two VB_2 derivatives.

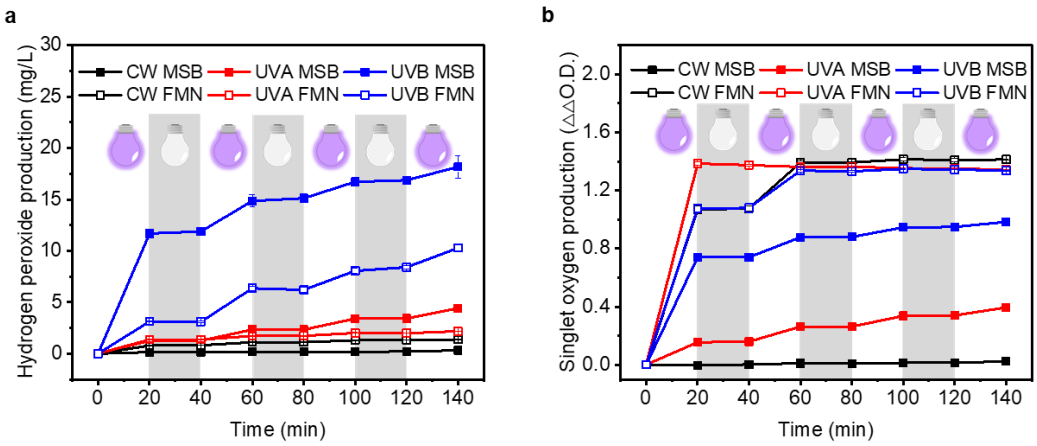

Figure 5.5. (a) Hydrogen peroxide and (b) singlet oxygen production of 20 μM FMN or MSB in 10% EtOH/H_2O solution under CW, UVA (365 nm), and UVB (312 nm) photoirradiation or dark conditions (irradiation in white and dark periods in gray).

As discussed above, the triplet state of the VB_2 derivatives was proven to be oxidative, and a certain amount of ROS was detected in RF and FMN solutions under photoirradiation. The oxidative property of the triplet VB_2 derivatives maybe not be as strong as the triplet water-soluble vitamin K_3, the MSB, based on the ESP-mapped electron density change before and after the excitation. To prove this, the H_2O_2 and $^1O_2$ production comparison between the FMN and MSB under various photoirradiation sources was performed and shown in Figures 5.5a and 5.5b. MSB exhibited very limited photoactivity under CW irradiation as discussed in Chapter 4. In contrast, FMN was photoactive under CW, UVA (365 nm), and UVB (312 nm) photoirradiation. FMN generates more H_2O_2 than MSB under CW, which is merely because of the poor light absorption of MSB in the CW region. Under UVA and UVB irradiation, MSB obviously generates more H_2O_2 than FMN. The H_2O_2 production distinction becomes the maximum under UVB irradiation. The H_2O_2 production of MSB is almost 3 times higher than that of FMN. In contrast, the $^1O_2$ production of FMN is way larger than that of MSB no matter under CW, UVA, or UVB. Especially, the $^1O_2$

production of FMN under UVA reaches a plateau after 20-min irradiation, which reveals that the produced $^1O_2$ quenched all $^1O_2$ detectors in the solution, indicating the robust $^1O_2$ generation capacity of FMN. Meanwhile, the largest $^1O_2$ production of FMN under UVA irradiation proves that FMN is most photoactive under the light in this wavelength. Overall, the productions of both H_2O_2 and $^1O_2$ prove that the triplet VB_2 is less oxidative than MSB in generating H_2O_2 via type I photoreaction yet a better $^1O_2$ generator under photoirradiation.

5.3.3 Photoinduced antibacterial function of RF and FMN in PBS solution.

The photoinduced antibacterial performance of RF and FMN in PBS solutions was evaluated by employing two typical generic bacteria including Gram-negative *E. coli* and Gram-positive *L. innocua*. Based on the above analysis, RF and FMN should potentially be used as photoinduced antibacterial agents due to the generation of the biocidal ROS under photoirradiation. In this case, 2 mM RF or FMN was dissolved in PBS solution and challenged by *E. coli* under UVA irradiation. PBS solution without VB_2 with bacteria under UVA irradiation or PBS solution with VB_2 and bacteria under dark conditions were employed as control groups to eliminate the influence caused by UVA irradiation or the VB_2 dark toxicity. As shown in Figure 5.6a, neither RF/PBS nor FMN/PBS group showed antibacterial function against *E. coli* under dark conditions after 30-min incubation. No apparent *E. coli* reduction was found in the PBS solution without RF or FMN added after 30-min UVA irradiation, which demonstrated that the short-time UVA irradiation caused non-significant bacterial inactivation. Interestingly, no obvious bacterial inactivation performance of RF or FMN was found in PBS after 30-min UVA irradiation. To exclude the concentration effect of VB_2 on the photoinduced antibacterial activity, PBS solutions with different RF or FMN concentrations (0, 0.1, 0.25, 0.5, 1, 2, and 4 mM) were challenged by *E. coli* under UVA irradiation for 30 min. As shown in Figures 5.6b and 5.6c, no apparent *E. coli*

reduction was noticed in the diluted VB_2 or concentrated VB_2 solution after 30-min UVA irradiation. Therefore, the VB_2 concentration may not be the determinant factor that causes the limited photo-induced antibacterial activity of the VB_2 in PBS. One possible reason could be the short UVA irradiation time which resulted in limited ROS production in PBS. Thus, the UVA irradiation time was prolonged to 90 min to further confirm the photoinduced antibacterial activity of VB_2 in PBS. As shown in Figure 5.6d, 2 mM of FMN in PBS was challenged by *E. coli* under UVA irradiation. Especially, the photoirradiation duration was prolonged to 60 min or 90 min to evaluate the photoinduced antibacterial activity of FMN under a longer-time UVA photoirradiation. The FMN containing PBS revealed no bacterial inactivation function under dark conditions after 90-min placement at room temperature. After 60-min UVA irradiation, a certain bacterial reduction was found in the FMN-free PBS solution (less than 1 log reduction), which may be caused by the UVA-induced protein crosslinking or DNA damage after a long-term UVA irradiation. However, no bacterial reduction was found in the UVA/FMN/PBS group, and even less than the UVA/PBS group, which demonstrated that FMN in PBS could protect bacterial cells from the UVA irradiation by absorbing the light energy. Meanwhile, the photoinduced antibacterial performance of FMN in PBS was tested against *L. innocua* under UVA irradiation, and the results are shown in Figure 5.6e. No *L. inncoua* was inactivated by FMN in PBS after 90-min UVA irradiation. The photoinduced antibacterial activity of FMN also demonstrated less oxidative triplet FMN than triplet MSB. According to the literature, a 5-log bacterial reduction (99.999%) of both *E. coli* and *L. innocua* was found in 2 mM MSB/PBS solution after 30-min UVA irradiation[26]. As discussed previously, MSB in PBS produces limited $HO\cdot$ and H_2O_2 under photoirradiation due to the lack of hydrogen donors. The active biocidal agent should be the oxidative triplet state. Therefore, the triplet MSB is much more oxidative than triplet VB_2, leading

to more bacterial inactivation. The photoinduced antibacterial activity of 2 mM FMN in 4% EtOH/PBS solution against *L. innocua* under UVA irradiation was also performed and shown in Figure 5.6f. Additional EtOH as potent hydrogen donors were added to evaluate the hydrogen donor effect on the photoinduced antibacterial activity of FMN in the solution system. After 90-min UVA irradiation, no *L. innocua* bacteria were inactivated comparing to the FMN-free/UVA group. Therefore, the photoinduced antibacterial function of VB_2 in solution is suspectable, which may be because that the distance between the produced ROS and the target microbes is too far in PBS solution due to the lack of affinity between them. Thus, the short-lived ROS could not diffuse to the microbes and function as biocidal agents efficiently.

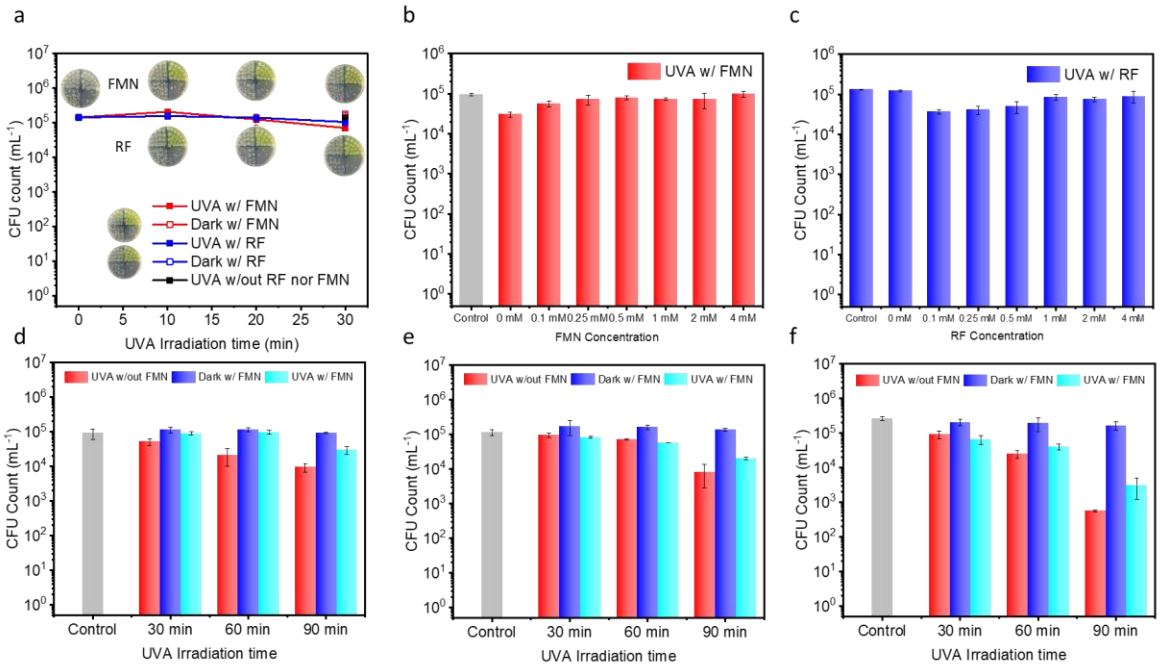

Figure 5.6. Photoinduced antibacterial function of RF and FMN in PBS solution. (a) 2 mM of RF or FMN in the PBS against *E. coli* under UVA (365 nm) irradiation. Different concentrations of (b) FMN and (c) RF in PBS against *E. coli* under UVA (365 nm) irradiation for 30 min. 2 mM of FMN in the PBS against (d) *E. coli* or (e) *L. innocua* under UVA (365 nm) irradiation for 30,

60, and 90 min. 2 mM of FMN in the 4%EtOH/PBS solution against (f) *L. innocua* under UVA (365 nm) irradiation for 30, 60, and 90 min.

To better evaluate the distance issue that may affect the photoinduced antibacterial activity of VB_2 derivatives in the solution system, another $^1O_2$ photogenerator, methylene blue (MB), was employed to inactivate *E. coli* (Figure 5.7a) and *L. innocua* (Figure 5.7b) under photoirradiation. 2 mM MB in the PBS solution exhibit certain *E. coli* and *L. innocua* reduction after 60-min CW and UVA irradiation. The higher photoinduced antibacterial activity of MB compared with FMN can be attributed to the positive charge in the MB molecular structure, which could interact with the negatively charged bacteria through electrostatic interaction[27]. The produced ROS could therefore efficiently inactivate bacterial cells due to the affinity and reduced distance between the photoactive site and the target microbes. It is worth noting that CW seems to be a stronger trigger light source than UVA irradiation for MB to inactivate bacteria, which could be explained by the $^1O_2$ production of MB under CW and UVA irradiation. As shown in Figure 5.7c, MB generated more $^1O_2$ under CW than UVA irradiation, which may be because that MB does not absorb light in the UVA region (365 nm). Interestingly, FMN produces more $^1O_2$ than MB under the same photoirradiation condition, yet a way weaker photoinduced antibacterial activity was found. This again proves that the photoinduced antibacterial function of VB_2 in the solution system is mainly determined by the distance between the photoactive site and the target microbes. To further demonstrate the hypothesis, photoinduced antibacterial activity of 2 mM FMN, 2 mM MB, and 2 mM FMN+2 mM MB in PBS solution was challenged by *E. coli* under UVA irradiation for 30 min. As shown in Figure 5.7d, 2 mM of FMN in PBS exhibit no bacterial reduction. Apparent bacterial reduction of 2 mM of MB in PBS was noticed after 30-min UVA irradiation. Surprisingly, no bacterial reduction in the 2 mM FMN+2 mM MB group was found. The addition of the FMN

with a higher $^1O_2$ production actually slows down the photoinduced antibacterial activity of the MB, which may be due to the charge neutralization between the negatively charged FMN and the positively charged MB, offsetting the electrostatic interaction between the MB and the microbes.

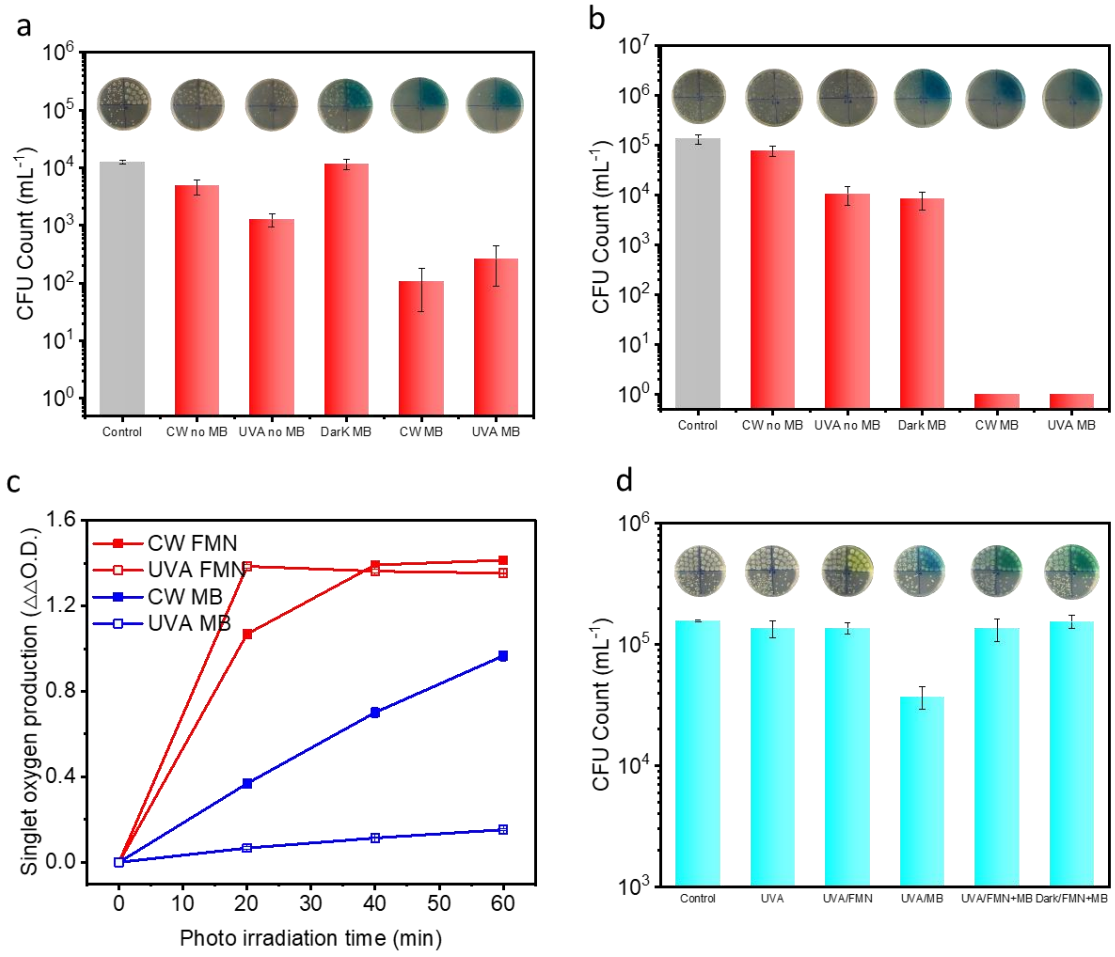

Figure 5.7. Photoinduced antibacterial activity of MB in PBS solution. 2 mM MB in PBS solution against (a) *E. coli* and (b) *L.inncoua* under CW and UVA (365 nm) irradiation for 60 min. (c) Photoinduced singlet oxygen production of 2 mM FMN or MB in PBS under CW and UVA irradiation. (d) Photoinduced antibacterial activity of 2 mM FMN, 2 mM MB, and 2 mM FMN+2 mM MB in PBS solution against *E. coli* under UVA irradiation for 30 min.

5.3.4 Photoinduced antibacterial activity of RF/PVA-co-PE and FMN/PVA-co-PE nanofibrous membranes.

Poly (vinyl alcohol-co-ethylene) (PVA-co-PE) is a hydrophilic polymer with excellent biocompatibility and has been used in the fabrication of photoinduced antibacterial and antiviral nanofibrous membranes due to its large specific surface area that could provide the photoactive chemicals with sufficient contact area with oxygen and microbes[10]. PVA-co-PE nanofibrous membranes containing benzophenone exhibited robust photoinduced antimicrobial activity against Gram-negative and Gram-positive bacteria, as well as viruses. RF or FMN was blended with PVA-co-PE polymer and electrospun into photoactive nanofibrous membranes (0.5 wt% of RF to polymer) with photoinduced antibacterial function. The morphology of the prepared VBNFMs and the fibrous diameter statistics are shown in Figures 5.8a, 5.8b, and 5.8c. An average fiber diameter from 200 nm to 250 nm was found in the nanofibrous membranes based on SEM imaging. A porous structure was noticed in all the VBNFMs, providing diffusion space for bacteria suspension and promoting better contact between the photoactive nanofibrous membranes and the microbes. No apparent hierarchies were found in either the RF/PVA-co-PE or FMN/PVA-co-PE nanofibrous membranes, indicating that the blending of RF and FMN did not change the architecture of the electrospun nanofibrous membranes. RF and FMN should be dispersed evenly and homogeneously in the PVA-co-PE polymers. To evaluate the photoinduced antibacterial activity of the prepared VBNFMs, *E. coli* and *L. innocua* were applied on the surface of the nanofibrous membranes and then placed under CW or UVA irradiation for certain durations. Bacteria on PVA-co-PE nanofibrous membranes without VB_2 under photoirradiation and bacteria on RF/PVA-co-PE or FMN/PVA-co-PE nanofibrous membranes under dark conditions were employed as control groups. The photoinduced antibacterial performance of the VBNFMs is shown in Figures 5.8d, 5.8e, 5.8f,

and 5.8g. In Figure 5.8d, no *E. coli* reduction was found in the PVA-co-PE/UVA group, demonstrating that neither PVA-co-PE nor 20-min UVA irradiation could cause bacterial inactivation. No *E. coli* reduction was found in the VBNFMs under dark conditions neither, revealing the low dark toxicity of the prepared nanofibrous membranes. In contrast, after 5-min UVA irradiation, *E. coli* on the RF/PVA-co-PE and the FMN/PVA-co-PE nanofibrous membranes were partially inactivated (90%). After 20-min UVA irradiation, a 5-log reduction of *E. coli* (99.999%) can be found on the two types VBNFMs. The photoinduced antibacterial performance of the VBNFMs was also evaluated under CW irradiation. After 20-min CW irradiation, around 2-log reduction of *E. coli* (99%) on VBNFMs was achieved (Figure 5.8e). *L. innocua* were also applied on the VBNFMs to demonstrate the non-selective photoinduced antibacterial function. As shown in Figure 5.8f, a 3-log reduction of *L. innocua* (99.9%) was achieved after 20-min UVA irradiation, which was still higher than the VBNFMs under CW irradiation (Figure 5.8g). After 20-min CW irradiation, only 1-log reduction of *L. innocua* (90%) was achieved by VBNFMs. Overall, the UVA irradiation is clearly a stronger trigger force than the CW irradiation on inducing the photoinduced antibacterial function of the VBNFMs, which is consistent with the larger ROS production of RF and FMN under UVA irradiation than CW. RF/PVA-co-PE and FMN/PVA-co-PE nanofibrous membranes exhibit comparable photoinduced antibacterial efficacy under UVA irradiation, which proves the nearly identical photoreactivity of RF and FMN in the polymer.

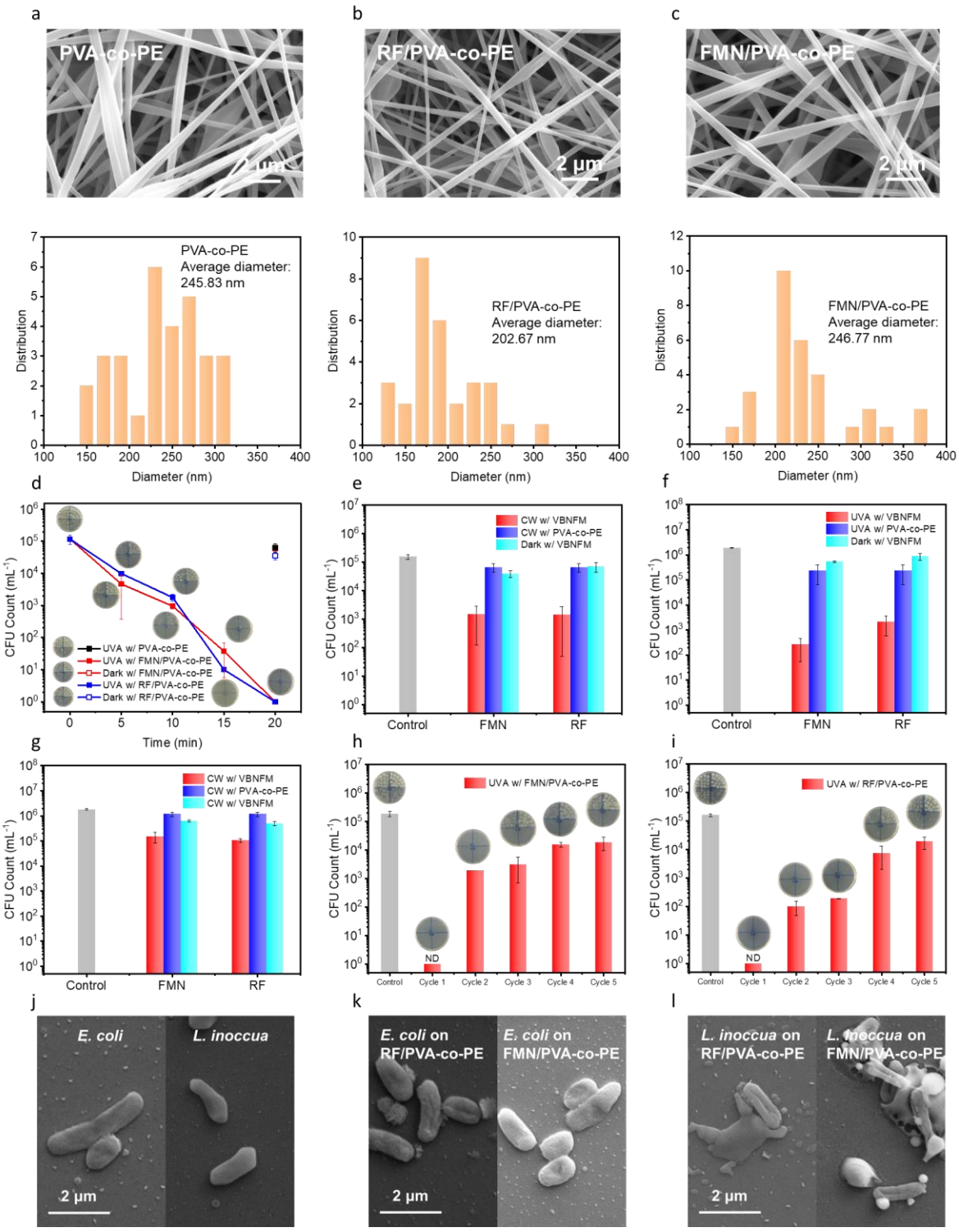

Figure 5.8. Photoinduced antibacterial activity of RF/PVA-co-PE and FMN/PVA-co-PE nanofibrous membranes. SEM images and nanofiber diameters of (a) PVA-co-PE, (b) RF/PVA-

co-PE, and (c) FMN/PVA-co-PE nanofibrous membranes (n=30). (d) Time-dependent photoinduced antibacterial activity of RF/PVA-co-PE and FMN/PVA-co-PE nanofibrous membranes against *E. coli* under UVA irradiation. (e) Photoinduced antibacterial activity of RF/PVA-co-PE and FMN/PVA-co-PE nanofibrous membranes against *E. coli* under CW irradiation for 20 min. Photoinduced antibacterial activity of RF/PVA-co-PE and FMN/PVA-co-PE nanofibrous membranes against *L.innocua* under (f) UVA and (g) CW irradiation for 20 min. Five-time cycle photoinduced bactericidal activity of (h) FMN/PVA-co-PE and (i) RF/PVA-co-PE nanofibrous membranes against *E. coli* under UVA irradiation (20 min/cycle). (j) SEM images of *E. coli* and *L. inncoua* in PBS solution. SEM images of (k) *E. coli* and (l) *L. innocua* on the FMN/PVA-co-PE and RF/PVA-co-PE nanofibrous membranes under UVA irradiation for 30 min.

The durability of the photoinduced antibacterial function of the VBNFMs was further determined by a bacterial accumulation test. The VBNFMs were challenged by *E. coli* five times under UVA irradiation. As shown in Figure 5.8h, FMN/PVA-co-PE nanofibrous membrane exhibited robust antibacterial function against *E. coli* in the first cycle. A 5-log bacterial reduction (99.999%) was found after the first-round 20-min UVA irradiation. Nevertheless, distinctive photoinduced antibacterial function decay was noticed in the second cycle. A 2-log less bacterial reduction (<99%) was achieved after the second-round 20-min UVA irradiation. Further photoinduced antibacterial function decay can be seen after the fifth cycle (<90%). Similarly, RF/PVA-co-PE nanofibrous membrane exhibits excellent photoinduced antibacterial function, and a 5-log bacterial reduction could be attained. Dramatic photoinduced antibacterial function decay was found after each photoinduced antibacterial cycle. The antibacterial function decay of the VBNFMs can be attributed to the photodegradation of RF and FMN. RF/PVA-co-PE nanofibrous membranes show slightly better durability than the FMN/PVA-co-PE nanofibrous membranes,

which could be because of the better photostability of the RF than FMN under UVA irradiation. In addition, the presence and accumulation of dead bacterial cells and the lysate of dead cells generated from each cycle of inactivation might play a protection effect over live cells by providing nutrients to the live cells or activating resistance mechanisms in live cells[28-30].

To prove the bacterial cell damage caused by the attack from oxidative ROS, SEM images of the bacteria in PBS solution or bacteria on VBNFMs under UVA irradiation were captured and shown in Figures 5.8j, 5.8k, and 5.8l. Either *E. coli* or *L. inncoa* in PBS solution maintain the intact and smooth cell structure (Figure 5.8g). In sharp contrast, bacteria on the VBNFMs under UVA irradiation for 30 min revealed the cell structure damage caused by ROS attack. Apparent cellular shrinkage was found, which proves the cell structure deformation of the bacteria on VBNFMs under UVA irradiation.

5.4 Conclusion

Photoactivity of two vitamin B_2 derivatives, riboflavin (RF) and flavin mononucleotide (FMN), was determined by combining a theoretical modeling study and wet-lab or empirical experiments. Both RF and FMN exhibit a certain amount of H_2O_2 and $^1O_2$ production via type I and type II photoreactions, respectively. RF and FMN were proven better $^1O_2$ generators yet worse H_2O_2 generators comparing to the water-soluble vitamin K_3. Under photoirradiation, both RF and FMN are photo-unstable due to the intramolecular hydrogen abstraction on the side chain or the $^1O_2$ oxidation. No photoinduced antibacterial function of RF of FMN was found in the solution systems, which may be due to the nonadjacent distance between the photoactive site and the target microbes, limiting the diffusion and function of the short-lived ROS. The apparent photoinduced antibacterial function of the electrospun RF/PVA-co-PE and FMN/PVA-co-PE nanofibrous membranes against Gram-negative *E. coli* (99.999% reduction under 20-min UVA irradiation) and

Gram-positive *L.innocua* (99.9% reduction under 20-min UVA irradiation) was observed. The biocompatible PVA-co-PE nanofibrous membrane matrix material with the ultra-high specific surface area provides photoactive VB_2 with sufficient and intimate contact with oxygen and bacteria. However, the durability of the photoinduced antibacterial function of the prepared VBNFMs is suspectable, which may be attributed to the poor photostability of RF and FMN under photoirradiation. The fabrication of the VBNFMs with high biocidal efficacy under photoirradiation may offer some insights into utilizing photoactive VB_2 as edible photoactive agents in the preparation of safe, green, and environmentally friendly photoinduced antimicrobial materials.

5.5 Reference

(1) Powers, H. J. Riboflavin (Vitamin B-2) and Health. *The American Journal of Clinical Nutrition* **2003,** *77* (6), 1352-1360.

(2) Saedisomeolia, A.; Ashoori, M. Riboflavin in Human Health: A Review of Current Evidences. *Advances in Food and Nutrition Research* **2018,** *83*, 57-81.

(3) Liu, T.; Soong, S.; Wilson, N. P.; Craig, C. B.; Cole, P.; Macaluso, M.; Butterworth, C. A Case Control Study of Nutritional Factors and Cervical Dysplasia. *Cancer Epidemiology and Prevention Biomarkers* **1993**, *2* (6), 525-530.

(4) Ball, G. Flavins: Riboflavin, FMN, and FAD (Vitamin B_2). *Vitamins in Foods: Analysis, Bioavailability and Stability* **2006**, 165-175.

(5) Knak, A.; Regensburger, J.; Maisch, T.; Bäumler, W. Exposure of Vitamins to UVB and UVA Radiation Generates Singlet Oxygen. *Photochemical & Photobiological Sciences* **2014,** *13* (5), 820-829.

(6) Cardoso, D. R.; Libardi, S. H.; Skibsted, L. H. Riboflavin as a Photosensitizer. Effects on Human Health and Food Quality. *Food & Function* **2012,** *3* (5), 487-502.

(7) Liang, J.-Y.; Yuann, J.-M. P.; Cheng, C.-W.; Jian, H.-L.; Lin, C.-C.; Chen, L.-Y. Blue Light Induced Free Radicals from Riboflavin on *E. coli* DNA Damage. *Journal of Photochemistry and Photobiology B: Biology* **2013,** *119*, 60-64.

(8) Su, L.; Huang, J.; Li, H.; Pan, Y.; Zhu, B.; Zhao, Y.; Liu, H. Chitosan-Riboflavin Composite Film Based on Photodynamic Inactivation Technology for Antibacterial Food Packaging. *International Journal of Biological Macromolecules* **2021,** *172*, 231-240.

(9) Xu, F.; Li, J.; Zhu, T.-T.; Yu, S.-S.; Zuo, C.; Yao, R.-S.; Qian, H.-S. A New Trick (Hydroxyl Radical Generation) of an Old Vitamin (B_2) for Near-Infrared-Triggered Photodynamic Therapy. *RSC Advances* **2016,** *6* (104), 102647-102656.

(10) Si, Y.; Zhang, Z.; Wu, W.; Fu, Q.; Huang, K.; Nitin, N.; Ding, B.; Sun, G. Daylight-Driven Rechargeable Antibacterial and Antiviral Nanofibrous Membranes for Bioprotective Applications. *Science Advances* **2018,** *4* (3), eaar5931.

(11) Liu, N.; Sun, G. Production of Reactive Oxygen Species by Photoactive Anthraquinone Compounds and Their Applications in Wastewater Treatment. *Industrial & Engineering Chemistry Research* **2011,** *50* (9), 5326-5333.

(12) Kraljić, I.; Mohsni, S. E. A New Method for the Detection of Singlet Oxygen in Aqueous Solutions. *Photochemistry and Photobiology* **1978,** *28* (4-5), 577-581.

(13) Decker, E. A.; Elias, R. J.; McClements, D. J. *Oxidation in Foods and Beverages and Antioxidant Applications: Management in Different Industry Sectors* **2010.**

(14) Lu, C.; Lin, W.; Wang, W.; Han, Z.; Yao, S.; Lin, N. Riboflavin (VB_2) Photosensitized Oxidation of 2′-Deoxyguanosine-5′-Monophosphate (DGMP) in Aqueous Solution: A Transient Intermediates Study. *Physical Chemistry Chemical Physics* **2000,** *2* (3), 329-334.

(15) Insińska-Rak, M.; Sikorski, M. Riboflavin Interactions with Oxygen—a Survey from the Photochemical Perspective. *Chemistry–A European Journal* **2014,** *20* (47), 15280-15291.

(16) Schnellbaecher, A.; Binder, D.; Bellmaine, S.; Zimmer, A. Vitamins in Cell Culture Media: Stability and Stabilization Strategies. *Biotechnology and Bioengineering* **2019,** *116* (6), 1537-1555.

(17) Bialas, C.; Barnard, D. T.; Auman, D. B.; McBride, R. A.; Jarocha, L. E.; Hore, P.; Dutton, P. L.; Stanley, R. J.; Moser, C. C. Ultrafast Flavin/Tryptophan Radical Pair Kinetics in a Magnetically Sensitive Artificial Protein. *Physical Chemistry Chemical Physics* **2019,** *21* (25), 13453-13461.

(18) Choe, E.; Huang, R.; Min, D. B. Chemical Reactions and Stability of Riboflavin in Foods. *Journal of Food Science* **2005,** *70* (1), R28-R36.

(19) Holzer, W.; Shirdel, J.; Zirak, P.; Penzkofer, A.; Hegemann, P.; Deutzmann, R.; Hochmuth, E. Photo-Induced Degradation of Some Flavins in Aqueous Solution. *Chemical Physics* **2005,** *308* (1-2), 69-78.

(20) Neacsu, M. V.; Ionita, G.; Topala, C.; Oprea, E.; Tecuceanu, V.; Matei, I. Poly (Ethylene Glycol)/β-Cyclodextrin Covalent Gel Networks: Host Matrices for Studying Radical Processes in Plant Extract–Riboflavin Systems Following UV Irradiation. *Chemical Papers* **2017,** *71* (3), 607-616.

(21) Remucal, C. K.; McNeill, K. Photosensitized Amino Acid Degradation in the Presence of Riboflavin and Its Derivatives. *Environmental Science & Technology* **2011,** *45* (12), 5230-5237.

(22) Bergh, V.; Bruzell, E.; Hegge, A.; Tønnesen, H. Influence of Formulation on Photoinactivation of Bacteria by Lumichrome. *Die Pharmazie-An International Journal of Pharmaceutical Sciences* **2015,** *70* (9), 574-580.

(23) Huang, R.; Kim, H. J.; Min, D. B. Photosensitizing Effect of Riboflavin, Lumiflavin, and Lumichrome on the Generation of Volatiles in Soy Milk. *Journal of Agricultural and Food Chemistry* **2006,** *54* (6), 2359-2364.

(24) Messner, K. R.; Imlay, J. A. Mechanism of Superoxide and Hydrogen Peroxide Formation by Fumarate Reductase, Succinate Dehydrogenase, and Aspartate Oxidase. *Journal of Biological Chemistry* **2002,** *277* (45), 42563-42571.

(25) Shibata, S.; Suenobu, T.; Fukuzumi, S. Direct Synthesis of Hydrogen Peroxide from Hydrogen and Oxygen by Using a Water-Soluble Iridium Complex and Flavin Mononucleotide. *Angewandte Chemie International Edition* **2013,** *52* (47), 12327-12331.

(26) Zhang, Z.; Wisuthiphaet, N.; Nitin, N.; Wang, L.; Kawakita, R.; Jeoh, T.; Sun, G. Photoactive Water-Soluble Vitamin K: A Novel Amphiphilic Photoinduced Antibacterial Agent. *ACS Sustainable Chemistry & Engineering* **2021,** *9* (24), 8280-8294.

(27) Xing, C.; Xu, Q.; Tang, H.; Liu, L.; Wang, S. Conjugated Polymer/Porphyrin Complexes for Efficient Energy Transfer and Improving Light-Activated Antibacterial Activity. *Journal of the American Chemical Society* **2009,** *131* (36), 13117-13124.

(28) Corchero, J. L.; Cubarsí, R.; Vila, P.; Arís, A.; Villaverde, A. Cell Lysis in Escherichia Coli Cultures Stimulates Growth and Biosynthesis of Recombinant Proteins in Surviving Cells. *Microbiological research* **2001,** *156* (1), 13-18.

(29) Takano, S.; Pawlowska, B. J.; Gudelj, I.; Yomo, T.; Tsuru, S. Density-Dependent Recycling Promotes the Long-Term Survival of Bacterial Populations During Periods of Starvation. *MBio* **2017,** *8* (1), e02336-16.

(30) Bhattacharyya, S.; Walker, D. M.; Harshey, R. M. Dead Cells Release a 'Necrosignal'that Activates Antibiotic Survival Pathways in Bacterial Swarms. *Nature communications* **2020,** *11* (1), 1-12.

Chapter 6. Conclusion

In this dissertation, the photochemistry and photochemical properties of a series of vitamin K and vitamin B derivatives were thoroughly studied and discussed. These vitamins include lipophilic vitamin K_1, vitamin K_2, vitamin K_3, and vitamin K_4, as well as water-soluble vitamin K_3 (MSB), riboflavin (RF), and flavin mononucleotide (FMN). A combination of theoretical models and well-designed experiments was employed to predict the photochemistry of vitamins and then experimentally confirm the speculative photochemical property. Some vitamin derivatives could efficiently generate oxidative triplet excited state (T_1) via rapid intersystem crossing (ISC) process under photoirradiation. Various reactive oxygen species (ROS) including hydroxyl radicals ($HO\cdot$), hydrogen peroxide (H_2O_2), and singlet oxygen ($^1O_2$) can be efficiently produced from vitamin T_1 with the presence of oxygen ($^3O_2$) via type I or type II photoreaction. The formed active species could non-selectively inactivate diverse microorganisms including bacteria and viruses. Meanwhile, the excellent photoinduced antimicrobial durability of some aromatic ketone vitamin derivatives was demonstrated, indicating the sustainable and recyclable photochemical reactions of the unique structure.

Among the lipophilic vitamin K derivatives, vitamin K_3 (menadione, VK_3) was proven the most efficient in generating ROS under either daylight (D65, 300-800 nm), UVA (365 nm), or UVB (312 nm) irradiation. Vitamin K_1 and vitamin K_2 exhibit comparable photoreactivity due to their similar molecular structures, which significantly lowers the photoreactivity of the two vitamin Ks due to the intramolecular electron transfer from the side-chain double bond to the carbonyl group, leading to the competition with the ISC process. Vitamin K_4 reveals poor photoactivity under either daylight or UVA irradiation because of its limited absorption in these regions. Compared with UVA and UVB irradiation, daylight provides VK_3 with weaker photoreactivity in

generating ROS, yet still triggers the excellent photoinduced antibacterial performance of VK_3 against both Gram-negative *E. coli* (99.9999% bacterial reduction in 60-min daylight irradiation) and Gram-positive *L. innocua* (99.999% bacterial reduction in 90-min daylight irradiation). Especially, VK_3 retains the highly efficient photoinduced antibacterial function (99.9999% bacterial reduction against *E. coli* and 99.999% against *L. inncoua*) even after 7 times repeated exposure to daylight irradiation and bacteria suspension. Inspired by the excellent photoactivity of the vitamin K derivatives, VK_1, VK_3, and VK_4 were blended with biocompatible poly (vinyl alcohol-co-ethylene) (PVA-co-PE) and electrospun into nanofibrous membranes, respectively. The prepared VK_3/PVA-co-PE nanofibrous membranes exhibit better ROS production comparing to VK_1 or VK_4 blended PVA-co-PE nanofibrous membranes under daylight, UVA, or UVB irradiation. VK_3/PVA-co-PE nanofibrous membranes show robust non-selective antimicrobial activity against Gram-negative *E. coli* (99.99999% bacterial reduction in 30-min daylight irradiation), Gram-positive *L. innocua* (99.9999% bacterial reduction in 60-min daylight irradiation), T7 bacteriophage virus (99.9999% viral reduction in 30-min daylight irradiation), and feline infectious peritonitis coronavirus (FIPV) (99.9% viral reduction in 30-min daylight irradiation). Moreover, the VK_3/PVA-co-PE nanofibrous membranes exhibit excellent durability against bacteria and T7 bacteriophage (99.9999% reduction after 5 cycles), which again proves the photoactivity of VK_3 we predicted.

The photochemistry and photochemical properties of the water-soluble vitamin K_3 (menadione sodium bisulfite, MSB) were also studied and discussed for the first time. MSB was proven most photoactive under UVB (312 nm) and less photoactive under UVA (365 nm), yet least photoactive under cool white (370-750 nm) irradiation. A certain amount of ROS including $HO\cdot$, H_2O_2, and $^1O_2$ could be detected from MSB under proper photoirradiation. Meanwhile, the

photoactivity of the water-soluble VK_3 was proven less photoactive than the lipophilic VK_3 under UVA irradiation, which is rationalized to the better absorption of the lipophilic VK_3 in the UVA region. Under UVA irradiation, MSB could non-selectively inactivate Gram-negative *E. coli* (99.999% bacterial reduction in 30 min) and Gram-positive *L. innocua* (99.999% bacterial reduction in 30 min) in the absence of hydrogen donors, indicating that triplet MSB is extremely oxidative and lethal to microorganisms. Meanwhile, the durability of MSB was proven with unchanged photoinduced antibacterial efficacy (99.999%) after 5 times of repeated exposure to UVA irradiation and bacterial suspension. Interestingly, organic solvent plays a significant role in the photoinduced antibacterial activity of MSB by tuning the distance between the photoactive MSB and the target microorganisms. The intimate contact between the photoactive site and bacteria provided by the organic solvent could promote the diffusion and function of the short-lived active species produced under photoirradiation.

Water-soluble vitamin B_2 (VB_2) derivatives, including riboflavin (RF) and flavin mononucleotide (FMN), were also proven photoactive in generating H_2O_2, and $^1O_2$ under photoirradiation. UVA (365 nm) was proven a better light source compared with cool white (370-750 nm) irradiation on the photoinduced generation of ROS from the vitamin B_2 derivatives. Comparing to vitamin K derivatives, VB_2 derivatives seem to be a better $^1O_2$ generator yet a less efficient H_2O_2 producer under photoirradiation due to the less-oxidative triplet excited state. Dramatic photodegradation of RF and FMN was found due to the intramolecular hydrogen abstraction on the ribityl side chain. Neither RF nor FMN in the solution system exhibits effective antibacterial activity under UVA irradiation, which could be because of the non-adjacent contact between the photoactive VB_2 and the bacteria due to the lack of affinity in the solutions. Therefore, RF and FMN were further blended with biocompatible PVA-co-PE and electrospun into

nanofibrous membranes (VBNFMs) with porous structure and ultra-high specific surface area that could provide the VB_2 and bacteria with sufficient and intimate contact. The prepared VBNFMs show apparent antibacterial activity against Gram-negative *E. coli* (99.999% bacterial reduction in 20 min) and Gram-positive *L. innocua* (99.9% bacterial reduction in 20 min) under UVA irradiation. However, reduced photoinduced antibacterial activity (90% bacterial reduction) of the VBNFMs was noticed after five-time exposures to UVA and bacteria suspension. The reduced antibacterial function of the VBNFMs could be attributed to the photodegradation of VB_2 in the nanomaterials.